

ABSTRACT

LI, YIZHEN. Seasonal and Interannual Variability of the Gulf of Maine Coastal Circulation and its Couplings with Regional Harmful Algal Blooms. (Under the direction of Dr. Ruoying He.)

In situ observations including long-term moored measurements and multi-year gulf-wide ship survey data are used along with realistic coupled bio-physical ocean model simulations to study interannual variability of surface wind, river runoff, and hydrographic conditions in the Gulf of Maine and their couplings with the *Alexandrium fundyense* blooms in the region. Complex transport pathways in the GOM are examined by numerical surface particle trackings based on realistic circulation hindcast, and are further quantified using Lagrangian probability density function, the connectivity matrix, source and destination functions. Results show that the interannual variability in coastal connectivity has a strong impact on the spatial distribution of *A. fundyense* blooms. Comparisons of coastal currents to toxicity closure maps of *A. fundyense* blooms also suggest a linkage between alongshore transport and the downstream extent of toxicity.

During the 10-year (2002-2011) period this study has focused on, several years stand out by having anomalous hydrographic conditions in response to local and upstream/offshore forcing variability. Due to limitations in initial, boundary, and surface forcing conditions, it is often a challenging task to predict these anomalous conditions using regional ocean models. As a proof-of-concept study, an advanced 4-dimensional variational data assimilation (4D-Var) method is applied to hindcast the anomalous water mass and circulation conditions

in summer 2012. By assimilating satellite and *in situ* observations in the GOM, the 4DVar system dynamically adjusts and incrementally refines model boundary condition, initial condition and surface forcing, thereby allowing for significant improvement in the prediction skill of our GOM regional ocean model.

The GOM regional circulation model is coupled with *A. fundyense* population dynamic model to study the germination, initiation, and development of an extensive *A. fundyense* bloom in 2008. As our previous bloom hindcast studies for 2005 and 2006, the coupled model is found to be capable of reproducing the hydrodynamics and the temporal and spatial distributions of *A. fundyense* cell concentration reasonably well. Model hindcast solutions are further used to diagnose 3-dimensional structures of the bloom, and physical and biological factors controlling the bloom dynamics. Results support the hypothesis that cyst abundance is a first-order predictor of overall magnitude of the *A. fundyense* bloom, and that ocean advections have significant impact on the cell concentration in the western Gulf of Maine.

Seasonal and Interannual Variability of the Gulf of Maine Coastal Circulation and its
Couplings with Regional Harmful Algal Blooms

by
Yizhen Li

A dissertation submitted to the Graduate Faculty of
North Carolina State University
in partial fulfillment of the
requirements for the Degree of
Doctor of Philosophy

Marine, Earth, and Atmospheric Sciences

Raleigh, North Carolina

2012

APPROVED BY:

Dr. Daniel. L. Kamykowski

Dr. Dennis J. McGillicuddy, Jr.

Dr. Ping-Tung Shaw

Dr. Gerald J. Janowitz

Dr. Ruoying He
Chair of Advisory Committee

BIOGRAPHY

Yizhen Li was born in a coastal city in the northeastern China. He received his bachelor's degree in marine science in 2004 and a master's degree in physical oceanography in 2007 at Ocean University of China. He joined the Department of Marine, Earth, and Atmospheric Sciences at North Carolina State University in fall 2007 to continue his graduate education. He received a M.S. in Marine Science in 2009, passed the Ph.D. preliminary exams in spring 2011, and is expected to complete his Ph.D. degree in August, 2012.

ACKNOWLEDGEMENTS

I am very grateful to the faculties and staffs in MEAS department for their generous assistance which makes my study possible. I am most grateful to my advisor, Dr. Ruoying He for his scientific insights, great instructions, and tireless research guidance, which taught me the way of doing science. Thanks for all resources and financial support he invested on me during past five years. I thank Dr. McGillicuddy, Dr. Kamykowski, Dr. Shaw, Dr. Janowitz, and Dr. Schnetzer for serving as my committee members. Thanks for all your useful comments and suggestions on my research. Special thanks to Dr. McGillicuddy for his guidance on the research directions and help with paper revisions. I am also grateful to Dr. D. Anderson (WHOI), Mr. J. Manning (NOAA), Dr. B. Powell (U. Hawaii) for many enlightening research discussions. Thanks to every member of Ocean Observing and Modeling Group, especially to Dr. K. Chen for useful discussions on data assimilation. I thank my parents Qi Li and Yunyu Zhao, who gave birth to me, strive to raise me up, and are always being supportive regardless what I do. I'd like to dedicate this dissertation to my beloved wife Hui Qian and our naughty son, Dennis Li. May my friendship with Shujiang Li, Meng Wang, Lei Wang be forever.

Research support provided by NOAA EOHAB-GOMTOX program is much appreciated.

TABLE OF CONTENTS

LIST OF TABLES	viii
LIST OF FIGURES	xi
Chapter I: Research Background	1
1.1 Mean circulation in the Gulf of Maine	1
1.2 Seasonal variability of coastal circulation	3
1.3 Interannual variability	6
1.4 The Harmful Algal Bloom and the Paralytic Shellfish Poisoning (PSP).....	8
1.5 The <i>A. fundyense</i> bloom dynamics.....	9
1.5.1 Historical observational studies of the <i>A. fundyense</i> blooms	10
1.5.2 Modeling studies of the <i>A. fundyense</i> Blooms	13
1.6 Research Objectives.....	16
References.....	20
Chapter II: Seasonal and Interannual Variability in Gulf of Maine Hydrodynamics: 2002-2011	27
Abstract.....	27
2.1 Introduction.....	28
2.2 Methods.....	31
2.3 Results.....	32

2.3.1 Seasonal and Interannual Variability in Wind forcing	32
2.3.2 River Discharge	34
2.3.3 Coastal Hydrography and Currents from moored observations	35
2.3.3.1 Temperature and Salinity	35
2.3.3.2 Salinity	36
2.3.3.3 Stratification.....	37
2.3.3.4 Hydrographic variability in Jordan Basin and the Northeast Channel	38
2.3.3.5 Currents.....	39
2.3.4 Ship-observed hydrography and geostrophic current	40
2.4. Discussion.....	41
2.4.1 Interannual variability in hydrodynamics	41
2.4.2 Impacts on coastal PSP toxicity	43
2.5. Summary and Conclusion.....	46
Acknowledgements.....	47
References.....	49
Chapter III: The Coastal Connectivity in the Gulf of Maine in Spring and Summer of 2004 -2009	53
Abstract.....	53
3.1 Introduction.....	55

3.1 Introduction.....	55
3.2 Data and methods.....	58
3.2.1 Hydrodynamic model, observations, and particle tracking tool	58
3.2.2 Lagrangian PDFs	62
3.3 Results.....	64
3.3.1 Particle Release.....	64
3.3.2 Validation of Circulation Model	65
3.3.3 Mean Lagrangian PDFs	67
3.3.4 Mean Connectivity Matrix, Source and Destination Strength.....	69
3.4 Discussions	73
3.4.1 Variability of the connectivity.....	73
3.4.2 Interannual variability in the source and destination locations at different advection time scales	75
3.4.3 Caveat on the model skill and particle tracking.....	77
3.5 Summary.....	78
Acknowledgements.....	81
References.....	82
Chapter IV: Variational Data Assimilative Modeling Investigation of the Gulf of Maine Coastal Circulation in Spring and Summer 2010	87

Abstract.....	87
4.1 Introduction.....	88
4.2 Data and Methods.....	90
4.2.1 Model settings.....	90
4.2.2 4D Variational Data Assimilation System.....	93
4.2.3 Assimilated data.....	96
4.2.4 Data Assimilation Setup.....	98
4.2.4.1 Covariance modeling.....	98
4.2.4.2 Assimilation window.....	99
4.3 Results.....	100
4.3.1 Cost function reduction.....	100
4.3.2 Effectiveness of the 4D-Var Algorithm.....	102
4.3.2.1 Surface Performance.....	102
4.3.2.2 Subsurface T/S statistics.....	103
4.3.2.3 Model skill assessment.....	105
4.4 Discussion.....	108
4.1 Depth-averaged temperature budget analysis.....	108
4.4.2 Evolution of the water mass and coastal circulation in the GOM.....	110
4.4.3 Co-variability of Currents and surface elevation.....	112

4.4.4 Advection time scale of Scotian Shelf Water (SSW) to the coastal GOM.....	114
4.5 Summary and future work	116
Acknowledgement	119
References.....	119
Chapter V: Diagnosing the Evolution of 2008 Alexandrium fundyense Bloom in the Gulf of	
Maine using in-situ Observations and Coupled Biophysical Model Simulations	
Abstract.....	127
5.1 Introduction.....	128
5.2 Data and Method.....	130
5.2.1 In-situ observations.....	130
5.2.2 Coupled bio-physical model	131
5.3 Model-Data Comparisons	135
5.3.1 Mooring Data.....	135
5.3.2 Surface Cell Concentration.....	136
5.3.3 Vertical Structure of Bloom	139
5.4. Discussions	140
5.4.1 Advection of cell flux.....	140
5.4.2 Germination potential and germination flux.....	142
5.4.3 Principal modes for the cell concentrations	143

5.5. Summaries.....	145
Acknowledgements.....	147
References.....	149
Chapter 6. Concluding Remarks.....	153
APPENDIX.....	211
Appendix: A. fundyense model parameterizations	212

LIST OF TABLES

Table 2.1. Geostrophic transports in 2005, 2006, 2007 and 2010. Each value is obtained by integrating the alongshelf geostrophic velocity over the upper 5-20m along a transect off the Casco Bay (see blue line in Figure1).....	155
Table 5.1. Monthly-mean and standard deviation (STD) of the integrated cell advection flux along various transects. The integrated cell advection flux was defined as $\int_0^x \int_{-H}^0 uc dx dz$, where x is the distance from initial station, and z the water depth. The flux is integrated from onshore to offshore and from 50m to surface. For cross-shelf transect, the cell flux is positive northeastward; While for the alongshore transect (e.g., D1D2), the cell flux is positive shoreward, and vice versa. Transect and station locations are shown in Figure 1. Units for the cell flux: cells·s ⁻¹	155

LIST OF FIGURES

Figure 1.1. Schematic showing the summer near-surface circulation in the GOM. Several branches are present, namely the WMCC, EMCC, as well as the nearshore Gulf of Maine Coastal Plume (GOMCP). Figure from Pettigrew et al., 2005.	156
Figure 1.2. A cartoon showing the life cycle of <i>A. fundyense</i> bloom. Courtesy of Donald Anderson, Woods Hole Oceanographic Institution.	157
Figure 1.3. (a) Cyst abundance 2004–2009. Minimum and maximum values are indicated in each panel. Open circles denote the locations of sediment samples used to construct the maps. (b) Spatial extent of PSP closures 2005–2010. Figure from <i>McGillicuddy et al.</i> , 2011.	158
Figure 2.1. Locations of the NERACOOS buoys (pink squares) and CTD stations (red dots) of gulf-wide ship surveys (a) <i>Oceanus</i> 412 in 2005, (b) <i>Oceanus</i> 425 in 2006, (c) <i>Endeavor</i> 435/437 in 2007 and <i>Oceanus</i> (d) 460/465/467 and <i>Endeavor</i> 476 in 2010, respectively. Also shown are 50-m, 100-m and 200-m isobaths. The blue solid line indicates the transect off Casco Bay that is used for computing geostrophic current transport shown in Table 1.	159
Figure 2.2. Cumulative upwelling indices (CUI) for 2004-2011 at (a) WGOM buoy B and (b) EGOM buoy I. The unit for the indices is $m^3 \times (100m)^{-1} \times 86400$	160
Figure 2.3. Monthly (April-July) and seasonal total river runoff of 4 major rivers (Canadian portion of the St. John, Penobscot, Androscoggin and Kennebec, and Merrimack) in the GOM. Units: $10^4 m^3 s^{-1}$	161
Figure 2.4. Daily river discharge time series for the St. John (U.S. portion), Penobscot, Androscoggin and Kennebec, and Merrimack rivers. Grey shaded areas indicate the summer months (February to August) of each year. Units: $10^4 m^3 s^{-1}$	162
Figure 2.5. Monthly mean near-surface (2-m) water temperature in April-July 2002-2011 observed at NERACOOS buoys B, E, I. Also shown by black open circles and corresponding error bars are the mean seasonal cycle and the associated standard deviations. Unit: °C.	163
Figure 2.6. Same as Figure 5, but for near-surface salinity.	164
Figure 2.7. Same as Figure 5 and Figure 6, but for the Vaisala frequency (N^2) based on density at 2-m and 50-m. Unit: $S^{-2} * 10^{-4}$	165
Figure 2.8. Time series of observed temperature at NERACOOS buoy M in Jordan Basin, February-September, 2004-2011. Black circles indicate the depths where observations are available. A 60-hour low-pass filter was applied to the time series to remove high-frequency noise.	166
Figure 2.9. Same as Figure 2.8, but for the salinity time series at buoy M.	167
Figure 2.10. T-S diagrams for deep waters (depth > 100m) in Jordan Basin. Temperature	

and salinity data are from buoy M in February-September, 2004-2011. Vertices of the mixing triangle are canonical end-member water-mass properties of Warm Slope Water (WSW), Scotian Shelf Water (SSW), and Labrador Slope Water (LSW) as described by *Smith et al.* (2001). Dotted contour lines represent density anomalies. 168

Figure 2.11. Monthly mean alongshore velocity in April-July, 2002-2010 observed at NERACOOS buoys B, E, I. The alongshore current is positive southwestward. Unit: cm s^{-1} 169

Figure 2.12. Dynamic height (in meters) and associated surface geostrophic velocity based on hydrographic data collected in May 2005, June 2006, June 2007, May1-10, 2010, May 27-June 3, 2010, June 30- July 8, 2010, and July 28- August 7, 2010, respectively. The dynamic height was computed assuming the level of no motion at bottom, integrated from the bottom to the surface. 170

Figure 3.1. Locations of 7 particle release regions in the Gulf of Maine, which include the Massachusetts Bay (Mass, in grey), the western Gulf of Maine (WGOM, in brown) coastal area, the eastern Gulf of Maine release (EGOM, in blue) coastal area, the Bay of Fundy (BOF, in red), the Wilkinson Basin (WK, in purple), the Jordan basin (JB, in orange), and the area Off the Penobscot Bay (OFFPB, in cyan). For each site, the initial release points are chosen based on a 6-km radius circular area. Red rectangular represents the location of NERACOOS buoy A and B. Also shown are the coastal bathymetry contours (50m, 150m, and 200m), and other important geographic sites and locations of five major rivers in the GOM. 171

Figure 3.2. Comparisons between model simulated and observed monthly surface currents at buoy B (upper 2 panels) and at buoy A (lower 2 panels). Each vector current time series is accompanied by its mean east and north velocity components (left-hand couplet), and each model/data comparison is quantified by its complex correlation coefficient r , phase angle difference θ (angular deviation of the model vectors from the data vector measured counterclockwise), and amplitude regression slope Rea (right-hand triplet within the bracket). 172

Figure 3.3. Comparisons between observed and simulated mean surface currents in $\text{cm}\cdot\text{s}^{-1}$. The observed surface currents are derived on a $1/2^\circ$ grid from long-term drifter data by *Manning et al.* (2009), whereas the modeled mean surface currents are derived by temporally averaging of regional model hindcast solutions from 2004 to 2009. Couplet inside each grid box indicates the mean current amplitude and direction. 173

Figure 3.4. Mean Lagrangian probability density functions (LPDFs) (unit: km^{-2}) for a single release site (site 41, as shown in Figure 1) in the BOF based on the tracking with (a) 10-days, (b) 20-days, (c) 40-days, and (d) 60-days as the advection time. 174

Figure 3.5. Mean Gulf of Maine coastal connectivity matrix based on the particle tracking using a) 10-days, b) 20-days, c) 40-days, and d) 50-days as the advection time scale. Y

axis outlines each source locations under study, whereas and X axis outlines each destination locations under study. Both axis runs from site 1 to site 96 as noted in Figure 1. The connectivity matrices are normalized so that the summation of mean connectivity over all possible combinations is one. Pink dashed line indicates the borderline between eastern and western GOM sites. 175

Figure 3.6. The source locations and source strength functions of surface particles that are transported to the (a) MASS, (b) WGOM coastal area, (c)BOF, (d) EGOM coastal area, (e) WK, (f) OFFPB, (g) JB, and (h) all sites in the GOM. 176

Figure 3.7. The destination locations and destination strength functions of surface particles that are transported from the (a) MASS, (b) WGOM coastal area, (c) BOF, (d) EGOM coastal area, (e) WK, (f) OFFPB, (g) JB, and (h) all sites in the GOM. 177

Figure 3.8. (a) Mean, (b) Standard Deviation (STD), (c) low-frequency (seasonal and interannual) variability, and (d) intra-seasonal variability of the GOM connectivity matrix. Notations are same as in Figure 5. 178

Figure 3.9. (a) Spring (FMA) and (b) Summer (MJJ) mean conditions for the connectivity matrix showing the seasonal variability of the GOM connectivity matrix. Notations are same as in Figure 3.5 and Figure 3.8. 179

Figure 3.10. The destination locations and strength functions of surface particles that are transported from the BOF in 2004-2009 (a)-(f); and the source location and strength of the surface particles that are transported to the MASS and coastal WGOM in 2004-2009 (g)-(l). 180

Figure 4.1. Model domain and bathymetry for the Gulf of Maine (GOM) 5-km model. 182

Figure 4.2. Observations assimilated into the GOM 4DVAR system: (a) Blended SST for April, 01, 2010; (b) NERACOOS temperature observations at 1-m at 0:00Z April, 01, 2010; Shipboard CTD observed (c) surface temperature for May, 1-10, 2010, and (d) surface salinity for May, 28-June, 03, 2010; (e) and (f) show the locations for the surface temperature and salinity observations collected by UK Met Office during the April, 01-July, 18, 2010. 183

Figure 4.3. Temporal evolution of observation counts within each 3-day data assimilation window during April-July18, 2010. Various data sources are shown in different colors—Satellite Sea Surface Temperature (SST), U.K. Met Office collected XBT temperature, CTD temperature, CTD Salinity, Argo temperature, Argo Salinity, Surface thermistor observed temperature. Additional datasets are temperature and salinity observations from gulf-wide ship surveys (positions are shown in **Figure 4.2c** and **d**), along with NERACOOS temperature and salinity observations. 184

Figure 4.4. 4DVAR cost function (J) as a function of number of iterations of inner loops for (a) the first assimilation window (Apr, 01- April, 04, 2010), and (b) last assimilation window (July 15-July 18, 2010). Solid line is the total cost function (J), and dash dotted

line is the background cost function (J_b). Theoretical minimum cost function ($J_{\min}=1/N_{\text{obs}}$) is shown in dotted line, and the cross represents nonlinear model cost function (J_{NL}) after data assimilation. 185

Figure 4.5. Spatial distribution of the temporal SST Root mean square error (RMSE) between observations and (a) forward model solutions and (b) DA posteriors solutions. Temporal evolution of spatial SST RMSE and BIAS between observations and (c) forward model solutions and (d) DA posteriors solutions..... 186

Figure 4.6. Vertical profiles of subsurface (a) temperature and (b) salinity BIAS between observations and forward and DA posterior model solutions. Temporal evolutions of subsurface (c) temperature and (d) salinity BIAS between observations and forward and DA posterior model solutions..... 187

Figure 4.7. Station locations of CTD stations for the Northeast Fisheries Science Center (NEFSC) ship survey data (blue dots) inside the model polygon (model boundaries are plotted in dashed black lines) during April, 01-July, 18, 2010. Also shown are the NERACCOS stations, the data of which were used for independent comparisons. Specifically, buoys A, B and E (pink squares) are used for T/S comparisons, and buoys B and I are used for current comparisons. 188

Figure 4.8. Scatter plots of observed temperature and salinity at buoy A, B and E against model forward and posterior solutions. Gray line represents the linear fitting based on model solutions. Doublets in the brackets are model-data RMSE and bias, respectively. The profiles are not assimilated into the model and are used as independent data. 189

Figure 4.9. Comparisons between NEFSC temperature and salinity data (left column) and forward model (central column) and DA posterior counterparts. X-axis is observation time, and y-axis denotes the depth of the data in meters..... 190

Figure 4.10. Scatter plots of observed NEFSC temperature and salinity data against model forward and posterior solutions. Gray lines represent the linear fitting based on model solutions. Formulations show the fitting slope and intercepts between model and observations..... 191

Figure 4.11. Comparisons of 2-m surface currents between observations and model forward and posterior solutions for buoy B in the western GOM and buoy I in the eastern GOM, respectively. Model solutions are not shown during middle May to early June when there is no observed current available. 192

Figure 4.12. Term-by-term diagnostics of depth-averaged temperature budget. (a) and (b) are advection and heat flux terms for forward model, and (c) and (d) are the DA posterior counterparts. (e) and (f) stand for the DA posterior and forward model differences in the two terms. Dotted grey line represents the contour of zero line in each panel. Unit for the plot a in $^{\circ}\text{C day}^{-1}$ 193

Figure 4.13. Monthly-mean model trajectories for the surface temperature and salinity for

model forward and posterior solutions, separately.....	194
Figure 4.14. Monthly-mean model trajectories for the bottom temperature and salinity for forward and posterior model solutions, separately.....	195
Figure 4.15. Monthly-mean model trajectories for the surface currents for model forward and posterior model solutions.	196
Figure 4.16. (a) First EOF of coastal current and sea surface height (SSH). Horizontal arrow stands for the current scale of 50 cm/s. Number inside the brackets represents the variances of mode 1; (b) first principal component (PC1, time series) of the EOF analysis. Blue line is the original 4-hourly data, and black line is the 7-day low-pass filtered counterpart.....	197
Figure 4.17. Snapshot at day 59 for the particles released from Scotian Shelf to the four destination areas of interest-- The Bay of Fundy (BOF), the eastern GOM (EGOM), the Jordan Basin (JB), and the western GOM (WGOM). Color represents the final depth of the particles in meters. Initial locations for the particle released near the Scotian Shelf in April 01, 2010 are shown in blue dots.	198
Figure 4.18. Temporal evolutions of percent of particles released from Scotian Shelf on April 1st that are transported to (a) Jordan Basin (JB), (b) eastern GOM (EGOM), (c) Bay of Fundy (BOF) and (d) western GOM (WGOM). Initial locations and destination polygons are defined in Figure 16.....	199
Figure 5.1. A map showing the spatial distribution of station locations for NERACOOS buoys A, B, F and I (grey triangle). Also shown are the station locations (crosses) in research cruise Oceanus 447 (OC 447) conducted on May 29-June 04, 2008. D1, E1, D2, E2 and D3 stand for five observational transects, whereas the two black solid lines in the eastern Gulf of Maine represent transects N1 and N2 where cell fluxes are sampled from the biophysical model.....	200
Figure 5.2. Comparisons of simulated and observed surface (2m) and sub-surface (10m) currents at NERACOOS mooring A and B. Current time series are sampled daily for better visualization. Each vector current time series is accompanied by its seasonal mean east and north velocity components (left-hand couplet), and each model-data comparison is quantified by its complex correlation coefficient, phase angle (or angular deviation of the model vectors from the data vector measured counterclockwise), and regression coefficient (right-hand triplet).....	201
Figure 5.3. Taylor diagrams comparing simulated and observed surface temperature (left panel) and salinity (right panel) at GoMOOS coastal buoy A, B, F in the western GOM and buoy I in the eastern GOM. The radial distances from the origin are proportional to the ratio standard deviations; the azimuthal positions indicate the correlation coefficient; and the distance between the “test” (modeled) points and the “reference” (observed) point indicates the centered RMS difference (RMSD).	202

Figure 5.4. Comparisons between observed (left column) and modeled (right column) surface *A. fundyense* cell concentrations from April to early June, 2008. Open circles represent the locations where observations were collected during each survey.....203

Figure 5.5. Same as Figure 4, but for the periods from middle June to middle August..204

Figure 5.6. Histogram showing point-by-point model-data misfit between observed and simulated surface cell concentrations at a total of 308 stations in the 2008 bloom season. X-axis stands for the model-data misfit and y-axis is the number of misfits. Grey vertical line represents the theoretical misfit for normal distribution, while black curve denotes the fitted normal distribution between observations and model. A log10 scale is used for better visualization purpose.....205

Figure 5.7. Same as Figure 5.3, but the Taylor diagrams comparing simulated and observed surface cell concentrations (in log10 scale) during the seven cruise surveys as shown in Figure 4 and Figure5. To avoid point-by-point concentration, we averaged the cell concentrations during each survey to compute the spatial-mean cell concentration. As such, the statistics shown in the Taylor diagram are indeed the temporal correlation coefficient, temporal root-mean-square different, and standard deviation.....206

Figure 5.8. Comparisons between simulated (left column) and observed (right column) *A. fundyense* cell concentration along several cross-shelf transects of for survey *OC445*. Open circle represents the depths where observations were available. X-axis is the distance from the onshore-most locations. A log10 scale was used for better visualizations.207

Figure 5.9. Same as Figure 5.8, but for survey *OC447* conducted in late May.....208

Figure 5.10. Time series of daily cell germination flux from cyst bed, bottom temperature, endogenous clock (percent of germination) and surface shortwave radiation. For the shortwave radiation in the bottom panel, the grey line denotes the 12-hourly data and black curve is its 30-day low-pass filtered rendition.....209

Figure 5.11. (a) First EOF mode of the cell concentration and (b) its principal component (PC1, black line), also shown in this panel are the normalized gulf-wide spatial-averaged net growth rate (pink dashed line) and normalized germination flux (blue solid line), (c) second EOF mode of the surface cell concentration, and (d) its principal component (PC2, black line). Note that the cell concentrations are integrated over the upper 50m water column, and are then transformed into a log scale form. For each PC, the modal contributions to the total variances are also shown. We focus on the coastal GOM and the offshore areas including the George Bank are not considered in the calculation.210

Figure A-1: Biological model summary adapted from *Stock et al. (2005)* and *He et al. (2008)*. (a) Germination rate $G(T, E(z))$ (% day⁻¹) at sediment surface as a function of temperature and light attenuation. Light was converted to depth using an attenuation

coefficient of 0.2 m^{-1} and a characteristic surface irradiance of 345.5 w m^{-2} . (b) Endogenous clock function (EC) showing the germination potential in percentage with respect to the maximum germination rate $G(T, E(z), t)$. (c) The light-saturated growth rate ($\mu_{\max}(T, S)$ in equation 6 in day^{-1}) as a function of temperature and salinity. We used the optimal growth rate $\mu_{\max}(T, S) = 0.58 \text{ day}^{-1}$. Box area represents the majority of range of temperature and salinity conditions in the model simulation. (d) Mortality rate (% of cells day^{-1}) as a function of Q^{10} formulation of temperature. 214

Figure A-2. Maps of the cyst abundance in the upper 1-cm sediment layer collected during fall season of 2004-2011 (in cm^{-2}). Scatted dots are the observation locations and colored plots represent the cyst abundance. 215

Chapter I: Research Background

1.1 Mean circulation in the Gulf of Maine

The Gulf of Maine (GOM) is a semi-closed marginal sea in the northwest Atlantic Ocean (**Figure 1.1**). The GOM encompasses rugged bottom topography, with Jordan and Georges Basins in the eastern GOM and Wilkinson Basin in the western GOM. These basins are separated by the 200-m isobath. The complex bottom bathymetric setting offshore of Penobscot and Casco bays can generate local upwelling/downwelling (*He et al.*, 2005). Five major rivers are St. John River, Penobscot River in the eastern GOM, and Kennebec, Androscoggin and Kennebec Rivers in the western GOM. At the seaward edge, the Georges Bank and the Browns Bank (with depth of <100m) limit the exchange between the gulf interior and the open ocean. Near the seaward edge, there is entrainment of slope waters through the Northeast Channel (NEC) deep inflow. Cold and fresh Scotian Shelf Water enters the gulf over the Scotian Shelf (e.g. *Chapman and Beardsley*, 1989), with an annual average of 0.14Sv through Cape Sable (*Smith*, 1983). The inflows have significant impact on the winter mixed layer depth (*Christensen and Pringle*, 2012). Downstream, the Great South Channel (GSC) provides an exit of the Maine coastal water connecting GOM to the Middle Atlantic Bight (MAB).

The major circulation in the GOM is the cyclonic Gulf of Maine Coastal Current (MCC),

with its cell centered in the eastern GOM referring as the Jordan Basin Gyre (*Bigelow, 1927; Brooks, 1985*). The MCC is consisted of two main branches, usually referred to as the Western Maine Coastal Current (WMCC) and the Eastern Maine Coastal Current (EMCC) (**Figure 1.1**). Upstream, the EMCC starts from the mouth of Bay of Fundy flowing southwest to Penobscot, as is fed by freshwater inflow from the Scotian Shelf and the transport fluxes from the Bay of Fundy gyre. The EMCC encounters a bifurcation offshore of Penobscot Bay, with a portion often directing offshore and recirculating in the Jordan Basin. The WMCC is fed by the inshore branch of the EMCC as well the fresh water inputs from the St. John, Kennebec, Androscoggin, Saco and Merrimack Rivers. Downstream, the WMCC reaches a branch point off Cape Ann, where a part of the flow episodically recirculates into Cape Cod and Massachusetts Bays, and rejoins the southward Stellwagen branch northeast of Cape Cod. Further downstream, the flow encounters another bifurcation, with a segment flowing towards the Middle Atlantic Bight (MAB), and the rest portion joining the recirculation around Georges Bank (GB), sometimes referred to as the Georges Bank eddy (*Limeburner and Beardsley, 1996*). There is also another coastal current system called the Gulf of Maine Coastal Plume (GOMCP, *Keafer et al., 2005*). It emanates freshwater from coastal river runoff, making direct connection between east and west, especially during summer when river runoff is large.

The Georges Bank (GB) is a shallow-sea region south of Northeast Channel. The

sub-tidal circulation over the Georges Bank is known as a clockwise eddy (*Bigelow, 1927*), with an average current speed of 10 cm s^{-1} . The largest current speed is in the periphery of the bank not at the center (*Limeburner and Beardsley, 1996*). A fraction of the shelf water flowing southwestward along the southern flank of GB turns northward through the center and eastern side of the GSC and recirculates around the bank. Dynamical factors that account for the clockwise pattern includes tidal rectification over the variable bottom topography, the horizontal density gradients, as well as wind stress (*Chen et al., 1995, Butman et al., 1987*).

1.2 Seasonal variability of coastal circulation

The MCC is a complex system with significant seasonality (e.g. *Day, 1958; Bumpus and Lauzier; Vermersch et al., 1979; Brown and Irish, 1992; Xue et al., 2000*). As described in 1.1, the transport discrepancy between western and eastern segments of the MCC is represented by veering offshore of Penobscot Bay. The offshore veering itself shows strong seasonality. It arises in spring, persists throughout the summer, and gradually diminishes during fall. In contrast, deep offshore veering is out of phase with the near-surface veering and occurs more in winter. These variations are associated with the seasonal fluctuations in the alongshore pressure gradient force (*Pettigrew et al., 2005*).

The spatial pattern of the gulf-wide circulation also undergoes seasonal variations. In the climatological manner, the gulf-wide circulation is strong and most coherent in summer, and

becomes less recognized in winter. Spring and fall are two transition seasons between summer and winter. Surface wind forcing transits from northwesterly to southwesterly as season progresses from winter to spring, and the southwesterly wind continues to strengthen deep into summer. In spring and summer, the coastal flow is southwestward, in the opposite direction of the wind stress. Specifically, in early spring, the cyclonic circulation in the interior GOM is ill-defined and the GB eddy is not apparent. In summer, besides the gulf-wide cyclonic circulation, there is usually a pair of linked recirculated cyclonic gyres within the Jordan Basin and Georges Basin, associated with the two dense slope water domes within the two basins. There is clear strengthening of anti-cyclonic gyre in Georges Bank during summer months as a result of stratification, (e.g. *Butman et al.*, 1987; *Lynch et al.*, 1997). In late summer, the gulf-wide circulation shows a transition towards the fall condition. While Scotian Shelf input increases, the prominent gulf-scale recirculating gyre envelopes both Georges Basin and Jordan Basin, and there is less spatial variability along the margin of the coastal current compared to early summer (*Lynch et al.*, 1997; *Xue et al.*, 2000). Deep in fall, the cyclonic gyre in the interior GOM is still clear, with its simplest pattern late in the season (*Brown and Irish*, 1992; *Lynch et al.*, 1997). In winter, the overall WMCC is generally a cyclonic current, but lacks of spatial coherence, suggesting the strong influence from the presence of mesoscale structures.

The seasonality of the circulation is directly related to the evolving density structures,

modulated by both local and remote forcing. Local factors include tidal-induced mixing, wind, surface heat flux, river runoff, evaporation and precipitation (E-P). Remote forcing includes the inflow from the Scotian Shelf, and the slope sea deep inflow. Specifically, wind changes from predominantly northwesterly in winter to southwesterly in summer, and becomes more upwelling-favorable. The winter cooling erodes the water stratification, while the summer warming reestablishes the stratification. Every summer, the freshened bulge near the estuary mouth typically induces upper-level coastal current with the coast to its right (*Chao and Biocourt, 1986*). The Penobscot Plume was found to be able to steer the coastal current offshore at times (*Lynch et al., 1997, Pettigrew et al., 1998*). Tide is also an important modulator of the density and circulation structure. The GOM, especially near the Bay of Fundy (BoF) is known for its near resonant semi-diurnal tidal responses (*Garrett, 1972*). Tidal mixing stirs the water column and keeps the GB, BoF (especially near the Grand Manan) and the eastern GOM vertically well mixed (*Lynch et al., 1997*), which is a significant contributor to the vernal cyclonic MCC and GB recirculation. The GB and western Scotian shelf are also largely influenced by strong tidal current with amplitude of up to 1m/s. (e.g. *Loder, 1980; Chen et al., 1995*). In addition to local forcing, boundary flux variations upstream over the Scotian Shelf and offshore in the Slope Sea also impose pronounced impact on the circulation within the interior gulf (e.g., *Smith et al., 2001; 2012*).

The abovementioned dynamic processes shape the circulation in the GOM in different

ways. Modeling studies showed that surface heat flux is critical in regulating the annual cycle of GOM circulation, and the river discharge helps to establish a clear annual cycle in surface salinity. The M_2 tide contributes to the seasonal circulation such as generating the Georges Bank gyre and the Browns Bank gyre, and to enhance the coastal current through tidal rectification and tidal mixing. In addition, the tidal mixing can lead to the shrinking of the momentum of the circulation system due to bottom friction (*Xue et al.*, 2000). The tidal rectification contributes more significantly to the eastern branch of the MCC. Wind-driven return flow near-shore is important to the details of the coastal current, but not on the seasonal time scale. Baroclinic effect (including the baroclinic pressure gradient, the effect of stratification on vertical mixing and the air-sea heat flux) contributes to offshore shifts and the exchanges across the boundary (*Lynch et al.*, 1997).

1.3 Interannual variability

Interannual variability in the coastal circulation: There is significant interannual variability in the circulation connectivity between eastern and western segments of the MCC. For example, most of the near-surface waters of EMCC turned offshore east of Penobscot Bay in summer 1998. In contrast, in summer 2000, the discrepancy between EMCC and WMCC was dramatically reduced, suggesting much of EMCC continued on to feed WMCC. In 2001, the condition showed intermediate case between 1998 and 2000 conditions — a portion of the EMCC veered offshore but part of it continued to feed the WMCC. During

2001 to 2005, current speed of EMCC exceeded WMCC by 50%-75%, suggesting a normal degree of continuity. The thermal gradient feature inferred from satellite sea surface temperature composites was consistent with the concept of extreme gate 'open' in 2000, 'ajar' in 2001, and 'close' in 1998, indicating the contribution from baroclinic pressure gradient (*Pettigrew et al., 2005; Luerssen et al., 2005*).

Interannual variability of the coastal hydrography: Besides the interannual variability of the coastal current, there is also pronounced interannual variability of the water properties. The relationship between the variability of temperature and salinity within the GOM and its adjacent ocean regions was a focus of several studies. The Empirical Orthogonal Function (EOF) analysis showed spatial coherence at interannual timescale in SST over a long region from the Southern Greenland and Labrador to Cape Hatteras over a length of over 1000-km (*Thompson et al., 1988*). Analysis of the historical data (1977-1987) exhibited high degree of coherent variability from Cape Hatteras to the central GOM. Specifically, both central MAB and WGOM showed coherent variability of lower salinity and higher SST in summer. However, the variations of the water properties in the eastern GOM were incoherent with the rest of the shelf region, likely because the eastern GOM is less influenced locally but instead is dominated by inflows from Scotian Shelf and from Slope Sea through the Northeast Channel (*Thompson et al., 1988; Mountain et al., 1994; Mountain et al., 1998*).

1.4 The Harmful Algal Bloom and the Paralytic Shellfish Poisoning (PSP)

Harmful algal bloom (HABs) has become one of major marine environmental problems in almost every part of U.S. coastal waters. This is a result of many factors, such as natural dispersal of species through human activities (e.g., ballast water discharge and shellfish seeding) and culture eutrophication (*Anderson et al.*, 2008).

The most significant HAB problem in the northeastern U.S. is caused by a phytoplankton species called *the Alexandrium fundyense* in the GOM, and its dynamics and coupling with circulation are of interest in this study herein. The *A. fundyense* bloom can lead to the Paralytic Shellfish Poisoning (*PSP*). While the affected resources are predominantly shellfish, higher trophic levels of the food web may also be impacted, such as lobsters, fish and large marine mammals like whales, and human being. These organisms are responsible for repeated closures of shellfish beds in both nearshore and offshore waters. The Georges Bank and Nantucket Shoals are also occasionally found to contain dangerous toxins. The associated PSP in the western GOM was sporadic and poorly documented prior to a major bloom in 1972. The toxicity continued at high levels until the early 1990s, decreased for a decade or so, and has recently shown signs of increase again. Specifically, the bloom in summer 2005 is considered one of the worst bloom during past 33 years (*Anderson et al.*, 2005a), causing the state shellfish bed closure from Bay of Fundy all the way to the Massachusetts Bay. The PSP also caused extensive closures of offshore waters, including the

ocean region near Wilkinson Basin. The closure can cause an estimate of four million dollars of lost in revenues from seafood industry each week. Each year, repeated blooms took place in the subsequent spring and summer in 2006-2012. **Figure 1.2** showed the closure maps for each year in 2005-2010. Monitoring and understanding the bloom dynamics therefore becomes critically important.

1.5 The *A. fundyense* bloom dynamics

Indeed, the dynamics of the *A. fundyense* bloom evolves complex interactions between biological and physical environments. A key element of the *A. fundyense* bloom dynamics is a dormant cyst stage that allows the species to overwinter (**Figure 1.3**). The vegetative cells are germinated from their cyst seedbeds during spring and summer when there is strong temperature and light stimulation (*Anderson, 1997*), and are delivered to shore by episodic wind forcing and coastal current (*Anderson et al., 2005b*). More in-situ physical and biological observations along with laboratory data have enabled the construction of a coupled physical-biological model to further investigate the dynamics of *A. fundyense* bloom (e.g., *Stock et al., 2005; McGillicuddy et al., 2005b; He et al., 2008; Li et al., 2009*). Earlier study (e.g., *Love et al., 2006*) suggested that the *A. fundyense* is only a small proportion of the phytoplankton assemblage in the GOM, and therefore has limited influence on the ambient conditions such as nutrient abundance and predator abundance. As such, a single component biological model is designed to represent the *A. fundyense* dynamics without invoking

modeling of the entire marine ecosystem. Previous studies of the *A. fundyense* bloom can be summarized as observational and numerical studies, separately.

1.5.1 Historical observational studies of the *A. fundyense* blooms

The earlier researches were important in that they provided observational basis for the further investigation of the bloom dynamics. The *A. fundyense* bloom ecology has been studied in the regional subdomains of the GOM since the 1980s, mainly in the eastern GOM and the Bay of Fundy. *Martin and White* (1988) documented abundant vegetative cells at the mouth of Bay of Fundy whose distribution generally overlapped with high concentrations of resting cysts in the underlying sediments (*White and Lewis*, 1982). The major contributions of these studies was the indication of the self-sustaining of the population—All of the various life stages (cysts, vegetative cells, gametes and zygotes) were found in the same area; fewer vegetative cells were found upstream inside the Bay of Fundy or on the Scotian Shelf; the local cyclonic gyre in the Bay of Fundy provided retentive physical environment for the self-sustaining of the populations. Besides the retentiveness, there was also an indication of significant efflux of organisms of high densities penetrating into the western GOM (*Martin and White.*, 1988). The *A. fundyense* blooms were studied in the western GOM as well. *Anderson and Keafer* (1985) noticed the presence of high concentration of cysts 30km northeast of Cape Ann. Hydrographic survey revealed cell concentrations on the order of hundreds to thousands of cells/L, associated with plumes of freshwater emanating from

riverine sources. They further suggested that the alongshore transport of cells in coastally trapped river plumes was responsible for the toxicity progression from north to south (*Franks and Anderson, 1992a; 1992b*).

The interconnections between the sub-regional blooms were studied during the first set of coordinated gulf-wide surveys during 1997-2001 in the Gulf of Maine Ecology and Oceanography of Harmful Algal Bloom (ECO HAB-GOM) program. A systematic cyst survey revealed that in the western GOM the cyst deposit broadly distributed in the offshore waters from the Casco Bay to the Penobscot Bay (*Anderson et al., 2005c*), much larger than previously discovered by *Anderson and Keafer (1985)*. Vegetative cells were also found distributed gulf-wide in character (e.g. *McGillicuddy et al., 2005b; Townsend et al., 2001*). The peak cell concentrations occurred in association with the MCC. Also evident from the ECOMHAB-GOM surveys (1998, 2000, 2001) was the persistence of high cell abundance at the mouth of Bay of Fundy, geographically associated with a large peak in the distribution of benthic cysts (*Townsend et al., 2005; McGillicuddy et al., 2005b*). With the observation of repeated blooms each year, *McGillicuddy et al. (2005b)* investigated the significant interannual variability of the blooms at interannual time scales. Moreover, *McGillicuddy et al. (2005a)* indicated that the bloom center of mass shifts progressively upstream from west to east with respect to the coastal current as the season progresses from June to August, suggesting a “seasonal shift” of the bloom dynamics.

Both the physical and biological environment may alter the *A. fundyense* bloom. The *A. fundyense* is only a small proportion of the phytoplankton assemblage in the GOM, and therefore has limited influence on the ambient conditions such as nutrient abundance and predator abundance (Love *et al.*, 2006). Oceanographic processes are also found important in controlling the relative concentrations of Dissolved Inorganic Nitrogen (*DIN*) and silicate, suggesting the possible interference of *A. fundyense* growth by diatoms (Townsend *et al.*, 2005).

Transport is important for the distribution of the bloom. Close relationship between the satellite-derived thermal front near Penobscot Bay and the cell distribution (Luerssen *et al.*, 2005) suggested that the alongshore connectivity of the MCC was important for the delivery of vegetative cells. The coastal current might also advect the advantageous conditions like high nutrient abundance from upstream. Keafer *et al.* (2005) used the observations of cell concentration in May and June 2001 to study the contribution of coastal transport to the distribution of *A. fundyense* cells. The harmful cells were not found in the western GOM but were present in the low-salinity coastal plume in the eastern GOM during May. In June, the cells were partly delivered offshore near Penobscot, and the rest that were transported into the western GOM were still within the ‘inside track’ of the WMCC. All these findings suggested the importance of Gulf of Maine Coastal Plume (*GOMCP*) to the delivery the cells germinated upstream. In summer 2005, The *A. fundyense* bloom was one of the most severe

in at least 33 years, associated with high cyst abundance in preceding fall (*Anderson et al.*, 2005a). Anomalously warmer and fresher water condition was present due to pronounced surface heating and river runoff. Currents were two times stronger than climatology. Surface winds were anomalous with both episodic northeasterly bursts and downwelling-favorable mean condition. All these factors may have favored more vigorous along-shore transport and aggregation of toxic cells in 2005 (*He and McGillicuddy*, 2008). A moderate condition in coastal current, cyst abundance and growth environment favors an overall moderate magnitude of bloom in summer 2006 (*Li et al.*, 2009). Unfavorable growing condition contributes to a retarded bloom in summer 2010 (*McGillicuddy et al.*, 2011).

1.5.2 Modeling studies of the *A.fundyense* Blooms

The increasing observations along with laboratory experiments set up the basis for constructing physical-biological models to further investigate the dynamics of *A.fundyense* blooms (e.g., *Stock et al.*, 2005; *McGillicuddy et al.*, 2005b; *He et al.*, 2008; *Li et al.*, 2009).

McGillicuddy et al. (2005b) utilized a population dynamic module coupled with the climatological circulation model to study the mechanism regulating the seasonal fluctuation of the bloom. The sensitivity experiments indicated that the germination of cells from resting cysts is a key aspect of the population dynamics near the coastal margin. The growth of the vegetative cells was limited primarily by temperature from April through June, whereas

nutrient limitation occurred in July and August in the western gulf. In this model, the seasonal shift in the center of mass was related to the changing in the growing conditions: growth was more rapid in the western GOM early in the season due to warmer temperature that facilitated the growth, whereas growth was more rapid in the eastern gulf later in the season due to the severe nutrient limitation in the western gulf. Besides, a simple model of encystment based on nutrient limitation was used to predict the encystment of the cyst bed. The retentive gyre in the Bay of Fundy was found to favor the encystment from local populations. The disadvantages in his model lied in that the germination flux from cyst bed was vertical-averaged, and therefore the up-swimming process of the cells wasn't taken into account. In addition, mortality of cells was not considered in the biological model.

Stock et al. (2005) utilized the biological model constructed from laboratory and field data that estimated the germination and growth rates of *A. fundyense* as a function of multiple environmental conditions, coupled with the ECOM climatological circulation model. Sensitivity experiments revealed the significance of including the nutrient limitation and a mortality term in the initiation and development of *A. fundyense* bloom. The diagnosis of the cell budget indicated that the size of the modeled bloom was largely set by the cyst abundance, whereas transport of cells from the eastern GOM became increasingly important later in the spring. Similar to *McGillicuddy et al. (2005)*, their results showed that the net growth was first limited by the temperature and then by nutrient, and mortality later in the

season. Interannual variability in cyst abundance, circulation are not taken into account in this model. The mortality function was set as constant, which is sufficient to study the bloom initiation, but can be problematic in capturing the demise of the bloom late in the season.

The ECOHAB GOMTOX project has provided continuous monitoring of cyst abundance, cell concentrations as well as coastal hydrography in recent years, allowing more detailed *A. fundyense* bloom model hindcasts, as well as nowcast/forecast exercises (see for example, the 2012 HAB forecast: <http://omglnx3.meas.ncsu.edu/GOMTOX/2012forecast/>). To understand the mechanism governing the 2005 bloom which is the most severe one (*Anderson et al.*, 2005a), *He et al.* (2008) conducted the model hindcast using the coupled bio-physical model. The nested ROMS (Regional Ocean Modeling System) model forced by realistic atmospheric forcing, river discharge and oceanic conditions was coupled with the biological model modified from *Stock et al.* (2005) to hindcast the 2005 bloom. The model well reproduced the GOM coastal circulation and the seasonal evolution of *A. fundyense* bloom in 2005. Model sensitivity experiments suggest the high abundance of cysts in the western GOM was the primary factor in determining the magnitude of the major bloom. Wind forcing was important in regulating the transport of the vegetative cells; river runoff resulted in stronger buoyant plumes that facilitated the cell transport to the western GOM, but had limited effect on the gulf-wide bloom distribution. An improvement in *A. fundyense* dynamics model made by *He et al.* (2008) is the inclusion of the mortality function that is

based on the Q10 formula (*Durbin and Durbin, 1992*). This allows the coupled biophysical model to capture the demise of the bloom late in the season. Further work by *Li et al. (2009)* performed a hindcast study on the 2006 bloom. Model results further support the hypothesis suggested by *He et al. (2008)* that the cyst abundance is a first order predictor for the bloom severity in the next season. Detailed model diagnostics of growth and mortality terms indicated that nutrient limitation was in effect throughout the bloom season. The temperature-dependent mortality term is critical for the seasonal shift of the bloom from the WGOM to the EGOM, as well as for the termination of the bloom later in the season.

1.6 Research Objectives

While there were historical observations and modeling experiments provided research background and motivation to study the bloom dynamics, there is still much unknown on how the blooms interact with the interannual variability of the coastal circulation and environment conditions.

The Gulf of Maine Ocean Observing System (GoMOOS, now part of NERACOOS, e.g., *Pettigrew et al., 2011*) provides over ten years of continuous T/S and current observations, and serves as very useful datasets (wind forcing, moored CTD T/S, and ADCP currents) for the quantification of interannual variations in the GOM. In addition, various ship survey opportunities funded by EGOHAB-GOMTOX project provide aboard

temperature, salinity and ACDP current observations, perfect for elucidation of the gulf-wide hydrography evolutions from year to year. Analysis of hydrographic condition can then be further used to investigate the intrinsic linkages between hydrography, alongshore transport, and *A. fundyense* bloom dynamics. The previous modeling work of GOM circulation (e.g., *He et al.*, 2008; *Li et al.*, 2009) set up the basis to study the transport of materials utilizing the spatial and temporal continuous model fields. Some case studies investigate the transport of materials in the GOM (e.g., *Hannah et al.*, 1998; *Xue et al.*, 2008; *Incze et al.*, 2010), but the coastal connectivity at interannual timescale is poorly studied. *Mitarai et al.* (2009) applied a more statistically comprehensive Lagrangian PDF (LPDF) method in conjunction with regional ocean circulation model solutions to quantify the coastal connectivity in the Southern California Bight (SCB). The relative importance of difference sources and sinks were further quantified based on the source and destination strengths computed from the connectivity matrix. The study lends a good example for the quantification of GOM coastal connectivity in the statistical manner.

The physical circulation model is known to have errors due to deficiencies in forcing agents, including surface forcing, initial and boundary conditions. The ideal way to improve understanding of the circulation is to combine observations and model together to provide the optimal estimate of model trajectories. In this regards, the newly available four-dimensional variational data assimilation (4DVAR) technique that is now a part of our circulation

modeling system ROMS (e.g., *Powell et al.*, 2008; *Moore et al.*, 2011abc) can be used to improve the hydrodynamic model prediction, which in turn enhances the fidelity of *A. fundyense* bloom simulations. Furthermore, a further investigation of the *A. fundyense* bloom dynamics using coupled biophysical model is necessary.

The object of the Ph.D. dissertation research is to investigate the seasonal and interannual variability of the GOM circulation and its couplings with regional *A. fundyense* bloom through integrated analysis of in situ observations along with comprehensive coupled bio-physical modeling. Our specific objectives include:

(i) Characterizing the seasonal and interannual variability of GOM coastal circulation and hydrography by analyzing extensive oceanographic and meteorological observations;

(ii) Quantifying the GOM coastal circulation connectivity based on the model hindcast solutions and the offline particle tracking (i.e., LTRANS, e.g. *North et al.*, 2005, 2006, 2008 and *Schlag et al.*, 2008). The focus will be on the connectivity in the spring- summer seasons in order to gain a useful physical framework for understanding the transport pathways of *A. fundyense* population.

(iii) Improving the ocean model performance by applying advanced four-dimensional variational data assimilation (*Powell et al.*, 2008; *Moore et al.* 2011abc). Extensive hydrodynamic observations, including the coastal sea levels, Gulf of Maine observing system

mooring data, satellite observed sea surface temperature, and GOMTOX ship-board CTDs data in summer 2010 will be assimilated into the system. Evolutions of the anomalous water mass and coastal circulation in 2010 will be simulated and analyzed;

(iv) Diagnosing the evolutions of 2008 *A. fundyense* bloom in the GOM using *in-situ* observations and coupled biophysical model simulations, with the focus on the vertical structures and cell advection fluxes of the *A. fundyense* bloom.

The remaining of the dissertation is organized as follows. We first present the investigation of seasonal and interannual variability in coastal hydrography in the GOM during 2002-2011 using extensive *in situ* observations. A modeling study of the coastal connectivity based on passive particle tracking is shown in Chapter II. Chapter III investigates the evolution of anomalous water mass and circulation condition in summer 2010 using the state-of-the-art variational data assimilation scheme. In Chapter IV, we present a case study of GOM coastal circulation and *A. fundyense* bloom in summer 2008, focusing on the elucidation of bloom evolution, and the quantification of cell flux and cyst germination rates. Chapter V provides a summary of this dissertation, followed by the *A. fundyense* model parameterizations in the appendix.

References

- Anderson, D.M., B.A. Keafer (1985), Dinoflagellate cyst dynamics in coastal and estuarine waters. Toxic dinoflagellates. *Proceedings of the third international conference*, Elsevier, New York.
- Anderson, D.M. (1997), Bloom dynamics of toxic Alexandrium species in the northeastern US. *Limnology and Oceanography*, 42, 1009-1022.
- Anderson D.M., Keafer, B.A., McGillicuddy, D.J., Mickelson, M.J., Keay, K.E., Libby, P.S., Manning, J.P., Mayo, C.A., Wittaker, D.K., Hickey, J. M., He, R., Lynch, D.R., Smith, K.W. (2005a), Initial observation of the 2005 Alexandrium fundyense bloom in the southern New England: general patterns and mechanisms. *Deep Sea Research II*, 52, 2856-2876.
- Anderson, D. M., Kulis, D. M, Keafer, B. A., Gribble, K.E., Marin, R., Scholin, C. A., (2005b). Identification and enumeration of Alexandrium spp. From the Gulf of Maine using molecular probes. *Deep Sea Research II*, 52 (19-21), 2467-2490.
- Anderson, D.M., C.A. Stock, B.A. Keafer, A. Bronzino, B. Thompson, D.J. McGillicuddy, M.D. Keller, P.A. Martrai, J. Martin (2005c), Alexandrium fundyense cyst dynamics in the Gulf of Maine, *Deep Sea Research II*, 52 (19-21), 2522-2542.
- Anderson D.M. and other 11 authors (2008), Harmful algal blooms and eutrophication: Examining linkage from selected coastal regions of the United States. *Harmful Algae*, doi: 10.1016/i.hal.2008.08.017.
- Aretxabaleta, A.L., McGillicuddy, D.J., Smith, K.W., Manning J.P. and D.R. Lynch, 2009. Model Simulations of the Bay of Fundy Gyre: 2. Hindcasts for 2005-2007 Reveal Interannual Variability in Retentiveness. *Journal of Geophysical Research*, 114, C09005, doi: 10.1029/2008JC004948.
- Bigelow, H.B., 1927. Physical Oceanography of the Gulf of Maine. *Fisheries Bulletin*, 40, 511–1027.
- Brooks, D. A. (1985), The vernal circulation in the Gulf of Maine, *Journal of Geophysical Research*, 90, 4687– 4705.
- Brown, W.S and James D. Irish (1992): The Annual Evolution of Geostrophic Flow in the Gulf of Maine: 1986-1987, *Journal of Physical Oceanography*, 22, 445-472.
- Bumpus, D.F. (1960): Sources of water contributed to the Bay of Fundy by surface circulation, *J. Fish. Res. Board Can.*, 17, 181-197.

- Butman, B., J. W. Loderm, and R. C. Beardsley, 1987: The seasonal mean circulation on Georges Bank: Observations and theory. R. H. Buckus, Ed., The MIT Press, 125–138.
- Chao, S.-Y., and W. C. Boicourt (1986): Onset of estuarine plumes. *Journal of Physical Oceanography*, 16, 2137–2149.
- Chapman, D.C. and R.C. Beardsley (1989): On the origin of shelf water in the Middle Atlantic Bight, *Journal of Physical Oceanography*, 19, 384-391.
- Christensen, M. K., and J. M. Pringle (2012): The frequency and cause of shallow winter mixed layers in the Gulf of Maine, *J. Geophys. Res.*, 117, C01025, doi: 10.1029/2011JC007358.
- Chen, C., R. C. Beardsley, and R. Limeburner (1995): A numerical study of stratified tidal rectification over finite-amplitude banks. Part II: Georges Bank. *J. Phys. Oceanogr.*, 25, 2111–2128.
- Churchill, J.H., N.R. Pettigrew, and R.P. Signell (2005): Structure and variability of the Western Maine Coastal Current, *Deep Sea Research Part II*, Vol. 52, 19-21, 2392-2410.
- Day, C.G., 1958: Surface circulation in the Gulf of Maine as deduced from drifter bottles, *Fisheries Bulletin*, 141, 443-471.
- Drinkwater, K., B. Petrie, and W. H. Sutcliffe Jr. (1979): Seasonal geostrophic volume transports along the Scotian Shelf, *Estuar. Coastal Mar. Sci.*, 2, 17-27.
- Durbin, E. G., and A. G. Durbin (1992), Effects of temperature and food abundance on grazing and short-term weight change in the marine copepod *Acartia hudsonica*, *Limnol. Oceanogr.*, 37, 361– 378.
- Eppley, R., J. Rogers, J. McCarthy (1969), Half-saturation constants for uptake of nitrate and ammonium by marine phytoplankton, *Limnology and Oceanography*, 14, 6, 912- 920
- Flather, R. A., 1976: A tidal model of the northwest European continental shelf. *Mem. Soc. Roy. Sci. Liege*, Ser. 6, 10, 141-164.
- Franks, P.J.S., Anderson, D.M. (1992a), Alongshore transport of a phytoplankton bloom in a buoyancy current: *Alexandrium tamarense* in the Gulf of Maine. *Marine Biology*, 112, 153–164.
- Franks, P.J.S., Anderson, D.M. (1992b), Toxic phytoplankton blooms in the southwestern Gulf of Maine: testing hypothesis of physical control using historical data, *Marine Biology*, 112, 165-174.
- Garrett, C.(1972), Tidal Resonance in the Bay of Fundy and Gulf of Maine, *Nature*, 238, 441

– 443, doi:10.1038/238441a0.

Hannah, C.G, C. E. Naimie, J.W. Loder and F. E. Werner, upper-ocean transport mechanisms from the Gulf of Maine to Georges Bank, with implications for canals supply (1998), *Continental Shelf Research*, vol.17, No. 15, pp 1887-1911.

He, R., D. J. McGillicuddy, D. R. Lynch, K.W. Smith, C.A. Stock, and J. P. Manning (2005), Data assimilative hindcast of the Gulf of Maine coastal circulation. *Journal of Geophysical Research*, 110, C10011, doi: 10.1029/2004JC002807.

He, R. and McGillicuddy D. J., 2008: The historic 2005 Toxic Bloom of Alexandrium fundyense in the west Gulf of Maine- Part 1: In Situ Observations of Coastal Hydrography and Circulation. *Journal of Geophysical Research*, 113, C07039, doi: 10.1029/2007JC004601.

He, R., McGillicuddy D. J., Keafer B.A, Anderson D. M., 2008: Gulf of Maine Harmful Algal Bloom in summer 2005- Part 2: Coupled Bio-physical Numerical Modeling, *Journal of Geophysical Research*, 113, C07040, doi: 10.1029 /2007 JC 004602.

He, R. and K. Chen (2010), Investigation of the Northeastern North America Coastal Circulation with a Regional Circulation Hindcast Experiment, *Continental Shelf Research*, submitted.

Hickey, B. M, E.L. Dobbins and Allen S.E. (2003), Local and remote forcing of currents and temperature in the central Southern California Bight, *Journal of Geophysical Research*, vol. 108, No.C3, 3081, doi: 10.1029/2000JC00313.

Kamykowski, D., Reed, and R.E., Kirkpatrick, G.J. (1992), Comparison of the sinking velocity, swimming velocity, rotation and path characteristics among six marine dinoflagellate species. *Marine Biology*, 113(2), 319-328.

Keafer, B.A., Churchill, J.H., McGillicuddy, D.J., Anderson D.M (2005): Bloom development and transport of toxic Alexandrium fundyense populations within a nearshore coastal plume in the Gulf of Maine. *Deep Sea Research II*, doi: 10.1016/j.dsr2.2005.06.016.

Li, Y., R., He, D. J. McGillicuddy, D. M. Anderson and B.A. Keafer (2009), Investigation of the 2006 Alexandrium fundyense Bloom in the Gulf of Maine: In situ Observations and Numerical Modeling. *Continental Shelf Research*, 10.1016/j.csr.2009.07.012

Limeburner, R., Beardsley, R.C. (1996). Near-surface recirculation over Georges Bank. *Deep Sea Research II*, 43, 1547–1574.

Love, R.C., Loder, T.C., Keafer, B.A., (2005), Nutrient conditions during Alexandrium fundyense blooms in the western Gulf of Maine, U.S.A. *Deep Sea Research II*, 52,

2450-2466.

Loder, J. W. (1980): Topographic rectification of tidal currents on the sides of Georges Bank. *Journal of Physical Oceanography*, 10, 1399–1416.

Luerssen R.M., A.C. Thomas and J. Hurst (2005). Relationships between satellite-measured thermal features and Alexandrium-imposed toxicity in the Gulf of Maine, *Deep Sea Research Part II*. 52: 2656-2673.

Luettich, R. A., J, J, Westerink, and N. W. Scheffner (1992), ADCIRC: An advanced three-dimensional circulation model for shelves, coasts and estuaries. *U.S. Army Engineer Waterways Experiment Station*.

Lynch, D.R., Holboke M.J., Maimie, C.E. (1997), The Maine coastal current: spring climatological circulation. *Continental Shelf Research*, 17, 605-639.

Marchesiello, P., J.C. McWilliams, and A.F. Shchepetkin (2001), Open boundary conditions for long-term integration of regional oceanic models. *Ocean Modeling*, 3, 1-20.

Martin, J.L., and A.A. White (1988), Distribution and abundance of the toxic dinoflagellate *Fonyaulax excavata* in the Bay of Fundy, *Canadian Journal of Fisheries and Aquatic Sciences*, 45(11):1968-1975.

McGillicuddy D.J., Anderson, D.M., Lynch, D.R., Townsend D.W. (2005a), Mechanisms regulating large-scale seasonal fluctuations in Alexandrium fundyense populations in the Gulf of Maine: Results from a physical-biological model. *Deep Sea Research II*, 52, 2698-2714.

McGillicuddy, D.J., D.M. Anderson, A.R. Solow, and D.W. Townsend (2005b), Interannual variability of Alexandrium fundyense abundance and shellfish toxicity in the Gulf of Maine, *Deep Sea Research II*, 52, 2843-2855.

McGillicuddy, D.J., Townsend, D.W., He, R., Keafer, B.A., Kleindinst, J.L., Li, Y., Manning, J.P., Mountain, D.G., Thomas, M.A., and D.M. Anderson (2011), Suppression of the 2010 Alexandrium fundyense bloom by changes in physical, biological, and chemical properties of the Gulf of Maine. *Limnology and Oceanography*, 56(6), 2411–2426.

Mellor L.G. and T. Yamada (1982), Development of a turbulence closure model for geophysical fluid problems, *Reviews of Geophysics and space physics*, 20-4, 851-875.

Mitarai, S., D. A. Siegel, J. R. Watson, C. Dong and J. C. McWilliams (2009), Quantifying connectivity in the coastal ocean with application to the Southern California Bight, *Journal of Geophysical Research*, vol. 114, C10026, doi:10.1029/2008JC005166, 2009

- Moore, A. M., H. G. Arango, G. Broquet, C. Edwards, M. Veneziani, B. Powell, D. Foley, J. D. Doyle, D. Costa, and P. Robinson (2011a): The Regional Ocean Modeling System (ROMS) 4-Dimensional Variational Data Assimilation Systems: part2 - Performance and Application to the California Current System. *Progress in Oceanography*, 91, 50-73.
- Moore, A. M., H. G. Arango, G. Broquet, B. Powell, A. T. Weaver, and J. Zavala-Garay (2011b): The Regional Ocean Modeling System (ROMS) 4-Dimensional Variational Data Assimilation Systems: part1 - System overview and formulation. *Progress in Oceanography*, 91, 34-49.
- Moore, A. M., H. G. Arango, G. Broquet, C. Edwards, M. Veneziani, B. Powell, D. Foley, J. D. Doyle, D. Costa, and P. Robinson (2011c): The Regional Ocean Modeling System (ROMS) 4-dimensional variational data assimilation systems, Part III: Observation impact and observation sensitivity in the California Current System. *Progress in Oceanography*, 91, 74-94.
- Mountain, D.G, and J.P. Manning (1994), Seasonal and interannual variability in the properties of the surface waters of the Gulf of Maine, *Continental Shelf Research*, 14, 1555-1581.
- Mountain, D.G, and M.H. Taylor (1998), Spatial coherence of interannual variability in water properties on the U.S. northeast shelf, *Journal of Geophysical Research*, 13(C2): 1083-1092.
- Naimie, C.E., J.W. Loder, and D.R. Lynch (1994): Seasonal variation of the 3D residual circulation on Georges Bank, *Journal of Geophysical Research*, 99, 15967-15989.
- North, E. W., R. R. Hood, S.-Y. Chao, and L. P. Sanford (2006): Using a random displacement model to simulate turbulent particle motion in a baroclinic frontal zone: a new implementation scheme and model performance tests. *Journal of Marine Systems* 60: 365-380.
- North, E. W., Z. Schlag, R. R. Hood, L. Zhong, M. Li, and T. Gross. 2006. Modeling dispersal of *Crassostrea ariakensis* oyster larvae in Chesapeake Bay. Final Report to Maryland Department of Natural Resources, July 31, 2006. 55 p.
- North, E. W., Z. Schlag, R. R. Hood, M. Li, L. Zhong, T. Gross, and V. S. Kennedy. 2008. Vertical swimming behavior influences the dispersal of simulated oyster larvae in a coupled particle-tracking and hydrodynamic model of Chesapeake Bay. *Marine Ecology Progress Series* 359: 99-115
- Pettigrew, N.R., D.W. Townsend, H. Xue, J.P. Wallinga, P.J. Brickey, and R.D. Hetland (1998), Observations of the Eastern Maine Coastal Current and its offshore extensions, *Journal of Geophysical Research*, 103, 30 623-640.

Pettigrew, N.R., Churchill, J.H., Janzen, C.D., Mangum, L.J., Signell, R.P., Thomas, A.C., Townsend, D.W., Wallinga, J.P., Xue, H.(2005): The kinematic and hydrographic structure of the Gulf of Maine coastal current. *Deep Sea Research, Part II* 52(19–21), 2369–2391.

Pettigrew, N. R., R.J. Fleming, and C.P. Fikes (2011): The history of the first decade of the observing system in the Gulf of Maine, and plans for the second decade, *MTS Journal*, September 2011, 1-10.

Powell, B.S., H.G. Arango, A.M. Moore, E. Di Lorenzo, R.F. Milliff and D. Foley (2008): 4DVAR data assimilation in the Intra-Americas Sea with the Regional Ocean Modeling System (ROMS), *Ocean Modelling*, Volume 25, Issues 3-4, 2008, Pages 173-188.

Schlag, Z., E. W. North, and K. Smith (2008): Larval TRANSPORT Lagrangian model (LTRANS) User's Guide. University of Maryland Center for Environmental Science, Horn Point Laboratory, Cambridge, MD. 146 pp.

Shchepetkin, A.F. and J.C. McWilliams (2005), a split-explicit, free-surface, topographic following-coordinate oceanic model. *Ocean Modelling*, 9, 347-404.

Smith. P.C. (1983): the mean and seasonal circulation off southeast Nova Scotia, *Journal of Physical Oceanography*, 13, 1034-1054.

Smith P.C, R.W. Houghton, R.G. Fairbanks., and D.G. Mountain (2001): Interannual variability of boundary fluxes and water mass properties in the Gulf of Maine and on Georges Bank: 1993-1997, *Deep-Sea Research II* 48: 37-70.

Smith, P.C. N.R. Pettigrew, P. Yeats, D.W. Townsend and G. Han (2012): A Regime Change in the Gulf of Maine. *Trans. Amer. Fish. Soc. (Proceedings of the Scientific Symposium on the Gulf of Maine, St. Andrews, NB, October 2009)*, in press.

Stock, C.A., McGillicuddy D.J., Solow, A.R., Anderson D.A (2005), Evaluating hypothesis for the initiation and development of Alexandrium fundyense blooms in the western Gulf of Maine using a coupled physical-biological model. *Deep Sea Research II*, 52, 2715-2744.

Townsend, D.W., N. R. Pettigrew, and A.C. Thomas (2001): Offshore blooms of the red tide dinoflagellate, *Alexandrium* spp., in the Gulf of Maine. *Continental Shelf Research*, 21, 347-369.

Townsend. D.W., N.R. Pettigrew, and A.C. Thomas (2005), On the nature of Alexandrium fundyense blooms in the Gulf of Maine, *Deep Sea Research II*, 52, 2603-2630.

Vermersch, J. A., R.C. Beardsley, and W.S. Brown (1979): Winter circulation in the western Gulf of Maine: Part 2: Current and pressure observations, *Journal of Physical Oceanography*, 9, 768-784.

White A.W., and C.M. Lewis (1982), Resting cysts of the toxic red tide dinoflagellate *Gonyaulax exavata* in Bay of Fundy sediments, *Canadian Journal of Fisheries and Aquatic Sciences*, 39, 1185-1194.

Xue H., F. Chai, and N.R. Pettigrew (2000), A model study of the seasonal circulation in the Gulf of Maine, *Journal of Physical Oceanography*, 30 (5): 1111-1135, 2000.

Xue, H, L. Incze, D. Xu, N. Wolff and N. Pettigrew (2008), Connectivity of lobster populations in the coastal Gulf of Maine, Part I: Circulation and larval transport potential, *Ecological Modeling*, e 210, 193-211.

Chapter II: Seasonal and Interannual Variability in Gulf of Maine

Hydrodynamics: 2002-2011

Yizhen Li¹, Ruoying He¹, Dennis J. McGillicuddy, Jr.²

1. Department of Maine, Earth and Atmospheric Sciences,
North Carolina State University

2. Department of Applied Ocean Physics and Engineering
Woods Hole Oceanographic Institution

Last modified: August 07, 2012. Submitted to *DSR-II*, in review.

KEYWORDS: Gulf of Maine, Upwelling Index, River Discharge, Hydrography, Interannual Variability

Abstract

In situ observations including long-term moored meteorological and oceanographic measurements and multi-year gulf-wide ship survey data are used to quantify interannual variability of surface wind, river runoff, and hydrographic conditions in the Gulf of Maine during summers 2002-2011. The cumulative upwelling index (CUI) shows that upwelling (downwelling)-favorable wind conditions were most persistent in 2010 (2005) over the 10-year study period. River discharge was highest in 2005; peak runoff occurred in early April in 2010 as opposed to late April to middle May in other years. Moored time series show that coastal water temperature was 0.5-2 °C warmer than average in summer 2010, and about 2° C colder than average in 2004. Coastal salinity in April 2010 was the lowest in the 10-year study period. Both moored ADCP current measurements and dynamic height/geostrophic velocity calculations based on gulf-wide ship survey data show May-June 2010 had one of

the weakest alongshore transports in the western Gulf of Maine during the 10-year study period, likely associated with intrusions of warm slope water and fresher-than-usual Scotian Shelf water. Such hydrodynamic variability has significant impacts on interannual variations of *Alexandrium fundyense* blooms. Comparisons of coastal currents to the Paralytic Shellfish Poisoning (PSP) closure maps resulting from *A. fundyense* blooms suggest an intrinsic linkage between alongshore transport and the downstream extent of toxicity.

2.1 Introduction

The Gulf of Maine (GOM) off the U.S. northeast coast is a marginal sea (**Figure 2.1**) having a large-scale cyclonic mean circulation (*Bigelow, 1927, Brooks and Townsend, 1989; Lynch et al., 1996; 1997; Pettigrew et al., 2005*). The nearshore flow known as the Maine Coastal Current (MCC) flows southwestward starting from the Bay of Fundy. Downstream, one branch of this current often veers offshore of Penobscot Bay. The remaining portion continues southwestward, as it is fed by the river runoff from Penobscot, Kennebec, Androscoggin, and Merrimack Rivers. The current bifurcates further downstream, one branch flows through the Great South Channel (GSC) towards the Middle Atlantic Bight (MAB), and the other flows northeast to Georges Bank.

While these mean circulation patterns are well known, significant variability have been observed on synoptic to interannual time scales. Both local forcing (i.e., tides, wind, heat flux and rivers) and upstream/deep ocean forcing contribute to such hydrodynamic

variability (e.g., *Lynch et al., 1997; Xue et al., 2000; Keafer et al., 2005; Pettigrew et al., 2005; Mountain and Manning, 1994; He and McGillicuddy, 2008*). *Pettigrew et al. (2005)* showed that during the three-year study period (1998-2000), there was significant disconnection between eastern and western segments of MCC in 1998, as compared to a more connected coastal flow in 2000, with 1999 being an intermediate case. Further analysis of the kinetic structure of the flow showed such variability is an outcome of the modulation of both wind forcing and river discharge. Moreover, eddies and meanders may affect the near-shore current variance at times (*Churchill et al., 2005*). The drifter study by *Manning et al. (2009)* suggested while the mean coastal current is centered near 100-m isobath, its path can deviate fairly frequently due to effects of wind forcing and small-scale baroclinic structures. Modeling studies (*Arexabaleta et al., 2009; Li et al., submitted to this issue*) also revealed significant interannual variability in the strength and transport pathways of the coastal current.

In addition to local forcing, inflows into the Gulf of Maine from the Scotian Shelf and through Northeast Channel have been found to be highly effective in modulating the GOM interior hydrography from time to time (e.g., *Smith et al., 2001; Brown and Irish, 1993; Houghton and Fairbanks, 2001; Bisagni and Smith, 1998; McGillicuddy et al., 2011*). *Mountain and Manning (1994)* studied the seasonal cycle and interannual variability in coastal hydrography. In the eastern Gulf the salinity cycle is dominated by the winter influx

of low salinity Scotian Shelf water, as opposed to that in the western Gulf, which is heavily influenced by the local runoff in spring. Because of the phase differences in temperature and salinity cycles, the western GOM is more stratified in spring and summer. On decadal time scales, there was less variability in temperature (1–2°C) during the period 1977–1987, compared to observed fluctuations of 4–6°C in 1960s. Further analysis confirmed that the temperature variability was driven by both local heat flux and boundary inflows with an advective origin (*Mountain et al.*, 1996). *Townsend et al.* (2011) found lower nitrate but higher silicate concentrations in the GOM interior since the 1970s, likely due to increased freshwater inflow from the Scotian Shelf. As such, the coastal current system in recent decades is comprised of a greater portion of nutrient-poor, cold shelf waters and less of the nutrient-rich, warm slope waters that were previously thought to dominate the nutrient flux into the gulf.

Long-term moored meteorological and oceanographic observations taken by a regional marine buoy network, along with multi-year gulf-wide ship surveys of the Gulf of Maine Toxicity (GOMTOX) project have provided a new opportunity to quantify the interannual variability of the GOM hydrodynamics in the recent years. Focusing on the late spring and summer periods (April 1 – August 1), we use these observations to investigate the interannual variations in local wind forcing, river discharge, and the gulf-wide hydrographic conditions during 2002-2011. A number of earlier studies have illustrated that changes in

atmospheric forcing, gulf hydrography and coastal circulation have significant impacts on the timing and magnitude of annually-occurring *Alexandrium fundyense* blooms and shellfish toxicity in the gulf (e.g., *Anderson et al.*, 2005, *He et al.*, 2008, *Li et al.*, 2009; *McGillicuddy et al.*, 2011; *Thomas et al.*, 2010). In this regard, a particular motivation of this research is to better quantify the seasonal and interannual variations in the Gulf of Maine hydrodynamics to provide a foundation for understanding the intrinsic linkage between regional hydrodynamics and *A. fundyense* blooms. Section 2.2 provides a brief description of observations used in this study. Section 2.3 offers analyses of the interannual variability of surface wind, river runoff, coastal hydrography and circulation, followed by a discussion in Section 2.4, and summary and conclusion in Section 2.5.

2.2 Methods

The majority of long-term time series observations used in this study were obtained from moorings of the Gulf of Maine Ocean Observing System (now part of the Northeast Coastal Ocean Observation System NERACOOS, <http://www.neracoos.org>, e.g., *Pettigrew et al.*, 2011), including hourly observations of surface wind speed and direction, ocean temperature, salinity and velocity. We focused on temperature and salinity documented at buoy B and E in the western GOM, and buoy I in the eastern GOM to highlight the hydrographic variability in the coastal region, which is a primary habitat of *A. fundyense*. Buoys M and N document variability in Jordan basin and the Northeast Channel, respectively,

which provides important information about offshore forcing that impacts the coastal region (**Figure 2.1a**, pink squares).

Temperature and salinity observations collected during GOMTOX shipboard surveys in the summers of 2005, 2006, 2007, and 2010 were also used to provide quasi-synoptic, gulf-wide hydrographic analyses (**Figure 2.1a**, b, c, and d). Additionally, river runoff time series collected from five major rivers in the GOM (i.e., the U.S portion of the St. John, Penobscot, Androscoggin, Kennebec, and Merrimack rivers; **Figure 2.1a**) were considered. Their daily discharge observations between 2002 and 2011 were obtained from the United States Geological Survey (USGS) river station measurements.

2.3 Results

2.3.1 Seasonal and Interannual Variability in Wind forcing

The long-term (2002-2011) seasonal mean wind fields over the GOM exhibit a directional shift that typically occurs in April-May. Northwesterly winds generally dominate the gulf in April. Southwesterly winds then become prevailing starting in May, and continue as the season progresses. Such southwesterly winds favor coastal upwelling circulation near the Maine coast. Earlier studies (e.g, *Anderson et al.*, 2005; *He and McGillicuddy*, 2008) have shown that outbreaks of consecutive strong northeasters can reverse the monthly mean wind field into downwelling favorable in some years (e.g. May 2005; also see *Butman et al.*

2008).

To quantify the temporal variability, hourly surface wind observations at buoys B and I were used to compute an Upwelling Index ($UI = \frac{\tau_x}{\rho f}$, i.e., the offshore component of the Ekman transport) following the method of *Schwing et al.* (1996), where τ_x is the alongshore component of wind stress calculated using the Large and Pond (1981) scheme, and f is the local Coriolis parameter. Positive (negative) UI represents upwelling (downwelling) favorable wind conditions, respectively. The cumulative UI (CUI) was computed by integrating the resulting UI over time (i.e., $CUI = \int UI dt$) between April 1 and August 1 of each year. The slope of CUI is particularly informative, in that the most upwelling favorable wind conditions are represented by the steepest rising trend shown in CUI. In contrast, a declining trend in CUI indicates that downwelling favorable winds (negative UI) become more dominant.

Significant interannual variability was revealed by CUI analyses on wind time series between April and August of 2004-2011 at buoy B in WGOM and buoy I in the EGOM (**Figure 2.2**). Among all 8 years, 2010 stands out as the year with the most persistent upwelling-favorable wind conditions, whereas 2005 is clearly the year with the most downwelling-favorable wind. Indeed, a sharp decline in 2005 CUI is associated with a series of strong northeasters occurred in the month of May, as indicated earlier by *He and McGillicuddy* (2008) and *Butman et al.* (2008).

Although the signals are not as strong as 2010, 2004, 2008 and 2009 are also characterized by largely by upwelling-favorable winds, as shown by a generally rising trend in their respective CUI time series. CUIs for 2006, 2007, and 2011 are relatively flat for most of the time period examined, suggesting the mean alongshore wind stress was significantly weaker during these three years compared to the other years. We note temporal patterns of CUIs at buoys B and I are generally very similar except during May-June of 2004 and June-July 2006. Some sub-regional wind field differences become apparent during these two periods, such that surface winds were more downwelling favorable in the EGOM than in the WGOM, resulting in larger declines in CUI at buoy I. Such spatial heterogeneity may be explained by differences in the storm tracks.

2.3.2 River Discharge

River runoff is an important factor influencing the salinity and density structure of the coastal GOM, especially in spring and summer seasons (*Keafer et al., 2005; Geyer et al., 2004; Brooks, 1994*). Based on daily discharge observations of the St. John river (U.S. portion only), the Penobscot river, the Androscoggin/Kennebec river, and the Merrimack river (see **Figure 2.1** for their geographic locations), we constructed monthly mean runoff time series in April, May, June and July for 2002- 2011. The cumulative monthly runoff from these 4 rivers was also computed to represent the total freshwater discharge into the gulf in each corresponding month (**Figure 2.3**).

For each river, the runoff is the largest in April and May, and generally declines by 40-70% by June and July. Significant interannual differences are seen in terms of monthly mean and total river discharge. In April, the largest monthly runoff ($\sim 18 \times 10^4 \text{ m}^3 \text{ s}^{-1}$) occurred in 2005, with other high runoff in 2008, 2009, 2010 and 2011. In May, the highest river discharge took place in 2011, with the second highest in 2005. The largest total river runoff in the months of June and July happened in 2006 and 2009, respectively. The total river runoff time series for the entire season (April – July) (**Figure 2.3**, bottom panel) display a similar pattern as those in the individual months. For 6 years (2005-2009 and 2011), the total river runoff was 50-100% larger than those in 2002, 2003, 2004 and 2010.

A detailed examination of the daily runoff time series (**Figure 2.4**) shows that while the overall river discharge in summer 2010 was relatively low, the peak runoff took place in the middle April, which was about two-three weeks earlier than when the peak runoff occurred in other years (early-middle May). Such differences in total discharge and timing of peak runoff can lead to the interannual variability of coastal salinity, which in turn alters water stratification, and the associated baroclinic circulation.

2.3.3 Coastal Hydrography and Currents from moored observations

2.3.3.1 Temperature and Salinity

10-year (2002-2011) temperature and salinity time series display variability on a wide

range of scales from synoptic to seasonal to interannual. To define the mean seasonal cycles, a least-squares harmonic fitting method was applied to hourly surface (2-m) temperature and salinity measurements at buoys B and E in the WGOM and buoy I in the EGOM, respectively, such that,

$$S_{seasonal} = const + a \sin(\omega t) + b \cos(\omega t),$$

where t is time in days, $\omega = 2\pi / 365d^{-1}$, and a and b are fitting coefficients of the harmonic signal. Both hourly observations and fitted seasonal cycles were then time- averaged over each month from April to July in 2002-2011. Comparisons of the resulting monthly mean pairs (observation vs. seasonal cycle) indicate how different surface temperature (**Figure 2.5**) and surface salinity (**Figure 2.6**) are from their corresponding seasonal cycles.

In all years, surface temperature increased monotonically from April to July. Two years stand out as having significant anomalies compared to the mean seasonal cycle. In 2004, the water was about 2°C colder than usual at all three stations (B, E, and I in both the east and western GOM). In contrast, in 2010, the water was significantly warmer (1-2°C) than the mean seasonal cycle at the same three stations. The 50-m temperature record (not shown) shows similar signals, suggesting such interannual variability extends well below the surface.

2.3.3.2 Salinity

The salinity measured by the coastal buoys (B, E, and I) exhibit pronounced interannual variations as well (**Figure 2.6**). We computed the salinity seasonal cycle and standard deviation error with the same harmonic fitting method used for the temperature (note there is a data gap at buoy B in summer 2011 so no analysis was made). All three buoys show the coastal water in 2005 was the freshest in the 10-year record. At buoy B for instance, the measured salinity was 2 units fresher in April and May and 1 unit fresher in June than their corresponding seasonal cycle values. Such freshening is consistent with 2005 having the largest runoff event in the time series (**Figure 2.3**). Conditions are less variable in other years, with salinity values generally falling within a standard deviation of the mean seasonal cycle. We note that salinity in April 2010 was highly anomalous. At all three buoy locations (in both WGOM and EGOM), salinity was 1- 2.5 unit fresher than the seasonal cycle. This coincides with the earlier freshening in April 2010 discussed in Section 2.3.2.

2.3.3.3 Stratification

Temperature and salinity observations at 2-m and 50-m can be used to compute the water column buoyancy (Väisälä) frequency N^2 following

$$N^2_{mid_depth} = -\frac{g}{\rho_0} \frac{\partial \rho}{\partial z} \approx -\frac{g}{\rho_0} \frac{\rho_{(-2m)} - \rho_{(-50m)}}{(-2m - (-50m))}, \text{ where } \rho_0 = 1027 \text{ kg/m}^3, g = 9.8 \text{ m/s}^2$$

Monthly means were calculated for each year between 2002 and 2011 (**Figure 2.7**). In most years, the stratification is dominated by temperature and increases gradually as the seasonal

warming progresses, reaching the highest values of N^2 in July. This was not the case in 2005 and 2010, when April had stronger stratification than May. Interannual variability is affected by the salinity anomaly introduced by larger (or earlier) than normal river discharge discussed earlier (section 2.3.2), resulting in lower salinity and density in the upper ocean that enhances water column stratification.

2.3.3.4 Hydrographic variability in Jordan Basin and the Northeast Channel

Buoy M collects subsurface temperature and salinity data in Jordan Basin (**Figure 2.8**). In addition to the expected seasonal cycle shown in the time series (between February and September) in each year, we also see significant interannual variability at depth (>100m). For example, in February-April 2004, April-August 2010, and February-May 2011, deep water temperature was up to 1-2°C warmer than during the same period in other years. The concurrent salinity time series in February-April 2004 and February-May 2011 (**Figure 2.9**) show that deep water salinity during these two periods was also slightly saltier than in other years. To determine the source of water properties, we conducted a water mass analysis based on the T-S data measured at buoy M following *Smith et al. (2001)* and *McGillicuddy et al. (2011)*. Results (**Figure 2.10**) clearly show Warm Slope Water properties (WSW) in 2011, 2010 and 2004, suggesting a bottom water intrusion taking place prior to the summer season. In 2010 for instance, a similar subsurface warming anomaly is also seen at Buoy N in the

Northeast Channel (not shown). The subsurface water was 2-5°C warmer in 2010 than in most of the years (except for 2006).

2.3.3.5 Currents

We applied the same monthly/seasonal mean analysis on the westward, alongshore surface (2-m) current measured by buoys B, E and I (**Figure 2.11**). Results show the monthly variations are smaller in the EGOM than in the WGOM. At buoy B (in WGOM), the largest April-, May-, June- and July- monthly mean velocities occurred in 2003, 2005, 2007, and 2009, respectively. In contrast, the weakest April-, May-, June-, and July- monthly mean velocities occurred in 2002, 2004, 2010, and 2006, respectively. In some months, a reversed (i.e., eastward) alongshore current is seen, such as in April 2004 at buoy E, and in July 2006 at buoy B. It is also noted that while the alongshore current at buoy I (EGOM) was normal in July 2007, the alongshore flow at buoy E (WGOM) was the weakest compared to flows in July of other years. This suggests that the western portion of MCC system may have been decoupled in July 2007, a finding that will later confirmed by the geostrophic calculations discussed in Section 2.3.4.

From the summer mean perspective, in the WGOM (at buoy B) 2005 had the strongest ($\sim 12 \text{ cm s}^{-1}$) westward alongshore velocity in the 10-year study period, whereas 2002 and 2010 had the weakest (5 cm s^{-1}). Similar features were observed at buoys E and I,

except that the coastal flow in buoy E and I in 2010 is not as weak as downstream, again suggesting offshore veering of MCC. Similar features in other years have been reported by *Pettigrew et al. (2005)* and *Churchill et al. (2005)*. Further analysis of the velocity time series at different depths (not shown) indicates that these kind of seasonal and interannual variations described above extend to at least 60-m below the surface, suggesting the overall transport in the upper water column would follow the same seasonal and interannual variability.

2.3.4 Ship-observed hydrography and geostrophic current

Quasi-synoptic, gulf-wide hydrographic data collected by GOMTOX ship surveys allowed us to examine the density structure and its corresponding dynamic height (DH) and geostrophic flow fields (**Figure 2.12**). We calculated DH by integrating density anomaly relative to the offshore starting point of each hydrographic sampling section, and the geostrophic velocity was computed to balance the local depth-varying pressure gradient that gives zero pressure gradient (and hence the level of no motion) at the seafloor (*Csanady, 1979; Loder et al., 1997; He and McGillicuddy, 2008*).

In May 2005, a strong DH gradient induced by the anomalously large freshwater input (*He and McGillicuddy, 2008*) led to a strong (20 cm s^{-1}) geostrophic flow, which was continuous from the EGOM to the WGOM. The calculations show that strong geostrophic

flows were also present in 2006, although its flow pattern in the WGOM appears to be more sluggish and less organized than in the EGOM. In May-July 2007, the cross-shore DH gradient and alongshore geostrophic current were strong in the EGOM, but currents in the WGOM became weaker (especially in late June, see *EN437* in **Figure 2.11**), which is consistent with weak alongshore current measured *in situ* at buoy B and E (top two panels, **Figure 2.11**). The cross-shelf DH gradient in May-June 2010 is an order of magnitude smaller than that in 2005-2007. As a result, the alongshore geostrophic currents were the weakest among this set of comparisons.

We can estimate the upper water-column geostrophic transport (**Table 2.1**) by integrating the geostrophic current between 5-20m along a transect off Casco Bay (blue line in **Figure 2.1d**). Alongshore transports were much larger in 2005 and 2006 than in other years. In 2007, the transport decreased sharply by nearly 70% from May to June. Similarly, very weak alongshore transports were also observed in May-June 2010. The flow transport started to pick up afterward, and transport doubled by the end of June. Analysis of de-tided ship-board ADCP current data (not shown) also suggests that the alongshore transport in 2010 was much weaker than those in 2005 and 2006.

2.4. Discussion

2.4.1 Interannual variability in hydrodynamics

As shown in previous sections, May-June 2010 had one of the weakest alongshore transports in our 10-year study period. What are the possible reasons? Mooring observations show that warmer and saltier than normal subsurface water (>100m) was prominent in Jordan Basin during February-August, 2010 (**Figure 2.8 and Figure 2.10**). Based on the T-S properties, we infer the anomaly originated from Warm Slope water (WSW, *Houghton and Fairbanks, 2001*) and a warm water intrusion through the Northeast Channel that penetrated into the gulf interior. Indeed, such warm water was also seen in the Northeast Channel and may be traced back to August-September, 2009 (*McGillicuddy et al., 2011*). The distance between buoys M (in Jordan Basin) and N (at the Northeast Channel) is about 210 km. If the intrusion started in February 2010, the estimated speed of the warm water intrusion would be $\sim 4 \text{ cm s}^{-1}$. If the intrusion started around September 2009, then the estimated intrusion speed would be $\sim 1 \text{ cm s}^{-1}$. In either case, it is conceivable that slow, but persistent bottom circulation would be able to deliver warm slope water into Jordan basin.

In average conditions, the Maine Coastal Current is largely driven by the cross-shelf pressure gradient between the coast and offshore basins (e.g., **Figure 2.12**). In 2010, the anomalous warm water in Jordan basin increased the dynamic height in offshore water, decreasing the cross-shelf pressure gradient, and consequently reducing the alongshore current.

In addition to the intrusion of WSW, the upwelling index (UI) time series between 2004

and 2011 indicates that 2010 had the most upwelling-favorable wind condition. Southwesterly wind prevailed throughout April-July (**Figure 2.2**), resulting in coastal divergence that also favors the reduction in the southwestward alongshore transport (e.g., *Fong et al.*, 1997; *Churchill et al.*, 2005).

In 2010, strong stratification developed in early April, which is several weeks earlier than in other years (**Figure 2.7**). This was associated with freshening (**Figure 2.6**) caused by the earlier peak of river discharge (**Figure 2.4**). In addition, the surface freshening further offshore (e.g., Jordan Basin M, **Figure 2.9**) suggests an advective origin, associated with the antecedent anomalous warmer- and fresher-than-usual inflow of Scotian Shelf Water (SSW) (*McGillicuddy et al.*, 2011). Thus, both earlier river runoff and upstream SSW inflow foster the early freshening and stronger stratification in spring and summer 2010.

2.4.2 Impacts on coastal PSP toxicity

Earlier studies have shown that hydrodynamic transport plays a key role in determining the degree to which offshore blooms of *A. fundyense* are exposed to coastal shellfish beds (*Franks and Anderson*, 1992a, b; *McGillicuddy et al.*, 2005a; *Stock et al.*, 2005; *He et al.*, 2008; *Li et al.*, 2009). Coastal toxicity data show the extent of PSP was much less than expected in 2010 based on the cyst abundance data collected in fall 2009 (*McGillicuddy et al.*, 2011). Our analysis reveals that reduction in coastal transport, along with the

upwelling-favorable wind conditions decelerated the delivery of the vegetative cells of *A. fundyense* to the western GOM. Ekman transport associated with upwelling favorable wind could also help to spread the cells in the offshore direction, rather than to concentrate them near the coast. The early freshening in April 2010 led to earlier-than-normal stratification that may have led to earlier-than-normal nutrient depletion, prior to the growing season for *A. fundyense*. Both early stratification and lower ambient nutrient concentrations associated with that year's water mass anomalies may have caused a temporal mismatch with *A. fundyense*'s endogenous clock that regulates the timing of cyst germination (*McGillicuddy et al.*, 2011). The nutrient depletion might also be part of long-term trend of decreased inflow of nutrient-rich slope water through the NEC (*Pettigrew et al.*, 2010; *Smith et al.*, 2012; *Townsend et al.*, 2010), and increased SSW inflow.

McGillicuddy et al. (2005b) showed that the relationship between *A. fundyense* vegetative cell abundance and coastal shellfish toxicity is not statistically significant during year of low cell concentrations. i.e., 1993, 1994, 2000, 2001 and 2002, suggesting that the interannual variability of toxicity may be regulated more by circulation transport than the population themselves. Further analysis of *McGillicuddy et al.* (2011) suggested that the correlation between the most southerly latitude of coastal shellfish toxicity closures and cyst abundance is significant during 2005-2009. However, the inclusion of 2010 in the analysis breaks up the relationship. Early depletion of nutrient due to early phytoplankton bloom in

2010 is a great contributor to the toxicity extent. In addition, we realized that the decreased current in the WGOM (**Figure 2.11, Figure 2.12**) may also contribute to the retreat of the southerly toxicity extent.

Besides 2010, the alongshore transport in the WGOM in June-July 2007 was also found to be largely reduced (by up to 70%) compared to those in the preceding months (**Figure 2.12**). The July condition at buoy E is also the weakest in 2007 compared to same month in other years (**Figure 2.11**). Comparisons with the extent of downstream toxicity closures of *McGillicuddy et al.* (2011) showed that the coincident PSP closures in 2007 did not extend to the coastal Massachusetts, presenting the smallest extension except in 2010. Although the summer-mean alongshore current in 2007 in the WGOM is not as low as 2010 (**Figure 2.11, brown bars**), the sharp decrease in the current amplitude from June to July may prevent the delivery of cell concentrations (and therefore toxicity) further downstream late in the bloom season. In contrast, the strong coastal flow in 2005 (e.g., *He and McGillicuddy*, 2008) favors toxicity closure that extended to the entire New England coasts, constituting one of the largest toxicity closure in the last 30 years (*Anderson et al.*, 2005). Due to limited observations, it is difficult to quantify the direct correlation between alongshore current and the southernmost extent of toxicity closure. No clear relationship was found between toxicity extent and NERACOOS current data, likely because the buoy locations are too sparse to be representative of entire circulation system. Geostrophic transport is in a sense too sparse in

time for correlation computation. Nevertheless, the lowest alongshore toxicity extent in 2010 and 2007 coincides with weakened alongshore currents in July 2007 and June 2010. In contrast, strong alongshore flow in 2005 coincides with a more extensive toxicity closure in the same year. While there is no inclination to omit the contribution of factors like nutrient condition in modulating bloom and toxicity, we found that all the results presented here underscore a possible linkage between coastal circulation and the alongshore extent of toxicity in the western GOM.

2.5. Summary and Conclusion

In situ observations including long-term moored meteorological and oceanographic measurements and multi-year gulf-wide ship survey data were used to quantify interannual variability of surface wind, river runoff, and hydrographic conditions in the Gulf of Maine during summers 2002-2011. Significant interannual variability was found in the local forcing (i.e., wind and river runoff). The cumulative upwelling index (CUI) showed that the upwelling (downwelling)-favorable wind conditions was most persistent in 2010 (2005) over the 9-year study period. River discharge was highest in 2005, whereas the peak runoff started in early April in 2010 as opposed to late April to mid-May in other years.

Coastal hydrography (temperature, salinity, stratification) influenced by both local and deep-ocean forcing also displayed strong interannual variations. Coastal water

temperature was 0.5-2 °C warmer than average in summer 2010, and about 2° C colder than average in 2004. Coastal salinity in April 2010 was the lowest in the 10-year study period. Both moored ADCP current measurements and dynamic height/geostrophic velocity calculations based on gulf-wide ship survey data show May-June 2010 had weak alongshore transport in the western Gulf of Maine. The reduction in alongshore current was likely due to a combined effect of a subsurface warm water intrusion through NEC, an anomalous warmer and fresher SSW (e.g., *McGillicuddy et al.*, 2011) that was also present in the interior Jordan Basin, as well as upwelling-favorable wind conditions. Nutrient concentrations were also low in 2010, possibly due to a decreasing trend in nutrient-rich warm slope water influx into the Gulf (*McGillicuddy et al.*, 2011). Earlier-than-usual stratification caused by early river discharge peaks and SSW inflow could have also caused the earlier-than-usual spring phytoplankton bloom that exhausted nutrient supply, thereby creating unfavorable conditions for *A. fundyense* growth in coastal waters. Such relationship between the extent of PSP closures and coastal transport are also seen in others years such as in 2005 and 2007, suggesting a possible intrinsic linkage between coastal hydrodynamics and the extent and severity of *A. fundyense* bloom and toxicity in the GOM.

Acknowledgements

We thank the Northeastern Regional Association of Coastal Ocean Observing Systems (NERACOOS) for providing the mooring data used in this study; we thank Linda Mangum for her assistance with these data River outflow data were supplied by the United States Geological Survey.

We gratefully acknowledge support of the National Oceanic Atmospheric Administration (grant NA06NOS4780245 for the Gulf of Maine Toxicity (GOMTOX) program). Additional support for DJM was provided by the Woods Hole Center for Oceans and Human Health through National Science Foundation grants OCE-0430724 and OCE-0911031 and National Institute of Environmental Health Sciences grant 1P50-ES01274201.

This is the Ecology and Oceanography of Harmful Algal Blooms Program contribution number XXX.

References

- Anderson D.M., Keafer, B.A., McGillicuddy, D.J., Mickelson, M.J., Keay, K.E., Libby, P.S., Manning, J.P., Mayo, C.A., Wittaker, D.K., Hickey, J. M., He, R., Lynch, D.R., Smith, K.W. (2005), Initial observation of the 2005 Alexandrium fundyense bloom in the southern New England: general patterns and mechanisms. *Deep Sea Research II*, 52, 2856-2876.
- Aretxabaleta, A.L., McGillicuddy, D.J., Smith, K.W., Manning J.P. and D.R. Lynch (2009): Model Simulations of the Bay of Fundy Gyre: 2. Hindcasts for 2005-2007 Reveal Interannual Variability in Retentiveness. *Journal of Geophysical Research*, 114, C09005, doi:10.1029/2008JC004948.
- Bigelow, H.B. (1927), Physical Oceanography of the Gulf of Maine, *Fisheries Bulletin*, 40, 511-1027.
- Bisagni, J. J. and Smith P.C. (1998), eddy-induced flow of Scotian Shelf water across Northeast Channel, Gulf of Maine, *Continental Shelf Research*, 18, 515-539.
- Brooks, D.A. (1994): A model study of the buoyancy-driven circulation in the Gulf of Maine, *Journal of Physical Oceanography* 24, 2387–2412.
- Brown, W.S. and Irish, J.D. (1993): The annual variation of the mass structure in the Gulf of Maine: 1986-1987. *Journal of Marine Research*, 51, 53-107.
- Butman, B., C. R. Sherwood and P.S. Dalyande (2008): "Northeast storms ranked by wind stress and wave-generated bottom stress observed in Massachusetts Bay, 1990–2006." *Continental Shelf Research*, 28(10–11): 1231-1245.
- Churchill, J.H., N.R. Pettigrew, and R.P. Signell (2005): Structure and Variability of the Western Maine Coastal Current. *Deep Sea Research II*, 52: 2392-2410.
- Csanady, G. T. (1979), The Pressure Field Along the Western Margin of the North Atlantic, *Journal of Geophysical Research*, 84(C8), 4905–4915, doi:10.1029/JC084iC08p04905.
- Fong, D.A., W.R. Geyer, and R.P. Signell (1997): The wind-forced response on a buoyant coastal current: Observations of the western Gulf of Maine plume, *Journal of Marine System*, 12, 1–4, pp 69–81
- Franks, P. J. S. and D. M. Anderson (1992a): Toxic phytoplankton blooms in the southwestern Gulf of Maine: Testing hypotheses of physical control using historical data. *Marine Biology* 112: 165-174.
- Franks, P. J. S. and D. M. Anderson (1992b): Alongshore transport of a toxic phytoplankton

bloom in a buoyancy current: *Alexandrium tamarensis* in the Gulf of Maine. *Marine Biology* 112: 153-164. Geyer, W.R., Signell, R.P., Fong, D.A., Wang, J., Anderson, D.M., Keafer, B.A.(2004): The freshwater transport and dynamics of the Western Maine Coastal Current, *Continental Shelf Research*, 24, 1339–1357.

He, R. and McGillicuddy D. J. (2008): The historic 2005 Toxic Bloom of *Alexandrium fundyense* in the west Gulf of Maine- Part 1: In Situ Observations of Coastal Hydrography and Circulation. *Journal of Geophysical Research*, 113, C07039, doi: 10.1029/2007JC004601.

He, R., McGillicuddy D. J., Keafer B.A, Anderson D. M. (2008): Gulf of Maine Harmful Algal Bloom in summer 2005- Part 2: Coupled Bio-physical Numerical Modeling, *Journal of Geophysical Research*, 113, C07040, doi: 10.1029 /2007 JC 004602.

Houghton, R.W. and Fairbanks R. G. (2001), Water sources for Georges Bank, *Deep-Sea Research II*, 48, 95-114.

Keafer B.A., Churchill, J.H., McGillicuddy, D.J., Anderson, D.M (2005), Bloom development and transport of toxic *Alexandrium fundyense* population within a coastal plume in the Gulf of Maine. *Deep Sea Research II*, 52, 2674-2697.

Large, W. G., and S. Pond (1981), Open ocean momentum flux measurements in moderate to strong winds, *Journal of Physical Oceanography*, 11, 324–336.

Limeburner, R., and Beardsley, R.C. (1996), Near-surface recirculation over Georges Bank. *Deep Sea Research II*, 43, 1547-1574.

Li, Y., He, R., D.J. McGillicuddy, D.M. Anderson, and B.A. Keafer (2009): Investigation of the 2006 *Alexandrium fundyense* Bloom in the Gulf of Maine: In situ Observations and Numerical Modeling, *Continental Shelf Research*, doi:10.1016/j.csr.2009.07.012

Li, Y., He, R., and J.P. Manning (2012): The coastal connectivity in the Gulf of Maine, submitted to *Deep Sea Research II*, this issue.

Loder, J.W., Han, G., Hannah C.G., Greeberg D.A., and Smith P.C. (1997), Hydrography and baroclinic circulation in the Scotian shelf region: winter vs. summer. *Canadian Journal of Fisheries and Aquatic Science Supplement*, 54, 40-56.

Lynch, D.R., J. T. Ipa., C. E. Naimie and F. E. Werner (1996), Comprehensive coastal circulation model with application to the Gulf of Maine. *Continental Shelf Research*, Vol. 16-7, 875-906

Lynch, D.R., M.J. Holboke, C.E. Naimie (1997), The Maine coastal current: Spring climatological circulation. *Continental Shelf Research*, 17 (6): 605-634, May, 1997.

Manning, J.P., D.J. McGillicuddy, N.R. Pettigrew, J.H. Churchill, and L.S. Incze (2009).

Drifter observations of the Gulf of Maine Coastal Current, *Continental Shelf Research*, 29 (7):835-845.

McGillicuddy, D.J., Anderson, D.M., Lynch, D.R., Townsend D.W. (2005a), Mechanisms regulating large-scale seasonal fluctuations in *Alexandrium fundyense* populations in the Gulf of Maine: Results from a physical-biological model. *Deep Sea Research II*, 52, 2698-2714.

McGillicuddy, D.J., Anderson, D.M., Solow, A.R., and D.W. Townsend, (2005b), Interannual variability of *Alexandrium fundyense* abundance and shellfish toxicity in the Gulf of Maine. *Deep-Sea Research II*, 52, 2843-2855.

McGillicuddy, D.J., Townsend, D.W., He, R., Keafer, B.A., Kleindinst, J.L., Li, Y., Manning, J.P., Mountain, D.G., Thomas, M.A., and D.M. Anderson (2011), Suppression of the 2010 *Alexandrium fundyense* bloom by changes in physical, biological, and chemical properties of the Gulf of Maine. *Limnology and Oceanography*, 56(6), 2411–2426.

Mountain, D.G. and Manning J.P. (1994), Seasonal and interannual variability in the properties of the surface waters of the Gulf of Maine, *Continental Shelf Research*, 14, 1555-1581.

Mountain, D.G., G. Strout, and R. Beardsley (1996), Surface heat flux in the Gulf of Maine. *Deep Sea Research II*, 43, 1533-1546.

Pettigrew, N. R., J. H. Churchill, C. D. Janzen, L. J. Mangum, R. P. Signell, A. C. Thomas, D. W. Townsend, J. P. Wallinga, and H. Xue (2005), The kinematic and hydrographic structure of the Gulf of Maine coastal current. *Deep Sea Research*, Part II, 52, 19-21, 2369-2391.

Pettigrew, N. R., R.J. Fleming, and C.P. Fikes (2011): The history of the first decade of the observing system in the Gulf of Maine, and plans for the second decade, *MTS Journal*, September 2011, 1-10.

Schwing, F. B., M. O'Farrell, J. M. Steger, and K. Baltz (1996), Coastal upwelling indices, West Coast of North America, 1946 – 1995, *NOAA Technical Memo. NOAA-TM-NMFS-SWFSC-231*, 144 pp.

Smith P.C, R.W. Houghton, R.G. Fairbanks., and D.G. Mountain (2001): Interannual variability of boundary fluxes and water mass properties in the Gulf of Maine and on Georges Bank: 1993-1997, *Deep-Sea Research II* 48: 37-70.

Smith, P.C. N.R. Pettigrew, P. Yeats, D.W. Townsend and G. Han (2012): A Regime Change in the Gulf of Maine. *Trans. Amer. Fish. Soc. (Proceedings of the Scientific Symposium on the Gulf of Maine, St. Andrews, NB, October 2009)*, in press.

Stock, C.A., McGillicuddy D.J., Solow, A.R., Anderson D.A (2005), Evaluating hypothesis for the initiation and development of *Alexandrium fundyense* blooms in the western Gulf of Maine using a coupled physical-biological model. *Deep Sea Research II*, 52, 2715-2744.

Thomas, A.C., R. Weatherbee, H. Xue and G. Liu (2010): Interannual variability of shellfish toxicity in the Gulf of Maine: Time and space patterns and links to environmental variability, *Harmful Algae*, 9, 458-480, doi:10.1016/j.hal.2010.03.002.

Townsend, D.W., N.D. Rebeck, M.A. Thomas, L. Karp-Boss, and R. M. Gettings. 2010. A changing nutrient regime in the Gulf of Maine. *Continental Shelf Research*, 30: 820-832.

Xue H., F. Chai and N.R. Pettigrew (2000): A model study of the seasonal circulation in the Gulf of Maine, *Journal of Physical Oceanography*, 30 (5): 1111-1135, 2000.

Chapter III: The Coastal Connectivity in the Gulf of Maine in Spring and Summer of 2004 -2009

Yizhen Li¹, Ruoying He¹, James P. Manning²

¹Department of Maine, Earth, and Atmospheric Sciences, North Carolina State University, 2800 Faucette
Drive, Raleigh, NC 27695

²National Oceanic Atmospheric Administration, Northeast Fisheries Science Center, 166 Water Street,
Woods Hole, MA 02543, USA

Last revised: July 28, 2012. Submitted to *Deep Sea Research II*, in revision.

Keywords: Gulf of Maine, Coastal Circulation, Connectivity, Lagrangian PDFs, Interannual Variability, Source and Destination Strengths

Abstract

The Gulf of Maine (GOM) coastal ocean connectivity in spring and summer seasons of 2004-2009 are studied using surface numerical particle trackings based on realistic regional ocean circulation hindcast solutions. Seven initial particle release sites are selected, including the Massachusetts Bay, the western GOM coastal area, the eastern GOM coastal area, the Bay of Fundy, the Wilkinson Basin, the Jordan Basin, and a region seaward of the Penobscot Bay. Surface particles are released every five days from February 1st through August 1st in each year, and their trajectory variability on the seasonal and inter-annual time scales are quantified by Lagrangian probability density function (LPDF) calculations. The coastal connectivity is further quantified using the connectivity matrix, source and destination

functions. Our results show that the interannual variability in coastal connectivity has strong impact on the spatial distribution of *A. fundyense* blooms in each year. In all years being studied here, particles released in the Bay of Fundy during summer 2009 display the largest destination strength along the coast of eastern GOM. At the same time, extensive *A. fundyense* bloom and high toxicity were observed in that area.

3.1 Introduction

The Gulf of Maine (GOM) is a semi-closed marginal sea off the U.S. northeast seaboard. While the mean circulation in the gulf is known to be cyclonic (*Bigelow, 1927; Lynch, 1997*), significant seasonal and interannual variations in coastal current and transport have long been identified by previous observational and modeling work (e.g., *Pettigrew et al., 2005; Manning et al., 2006; 2009; He and McGillicuddy, 2008; Xue et al., 2000*). One of major research focuses in the GOM is the dispersion of biological species by the Gulf of Maine coastal current. *Hannah (1998)* used model generated climatological mean circulation to study the upper-ocean transport mechanisms for the copepod *Calanus finmarchicus*, which is the dominant contributor to the annual zooplankton bloom in the GOM. Their results showed that the southward surface Ekman drift induced by northwesterly wind can act as a conveyor belt, transporting the copepod species from the GOM to the Georges Bank in winter and spring seasons. Recent study by *Xue et al. (2008)* focused on the early life stage of lobsters in the GOM. They coupled a realistic circulation hindcast model (Princeton Ocean Model) with an individual based biological model that considered lobster egg production, temperature-dependent larval growth, stage-explicit vertical distributions. Numerical lobster larvae were released three times each month from June to September within the 100-m isobath near the coastal area. This study found relatively lower accumulations of early stage lobsters along the eastern Maine coast than along the western Maine coast. Significant

interannual variability in particle distributions were also identified between 2002 and 2004. Using the same model setup but include mortality in the biological model, a further study of *Incze et al. (2010)* focused on the relative contributions of different source regions to the final-distribution of postlarvae along the coastal zone. A connectivity matrix was constructed to show the connection between different coastal locations. This study showed strong interannual variability in the postlarvae abundance in response to circulation and temperature variations. *Manning and Churchill (2006)* and *Manning et al., (2009)* provided drifter dispersion studies in the GOM. The latter work in particular utilized observed drifter trajectories collected from 1988 to 2007 to describe the Maine Coastal Current (MCC) and the coastal transit time along different isobaths.

A more statistically comprehensive Lagrangian PDF (LPDF) method was introduced by *Mitarai et al. (2009)* to describe the coastal connectivity in the Southern California Bight (SCB). The LPDFs describe the probability density function of particle displacement for a given advection time. Driven by simulated ocean current, their ensemble particle dispersal patterns were quantified by LPDFs, exhibiting a strong dependence of particle dispersions on initial release locations and advection time scales. Moreover, pronounced dispersion variability on seasonal to interannual timescales was shown to be largely determined by eddy activities and synoptic wind-forcing variations in SCB. LPDFs were also used to derive the connectivity matrix in the study. Based on the connectivity matrix, the source and destination

strengths were further computed at each coastal location being studied in that research. In general, the source (destination) strength represents where the released parcels come from (arrive), a robust method for quantifying connections between different oceanic domains. Detailed mathematical formulation of LPDFs, connectivity, and source and destination strengths are shown in Section 3.2.2.

Here, we intend to further quantify the GOM Lagrangian connectivity using a similar LPDF method and valuable drifter observations documented by *Manning et al.* (2009). First, the GOM coastal area is highly energetic due to its unique circulation features. There is high continuity between the eastern portion of Maine Coastal Current (MCC) and western MCC at certain years (e.g., 2000, 2003), as opposed to disrupted coastal flow in other years (e.g., 1998 and 2002) when EMCC veers offshore southeast of Penobscot Bay (*Pettigrew et al.*, 2005; *Xue et al.*, 2008). In addition, the Bay of Fundy gyre shows high self-retentiveness as in the climatological condition and also strong interannual variability in the leakage of the transport to the EGOM through the BOF exit pathways (*Arexabaleta et al.*, 2008; 2009). Besides, the Jordan Basin gyre shows strong seasonal variability with higher intensity in summer compared to spring (*Beardsley et al.*, 1997). All these wonderful work provide excellent foundation for us to further investigate the coastal circulation dynamics through numerical particle tracking approach, as well to compare our results with previous findings. In addition, our key scientific motivations are to better understand the role of ocean

circulation in affecting the harmful algal bloom (*A. fundyense*) distributions both onshore and offshore during the bloom season (spring and summer months) at intra- and inter-annual time scales. *A. fundyense* cells are initiated from cyst germination in early spring of each year. The resulting blooms (of different intensity in each year) are present in various GOM coastal regions throughout the summer. How does the coastal circulation variability influence their dispersions: i.e., which *A. fundyense* source location(s) are relatively more important, and where their most likely destinations reside are key questions we seek to answer. We start in Section 3.2 with an introduction of our GOM coastal circulation model, a brief overview of coastal connectivity and Lagrangian PDF concepts. Section 3.3 presents the model-data comparisons, GOM LPDF results, and connectivity, source and destination strength calculations. Section 3.4 discusses connectivity variability on both seasonal and annual time scales, and their possible driving mechanisms, followed a summary and future work in Section 3.5.

3.2 Data and methods

3.2.1 Hydrodynamic model, observations, and particle tracking tool

The GOM circulation hindcast were performed using a regional implementation based on the Regional Ocean Modeling System (*Haidvogel et al., 2008; Shchepetkin and McWilliams, 2005*). ROMS is a free-surface, hydrostatic, primitive-equation model that employs split-explicit separation of fast barotropic and slow baroclinic modes and vertically

stretched terrain-following coordinates. We implemented a multi-nested configuration consisting of circulation downscaling from a global data assimilative Hybrid Coordinate Ocean Model (HYCOM/NCODA) to a shelf-wide ROMS model, and subsequently to the GOM ROMS model (*He et al.*, 2008). The global HYCOM assimilates satellite observed sea surface temperature and height, and ARGO measured temperature and salinity profiling data, providing daily data assimilative global circulation at about 10 km resolution (<http://hycom.rsmas.miami.edu/dataserver>). Inside HYCOM we have embedded the shelf-scale ROMS model that encompasses both the Mid-Atlantic Bight (MAB) and GOM (hereafter MABGOM ROMS) via a one-way nesting approach. Horizontal resolution of MABGOM ROMS is 5(10) km in the across- (along-) shelf direction. Vertically there are 36 terrain-following levels in the water column with higher resolution near the surface and bottom to better resolve boundary layer dynamics. For the purpose of one-way nesting, MABGOM ROMS open boundary conditions (OBCs) were applied to tracers and baroclinic velocity following the method of *Marchesiello et al.* (2001), whereby Orlandi-type radiation conditions were used in conjunction with relaxation. Free surface and depth-averaged velocity boundary conditions were specified using the method of *Flather* (1976) with the external values provided by HYCOM. Since HYCOM solutions do not include tides, tidal harmonics (M_2 , S_2 , N_2 , K_2 , K_1 , O_1 , Q_1) from an ADCIRC simulation of the western Atlantic (*Luettich et al.*, 1992) were also superimposed. Analysis of tidal interior solution confirmed

the approach yielded accurate tidal predictions as compared with earlier results (e.g. *Moody et al.*, 1984; *Xue et al.*, 2000; *He et al.*, 2008). The *Mellor-Yamada* (1982) closure scheme is applied to compute the vertical turbulent mixing, as well as the quadratic drag formulation for the bottom friction specification. The same one-way nesting approach and OBC treatment were applied subsequently to downscale the shelf-scale MABGOM circulation to the inner-most GOM model. The GOM ROMS has a spatial resolution of 1 (3)-km in the across-shelf (alongshore) direction, and also has 36 vertical layers. Such multi-nested downscaling configuration enables the high-resolution GOM ROMS to achieve numerically accurate and dynamically consistent boundary forcing from its large scale “parent” model. Indeed, earlier studies (e.g., *He et al.*, 2005) showed that significant skill improvement in modeling GOM hydrography and transport can be achieved by using more accurate OBCs specifications.

Surface atmospheric forcing used in our regional ROMS simulations, including cloud fraction, precipitation, surface pressure and humidity, air temperature, surface wind, and shortwave radiation were obtained from the National Center for Environmental Prediction (NCEP), North America Regional Reanalysis (NARR). Spatial and temporal resolutions of these forcing fields are 32- km and 3 hours, respectively. They were applied in the standard bulk flux formulation to derive wind stress and net surface heat flux needed by the simulations. To further constrain the surface heat flux, we also followed the same approach

used in *He and Weisberg* (2003) to relax the modeled SST field to NOAA Coast Watch daily, 1/10 degree cloud-free SST product with a timescale of 0.5 day. The GOM circulation model has been coupled with an *A. fundyense* population dynamic model to simulate the GOM circulation and harmful algal (*A. fundyense*) bloom. Interested readers are referred to *He et al.* (2008) and *Li et al.* (2009) for a more detailed description of that coupled biophysical model.

In-situ observations used in this study include time series of wind and ocean current measured by moorings of the Gulf of Maine Ocean Observing System (now part of the Northeast Coastal Ocean Observation System NERACOOS, <http://www.neracoos.org>, e.g., *Pettigrew et al.*, 2011), and the long-term drifter statistics provided by *Manning et al.* (2009).

The numerical surface particle trajectories were calculated using the Larval Transport model (LTRANS), which is an offline particle tracking model that runs with GOM ROMS simulated surface ocean currents archives. Our objective is to understand the transport pathways of vegetative *A. fundyense* cells at the ocean surface. As such, numerical particles are isobaric such that they are ‘drogued’ at 1-meter and are not impacted by the vertical velocity. LTRANS model tracking includes a 4th-order Runge-Kutta scheme for advection. In this study, we also activated the random displacement module to mimic the sub-grid scale turbulent diffusion. To avoid possible beaching (hitting the land-sea boundary or an island) of the particles, reflective horizontal boundary condition was applied to keep particles within

the model ocean domain. Once a particle hits the land boundary, it is reflected back using the same angle of its approaching to the boundary. More detailed information on LTRANS is given by *North et al.* (2005; 2006; 2008) and *Schlag et al.* (2008).

3.2.2 Lagrangian PDFs

Following *Mitarai et al.* (2009), we first define the Lagrangian Probability Functions (LPDFs) as the probability density of particle displacement. For a given set of advection time scale τ , sampling space variable ε , initial position \mathbf{a} , and the position of n-th particle $X_n(\tau, \mathbf{a})$, the discrete representation of LPDFs $f'_x(\varepsilon; \tau, \mathbf{a})$ is defined as:

$$f'_x(\varepsilon; \tau, \mathbf{a}) = \frac{1}{N} \sum_{n=1}^N \delta(X_n(\tau, \mathbf{a}) - \varepsilon) \dots \dots \dots (1)$$

where N is the total number of Lagrangian particles, and δ is the Dirac delta function.

The Dirac function is defined as the Heaviside function H in a unit area (i.e., $\delta = \frac{dH}{dxdy}$),

where the Heaviside function H is typically known as the unit step function, such that

$$H(x) = \begin{cases} 0 & \text{if } n < x \\ 1 & \text{if } n \geq x \end{cases}, \text{ where } n \text{ is the integer (grid number) along the directional axis } x. \text{ As such,}$$

f'_x is also in the unit of reciprocal area.

The discrete LPDF f'_x can be expressed as spatially-averaged LPDFs over the surrounding area of each release site, that is:

$$f'_x(\varepsilon; \tau, \mathbf{a}) \approx \frac{1}{\pi R^2} \int_{|r| \leq R} f'_x(\varepsilon; \tau, \mathbf{a} + r) r dr \dots \dots \dots (2)$$

where R is the radius of each release site (taken as 6-km in this study). A smooth operator (Gaussian filter with radius of 6 km) was then applied to remove subgrid-scale noises to get the LPDF f_X .

Based on the probability density (LPDF), the coastal connectivity $C_{j,i}$ is then defined as the probability of a water parcel that moves from source j to destination i over a time interval τ . For a given set of source location x_j and a destination location x_i , the value of $C_{j,i}$ is evaluated from the LPDF as:

$$C_{j,i}(\tau) = f_X(\varepsilon = x_i; \tau, a = x_j)(\pi R^2) \dots \dots \dots (3)$$

The connectivity matrix can be normalized by the surrounding area πR^2 of each release site to convert probability densities into probabilities.

Once we have the connectivity matrix, the destination strength $D_i(\tau)$, representing the relative ‘attractiveness’ of site i for all Lagrangian particles released in the study domain over a release time τ , can be calculated by summing the connectivity matrix over all source sites in the domain, i.e.,

$$D_i(\tau) = \sum_{j \subseteq J} C_{j,i}(\tau), J = j_1, j_2, \dots, j_N \dots \dots \dots (4)$$

Put simply, it tells where the particles from all source sites come from.

Similarly, the source strength $S_j(\tau)$ measuring the relative success of particles moving from site j to other places in the domain within an advection time scale τ , can be calculated by summing the connectivity matrix over all selected destination sites in the domain as:

$$S_j(\tau) = \sum_{i \in I} C_{j,i}(\tau), I = i_1, i_2, \dots, i_N \dots \dots \dots (5)$$

Put simply, it presents where the particles from certain destinations come from.

3.3 Results

3.3.1 Particle Release

We selected a set of particle release centers in the GOM (**Figure 3.1**), including domains at the Massachusetts Bay (MA, sites 1-7), the western GOM (WGOM, sites 8-23) coastal area, the eastern GOM (sites 24-36, EGOM) coastal area, the Bay of Fundy (BOF, sites 37-48), the Wilkinson Basin (WK, sites 49-66), a region seaward of the Penobscot Bay (OFFPB, sites 67-78), and the Jordan Basin (JB, sites 79-96). As shown in equation (2), each releases site centered in the domains defined above covers a 6-km radius circular area, a same approach used by *Mitarai et al.* (2009) for the quantification of coastal connectivity. We chose sites 8-23 and sites 24-36 with their centers along the 50-m isobaths in the EGOM and WGOM coastal areas respectively, with an approximately 12-km spacing along the shore. Given the minimum water depth of the circulation model (10-m), the circular areas therefore cover most coastal waters up to 100-m deep or shallower, an area where repetitive shellfish bed closure takes place every year. Meanwhile, offshore particle releases covers most deep basin locations within 200-m isobaths. Among these sites, BOF, OFFPB, and JB are known to be important cyst germination (“source”) locations for *A. fundyense* blooms (e.g., *Anderson et al.*, 2005). We chose the EGOM and WGOM coastal areas because the

shoreward areas of these sites are “destination” regions often affected by *A. fundyense* bloom and its toxicity every year (McGillicuddy *et al.*, 2005).

We focused on the subtidal transport in spring and summer seasons, and for this purpose, surface particle trajectories were computed by LTRANS using the sub-tidal (12.42hr averaged) surface velocity archives simulated in each year from Feb 1st through Aug 1st in 2004 and 2009. A total of 1531 particles were released within the radius of 6km of each of these sites every 5 days, resulting over 6 years a total of 19,841,760 particle trajectories that were used to quantify connections among different GOM coastal regions.

3.3.2 Validation of Circulation Model

Because the utility of simulated particle trajectories is based on the quality of ocean current simulation, extensive model-data comparisons had been performed to gauge the performance of the GOM regional ocean model. Examples of model validations on synoptic to seasonal time scale were given in *He et al.* (2008), which compared the model hindcast solutions in 2005 with observed sea-level, currents, surface temperature and salinity; and in *Li et al.* (2009), which compared model solutions with a similar set of observations in the 2006. Additional comparisons were also conducted to gauge modeled current against observations in spring and summer 2008 (*Li et al.*, in prep.). All results suggested that the model reasonably captured the hydrography and circulation variability at synoptic to seasonal

timescales.

To further compare the low-frequency variability, in this study additional comparisons were made between simulated and observed monthly mean surface currents over the 6-year period. Taking GoMOOS moorings A and B for example (**Figure 2**) reasonable model-data agreements are seen at both locations. The model generally reproduced the observed temporal variability as indicated by > 0.5 complex correlation coefficients. In terms of mean velocity speed, the model underestimated (overestimated) observations at buoy A (B), as shown by an amplitude regression slope of 0.6 (1.1), respectively. The implication of the over-/under- estimation of the coastal currents on the particle trajectory simulation will be discussed in Section 3.5.

Manning et al. (2009) derived a 0.5-degree GOM mean surface current field based on long-term drifter observations over a long-term period of 1988-2007, and the majority of these drifter observations were collected during spring and summer seasons. This dataset provided another valuable way for validating model simulated surface current fields. To do that, we averaged modeled surface velocity over February –August period in 2004-2009 and remapped the resulting mean field from the ROMS model grid to the same 0.5×0.5 degree drifter analysis grid (**Figure 3.3**). Direct comparison shows that the major GOM circulation features including the mean inflow from the Nova Scotia, the cyclonic Maine Coastal Current (MCC), and the Georges Bank recirculation are all well reproduced by the model, although

the model seems underestimate the cyclonic Jordan Basin gyre. Within each $0.5^{\circ} \times 0.5^{\circ}$ grid box, statistic comparisons on mean velocity speed and direction are provided (numbers inside each grid box), indicating the modeled coastal current speed generally resemble observational counterpart.

Both synoptic and seasonal scale model/data comparisons presented in previous studies (*He et al.*, 2008; *Li et al.*, 2009) and the long-term mean comparisons in this study indicate that the GOM ROMS model has reasonable skill in reproducing observed surface circulation, lending us the confidence that the offline Lagrangian transport analysis is couched in a realistic GOM hydrodynamic settings.

3.3.3 Mean Lagrangian PDFs

Because the Lagrangian particle trajectories in the GOM are dependent upon the locations and timings of their releases, a quantification of the dispersal patterns in a statistical approach is necessary. Based on the particle releases over the 6-year period, we computed the mean LPDFs for February-August period according to the formulations in *Section 2.2*. For example, depending on the length of tracking period (advection time τ), the time-averaged LPDFs for the BOF release show different spatial structures (**Figure 3.4**). Strong self-sustenance is present for the case with an advection time scale of 10-day, while a more gulf-wide dispersion is seen for the case with an advection time scale of 50-day. An estimated probability of particles within or outside the BOF can be achieved by integrating the LPDFs

over the study area (i.e., $\iint f(x)dxdy$). In such a case, the BOF has an area of about 3×10^4 km², the mean LPDF for a 10-day advection time scale within the BOF exceeds 3×10^{-5} km⁻². Integrating the LPDF over BOF areas shows the probability of particles remaining within the BOF is 82.7%, and only 15% particles can move out of the BOF. The particles become more dispersed as the advection time scale increases to 20-day. An integration of LPDFs over the BOF show that 66.9% remains in the BOF, and 25.9% of particles released in the BOF can enter the EGOM area. The mean LPDFs associated with the advection time of 40-day show a more gulf-wide dispersion pattern. The mean LPDFs associated with 60-day advection time scale essentially show similar dispersion patterns, suggesting at least on the monthly to seasonal advection time scale of interest for the HAB bloom, LPDF pattern can be well represented by its distribution map at 40-day advection timescale. Spatial patterns of LPDFs released from other study sites also suggest that 40-day is an appropriate time scale to understand and quantify the probability of particles being transported in various areas of the GOM. *Manning et al.* (2009) showed that the mean transit time for drifters to travel from the BOF to the Great South Channel (GSC) is less than two months, so a 40-day period is an appropriate time scale that can allow us to study and quantify the coastal inter-connectivity of the entire GOM at monthly timescale. We note that for the 60-day release, 46.9 % of the particles remain in the BOF. This is in good agreement with the BOF gyre retention estimate of *Aretxabaleta et al.* (2009), which shows that 42.6% of particles remain in the BOF based

on their 60-day tracking of near-surface particles released from the BOF.

3.3.4 Mean Connectivity Matrix, Source and Destination Strength

Based on equation (3), the connectivity matrix can be quantified using the LPDFs for given destination and source locations, illustrating the degree to which any two sites among all possible location combinations are connected over a designated advection timescale. **Figure 3.5** shows the mean coastal connectivity matrix for the advection time τ being 10-day, 20-day, 40-day, and 50-day, respectively. The X-axis represents all destinations, and Y-axis represents all source locations. For the case with the advection timescale τ being 10-day (**Figure 3.5a**), the self-connectivity dominates. There are clear connections between immediately adjacent locations due to the coastal circulation transport, such as between the EGOM coastal area and the WGOM coastal area, between BOF and EGOM, and between WGOM and the Massachusetts Bay. The connectivity pattern becomes more spread as the advection time increases to 20-day (**Figure 3.5b**) and 40-day (**Figure 3.5c**). We note the connectivity pattern with 50-day as the advection time scale (**Figure 3.5d**) is similar to that of 40-day, reconfirming that 40-day is an appropriate timescale for evaluating the coastal connectivity at monthly to seasonal advection timescale.

The connectivity matrix for the case with 40-day as the advection time scale (**Figure 3.5c**) shows some interesting features. First, while the BOF releases show the strongest self-connectivity, these particles can leak out, travel to and connect with almost all other

GOM sites under study. Second, similar to BOF releases, JB releases also show strong self-sustenance, although the strength is not as intensive as the BOF releases. JB releases are connected to various locations under study except the WGOM coastal area, the EGOM coastal area, and the Massachusetts Bay. The connectivity between JB and other regions are largely homogeneous.

To better quantify the connectivity among different release domains, the spatial distribution of source (**Figure 3.6**) and destination (**Figure 3.7**) strengths were calculated to show the coastal connectivity from an integrated perspective. The destination (source) strengths are the partial summation of the connectivity matrix over certain source (destination) locations, which are not readily visible in the connectivity matrix due to the often heterogeneity nature. The source (destination) strength is normalized into a percentage of the total released particles arriving at (originating from) a certain domain.

Source strength to the MASS (**Figure 3.6a**) decreases monotonically from Cape Cod Bay to the coastal sites upstream in the WGOM. The strongest source location to the MASS is near the head of Cape Ann. Neither offshore sites nor coastal EGOM and BOF are very good sources for the MASS. For the coastal WGOM area (**Figure 3.6b**), both the coastal EGOM and BOF are good sources. Much fewer particles coming from OFFPB and JB are able to travel to coastal WGOM. For the BOF area (**Figure 3.6c**), our results show most of locations are connected with themselves. Among all the domains of interest, there are some

minor contributions from JB. For the coastal EGOM (**Figure 3.6d**), the source is predominated by BOF input. There are multiple sources for WK (**Figure 3.6e**), including BOF, EGOM, and JB. This indicates that input from these various locations can play important roles in modulating marine material properties in WK. More particles transported to OFFPB (**Figure 3.6f**) are from JB, OFFPB and coastal EGOM. For JB (**Figure 3.6g**), the sources particles are largely from the interior basin, plus some contributions from EGOM and BOF. There is essentially no contribution from WGOM or MASS. If we consider all 96 release locations from 7 sub-regions as a whole, BOF and JB are the two regions having the strongest source strength, suggesting they play a predominant role in terms of coastal connectivity among all coastal GOM sites. We noted that BOF and JB are treated in the same density of initial particles released, and demonstrate the coastal circulation variability only. More detailed analysis of relative importance of the two regions with respect to HAB bloom dynamics requires taking more biological processes into consideration. It is also noticed that the calculations are only the relative portions to the domain of interest under study, and demonstrate the degree of connectivity between different oceanic areas we have chosen. For example, the source strength for the BOF (**Figure 3.6c**) shows higher strength in BOF than in JB, and destination strength is comparatively lower in other coastal and offshore areas. This does not necessarily mean that there are no connections between BOF and other source locations beyond the domain we chose. For example, there can be interconnections between

south of the Scotian Shelf and BOF, although they are not taken into consideration in the study for our interest.

The destination (**Figure 3.7**) strength represents the attractiveness of various destinations for the released particles. For the two downstream domains - MASS and WK (**Figure 3.7a** and **Figure 3.7e**), there are very confined connectivity, essentially just with themselves. The WGOM (**Figure 3.7b**) releases can spread into the MASS, WK, and some to OFFPB. The destination strength for the BOF releases (**Figure 3.7c**) shows high intensity in the BOF itself, as well as along the coast of both EGOM and WGOM. Releases from coastal EGOM (**Figure 3.7d**) can reach all offshore sites (JB, OFFPB, WK), as well as WGOM coastal area and MASS. OFFPB (**Figure 3.7f**) releases show strongest destination strength in WK and OFFPB. It seems that there is little chance these particles can be transported to coastal sites. For particles released from JB (**Figure 3.7g**), most of them are self-retained in JB, while the rest can travel to BOF and WK. If we consider all 96 destination locations from 7 sub-regions as a whole (**Figure 3.7h**), WK and BOF are the two most 'attractive' domains that have the strongest destination strengths. Again, all these calculations are with respect to the destination locations we've chosen. Destinations strengths to domains beyond our study area are not taken into account herein.

To summarize, among all the domains we chose, the BOF and JB are two strongest source regions in the GOM, whereas WK and BOF are two destination regions having the

largest “attractiveness”. Overall, offshore sites have higher destination strength relative to the coastal sites.

3.4 Discussions

3.4.1 Variability of the connectivity

While the long-term mean connectivity among coastal sites is quantified based on connectivity matrix, source and destination strengths in section 3.3, the connectivity has strong temporal variability at shorter timescales. To quantify such variability relative to the temporal mean connectivity matrix (**Figure 3.8a**), we computed the standard deviation (STD) (**Figure 3.8b**) relative to the mean over the 5-year (2004-2009) under study. Indeed, the STD of the connectivity matrix shows substantial variability, highlighting the varying and inhomogenous nature of the coastal circulation in each year. Such time-varying characteristics of the connectivity stem from seasonal to interannual variability in the coastal circulation and transport, as well as shorter duration, eddy-induced water parcel transport. Following *Mitarai et al.* (2009), we temporally filtered the connectivity time series and calculate the root-mean variance in the interannual and seasonal frequency bands (i.e., Fourier modes with time periods of 6-months or longer). The variability other than interannual- and seasonal- band were termed as intra-seasonal band, or ‘eddy-induced variability’ (*Mitarai et al.*, 2009). By doing this, we separated the STD of connectivity into the interannual and seasonal lower frequency part (**Figure 3.8c**) and intra-seasonal higher frequency variability (**Figure 3.8d**).

We note that the seasonal and interannual variability is 3 times larger than the mean (Figure 8a), and completely dominates the total connectivity variances. The higher frequency, eddy-driven variability is comparable to the mean condition, but much weaker than the lower-frequency seasonal and interannual signals. Previous studies of *Churchill et al. (2005)* showed that eddies and meanders can affect the coastal flow variance from time to time. However, our results show that in terms of the connectivity variations, the eddy-driven variability is not a dominant factor.

While the seasonal and interannual variability are not distinguished based on the spectrum of the STD, we further analyzed the seasonal variability of the connectivity matrix, comparing spring (FMA mean) condition to the summer (MJJ mean) condition. Results are shown in **Figure 3.9**. While both spring and summer condition encompasses the mean circulation pattern in the GOM, there are some detailed differences. There appears to be more connections between WGOM and WK during spring as compared to summer. The BOF releases show more leakage in summer to the WGOM compared to spring, as the self-retention within BOF shrinks in size. This is consistent with the modeling results of *Arexabaleta et al. (2008)* showing the stream flow near the mouth of BOF is larger during stratified season compared to spring. While there are more connections between JB and OFFPB area in spring, the JB release becomes increasingly self-retentive in summer. This is largely caused by the enhanced Jordan Basin gyre which intensified in stratified season (e.g.,

Beardsley et al., 1997; Lynch et al., 1997). In addition, there are also increased particles from JB penetrating into the BOF as season progresses from spring to summer. All these findings further confirm the strong variability in the connectivity matrix as opposed to the mean condition, a result of highly dynamic coastal circulation system in the GOM.

3.4.2 Interannual variability in the source and destination locations at different advection time scales

The interannual variability in connectivity can translate into significant modulations in transport pathways, and changes in source/destination function intensities. BOF is one of the ‘hotspot’ for the initiation for the *A. fundyense* blooms, and it is therefore of specific interest to investigate the destination strengths for that area. For BOF particle releases, the dominant self-retention pattern is controlled by the BOF gyre, which is well documented by *Aretxabaleta et al. (2009)*. However our results show the destination strengths (**Figure 3.10a-f**) are highly variable each year between 2004 and 2009. A sample value of 0.1 indicates that 10% of the particles released from this site are found somewhere near the BOF after the advection of 40 days. In 2004, most of particles released from the BOF remained within the BOF. The flow became leakier in 2005, and as a result, some particles traveled to the coastal zones near the Penobscot Bay. The BOF flow became more retentive in 2007 and 2008, and except in OFFPB region, very few particles were found outside the BOF. In contrast, more particles traveled from BOF to WGOM coastal area in 2006 and to the EGOM

coastal area in 2009, respectively. In the latter case, the strong connection between BOF and EGOM in 2009 corresponds to strong *A. fundyense* bloom and high toxicity occurred that summer near the EGOM coast (*Anderson and McGillicuddy*, personal communication), suggesting changes in coastal connectivity and transport play a major role in reshaping the temporal and spatial distributions of *A. fundyense* bloom.

Other domains of interest are the MASS and coastal WGOM, which tend to be the destination locations of repetitive *A. fundyense* blooms occurrence in each summer. The relative contributions of each source regions to the WGOM can be depicted by the source strength functions shown in (**Figure 3.10g-l**). In 2004 and 2009, coastal WGOM and MASS act as the major sources for these regions themselves. In 2005-2008 however, both WGOM and BOF became more important sources. Such analyses provide useful information to trace possible sources of *A. fundyense* bloom, and gauge relative contributions of different source regions in each year.

One interesting aspect is to investigate whether the interannual variability presented here are highly variable at different advection time scales at monthly to seasonal time frequency. To do this, we compared the BOF destination strengths in 2006 and 2009, using advection times of 30, 40, and 50-days, respectively (**Figure 3.11**). We found that there were more particles reaching the WGOM in 2006, and more reaching the EGOM in 2009. But within each year, the spatial distributions of the destination remain largely the same regardless of the advection

time scales being used. The results suggest that the interannual variability of coastal connectivity is not highly sensitive to the change of advection time scales at monthly to bimonthly time scale.

Another point of interest is the degree of connectivity between EMCC and WMCC. Contrasting destination strength functions of 2006 and 2009 clearly shows that 2006 is more a ‘flow-through’ year, with more particles from BOF advected into the WGOM. In 2009, however, more particles are concentrated in the EGOM coastal area. There are also more particles in the OFFPB area in 2009 compared to 2006, suggesting a strong discontinuity of the MCC with an offshore veering southeast of Penobscot Bay. Such a finding is consistent with a general feature documented by various previous studies (*Pettigrew et al.*, 2005; *Xue et al.*, 2008; *Incze et al.*, 2010).

3.4.3 Caveat on the model skill and particle tracking

In Section 3.3.2, we compared the modeled coastal current speed with observational counterpart. One caveat we note is our model average was for the February-August period of 2004-2009 alone, whereas the drifter derived mean flow was averaged over ~20 years (1988-2007). So some discrepancies such the intensity of Jordan Basin gyre in this comparison can be attributed to this time scale mismatch. In addition, our analysis focused on the variability at seasonal to interannual timescale, and we used the M2 tidal-averaged velocity field for the particle tracking. We do note that spring-neap cycle remains in the M2

tidal average, although the resulting impact on interannual variability of the connectivity can be trivial.

3.5 Summary

The Gulf of Maine (GOM) coastal ocean connectivity in spring and summer seasons of 2004-2009 were studied using surface numerical particle trackings based on realistic regional ocean circulation hindcast solutions. Seven initial particle release domains were selected, including the Massachusetts Bay (MA), the WGOM coastal area, the EGOM coastal area, the Bay of Fundy (BOF), the Wilkinson Basin (WK), the Jordan Basin (JB), and a coastal area Off the Penobscot Bay (OFFPB). At each location, clusters of surface particles were released every five days from 01 February to 01 August in each year and tracked using the LTRANS model. The resulting particle trajectory variability on the seasonal and interannual time scales were quantified by Lagrangian probability density function (LPDF) calculations. The coastal connectivity was further quantified using the connectivity matrix, source and destination functions.

We chose 40-day as the advection time to study the coastal connectivity. Mean LPDFs highlight the mean transport patterns in the GOM, including the MCC, BOF gyre, and Jordan Basin Gyre. LPDFs have significant variability on the seasonal and inter-annual time scales. Such seasonal and interannual variability are much stronger than both the mean and the high frequency eddy-driven variations.

Overall, the mean connectivity matrix shows that the BOF and JB are two strongest source regions in the GOM, whereas WK and BOF are two destination regions having the largest “attractiveness”. Offshore sites have higher destination strength relative to the coastal sites.

On the interannual time scale, the BOF particles had the strongest destination strength at the EGOM coastal area in spring and summer 2009. This coincides with the observed strong *A. fundyense* bloom and toxicity concentrations in that area in June/July 2009, highlighting the important linkage between coastal transport and bloom distribution. However, the destination strengths for the BOF didn’t explain the shellfish toxicity extent along the coastal WGOM in summer 2009. In addition, none of destination strengths for OFFPB, JB and coastal GOM show strong destination strengths in the WGOM in 2009. Previous study showed that delivery of offshore materials such as *A. fundyense* cells can be important for the blooms near the coast (McGillicuddy *et al.*, 2003). A further study taking more offshore locations in the GOM (e.g., near 150-m isobath) is needed in this regard. In addition, in the work presented here the particle densities are the same everywhere for all release locations. To better interpret patterns for HAB dynamics, particle release with increased particle density (e.g., Incze *et al.*, 2010) near the source region (e.g., based cyst abundance) along with coupled biophysical modeling work are needed in the future.

The LPDFs and connectivity matrix, source and destination strengths provide a

quantitative and statistical means to describe the coastal circulation and transport pathways and their seasonal and interannual variations in the Lagrangian framework. Our study focused on the details of the coastal connectivity covering extensive onshore and offshore locations, aiming to better understand hydrodynamic transport of *A. fundyense* blooms during spring and summer months. Our study compliments earlier studies by *Xue et al.* (2009) and *Incze et al.* (2010), which focused on the transport of the lobster larvae in the fall and winter months.

Our connectivity matrix calculation was based on the 40-day advection time, which was shown to be a sufficient time scale to evaluate the connectivity on monthly to seasonal time scale (e.g., **Figure 3.4** and **Figure 3.5**). Experiments (**Figure 3.10**) suggest that the resulting interannual variability of coastal connectivity is not sensitive to the change of advection time scales from monthly to bimonthly frequency. A caveat we note is although our circulation hindcast model well reproduces the overall seasonal and interannual variability of coastal circulation (**Figure 3.2**), the model overestimates the current amplitude at some locations (e.g., at buoy B) and underestimate currents in other locations (e.g. at buoy A). Such hydrodynamic errors can populate into the particle tracking, which may further add uncertainties in coastal connectivity matrix. More accurate representations of coastal circulation and transport pathways require advanced data assimilative modeling approach, which is an ongoing research that will be reported in a future correspondence.

In addition, although numerical model solution provides useful toolset for quantifying coastal connectivity, they are indeed a smoothed rendition of reality. Due to limited spatial resolution of the circulation model (2-3km), we focused on the impact of coastal circulation on the regional *A. fundyense* bloom distribution, and the coastal embayment and estuarine (e.g., Penobscot Bay, Casco Bay) are not considered in this computation. A higher resolution circulation model focusing on these coastal regions is needed to accurately resolve the river plume dynamics and circulation variations within these areas. Meanwhile, improved observational network design and integrated analysis of in situ observations can provide another useful asset to the understanding of coastal hydrography and circulation dynamics at both seasonal and interannual timescales (e.g., *Li et al.*, submitted to this issue).

Acknowledgements

We thank the Northeastern Regional Association of Coastal Ocean Observing Systems (NERACOOS) for providing the mooring data used in this study; We are grateful to Drs. S. Mitarai, D. Siegel and P. Niiler for their helpful discussions on the concepts of LPDFs and eddy diffusivity. Research supports provided by the National Oceanic Atmospheric Administration (grant NA06NOS4780245 for the Gulf of Maine Toxicity (GOMTOX) program) are greatly appreciated.

References

Anderson D.M. , B.A. Keafer, D.J. McGillicuddy, M.J. Mickelson, K.E. Keay, P.S. Libby, J.P. Manning, C.A. Mayo, D.K. Wittaker, J.M. Hickey, R. He, D.R. Lynch and K.W. Smith (2005), Initial observation of the 2005 *Alexandrium fundyense* bloom in the southern New England: general patterns and mechanisms, *Deep Sea Research II* , 52 (2005), 2856–2876.

Aretxabaleta, A.L., McGillicuddy, D.J., Smith, K.W., and D.R. Lynch (2008), Model Simulations of the Bay of Fundy Gyre: 1. Climatological Results. *Journal of Geophysical Research*, 113, C10027, doi:10.1029/2007JC004480.

Aretxabaleta, A.L., McGillicuddy, D.J., Smith, K.W., Manning J.P. and D.R. Lynch (2009), Model simulations of the Bay of Fundy Gyre: 2. Hindcasts for 2005-2007 reveal interannual variability in retentiveness. *Journal of Geophysical Research*, 114, C09005, doi: 10.1029/2008JC004948.

Beardsley, R. C., B. Butman, W. R. Geyer, and P. Smith (1997). Physical oceanography of the Gulf of Maine: An update, p.39–52. In G. T. WALLACE and E. F. BRAASCH [eds.], *Proceedings of the Gulf of Maine ecosystem dynamics scientific symposium and workshop*. Regional Association for Research in the Gulf of Maine.

Bigelow, H.B. (1927), Physical Oceanography of the Gulf of Maine, *Fisheries Bulletin*, 40, 511-1027.

Churchill, J. H., N. R. Pettigrew and R. P. Signell (2005), Structure and variability of the Western Maine Coastal Current, *Deep Sea Research Part II: Topical Studies in Oceanography*, Volume 52, Issues 19-21, September-October 2005, Pages 2392-2410 .

Flather, R. A., 1976: A tidal model of the northwest European continental shelf. *Mem. Soc. Roy. Sci. Liege*, Ser. 6, 10, 141-164.

Haidvogel, D.B., H. Arango, W.P. Budgell, B.D. Cornuelle, E. Curchitser, E. Di Lorenzo, K. Fennel, W.R. Geyer, A.J. Hermann, L. Lanerolle, J. Levin, J.C. McWilliams, A.J. Miller, A.M. Moore, T.M. Powell, A.F. Shchepetkin, C.R. Sherwood, R.P. Signell, J.C. Warner, J. Wilkin (2008): Ocean forecasting in terrain-following coordinates: Formulation and skill assessment of the Regional Ocean Modeling System, *Journal of Computational Physics*, Volume: 227, Issue: 7, pp 3595-3624.

Hannah, C.G, C. E. Naimie, J.W. Loder and F. E. Werner (1998), upper-ocean transport mechanisms from the Gulf of Maine to Georges Bank, with implications for calanus supply, *Continental Shelf Research*, vol.17, No. 15, pp 1887-1911.

He, R., Weisberg, R.H. (2003), West Florida shelf circulation and temperature budget for the 1998 fall transition. *Continental Shelf Research*, 23, 777-800.

He, R., D. J. McGillicuddy, D. R. Lynch, K.W. Smith, C.A. Stock, and J. P. Manning (2005), Data assimilative hindcast of the Gulf of Maine coastal circulation. *Journal of Geophysical Research*, 110, C10011, doi: 10.1029/2004JC002807.

He, R., and D. McGillicuddy (2008), Gulf of Maine Harmful Algal Bloom in Summer 2005: Part 1. In-situ observations of coastal hydrography and circulation, *Journal of Geophysical Research*, 113, C07039, doi:10.1029/2007JC004691.

He, R., D. McGillicuddy., D. Anderson, B. Keafer (2008), Gulf of Maine circulation and harmful algal bloom in summer 2005: Part 2: bio-physical numerical modeling, *Journal of Geophysical Research-Oceans*, 113, C07040, doi:10.1029/2007JC004602.

Incze, L., Xue, H., Wolff, N., Xu, D., Wilson, C., Steneck, R., Wahle, R., Lawton, P., Pettigrew, N. and Chen, Y. (2010), Connectivity of lobster (*Homarus americanus*) populations in the coastal Gulf of Maine: part II. Coupled biophysical dynamics. *Fisheries*

Oceanography, 19: 1–20. doi: 10.1111/j.1365-2419.2009.00522.x.

Li, Y., He, R., D. McGillicuddy, D. Anderson, B. Keafer (2009), Investigation of 2006 *Alexandrium fundyense* bloom in the Gulf of Maine: In situ observations and Numerical modeling. *Continental Shelf Research*, 10.1016/j.csr.2009.07.012.

Li, Y., He, R., and D. J. McGillicuddy (2012): Seasonal and Interannual Variability in Gulf of Maine Hydrodynamics: 2002-2011, submitted to *Deep Sea Research II*, this issue.

Luettich, R. A., J. C. Muccino, and M. G. G. Foreman (2002), Considerations in the calculation of vertical velocity in three-dimensional circulation models, *Journal of Atmospheric and Oceanic Technology*. 19, 2063– 2076.

Lynch, D.R., J. T. Ipa., C. E. Naimie and F. E. Werner (1996), Comprehensive coastal circulation model with application to the Gulf of Maine. *Continental Shelf Research*, Vol. 16-7, 875-906

Lynch, D.R., M.J. Holboke, C.E. Naimie (1997), The Maine coastal current: Spring climatological circulation. *Continental Shelf Research*, 17 (6): 605-634 MAY, 1997.

Manning, J.P. and J.H. Churchill (2006), Estimates of dispersion from clustered-drifter deployments on the southern flank of Georges Bank, *Deep Sea Research II*, 53, 2501-2519.

Manning, J.P., D.J. McGillicuddy, N.R. Pettigrew, J.H. Churchill and L.S. Incze (2009), Drifter observations of the Gulf of Maine coastal current, doi:10.1016/j.csr.2008.12.008.

Marchesiello, P., J.C. McWilliams, and A.F. Shchepetkin (2001), Open boundary conditions for long-term integration of regional oceanic models. *Ocean Modeling*, 3, 1-20.

McGillicuddy, D.J., Signell, R.P., Stock, C.A., Keafer, B.A., Keller, M.D., Hetland, R.D. and D.M. Anderson, 2003. A mechanism for offshore initiation of harmful algal blooms in the coastal Gulf of Maine. *Journal of Plankton Research*, 25(9), 1131-1138.

McGillicuddy, D.J., Anderson, D.M., Solow, A.R., and D.W. Townsend, 2005. Interannual variability of *Alexandrium fundyense* abundance and shellfish toxicity in the Gulf of Maine. *Deep-Sea Research II*, **52**, 2843-2855.

Mellor L.G. and T. Yamada (1982), Development of a turbulence closure model for geophysical fluid problems, *Reviews of Geophysics and space physics*, 20-4, 851-875.

Mitarai, S., D. A. Siegel, J. R. Watson, C. Dong, and J. C. McWilliams (2009), Quantifying connectivity in the coastal ocean with application to the Southern California Bight, *J. Geophys. Res.*, 114, C10026, doi: 10.1029/2008JC005166.

Moody, J.A., et al. (1984), Atlas of tidal elevation and current observations on the Northeast American continental shelf and slope. *US Geological Survey Bulletin* ,1611 122pp.

North, E. W., R. R. Hood, S.-Y. Chao, and L. P. Sanford (2006): Using a random displacement model to simulate turbulent particle motion in a baroclinic frontal zone: a new implementation scheme and model performance tests. *Journal of Marine Systems* 60: 365-380.

North, E. W., Z. Schlag, R. R. Hood, L. Zhong, M. Li, and T. Gross (2006), Modeling dispersal of *Crassostrea ariakensis* oyster larvae in Chesapeake Bay. *Final Report to Maryland Department of Natural Resources*, July 31, 2006. 55 p.

North, E. W., Z. Schlag, R. R. Hood, M. Li, L. Zhong, T. Gross, and V. S. Kennedy (2008), Vertical swimming behavior influences the dispersal of simulated oyster larvae in a coupled particle-tracking and hydrodynamic model of Chesapeake Bay. *Marine Ecology Progress Series* 359: 99-115

Schlag, Z., E. W. North, and K. Smith (2008), *Larval TRANSport Lagrangian model (LTRANS) User's Guide*. University of Maryland Center for Environmental Science, Horn Point Laboratory. Cambridge, MD. 146 pp.

Pettigrew, N. R., J. H. Churchill, C. D. Janzen, L. J. Mangum, R. P. Signell, A. C. Thomas, D. W. Townsend, J. P. Wallinga, and H. Xue (2005), The kinematic and hydrographic structure of the Gulf of Maine coastal current. *Deep Sea Research, Part II*, 52, 19-21, 2369-2391

Pettigrew, N. R., R.J. Fleming, and C.P. Fikes (2011): The history of the first decade of the observing system in the Gulf of Maine, and plans for the second decade, *MTS Journal*, September 2011, 1-10.

Shchepetkin, A.F. and J.C. McWilliams (2005), The Regional Ocean Modeling System (ROMS): A split-explicit, free-surface, topography-following coordinates ocean model, *Ocean Modelling*, Volume 9, Issue 4, pp 347-404.

Xue, H., F. Chai, and N. R. Pettigrew (2000), A model study of seasonal circulation in the Gulf of Maine. *Journal of Physical Oceanography*, 30, 1111-1135.

Xue, H, L. Incze, D. Xu, N. Wolff and N. Pettigrew (2008), Connectivity of lobster populations in the coastal Gulf of Maine, Part I: Circulation and larval transport potential, *Ecological Modeling*, 210, 193-211.

Chapter IV: Variational Data Assimilative Modeling Investigation of the Gulf of Maine Coastal Circulation in Spring and Summer

2010

Ruoying He¹, Yizhen Li¹, Ke Chen¹

¹Department of Marine, Earth and Atmospheric Sciences,
North Carolina State University, Raleigh, NC 27695

To be submitted to the *Journal of Geophysical Research—Oceans or DSR II*

Abstract

A data assimilative ocean circulation model is used to hindcast the Gulf of Maine circulation in spring and summer 2010. Using the recently developed Incremental Strong constraint 4D Variational (I4D-Var) data assimilation algorithm, the model assimilates satellite observed sea surface temperature (SST), in-situ temperature and salinity profiles measured by expendable bathythermograph, Argo floats, and shipboard CTD casts. The model performance is significantly improved after data assimilation. The data-assimilative hindcast reasonably well reproduced the temporal and spatial evolutions of ocean state variables including coastal flows and temperature and salinity properties. It is found that the low sea level center southwest of Scotian Shelf is important in shaping the gulf-wide circulation structure during the study period. The estimated time scale for the Scotian Shelf Waters to travel to the Jordan Basin is about 60 days. The study highlights the importance of resolving upstream and offshore forcing conditions in refining the coastal circulation in the GOM.

4.1 Introduction

The Gulf of Maine (GOM) encompasses a coastal area of the northeastern North America between Nova Scotia in the northeast and Cape Cod in the southwest. The region is dominated by a cyclonic circulation (e.g., *Bigelow*, 1928, *Lynch et al.*, 1996) that is influenced by local forcing such as wind, heat flux, river discharge (*Keafer et al.*, 2005), tidal rectification (*Lynch et al.*, 1996; 1997) and upstream and deep-ocean forcing. It is known that cold and fresh Scotian Shelf Waters (SSW) enter the gulf through Cape Sable with an annual mean transport rate of 0.14 Sv (e.g. *Chapman and Beardsley*, 1989; *Smith*, 1983), and that warm slope waters can enter the GOM through the Northeast Channel (e.g., *Townsend et al.*, 2010; *Pettigrew et al.*, 2011).

Numerical modeling has long been a major approach to advance our understanding of GOM circulation dynamics and variability. Earlier modeling studies have focused on various aspects of GOM circulation, such as climatological mean states (*Lynch et al.*, 1997; *Xue et al.*, 2000), or synoptic to seasonal scale hindcast (*Hetland et al.*, 2005; *He and McGillicuddy et al.*, 2008; and *Li et al.*, 2009). In these studies, ocean models were solved as initial- and boundary- value problems (so called “forward” model), and observations were used only for model validation purpose.

Coastal sea level and velocity observations were used in a number of studies (*Signell et al.* 1994; *Lynch et al.*, 1998; *He et al.*, 2005; *Arexabaleta et al.*, 2009) to refine model open

boundary conditions, which in turn help to improve prediction skills of forward models. The underlying assumption is the open boundary condition is least available information in terms of driving a regional ocean model, and that both surface forcing and model initial conditions are error free.

Recent advancements in 4-dimensional variational data assimilation (4D-Var) techniques (*Powell et al.*, 2008; *Broquet et al.*, 2009ab, *Moore et al.*, 2011a) provide a nice step forward, in that it allows observations to be used to constrain models by refining boundary condition, initial condition, and surface forcing, and therefore holds a great promise in realistically simulating coastal ocean state variables in a dynamically consistent and numerical accurate manner.

In summer 2010, anomalous hydrographic condition was noted (*McGillicuddy et al.*, 2011). It appears that there were more intrusions of both Scotian Shelf Water (SSW) and Slope Sea waters. The resulting changes of gulf-wide hydrography were accompanied by a weakened coastal flow in the western GOM, especially in the month of June (*Li et al.*, submitted, 2012). Because of the challenge of direct modeling these processes using forward regional ocean model, we intend to utilize observations taken from regional ocean observing network, gulf-wide ship surveys, and operational satellite data, along with the recently developed 4DVar data assimilation technique to perform a data assimilative (DA) model hindcast of the coastal circulation and hydrography in summer 2010. The skill of DA

hindcast model in reproducing anomalous water mass and coastal circulation is evaluated by comparing independent observations that are not assimilated. Important processes that lead to anomalous water mass and circulation conditions will be diagnosed.

The remainder of the paper is organized as follows. Section 4.2 introduces our regional forward model and DA system and observations being used. Section 4.3 presents DA hindcast results and its comparisons with independent observations. In-depth discussions of coastal circulation dynamics and water mass evolutions in spring and summer 2010 are given in Section 4.4, followed by summary and future work in Section 4.5.

4.2 Data and Methods

4.2.1 Model settings

The GOM circulation hindcast was performed using a regional setup of the Regional Ocean Modeling System (ROMS, *Haidvogel et al., 2008; Shchepetkin and McWilliams, 2005*). ROMS employs split-explicit separation of fast barotropic and slow baroclinic modes, and is formulated in vertically stretched terrain-following coordinates.

For the hydrodynamic open boundary conditions (OBCs), a multi-nested configuration was implemented to downscale a global data assimilative Hybrid Coordinate Ocean Model (HYCOM, <http://hycom.rsmas.miami.edu/dataserver>) solutions to a shelf-wide ROMS model and subsequently to the GOM ROMS model (*He et al., 2008*) via a one-way nesting approach. The shelf-scale ROMS has a spatial resolution of 10-km (5-km) in the alongshore

(cross-shelf) direction, and 36 terrain-following vertical levels that have higher resolutions near the surface and bottom to better resolve boundary layers. The method of *Marchesiello et al. (2001)* was applied to prescribe boundary values of tracers and baroclinic velocity. For the free surface and depth-averaged velocity boundary conditions, the method of *Flather (1976)* was used with the external values provided by HYCOM. The *Mellor-Yamada (1982)* closure scheme and the quadratic drag formulation were applied to compute the vertical turbulent mixing and the bottom friction specification.

The GOM ROMS (**Figure 4.1**) has a spatial resolution of 6-km (4-km) in the alongshore (cross-shelf) direction, and 36 terrain-following vertical levels. Because the current implementations of ROMS 4D-Var tangent-linear and adjoint models do not allow for radiation boundary conditions, the clamped boundary conditions were used to tie the 3-dimensional model temperature, salinity and velocity with values at open boundaries. We employed a 6-grid-point sponge layer (with 5-time higher viscosity) near all three open boundaries to alleviate any wave reflections produced by the clamped conditions. Within the sponge layers, the climatological tracer nudging was applied to relax temperature, salinity to the shelf-scale ROMS solutions over a time scale of 4 days. As the shelf-scale ROMS, the method of *Flather (1976)* was used for the free surface and depth-averaged velocity boundary conditions. We also superimposed along open boundaries M_2 tidal sea level and depth-averaged velocity using harmonics derived from an ADCIRC simulation of the

western Atlantic (*Luettich et al.*, 1992).

Surface atmospheric forcing, including cloud fraction, precipitation, surface pressure and humidity, air temperature, surface wind, and shortwave radiation were obtained from the National Center for Environmental Prediction (NCEP), North America Regional Reanalysis (NARR). Spatial and temporal resolutions of these forcing fields are 32-km and 3-hour, respectively. They were applied in the standard bulk flux formulation (*Fairall et al.*, 1996; 2003) to derive wind stress and net surface heat flux needed by the simulations. To further constrain the surface net heat flux, we also followed the same approach used in *He and Weisberg* (2003) to relax the modeled SST field to NOAA Coast Watch daily, 1/10 degree cloud-free SST product with a timescale of 3 days. Fresh water runoff from five major rivers was also considered. These include the U.S. portion of the St Johns River, the Penobscot River, the Kennebec River, the Androscoggin River, and the Merrimack River. For each of them, United State Geological Survey (USGS) real-time river runoff measurement was used to specify freshwater volume transport.

The hindcast experiment focused on a three and a half month period from April, 01 to July 18, 2010. The non-data assimilative forward model simulation was in fact ran for six and half years from February 1st, 2004 to August 1st, 2010 to provide the background state for the DA experiment. GOM forward solutions were compared against extensive observations including coastal sea levels, coastal mooring documented T/S profiles and circulation. The

low frequency circulation variability were reasonably well captured as demonstrated by earlier studies (e.g., *He et al.*, 2008; *Li et al.*, 2009; *Li et al.*, 2012, submitted). However, the anomalous hydrographic conditions in 2010 (*McGillicuddy et al.*, 2011) were not well simulated by the HYCOM model, and nor by subsequent shelf-scale ROMS and GOM ROMS simulations. Our goal is therefore to apply extensive regional observations, and 4D-Var data assimilation technique to produce optimal GOM ROMS simulation in spring to summer 2010, from which the underlying dynamics driving anomalous water mass and circulation conditions can be gleaned.

4.2.2 4D Variational Data Assimilation System

The ROMS-4-Dimensional Variational (4D-Var) Data Assimilation system includes the nonlinear forward model (NLROMS), the tangent linear model (TLROMS) and its adjoint model (ADROMS). The system provides powerful toolsets for conducting various types of model prediction and analyses of complex ocean hydrography (*Moore et al.*, 2004; *Di Lorenzo et al.*, 2007; *Powell et al.*, 2008; *Broquet et al.*, 2009ab; *Moore et al.*, 2011b). Among which, the ROMS I4D-Var method is based on the incremental formulation described by *Weaver et al.* (2003). A brief overview of this method and important concepts are given below to aid discussions in later sections. More details on its implementation in ROMS can be found in *Powell et al.* (2008) and *Moore et al.* (2011a).

The ROMS prognostic variables are comprised of: the sea surface displacement η , the

potential temperature T , salinity S , and the horizontal velocity (u, v) . When the primitive equations are discretized and arranged on the ROMS grid, the individual grid point values at time t_i define the components of a state vector $\mathbf{x}(t_i) = (T, S, \eta, u, v)^T$, where superscript T denotes vector transpose. The state-vector is propagated forward in time by the discretized nonlinear model (NLM) subject to surface boundary conditions $\mathbf{f}(\mathbf{t}_i)$ for momentum, heat and freshwater fluxes, the lateral open boundary conditions $\mathbf{b}(\mathbf{t}_i)$. The state vector evolves according to

$$\mathbf{x}(t_i) = M(t_i, t_{i-1})(\mathbf{x}(t_{i-1}), \mathbf{f}(t_i), \mathbf{b}(t_i)) \dots \dots \dots (1)$$

where $M(t_i, t_{i-1})$ represents NLROMS acting on $\mathbf{x}(t_{i-1})$, and subject to forcing $\mathbf{f}(t_i)$, boundary condition $\mathbf{b}(t_i)$ during the time interval $[t_i, t_{i-1}]$.

The goal of 4DVAR is to identify the best estimate circulation, also referred as the analysis or posterior, namely $\mathbf{x}^a(t)$, which minimizes in a least-squares sense, the difference between the model and the observations. The solution $\mathbf{x}(t_i)$ of NLROMS will depend upon the choice of initial conditions $\mathbf{x}(t_0)$, boundary conditions $\mathbf{b}(t)$ and surface forcing $\mathbf{f}(t)$, all of which are subject to errors and uncertainties. As such, $\mathbf{x}(t_0)$, $\mathbf{b}(t)$ and $\mathbf{f}(t)$ are referred as control variables, and the problem in 4DVAR is reduced to identifying the appropriate combination of control variables that yield the best estimate $\mathbf{x}^a(t)$.

According to Courtier (1997), the control variable increment is introduced as

$$\delta \mathbf{z} = (\delta \mathbf{x}(t_0)^T, \delta \mathbf{f}^T(t_1), \dots, \delta \mathbf{f}^T(t_k), \dots, \mathbf{b}^T(t_1), \dots, \delta \mathbf{b}^T(t_k), \dots, \boldsymbol{\eta}^T(t_1), \dots, \boldsymbol{\eta}^T(t_k) \dots)^T \quad (2)$$

which describes all the control variable increments. In the incremental 4DVAR approach, we seek to minimize the quadratic cost function $J=J_b+J_o$, given by

$$J_b = \frac{1}{2} \delta z^T D^{-1} \delta z \quad (3)$$

$$J_o = \frac{1}{2} (G \delta z - d)^T R^{-1} (G \delta z - d) \quad (4)$$

where G is tangent linear model interpolated at observational space. $d = y^o - H(x^b(t))$ are the innovation vectors of length N_{obs} , where y^o are observations and H is an operator that samples NLM trajectory at observational locations. D and R are model background and observation error covariance matrix that will be discussed later. We seek a solution for increment of control variable δz^a shown in eq. (2), for which the total cost function J reaches a minimum value and the gradient of J vanishes. δz^a is identified iteratively by solving a sequence of linear least squares minimizations (inner-loops) repeated with periodic updates of G (outer-loops). In ROMS 4D-Var a conjugate-gradient (CG) algorithm based on *Fisher* (1998) is used to achieve the minimization. The minimization procedure is terminated when $\|\nabla J\| \leq \varepsilon$. This typically requires a large number of iterations that are computationally prohibitive, so instead the numbers of outer- and inner-loops are fixed to yield a good estimate of the minimum J (e.g., *Broquet et al.*, 2009a). During each inner-loop, TLROMS is used to propagate the increments forward in time to evaluate (4), and ADROMS yields $\nabla J(\delta z)$, which is used by the CG algorithm to identify the minimum of J . The best estimate δz^a will be found at the end of iteration. In this study, the ROMS 4D-Var was allowed to

adjust the initial conditions, boundary conditions and surface forcing, so the optimal increment δz^a is applied to initial, boundary and surface conditions respectively after the minimization process.

Data assimilation is applied within each of many sequential time windows that together span the entire analysis period (*Broquet et al., 2009ab*), thus in each assimilation window the tangent linear approximation should be valid given the relative short assimilation period. At the beginning of each assimilation window, the initial condition derived from last snapshot of previous DA window (or directly given for the first window) is used to compute a forecast with NLROMS. This forecast provides the background trajectory or the optimal model trajectory when observational data is not available in the current assimilation window. Then ROMS 4D-Var inner loop starts with CG algorithm to yield an estimate of optimal increment δz^a which will be used to adjust control variables. The adjusted control variables are further used to compute the model trajectory after all designated outer and inner loops within one assimilation window.

4.2.3 Assimilated data

Various in situ and satellite-based observations were assimilated in this study, including:

NOAA CoastWatch blended SST: The SST product (coastwatch.noaa.gov) is a blended product of SST observations from GEOS, AVHRR and MODIS satellites. This product is available daily (with some missing snapshots due to failure of sensors) from July 2002 to

present with a horizontal resolution of 10-km. An observational error of 0.4 °C was chosen in this study.

In-situ temperature and salinity time series: These hourly profile data were measured by moorings of the Gulf of Maine Ocean Observing System (now part of the Northeast Coastal Ocean Observation System NERACOOS, <http://www.neracoos.org>, e.g., *Pettigrew et al.*, 2011). T/S from buoy F, I, M and I (Figure 2) was assimilated at a 4-hour interval. Additional hydrographic data quality-controlled and archived by the UK Met Office Hadley Center (http://hadobs.metoffice.com/en3/data/EN3_v2a/, *Ingleby and Huddleston*, 2007) were assimilated. These observations contain *in situ* data from a variety of instruments and platforms including expendable bathythermographs (XBT), Argo floats, opportunistic surface themistor temperature measurements, and T/S profiles from Global Temperature Salinity Profile Program (GTSPP). In this study, we used 0.1°C and 0.03 as the measurement errors for in-situ temperature and salinity, respectively.

Shipboard CTD data: CTD casts were collected during three GOMTOX ship surveys in 2010, including *Oceanus* 465 (01-10 May), *Endeavor* 460 (27 May-03 June), and *Oceanus* 467 (30 June-08 July). CTD Vertical profiles ranged from 2-m to 200-m (or near bottom for coastal regions), and we averaged all CTD data into 5-m bins. As for other in-situ T-, S-profile data, we used 0.1°C and 0.03 as the observational errors for temperature and salinity, respectively.

All observations were combined and averaged respectively to form “super observations”, so that within each model grid cell and at each model time step each type of observation only has one realization. This procedure significantly reduces data redundancy, and the standard deviation of the observations that contribute to each “super observation” was used as a measure of the error of representativeness.

The spatial distributions of super observations of SST, UK MET office T/S profiles, NERACOOS buoy T/S, and ship CTD observations are shown in **Figure 4.2**. SST on the first day of DA cycle (April 01, 2010) are shown, along with positions of all available *in situ* temperature and salinity profiles over the ~110-day study period. The temporal distribution of super observations (**Figure 4.3**) shows that the majority of observations feeding the DA system are satellite observed SST that had a total of 283050 realizations. *In situ* NERACOOS buoy T/S profiles contribute a total of 11754 T/S observations. Shipboard CTD casts have a total of 15462 observations. While the T/S profile data are less in number, they provide vital subsurface information to constrain model hydrodynamics.

4.2.4 Data Assimilation Setup

4.2.4.1 Covariance modeling

The parameterization of model background error covariance matrix **D** determines the way that observational information is propagated to non-observational variables. Therefore proper definition of **D** has critical influence on the data assimilation performance. **D** contains

initial condition background (or prior) error covariance matrix \mathbf{D}_x , open boundary condition background error covariance matrix \mathbf{D}_b , surface forcing background error covariance matrix \mathbf{D}_f , and prior model error covariance matrix \mathbf{Q} (serves for weak constraint 4DVAR, not used in this study). Each error covariance matrix can be expressed as $\mathbf{D} = \Sigma \mathbf{C} \Sigma$, where Σ is the diagonal matrix of error standard deviations, and \mathbf{C} is a univariate correlation matrix. The main source of background error is the model bias and spatial mismatch from observations. The standard deviation Σ is computed on a monthly basis based on the GOM forward simulation over 2004-2010. The univariate correlation matrix is further factorized as $\mathbf{C} = \Lambda \mathbf{L}_v^{1/2} \mathbf{L}_h^{1/2} \mathbf{W}^{-1} \mathbf{L}_v^{T/2} \mathbf{L}_h^{T/2} \Lambda$, where Λ is a matrix of normalization coefficients, L_v (L_h) is the vertical (horizontal) correlation function, \mathbf{W} is the diagonal matrix of grid volumes (*Moore et al.*, 2011a). The correlation matrices, L_v and L_h , with their associated normalization factors Λ , were computed as solutions of diffusion equations following *Derber and Rosati* (1989) and *Weaver and Courtier* (2001). The length scales chosen for L_v and L_h represent the decorrelation scales from a typical increment, and are currently assumed to be homogenous and isotropic. In the current setup, a spatial decorrelation scale of 50-km is chosen for L_h , and 30-m for L_v . Both are reasonable values for the study of coastal ocean.

4.2.4.2 Assimilation window

We ran ROMS I4D-VAR from Apr1st, 2010 to July 18th, 2010, covering the the period when some anomalous hydrographic conditions were observed. An assimilation window of

3-day was chosen, which is short enough to guarantee tangent linear approximation (*Wilkin et al., 2008; Powell et al., 2008; Broquet et al., 2009a*) is about valid. By doing so, 3 days of observations can be utilized during each window and the ending snapshot of the 3rd day serves as background initial condition for the next assimilation window. A total of 36 DA windows were performed individually and the posterior information is carried over from one window to the next.

Choosing the numbers of inner- and outer-loops is a trade-off among computational cost, the level of convergence of the CG algorithm, and the need to update the cost function shape. In our case, we chose 1 outer loop and 20 inner loops for each DA window. We found that 20 loops are sufficient to yield a reasonable estimate of the minimum of J , in the sense that the rate of change in J indicated by the differences between its final value and the optimal solution is small (less than 5%) compared with the difference between the initial and final values of J .

4.3 Results

4.3.1 Cost function reduction

The performance of the GOM 4DVAR system can be initially evaluated by the reduction of the cost function (**Figure 4.4**). During the first assimilation window (April 01-04, 2010), the total cost function is effectively reduced in the first 7 inner loops, with reductions ranging from more than 30% to about 5%. After 12 inner loops, the reduction of cost function stays

below 5% and approaches zero in the 16th loop. This suggests 20 inner loops are good enough to yield a good minimization of cost function. The theoretical minimum value J_{\min} of total cost function J would have a mean of $N_{\text{obs}}/2$ (Weaver *et al.*, 2003), in which N_{obs} is the number of assimilated observations in each window. In our case, after 20 loops, the final value of cost function is approaching the theoretical value, which is common in 4DVAR data assimilation. The total cost function (**Figure 4.4**) in the last assimilation window (July 15-18, 2010) is smaller than that in the first window. The final value of J also approaches the J_{\min} , indicating a good fitting to the observations. Overall, ~90% of the total cost function reductions are achieved in window 1 and window 36, respectively. The fact that the final non-linear cost function approximately coincides with J value indicates the choice of using 3-day as the assimilation window for tangent linear approximation is reasonable.

The behavior of cost function depends closely on the parameterizations of **D** and **R**. In our DA experiments, background cost function J_o is much larger than observational cost function J_b ($J_o \sim 10 J_b$, **Figure 4.5**). As a result, while J is approaching its minimum, J_b continues to increase, suggesting the model is deviating from its background state without changing the overall fit of the DA model trajectories to the observations (e.g., Broquet *et al.*, 2009a). Sensitivity experiments show that the termination of DA at 20th loop would prevent the excessive divergence of the model from basic state while still ensuring a good fit to observations. The overall performance of cost functions in all windows shows our choice of

background error and observational errors are appropriate.

4.3.2 Effectiveness of the 4D-Var Algorithm

4.3.2.1 Surface Performance

The improvement of circulation simulated by the GOM 4D-Var system can be evaluated

using the Root Mean Square Error $\sqrt{\frac{1}{N} \sum_{i=1}^N (x_i - y_i)^2}$ (RMSE, thereafter), where x_i and

y_i are the simulated and observed data at a given time and location. First, the spatial RMSE

of SST was computed at each satellite observational locations over the entire DA period

(April 01- July 18) (**Figure 4.5a**). Large RMSEs are found in the forward model in regions

near Nantucket Islands, the eastern GOM and the BOF where there is strong tidal mixing.

The RMSE is significantly reduced after data assimilation (**Figure 4.5b**). The maximum

RMSE value of the posterior solution is less than 3°C (as opposed to a maximum of 6°C in

the forward simulation). The performance of DA system was also evaluated in time series of

spatial RMSE, based on model realizations at all assimilated observation locations. As shown

in **Figure 4.5c**, the RMSE between the forward model and observations ranges from 1.5°C to

more than 3°C. By assimilating surface SST data, RMSE was effectively reduced throughout

the region. The DA prior SST RMSE stays less than 1°C.

In addition to RMSE, we also computed the model-observation error bias $\frac{1}{N} \sum_{i=1}^N (x_i - y_i)$,

where N is the number of observations, and x_i and y_i are simulated and observed state

variables at each observational point, respectively. The error bias reflects the average discrepancy between model and observation. It is one constituent of RMSE (*Taylor, 2001*), in that $(\text{RMSE})^2 = (\text{Error Bias})^2 + (\text{Error STD})^2$. We used the error STD as defined by $\text{STD} = \left(\frac{1}{N} \sum_{i=1}^N (x_i - \bar{x} - y_i - \bar{y})^2 \right)^{\frac{1}{2}}$, where $\bar{x} = \frac{1}{N} \sum_{i=1}^N (x_i)$ and $\bar{y} = \frac{1}{N} \sum_{i=1}^N (y_i)$. Different from RMSE, the error bias provides more specific information on whether the model overestimates or underestimates observations. This skill evolution shows that the forward simulation has ~ 1.5 °C bias, overestimating SST throughout the observational period. Such a bias is dramatically reduced to close to zero in the DA posterior simulation, which provides much better realizations of surface temperature.

4.3.2.2 Subsurface T/S statistics

The efficiency of 4DVAR data assimilation was further validated against subsurface hydrographic observations. Same statistics of RMSE and BIAS were computed based on the subsurface T/S misfits between model and observations. Similar as the method of computing RMSE, the vertical profile of temporal bias can be computed at each vertical layer over the entire observational period (**Figure 4.6a**). Near the sea surface, the forward solution has a temperature bias of 2°C, suggesting the forward model is overestimating temperature in the upper water column. In contrast, temperature bias decreases at depth and becomes negative around ~ 50 -m. By 90-m, the temperature bias exceeds -2°C. The vertical distribution of

temperature bias suggests the forward model overall overestimates (underestimate) observed temperature in upper (lower) water column. Data assimilation significantly reduces such bias. The temperature bias in the DA prior simulation is $\sim 1^{\circ}\text{C}$, which is further reduced to $\sim 0.3^{\circ}\text{C}$ in the DA posterior simulation.

Similar improvement is seen in salinity (**Figure 4.6b**). The forward simulation overestimates the upper water column salinity by 0.8 and underestimates the salinity at depth by 0.8. After data assimilation, the upper water column salinity bias is reduced to ~ 0.1 and the subsurface bias is reduced to less than 0.2.

Time series of spatial RMSE between model and observations (**Figure 4.6c and e**) showed the temperature (salinity) RMSE is reduced from 2-3 $^{\circ}\text{C}$ (0.5-1) to $\sim 1^{\circ}\text{C}$ (0.2), suggesting DA posterior produces more accurate subsurface information. Time series of the spatial bias (**Figure 4.6d and f**) provides yet another view of the performance of data assimilation. The temperature bias (**Figure 4.6d**) in the forward simulation ranges from -1.8°C at the beginning of the study period to 2.5°C at the end of study period. Such bias in temperature fields is effectively reduced after data assimilation. Both the DA prior and posterior simulations show that the temperature bias is reduced to a much smaller range between -0.8°C and 1°C . Similar improvement is evident also for salinity (**Figure 4.6f**). After data assimilation, the salinity bias is reduced to close to zero over the entire assimilation period, as opposed to up to 0.8 in the forward simulation.

Overall, our comparisons indicate the 4DVAR is effective in reducing the misfits between model and assimilated observations. Although most of data being assimilated are satellite SST (**Figure 4.3**), our results show the assimilation is also helpful to improve the model's fidelity in resolving the subsurface hydrographic structures.

4.3.2.3 Model skill assessment

A more rigorous evaluation of data assimilative simulation can be achieved by comparing model fields with independent observations (i.e., data that have not been assimilated). Spatial distributions of these independent data are shown in **Figure 4.7**, including ocean velocity observations measured by NERACOOS coastal buoys B (WGOM), and I (EGOM), and CTD temperature and salinity at 2-m, 20-m and 50-m at buoys A, B, and E in the western GOM. In addition, ship observed temperature and salinity profiles from the NOAA Northeast Fisheries Science Center (NEFSC, <http://www.nefsc.noaa.gov/epd/ocean/MainPage/ioos.html>) shelf survey on April, 01- July 18, 2010 were also used to validate the DA model solutions.

Comparisons with NERACOOS buoy T/S: A direct point-by-point comparison was made to estimate the DA model skill in reproducing the hourly temperature and salinity data at NERACCOS buoy A, B and E (**Figure 4.8**). The numbers in the doublets stand for RMSE and BIAS between model and observations. The forward model overestimates the observed temperature (salinity) by 2.7°C and 0.6, with an RMSE being 3.1°C and 1.8, respectively.

Compared to the forward model simulation, the DA posterior simulation provides better agreement for both temperature and salinity. For temperature (salinity), RMSE between model and observations are reduced to 1.8°C and 0.7 after DA. The model-data biases are reduced to 0.61°C and -0.02 for temperature and salinity, respectively.

Comparisons with the NEFSC data: The NEFSC data have wider range of spatial coverage, and in total, 399 temperature and salinity profiles are available for comparisons. We note that among these observations, April 01-10, June 01-15 are two periods when the maximum water depth exceeds 200-m, and warm and salty slope waters permeate the Northeast Channel (NEC), northern flank of Georges Bank, as well as Jordan and Wilkinson Basin (**Figure 4.9**). For comparison, we sampled the simulated temperature and salinity fields at the same observational time and locations (**Figure 4.9**).

The initial NEFSC survey on 01-10 April was conducted from the Great South Channel (GSC) to the NEC. CTD data show that the bottom waters (greater than 50-m) had temperature exceeding ~13°C and salinity approaching as high as 36. The forward model simulation tends to overestimate surface temperature by over 1°C but underestimate the subsurface temperature even more significantly. The bottom salinity is also 1 unit fresher than the observations. After DA, we see simulated bottom water temperature and salinity compare favorably with in-situ T/S data. From middle April to May, NEFSC data show an obviously freshening in the upper column near the coastal GOM. Surface temperature is

overestimated and bottom temperature is underestimated by the forward model. DA solutions have much better agreement with observations. During the first two weeks of June, observations are concentrated in the Jordan and Wilkinson Basins in the GOM. The forward model simulation fails to get the bottom (>100-m) warm and salty waters, and overestimates the surface layer (< 100m) temperature by 1°C. In late June and early July, forward model fails to capture the freshening event. All of these deficiencies are corrected in the DA simulation. The total temperature and salinity RMSEs are reduced from 3.21°C to 2.05°C and 0.90 to 0.64, representing a roughly 40% error reduction in the DA simulation.

Point-by-point comparisons show the DA model skill improvement in resolving observed temperature and salinity characteristics (**Figure 4.10**). In the forward model, both observed temperature and salinity show large intercepts, and the slope suggests relatively lower correlation coefficients between model and observations. The DA posterior solutions show much better agreements with observations. Slope for temperature (salinity) increases to 0.78 (0.94), and intercepts is much smaller. All these results suggest that the DA model reasonably well improved the ocean state variable characteristics at the subsurface.

In addition to T/S profiles, the coastal velocity time series comparisons also show significant skill improvement in the DA posterior (**Figure 4.11**). Before DA, the forward model simulated current at buoy B displays a strong reversal in April, which is not observed. An observed flow reversal is found in late June at buoy B, but the forward model fails to

capture it. The DA posterior solutions reproduce the temporal evolution of the currents in the western GOM well. The complex correlation coefficients between observed and model velocity time series increase from 0.3 for the forward model simulation to 0.8 for the DA posterior simulation. Overall, the variability of the circulation is much better resolved in the DA posterior. Coefficients for currents at buoy I decrease from 1.3 to 1.1, suggesting the DA model is better representation of current in the EGOM as well.

To sum up, model comparisons against independent hydrographic and velocity data show significant model skill improvement in the DA posterior solutions, and the gulf- wide water mass properties are much better resolved.

4.4 Discussion

4.1 Depth-averaged temperature budget analysis

To analyze the contribution of surface heat flux and the advection effect to the temperature variability in forward and DA posterior solutions, we can diagnose the temperature equation following *He and Weisberg (2002)*:

$$\frac{\partial T}{\partial t} + (u \frac{\partial T}{\partial x} + v \frac{\partial T}{\partial y} + w \frac{\partial T}{\partial z}) = \frac{\partial}{\partial z} (K_H \frac{\partial T}{\partial z}) \dots \dots \dots (5)$$

(a) (b) (c)

Where T is the temperature, u, v, w are the velocity, and K_H the vertical diffusivity coefficient. The term (a) represents the local time rate of change as a result of (b) the

advective rate of change, and (c) the vertical diffusion. The horizontal diffusion terms are usually an order of magnitude less than the vertical diffusion and are therefore not considered. In the depth-averaged sense, the model can be represented by depth-averaging equation (5) from ocean top to bottom:

$$\frac{dT}{dt} + \underbrace{\left(u \frac{\partial T}{\partial x} + v \frac{\partial T}{\partial y} + w \frac{\partial T}{\partial z}\right)}_{(a)} = \underbrace{\frac{Q(t)}{\rho C_p}}_{(c)} \dots\dots\dots(6),$$

Where T is the depth-average temperature, and Q is the surface heat flux, ρ and Cp are sea water density and specific heat capacity respectively. We looked into the contribution of advection term (b) and heat flux term (c) in contributing to the seasonal warming during summer 2010. To do this, we averaged equation (6) with time from April 1st to July 18th, 2010. The spatial distributions of terms (b) and (c) in equation 6 for forward and posterior solutions are shown in **Figure 4.12**. In the forward model, the depth-averaged advection term (**Figure 4.12a**) is positive in the offshore area near the slope region and Scotian Shelf, and is highest near Cape Cod. The value is negative in the EGOM, BOF and Jordan Basin, suggesting the net contribution from advection is to increase the water temperature in these regions. The DA posterior (**Figure 4.12c**) showed overall similar spatial pattern but the negative values are limited in the Jordan Basin and BOF. This is likely caused by increased intrusion of warm slope water into the area. The difference between posterior and forward terms (**Figure 4.12 e**) showed positive anomalies in the advection term in the WGOM,

Georges Bank and BOF. This suggest DA posterior tend to decrease the warming rate in these area through the adjustment of advection flux. The heat flux term (**Figure 4.12b and d**) is overall larger than advection in shallow water within depth of less than 100-m, but are lower in deep basins and slope region. They are especially high in the BOF and Georges Bank where tidal mixing is strong. The difference between DA posterior and forward model solutions in heat flux term (**Figure 4.12f**) is also positive in Georges Bank and BOF. We also noted negative values in the Scotian Shelf, suggesting a major adjustment of heat flux term near the eastern boundary. As such, the depth-averaged temperature budget analysis suggest that both advection and surface heat flux plays important roles in correcting the warming trend. Both terms are high near the area with strong tides, such as Georges Bank and Bay of Fundy. Adjustment to the advection term (**Figure 4.12e**) is even larger than the heat flux adjustment (**Figure 4.12f**) in these regions. This partly explains the way DA eliminates the large bias in the SST observations (**Figure 4.5**). Further analysis is needed to separate horizontal advection to vertical advection fluxes for a thorough understanding of temperature budget variability.

4.4.2 Evolution of the water mass and coastal circulation in the GOM

The spatial and temporal continuous DA model solutions enable us to analyze the hydrography variability in the GOM in spring-summer 2010. Monthly-mean surface temperature and salinity maps (**Figure 4.13**) show some noticeable differences between

forward and DA posterior solutions. The temperature field produced by the DA simulation tends to be ~ 1 °C cooler than those by the forward simulation, especially at the Georges Bank and Bay of Fundy. This suggests that the tidal mixing in the forward model provides is insufficient, a problem solved in the posterior simulation through DA. Surface Salinity fields produced by the DA simulation are essentially similar those by the forward model with respect to the temporal evolution of salinity. After DA, salinity in the vicinity of eastern boundary near Cape Sable become much fresher, suggesting a correction to the boundary salinity fluxes can effectively change interior salinity fields. Near the slope region, the DA model produced salinity is in fact saltier than that produced by the forward model, suggesting a possible intrusion of salt slope waters from the model deep ocean boundary. Bottom temperature near NEC and Jordan Basin is 0.6 °C warmer after DA, due to the assimilation of buoy M and N temperature which is representative of slope water (Bottom panel, **Figure 4.14**). Without DA, bottom salty water (salinity >35 , *Smith et al.*, 2001) is only available in the slope region and southern flank of Wilkinson Basin. After the DA, the bottom slope water permeates in both Jordan and Wilkinson Basins. The slope water is present since the starting of model simulation (April 01). The salty water occupies the deep basins in the GOM in June, and seems to retreat in July. In fact, analysis of the T/S profiles from buoys near the Jordan Basin suggests that the slope water intrusion was initiated in late fall 2009 or early spring in 2010. Therefore, the time span for the DA presented in this study is not long enough to study

the entire evolution of the slope water intrusion.

The gulf-wide circulation is also significantly refined through with DA (**Figure 4.15**). Compared to the surface circulation produced by the forward simulation, a great portion of the coastal currents veer offshore of Portland Harbor in April, significantly reduced alongshelf transport in the WGOM. The DA simulation also shows that a semi-closed gyre is present in the Jordan Basin and the eastern GOM, connecting the eastern GOM coastal waters with Scotian Shelf waters and waters in the Bay of Fundy. Such a current feature may facilitate the delivery of fresh water from Scotian Shelf into the Gulf. In May, the surface elevation offshore of Penobscot Bay increases compared to April condition. The resulting pressure gradient between Penobscot Bay and the Jordan Basin increases, leading to a stronger cyclonic gyre that helps to move coastal water offshore, and the Jordan Basin gyre becomes clearer compared to the forward model. The current in the western GOM becomes less organized in June and July. This is consistent with geostrophic transport and ADCP observations from ship survey (*Li et al.*, 2012, submitted).

4.4.3 Co-variability of Currents and surface elevation

EOF analysis has been widely used to study the coastal, shelf, and estuarine hydrography dynamics (e.g., *He et al.*, 2003, *Mountain et al.*, 1994). One way to trim out the major variability of geostrophic current is to examine the EOF decomposition of currents (u , v) and surface topography (η) altogether.

By organizing matrix A in an $M \times N$ matrix, such that,

$$A = \begin{pmatrix} \eta \\ u \\ v \end{pmatrix} \dots \dots \dots (5)$$

where M and N represent the spatial (12000×3 grid points) and the temporal elements (648 snapshots (every 4 hour) from April 01 to July 18, 2010), respectively, matrix $A(x, y, t)$ can be represented by $A(x, y, t) = \sum_{n=1}^N a_n(t) F_n(x, y)$, where $a_n(t)$ are the temporal evolution functions and $F_n(x, y)$ the spatial eigen-functions for each EOF mode respectively.

The first EOF mode (**Figure 4.16**) accounts for 88% of the total variances, and therefore is considered the dominant mode of coastal current and sea level variability. The eigenfunction (**Figure 4.16a**) shows a clear co-variability of sea level and current in the GOM. When there is an increase in temporal mode (**Figure 4.16b**), there are higher η increase near the coast and Georges Bank, but lower η increase in the offshore basins and Northeast Channel. A double gyre feature is present in the Jordan Basin and Wilkinson Basin. The spatial heterogeneity leads to an increased offshore pressure gradient near the GOM, and a co-varied alongshore current. Similarly, there is an increased offshore outflow of surface waters from the GOM interior into the slope region, an obvious increase in the circulation magnitude. This suggests a notable geostrophic balance in the GOM is dominant in terms of circulation dynamic in the GOM during spring and summer 2010.

The first principal component (PC1, **Figure 4.16b**) showed how the spatial co-variability (in a sense, the alongshore transport) evolves with time. It increases from April to May before reaching the first peak in May 1st. Right after the peak flow, the flow reaches the first minimum until May 20th. This is consistent with geostrophic computations based on ship CTD casts during May 01-10, as well as shipboard ADCP tracks (*Li et al.*, 2012, submitted). During May 20-25th, there is the highest peak over the entire study period. Another low occurs in late May to early June, followed by an increase around June 08. Deep into June, the value drops dramatically and reaches the lowest level in June 22. This indicates that the entire mode of the circulation became diffused and weakened. The flow again recovered to becomes stronger in July; a feature confirmed by coastal current observations and shipboard ADCP tracks (*Li et al.*, 2012, submitted). It is reminded that the DA system doesn't assimilate any current observations. The assimilation of hydrography data, especially the ship T/S profiles shows rigorous improvement in producing the circulation dynamics, and demonstrates the importance of integrated observational network in the better understanding the dynamics of coastal processes.

4.4.4 Advection time scale of Scotian Shelf Water (SSW) to the coastal GOM

The SSW is the water mass with fresher salinity and colder temperature. Observations from Canadian Atlantic Zone Monitoring Program (AZMP) indicate that the SSW is

fresher-than-usual in 2010 compared to other years. The onset of the anomaly is some time near January 2010 (McGillicuddy *et al.*, 2011). Similar water mass properties are also found in upper 50-m the NERACOOS buoy M in the Jordan Basin throughout the spring and summer (Li *et al.*, submitted). It is therefore of interest to investigate the advection time scale of SSW to be transported to the Jordan Basin (JB), Bay and Fundy (BOF), eastern GOM (EGOM), and the downstream western GOM (WGOM) (**Figure 4.17**). The scale is estimated based on the passive particle releases initiated from the Scotian Shelf using the space-time continuous model current field. A rectangular area is selected as initial condition (**Figure 4.17**, blue dot arrays), and vertical depths are chosen at 0m to 200m with a 10m bin. A total number of $N_o=8111$ particles are released from April 01, 2010, the starting date for the model simulation, and are allowed to advect to the end of the simulation (July 18, 2010), At each advection t_i , we first count the number of particles inside each polygon (N), then for a certain polygon, the advection time scale τ can be estimated as:

$$\tau = \left(\sum_{i=0}^{\infty} t_i \cdot \frac{N_i}{N_o} \right) / \left(\sum_{i=0}^{\infty} \frac{N_i}{N_o} \right) \dots\dots\dots (6)$$

where i is the index for each advection time. For the limited simulation period, time series of the percent of total particles $\left(\frac{N_i}{N_o} \right)$ reaching each polygon are shown in **Figure 4.18**.

Particles started to arrive at JB after 20-days, and arrives the peak in May to late June. There

is a gradual decrease of the percentage as the season goes to July. Particles reach EGOM ~one week later than to the JB, and the peak value of the evolution appears within 50-80 days. Peak percentage to the BOF shows up at ~day 70. The WGOM time series, however, continue to increase over the simulation period and hasn't maximized during the three and half month window. Applying equation (3) to JB, EGOM and BOF by approximately integrating t_i from zero to 105 days (length of the simulation window) gives the mean advection time τ of 59, 70, and 68 days, respectively. The advection timescale to the WGOM is not quantified due to insufficient advection time when high-percentage information can be available.

The snapshot on day 59 (mean advection time to JB) for the location of the particles and their corresponding depths are presented in **Figure 4.17**. Particles advected into the slope region dig deep (>200m). The BOF and EGOM particles remains within the upper 50-m. In the JB, 50% of particles remains in the upper 50-m, whereas the rest reaches 150-m water depth following the vertical movement of the circulation. This suggests possible mixing processes in the basin interior.

4.5 Summary and future work

In this study, the recently developed, strong constraint ROMS 4D-Var system was applied to the 4-km GOM model to hindcast the coastal hydrography and circulation in spring and summer 2010. Overall, data assimilative model hindcast reproduced all observed

features reasonably well. Specifically:

Surface SST error BIAS and RMSE were both greatly reduced after data assimilation. Subsurface T/S was also greatly improved in terms of both vertical structures and temporal evolution as shown in the model-data misfit statistics. Both suggest the effectiveness of the 4DVAR algorithm. Independent hydrography data from NEFSC archives were compared with both forward and posterior model trajectories. Results showed a better fit of model posterior to the T/S profiles compared to forward run. Comparisons with coastal current documented by NERACOOS coastal buoys revealed a clear skill enhancement of DA system in producing the evolution of coastal circulation. It is encouraging because neither direct current observations nor SSH data was assimilated into the system, and suggested that the better performance in understanding the coastal circulation dynamics can be achieved through the assimilation of limited hydrographic data. We do note, however, that the modeled coastal current is sensitive to the model errors we choose. 22 experiments are conducted with varied temperature and salinity errors, and this experiment presented herein provides the most reasonable coastal current variability compared to buoy observations.

Analysis of model field showed the evolution of water masses during summer 2010. The low pressure center in the eastern GOM is an important feature. The pressure gradient between the low pressure center and waters offshore of Penobscot Bay produces a strong offshore transport of the circulation in May and June, thereby reducing the coastal flow in the

western GOM. The coastal flow in the western GOM becomes more organized in July when the low level center is diffused. Remote forcing (salt flux near Scotian Shelf and slope water inflow) play an important role in the modulation of coastal transport properties. The major variability in coastal current is presented through EOF decomposition analysis. The EOF mode shows large spatial coherence, and time mode shows an obvious suppression of coastal flow in June 2010.

Model posterior solutions were used to estimate water mass evolution information. The advection time scales for SSW to reach the JB, BOF and EGOM were estimated using passive particle release. Mean advection time is 59, 70, and 68 days for JB, BOF, EGOM, separately. SSW reaches JB a week earlier than BOF and EGOM. Particles in the JB can reach as deep as 150-m, revealing possible mixing processes in the basin interior.

It is noted that we didn't assimilate satellite SSH observations due to their quality issue near the GOM coast. Further constrains of the surface elevation can be achieved through the assimilation of along-track satellite sea level anomalies. The challenge underlies in that GOM is known for its strong tidal rectification and associated mixing processes, especially in the Bay of Fundy, Georges Bank and eastern GOM, and the real-time absolute SSH pattern is highly unknown (*Lynch et al.*, 1996). Assimilation of coastal sea level can also be important in constraining the barotropic tidal information (e.g., *He et al.*, 2005). There are still differences between observation and DA model solutions. On one hand, we note that the

observations in GOM coast are sparse. On the other hand, the homogenous vertical decorrelation scale used in the DA simulation may over-smooth the solution. Nevertheless, the successful improvement of both water mass and coastal circulation suggest that the importance of upstream/remote forcing and data from the observational network in constraining the coastal circulation in the GOM. The water mass and circulation dynamics are better understood through analyses of model results from data assimilation.

Acknowledgement

Research support was provided by National Oceanic and Atmospheric Administration grant NA06NOS4780245 for the Gulf of Maine Toxicity (GOMTOX) program. We are very grateful for the outstanding efforts of the officers, crews, and shore support of R/V Oceanus, R/V Endeavor as well as the hard work of all those who participated in the seagoing science teams.

References

- Aretxabaleta, A.L., McGillicuddy, D.J., Smith, K.W., Manning J.P. and D.R. Lynch, 2009. Model Simulations of the Bay of Fundy Gyre: 2. Hindcasts for 2005-2007 Reveal Interannual Variability in Retentiveness. *Journal of Geophysical Research*, 114, C09005, doi:10.1029/2008JC004948.
- Bigelow, H.B. (1927), Physical Oceanography of the Gulf of Maine, *Fisheries Bulletin*, 40, 511-1027.
- Broquet, G., C. A. Edwards, A. M. Moore, B. S. Powell, M. Veneziani, and J. D.

Doyle(2009a): Application of 4D-Variational data assimilation to the California Current System, *Dynamics of Atmospheres and Oceans*, 48, 69-92.

Broquet, G., A.M. Moore, H. G. Arango, C. A. Edwards and Brian S. Powell (2009b): Ocean State and Surface Forcing Correction using the ROMS-IS4DVAR Data Assimilation System, *Mercator Ocean Quarterly Newsletter*, 34, pp 5-13.

Chapman, D.C. and R.C. Beardsley (1989): On the origin of shelf water in the Middle Atlantic Bight, *Journal of Physical Oceanography*, 19, 384-391.

Courtier, P., Thépaut, J.N., Hollingsworth, A. (1994): A strategy for operational implementation of 4D-Var, using an incremental approach. *Quart. J. Roy. Meteorol. Soc.* 120, 1367–1387.

Courtier, P., 1997: Dual formulation of four-dimensional variational assimilation. *Q. J. R. Meteorol. Soc.*, 123, 2449-2461.

Curry, R. (2003). HydroBase 2.0: a database of hydrographic profiles and tools for climatological analysis. *Woods Hole Oceanographic Institution Technical Report, Woods Hole*, 80 pp.

Derber, J. and A. Rosati, 1989: A global oceanic data assimilation system. *Journal of Physical Oceanography*, 19, 1333-1347. Di Lorenzo, E., Moore, A.M., Arango, H.G., Cornuelle, B.D., Miller, A.J., Powell, B.S., Chua, B.S., Bennett, A.F.(2007). Weak and strong constraint data assimilation in the inverse Regional Ocean Modeling System (ROMS): development and application for a baroclinic coastal upwelling system, *Ocean Modelling*. 16, 160 - 187.

Doyle, J. D., Q. Jiang, and J. Farrara (2009) : High-resolution atmospheric modeling over the Monterey Bay during AOSN II, *Deep-Sea Res., Part II*, **56**, 87-99.

Fairall, C.W., Bradley, E.F., Rogers, D.P., Edson, J.B., Young, G.S., 1996. Bulk

parameterization of air - sea fluxes for tropical ocean - global atmosphere coupled ocean-atmosphere response experiment. *J. Geophys. Res.*, 101, 3747 - 3764.

Fairall, C. W., E. F. Bradley, J. E. Hare, A. A. Garchev, and J. Edson, 2003: Bulk parameterization of air-sea fluxes: Updates and verification for the COARE algorithm. *Journal of Climate*, 16, 571-591.

Flather, R. A., 1976: A tidal model of the northwest European continental shelf. *Mem. Soc. R. Sci. Liege*, 6, 141-164.

Garrett, C.(1972), Tidal Resonance in the Bay of Fundy and Gulf of Maine, *Nature*, 238, 441 - 443, doi:10.1038/238441a0.

Haidvogel, D. B., H. Arango, W. P. Budgell, B. D. Cornuelle, E. Curchitser, E. Di Lorenzo, K. Fennel, W. R. Geyer, A. J. Hermann, L. Lanerolle, J. Levin, J. C. McWilliams, A. J. Miller, A. M. Moore, T. M. Powell, A. F. Shchepetkin, C. R. Sherwood, R. P. Signell, J. C. Warner, and J. Wilkin, 2008: Ocean forecasting in terrain-following coordinates: Formulation and skill assessment of the Regional Ocean Modeling System. *Journal of Computational Physics*, 227, 3595-3624.

He, R. and K. Chen: Investigation of Northeastern North America Coastal Circulation Using a Regional Circulation Hindcast Model, in revision.

He, R., R. H. Weisberg (2002), West Florida Shelf Circulation and Heat Budget for 1999 Spring Transition. *Continental Shelf Research*, Vol. 22, 5, 719-748.

He, R., R. H. Weisberg, H. Zhang, F. E. Muller-Karger, and R.W. Helber (2003), A Cloud Free Satellite-derived, Sea Surface Temperature Analysis for the West Florida Shelf. *Geophysical Research Letters*, Vol. 30, 15, 1811, doi: 10.1029/2003GL017673

He, R., Y. Liu and R. H. Weisberg (2004), Coastal Ocean Wind Fields Gauged Against the

Performance of an Ocean Circulation Model. *Geophysical Research Letters*, Vol. 31, 14, 14303, doi:10.1029 / 2003GL019261.

He, R., D. J. McGillicuddy, K. W. Smith, D. R. Lynch, C. A. Stock, and J. P. Manning (2005), Data Assimilative Hindcast of the Gulf of Maine Coastal Circulation. *Journal of Geophysical Research*, Vol. 110, C10, C10011, doi:10.1029/2004JC002807.

He, R. and McGillicuddy D. J. (2008): The historic 2005 Toxic Bloom of *Alexandrium fundyense* in the west Gulf of Maine- Part 1: In Situ Observations of Coastal Hydrography and Circulation. *Journal of Geophysical Research*, 113,C07039, doi: 10.1029/2007JC004601.

Hetland, R. D., and R. P. Signell, (2005), Modeling Coastal Current Transport in the Gulf of Maine, *Deep Sea Res. II*, 52, 2430-2449.

Ingleby, B. and M. Huddleston, 2007: Quality control of ocean temperature and salinity profiles - historical and real-time data. *Journal of Marine Systems*, 65, 158-175.

Keafer B.A., Churchill, J.H., McGillicuddy, D.J., Anderson, D.M (2005), Bloom development and transport of toxic *Alexandrium fundyense* population within a coastal plume in the Gulf of Maine. *Deep Sea Research II*, 52, 2674-2697.

Limeburner, R., and Beardsley, R.C. (1996), Near-surface recirculation over Georges Bank. *Deep Sea Research II*, 43, 1547-1574.

Li, Y., He, R., D.J.McGillicuddy, D.M. Anderson, and B.A.Keafer (2009): Investigation of the 2006 *Alexandrium fundyense* Bloom in the Gulf of Maine: In situ Observations and Numerical Modeling, *Continental Shelf Research*, doi:10.1016/j.csr.2009.07.012.

Li, Y., R. He, and D. J. McGillicuddy (2012): Seasonal and Interannual Variability in Gulf of Maine Hydrodynamics: 2002-2011, submitted to *Deep Sea Research II*.

Li, Z., Y. Chao, J.C. McWilliams, and K. Ide (2008): A three-dimensional variational data assimilation scheme for the Regional Ocean Modeling System: Implementation and basic experiments. *J. Geophys. Res.*, doi:10.1029/2006JC004042.

Luetich, R. A., J. J. Westerink, and N. W. Scheffner (1992), ADCIRC: An advanced three-dimensional circulation model for shelves, coasts and estuaries. U.S. Army Engineer Waterways Experiment Station.

Lynch, D.R., J. T. Ipa., C. E. Naimie and F. E. Werner (1996), Comprehensive coastal circulation model with application to the Gulf of Maine. *Continental Shelf Research*, Vol. 16-7, 875-906

Lynch, D.R., M.J. Holboke, C.E. Naimie (1997), The Maine coastal current: Spring climatological circulation. *Continental Shelf Research*, 17 (6): 605-634, May, 1997.

Lynch, D. R., C. E. Naimie, and C. G. Hannah (1998), Hindcasting the Georges Bank circulation, Part I: Detiding, *Continental Shelf Research*, 18, 607–639.

Marchesiello, P., J.C. McWilliams, and A.F. Shchepetkin (2001), Open boundary conditions for long-term integration of regional oceanic models. *Ocean Modeling*, 3, 1-20.

McGillicuddy, D.J., Townsend, D.W., He, R., Keafer, B.A., Kleindinst, J.L., Li, Y., Manning, J.P., Mountain, D.G., Thomas, M.A., and D.M. Anderson (2011), Suppression of the 2010 Alexandrium fundyense bloom by changes in physical, biological, and chemical properties of the Gulf of Maine. *Limnology and Oceanography*, 56(6), 2411–2426.

Mellor L.G. and T. Yamada (1982), Development of a turbulence closure model for geophysical fluid problems, *Reviews of Geophysics and space physics*, 20-4, 851-875.

Moore, A. M., H. G. Arango, E. D. Lorenzo, B. D. Cornuelle, A. J. Miller, and D. J. Neilson, 2004: A Comprehensive ocean prediction and analysis system based on the tangent linear and

adjoint of a regional ocean model. *Ocean Modeling*, 7, 227-258.

Moore, A. M., H. G. Arango, G. Broquet, C. Edwards, M. Veneziani, B. Powell, D. Foley, J. D. Doyle, D. Costa, and P. Robinson (2011a): The Regional Ocean Modeling System (ROMS) 4-Dimensional Variational Data Assimilation Systems: part2 - Performance and Application to the California Current System. *Progress in Oceanography*, 91, 50-73.

Moore, A. M., H. G. Arango, G. Broquet, B. Powell, A. T. Weaver, and J. Zavala-Garay (2011b): The Regional Ocean Modeling System (ROMS) 4-Dimensional Variational Data Assimilation Systems: part1 - System overview and formulation. *Progress in Oceanography*, 91, 34-49.

Moore, A. M., H. G. Arango, G. Broquet, C. Edwards, M. Veneziani, B. Powell, D. Foley, J. D. Doyle, D. Costa, and P. Robinson (2011c): The Regional Ocean Modeling System (ROMS) 4-dimensional variational data assimilation systems, Part III: Observation impact and observation sensitivity in the California Current System. *Progress in Oceanography*, 91, 74-94.

Mountain, D.G. and Manning J.P. (1994), Seasonal and interannual variability in the properties of the surface waters of the Gulf of Maine, *Continental Shelf Research*, 14, 1555-1581.

Pettigrew, N. R., J. H. Churchill, C. D. Janzen, L. J. Mangum, R. P. Signell, A. C. Thomas, D. W. Townsend, J. P. Wallinga, and H. Xue (2005), The kinematic and hydrographic structure of the Gulf of Maine coastal current. *Deep Sea Research, Part II*, 52, 19-21, 2369-2391.

Pettigrew, N. R., R.J. Fleming, and C.P. Fikes (2011): The history of the first decade of the observing system in the Gulf of Maine, and plans for the second decade, *MTS Journal*, September 2011, 1-10.

Powell, B. S., H. Arango, A. M. Moore, E. D. Lorzenzo, and D. F. R.F. Milliff, 2008: 4DVAR

Data Assimilation in the Intra-Americas Sea with the Regional Ocean Modeling System (ROMS). *Ocean Modeling*, 25, 173-188.

Townsend, D.W., N.D. Rebeck, M.A. Thomas, L. Karp-Boss, and R. M. Gettings (2010): A changing nutrient regime in the Gulf of Maine. *Continental Shelf Research*, 30: 820-832.

Shchepetkin, A.F. and J.C. McWilliams (2005), a split-explicit, free-surface, topographic following-coordinate oceanic model. *Ocean Modelling*, 9, 347-404.

Signell, R. P., H. L. Jenter, and A. F. Blumberg (1994), Modeling the seasonal circulation in Massachusetts Bay, in *Proceedings of 3rd International Conference on Estuarine and Coastal Modeling*, pp. 578–590, edited by M. L. Spaulding, Am. Soc. of Civ. Eng., Reston, Va.

Smith. P.C. (1983): the mean and seasonal circulation off southeast Nova Scotia, *Journal of Physical Oceanography*, 13, 1034-1054.

Smith P.C, R.W. Houghton, R.G. Fairbanks., and D.G. Mountain (2001): Interannual variability of boundary fluxes and water mass properties in the Gulf of Maine and on Georges Bank: 1993-1997, *Deep-Sea Research II* 48: 37-70.

Townsend, D.W., N.D. Rebeck, M.A. Thomas, L. Karp-Boss, and R. M. Gettings (2010): A changing nutrient regime in the Gulf of Maine. *Continental Shelf Research*, 30: 820-832.

Tshimanga, J., Gratton, S., Weaver, A.T., Sartenaer, A.(2008): Limited-memory preconditioners with application to incremental variational data assimilation. *Quarterly Journal of the Royal Meteorological Society*, 134, 751-769.

Weaver, A. T. and P. Courtier, 2001: Correlation modelling on the sphere using a generalized diffusion equation. *Quarterly Journal of the Royal Meteorological Society*, 127, 1815-1846.

Weaver, A. T., J. Vialard, and D. L. T. Anderson (2003): Three- and four-dimensional variational data assimilation with a general circulation model of the tropical Pacific Ocean. Part1: Formulation, internal diagnostics, and consistency checks. *Monthly Weather Review*, 131, 1360-1378.

Wilkin, J., J. Zavala-Garay, J. Levin, and W. G. Zhang, 2008: Four-Dimensional Variational Assimilation of Satellite Temperature and Sea Level Data in the Coastal Ocean and Adjacent Deep Sea. *Geoscience and Remote Sensing Symposium, 2008. IGARSS 2008. IEEE International*, III - 427-III - 430.

Xue H., F., Chai, and N.R, Pettigrew (2000), A model study of the seasonal circulation in the Gulf of Maine, *Journal of Physical Oceanography*, 30 (5): 1111-1135, 2000.

Chapter V: Diagnosing the Evolution of 2008 *Alexandrium fundyense* Bloom in the Gulf of Maine using in-situ Observations and Coupled Biophysical Model Simulations

Yizhen Li¹, Ruoying He^{1*}, Dennis J. McGillicuddy Jr.², and Donald M. Anderson³

¹Department of Marine, Earth & Atmospheric Sciences, North Carolina State University, 2800 Faucette Drive, Raleigh, NC 27695

²Applied Ocean Physics & Engineering, Woods Hole Oceanographic Institution

³Biology Department, Woods Hole Oceanographic Institution

To be submitted to *Harmful Algae* or *Deep Sea Research II*

Last Modified: July, 2012

KEYWORDS: *Alexandrium fundyense* bloom, Numerical Modeling, Gulf of Maine

Abstract

A tremendous *Alexandrium fundyense* bloom took place in the Gulf of Maine in spring and summer 2008, causing extensive shellfish bed closures in the New England coastal region. The evolution of this bloom was investigated using both *in situ* observations and coupled bio-physical model simulations. Model validations against observations suggested that the model was able to resolve the seasonal evolutions of the coastal hydrodynamics, as well as the temporal variations and three-dimensional spatial distributions of *A. fundyense* bloom reasonably well. Calculations of cell fluxes showed the bloom conditions in the

upstream and offshore waters have significant impact on the cell concentration in the western Gulf of Maine coastal region. EOF analysis was applied on simulated upper (50-m) water column bloom concentration over the entire bloom season (March 15th –August 15th, 2008). Results suggested the top two modes can account for 98% of total variance. The 1st mode is dominated by the gulf-wide seasonal bloom evolution, and is closely linked with cell net growth rate and germination flux, whereas the 2nd model well represents the seasonal shift of the center of the bloom from western GOM to the eastern GOM as season progresses from June to July and August .

5.1 Introduction

The reoccurring, toxic dinoflagellate *Alexandrium fundyense* bloom has become a serious environmental and public health problem in the Gulf of Maine (GOM) and New England coastal ocean (e.g. *Anderson et al.*, 2005a). The neurotoxins in the harmful cells can lead to paralytic shellfish poisoning (PSP), a potentially fatal disorder for humans after ingestion of shellfish that is contaminated by *A. fundyense* toxins. Such toxicity can also kill sea birds and large marine mammals, causing significant disturbance to the well-being of marine ecosystem. Earlier observational and modeling studies on *A. fundyense* bloom dynamics (e.g., *Franks*, 1992; *Townsend et al.*, 2005; *Anderson et al.*, 2005a; 2005c; *Stock et al.*, 2005; *McGillicuddy et al.*, 2005; *He et al.*, 2008; *Li et al.*, 2009; *McGillicuddy et al.*, 2011) have revealed that the magnitude and distribution of this harmful bloom are regulated by a suite of physical and biological processes. The physical transport in particular is largely

determined by the cyclonic GOM coastal circulation that generally consists of the Eastern Maine Coastal Current (EMCC) and the western Maine Coastal Current (WMCC) (*Bigelow, 1927; Lynch et al., 1996, 1997*). Subject to both local (wind, heat fluxes, rivers, tides) and remote (upstream and offshore ocean) forcing influence, the GOM coastal circulation and water mass characteristics present significant seasonal and interannual variability (e.g., *Xue et al., 2000, Mountain et al., 1994; Loder et al., 1997; Li et al., in revision*), which in turn alters the timing and magnitude of *A. fundyense* blooms in each year (e.g., *Anderson et al., 2005a; He and McGillicuddy, 2008; He et al., 2008; McGillicuddy et al., 2011*). For instance, *Anderson et al. (2005a)* showed that the extensive *A. fundyense* bloom in summer 2005 (the largest in at least 33-years) was related to anomalous hydrographic and biological conditions. Follow-up observational and modeling analyses (*He and McGillicuddy, 2008; He et al., 2008*) suggested the high abundance of cysts in western GOM was the primary cause of the 2005 bloom. As a part of GOMTOX project funded by NOAA ECOHAB program, a large amount of *in-situ* physical and biological observations were collected in summers of 2005 through 2010 to quantify coastal hydrography and *A. fundyense* cell distributions. Data indicated *A. fundyense* bloom in 2008 was one of the most extensive in recent years. It is of interest to understand why 2008 was different from other bloom years, and we intend to address this question by combining *in-situ* observations with coupled biophysical model simulations to characterize the temporal and spatial evolutions of the bloom and to elucidate the underlying physical and biological mechanisms driving the bloom.

Different from our previous studies on the GOM *A. fundyense* blooms (*Stock et al., 2005;*

McGillicuddy et al., 2005; He et al., 2008; Li et al., 2009), we focus on the seasonal variability of cell transport flux and the vertical structure of the bloom in this study. Section 5.2 provides a brief description of observations and biophysical model that we utilized. Section 5.3 offers model-data comparisons to gauge the model's fidelity in reproducing coastal hydrodynamics and *A. fundyense* bloom distributions. Detailed model analyses on coastal ocean transport and the bloom dynamics are given in Section 5.4, followed by summaries in Section 5.5.

5.2 Data and Method

5.2.1 In-situ observations

Intensive ship surveys were conducted in spring-summer 2008, including in chronological order: 1) *R/V Conn* survey conducted between April 15th and 16th offshore of Boston harbor; 2) *R/V Oceanus* survey (*OC445*) conducted between April 29th and May 5th over the coastal area between the north tail of Cape Cod and Cape Ann; 3) Mass Bay survey conducted between May 15th and 16th; 4) *R/V Oceanus* survey (*OC447*) conducted between May 29th and June 4th, covering the same area and stations as *OC445*; 5) a Mass Bay survey conducted on June 16th -17th, and 6) another Mass bay survey conducted on June 24th; and lastly 7) *R/V Endeavor* survey (*EN451*) conducted between August 7th -13th over the entire gulf coastal areas.. In each of these surveys, water samples were collected for enumeration of *A. fundyense* cells (*Anderson et al. 2005b*) at the ocean surface. *OC445* and *OC447*

additionally also had subsurface cell concentration samplings. We highlighted five cross-shelf transects (indicated by D1, E1, D2, E2 and D3, respectively in **Figure 5.1**) used by these two surveys for subsurface bloom analysis later in this study.

Finally, ocean velocity and temperature and salinity data measured by the regional ocean observing system (NERACOOS, <http://www.neracoos.org>) were also utilized (triangles in **Figure 1**) in this research.

5.2.2 Coupled bio-physical model

We used a coupled biophysical model described by *He et al.* (2008) and *Li et al.* (2009) to hindcast time-space continuous hydrodynamics and *A. fundyense* fields. The modeling system consists of a circulation module and an *A. fundyense* population dynamics module.

The circulation module is based on the Regional Ocean Modeling System (ROMS, <http://www.myroms.org/>), which is a free-surface, hydrostatic, primitive-equation model. ROMS employs split-explicit separation of fast barotropic and slow baroclinic modes, and is formulated in vertically stretched terrain-following coordinates (*Shchepetkin and McWilliams*, 2005). For the hydrodynamic open boundary conditions (OBCs), a multi-nested configuration was implemented to downscale a global data assimilative Hybrid Coordinate Ocean Model (HYCOM, <http://hycom.rsmas.miami.edu/dataserver>) solutions to a shelf-wide ROMS model and subsequently to the GOM ROMS model (*He et al.*, 2008) via a one-way nesting approach. Such a multi-nested model downscaling configuration enables the

high-resolution GOM ROMS to achieve numerically accurate and dynamically consistent boundary forcing from its large scale “parent” models, a step that is crucial for resolving GOM hydrography and coastal transport, both of which are important for *A. fundyense* bloom dynamics (He *et al.*, 2008) . The method of Marchesiello *et al.* (2001) was applied to prescribe boundary values of tracers and baroclinic velocity, For the free surface and depth-averaged velocity boundary conditions, the method of Flather (1976) was used with the external values provided by ”parent” model. Because HYCOM does not consider tides, we also superimposed along open boundaries tidal (M_2 , S_2 , N_2 , K_2 , K_1 , O_1 , Q_1) sea level and depth-averaged velocity using harmonics derived from an ADCIRC simulation of the western Atlantic (Luettich *et al.*, 1992). The Mellor-Yamada (1982) closure scheme and the quadratic drag formulation were applied to compute the vertical turbulent mixing and the bottom friction specification. The GOM ROMS has a spatial resolution of 3-km (2-km) in the alongshore (cross-shelf) direction, and 36 terrain-following vertical levels that have higher resolutions near the surface and bottom to better resolve boundary layers.

The biological module is a single component *A. fundyense* model that contains parameterizations of *A. fundyense* germination, growth and mortality (Anderson *et al.*, 2005a; Stock *et al.*, 2005; McGillicuddy *et al.*, 2005; He *et al.*, 2008; Li *et al.*, 2009). Fundamental to the construction of this model is that *A. fundyense* is a minor constituent of phytoplankton community in the GOM, and thus it is considered to have little effect on ambient

environmental conditions such as nutrient concentration (*Love et al.*, 2006) and predator abundance. The evolution of *A. fundyense* is then expressed as a single advection-diffusion-reaction equation:

$$\frac{\partial C}{\partial t} + \nabla \cdot ((\vec{u} + w_a)C) = \nabla \cdot K \nabla C + (\mu - m)C + F_g \quad (1)$$

where C is the cell concentration of *A. fundyense*, \vec{u} and w_a are the fluid velocity and *A. fundyense* up-swimming velocity, taken as 10 m day^{-1} (*Kamykowski et al.*, 1992) in the ocean interior and tapered to zero to the ocean surface; K is the diffusivity coefficient, μ and m are the cell growth and mortality terms respectively, and F_g is the germination flux from *A. fundyense* cyst sediment layer to vegetative cells in the water column. We consider the germination from the upper 1-cm sediment layer. The growth term μ is dependent on temperature (T), salinity (S), solar non-spectral irradiance (E) and nutrient (NO_3 in our model) concentration. Detailed formulations of these terms are presented in *Stock et al.* (2005) and later in *He et al.* (2008) for an improved temperature dependent mortality formulation.

The initial *A. fundyense* cell concentration in the model was set to zero everywhere. No-gradient boundary conditions were applied to cell concentration along model open boundaries. Due to the lack of nutrient observations, monthly climatological nutrient generated by University of Maine (*Rebuck*, 2011) was adopted and linearly interpolated at each time step of the model simulation. Cells geminate from their benthic cyst stage in early spring, a process triggered by their endogenous clock modulated by ambient water

temperature and light conditions (*Anderson, 1997*). Information about cyst abundance and distributions were derived from a gulf-wide sediment core survey conducted in fall 2007. We assume changes in cyst abundance are negligible before germination and throughout the bloom season. Thus, the resulting germination flux (F_g) is controlled by *A. fundyense* endogenous clock, and ambient water temperature and light conditions that are evolving over the time (*Stock et al., 2005*).

For both shelf-scale ROMS and GOM ROMS hindcasts, the surface atmospheric forcing, including cloud fraction, precipitation, surface pressure and humidity, air temperature, surface wind, and shortwave radiation were obtained from the National Center for Environmental Prediction (NCEP), North America Regional Reanalysis (NARR). Spatial and temporal resolutions of these forcing fields are 32- km and 3 hours, respectively. They were applied in the standard bulk flux formulation to derive wind stress and net surface heat flux needed by the simulations. To further constrain the surface heat flux, we also followed the same approach used in *He and Weisberg (2003)* to relax the modeled SST field to NOAA Coast Watch daily, 1/10 degree cloud-free SST product with a timescale of 0.5 day. GOM ROMS also incorporates river runoff as an important forcing agent, for which observed daily river runoff time series from United States Geological Survey (USGS) were used to provide freshwater input to the model.

Given the nature of the one-way nesting, model hindcasts were performed in a sequential

order. The nested shelf-scale ROMS hindcast was performed first, in which only the hydrodynamics was computed; then with the initial condition and OBCs from shelf-scale ROMS, the nested GOM ROMS hindcast was carried out, in which both hydrodynamics and the *A. fundyense* cell concentration were simulated simultaneously. The GOM ROMS physical-biological coupled simulation was carried out from March 15th to August 15th, 2008 to encompass the entire bloom season.

5.3 Model-Data Comparisons

Extensive model-data comparisons were performed to gauge the utility of the model. We presented below several different types of comparisons for validating the coupled GOM model.

5.3.1 Mooring Data

NERACOOS moorings provide surface and subsurface velocity measurements from surface current meters and Acoustic Doppler Current Profilers (ADCP), allowing for direct comparisons with simulated velocity. At moorings A and B (**Figure 5.2**) for instance, time series comparisons at two different depths: 2-m and 10-m were shown and quantified by a complex correlation analysis (*He and Weisberg, 2002*). We see simulated and observed currents compare reasonably well with each other. Correlation coefficients range between 0.5 and 0.7, and orientations between simulation and observation agree to between 3° and 17°.

Both observed and modeled velocity time series show predominating southwestward flow, although at mooring A, the regression coefficients are 0.5 and 0.4 for velocity comparisons at 2-m and 10-m respectively, suggesting the model overall underestimates the current magnitude by 50% at this location. Better agreement is seen at mooring B, where the regression coefficients are 0.9 and 0.8 for velocity comparisons at 2-m and 10-m.

The model performance was also gauged in reproducing coastal surface temperature and salinity variability at buoy A, B, F and I using Taylor diagram approach (**Figure 5.3**). Good temperature agreements are seen. The correlation coefficients at all 4 sites are greater than 0.95, while the root-mean square differences (RMSD) are all smaller than 0.3°C. Comparisons of salinity are also reasonable. The correlations between observed and simulated salinity are all greater than 0.52. The standard deviations are all near the value of 1, suggesting a good match of observed and model variability. Direct time series comparisons and the least-square fitting analysis (not shown) indicate the model captures both the seasonal warming and freshening at these sites fairly well.

In summary, these comparisons suggest the model is in general capable of reproducing observed transport and hydrographic variability, lending confidence that the biological model is couched in a realistic physical environment.

5.3.2 Surface Cell Concentration

To validate the *A. fundyense* population dynamics model, direct comparisons (**Figure**

5.4, 5) were made between simulated and observed surface cell concentrations throughout the season (April–August). In situ cell observations were collected by a series of ship surveys in the Massachusetts Bay, WGOM and EGOM at different time. To quantify model-data comparisons, we extracted model simulated cell concentration at each sampling station, and computed point-by-point model-data misfit.

The survey conducted on April 15th-16th (**Figure 5.4a**) showed that a very low concentration (< 20 cells L⁻¹) bloom was present in the offshore waters of the Mass Bay. Modeled bloom at that time (**Figure 5.4b**) showed similar distribution at these locations. Ship survey during April 29-May 05 (**Figure 5.4c**) observed a bigger bloom (with cell concentration higher than 100 cells L⁻¹) in the coastal waters between Cape Ann and Casco Bay, but did not detect any bloom offshore of 150m isobath and south of Cape Ann. The model simulation (**Figure 5.4d**) produced a similar cell spatial distribution, although significantly overestimated the bloom magnitude. Two weeks later, ship survey on May 15th-16th indicated that the bloom in the waters surrounding Mass Bay and Cape Code had elevated, with concentration exceeding 1000 cells L⁻¹ (**Figure 5.4e**). The model reproduced most of said features, but overestimated the offshore extension of this bloom. By the end of May (May 29th-June 04th) another survey covering the WGOM, Mass Bay and Cape Cod coastal areas indicated high concentration bloom offshore of west Main and New Hampshire, and the bloom was transported further downstream, and made into coastal waters in

Nantucket Sound. Model overestimated the bloom surrounding the Cape Cod Bay, and underestimated cell concentration in the WGOM (**Figure 5.4g, 4h**).

The intensity of bloom started to decay afterward. A ship survey on June 16-17 (**Figure 5.5a**) showed that while there were some high concentration cell patches in the Mass Bay, cell concentrations in most of this area had dropped to less than 200 cells L⁻¹, a feature shown by the model simulation (**Figure 5.5b**) as well. By June 24, another ship survey (**Figure 5.5c**) detected essentially no bloom in the Mass Bay, so was suggested by the model simulation (**Figure 5.5d**). In middle August, a large-scale survey was made to sample cell concentration offshore of WGOM and the entire eastern GOM. Observations show that no bloom in the offshore water of WGOM, and low to medium level bloom in the EGOM (**Figure 5.5e**). Model reproduced such spatial distribution and regional contrast, albeit generally overestimated the bloom concentration in the EGOM, and failed to capture some small but high-concentration bloom patches in the Bay of Fundy (**Figure 5.5f**).

Collectively there were 308 bloom samples from all the abovementioned ship surveys. To summarize differences between observed and simulated cell concentrations for all these samples, a misfit histogram was used to show these model-data comparisons (**Figure 5.6**). We found for 86% of these 308 comparisons, the model-data misfit was within the range of ± 50 cells L⁻¹, suggesting the *A. fundyense* population model has intrinsic skill in re-producing the temporal and spatial distribution of bloom. We note that the misfit histogram shows a

normal distribution. A fitted normal distribution curve further shows the center of mass is a bit to the right of zero mean, indicating the model overall has overestimated the overall bloom concentrations during all the periods being examined.

Previous studies (*Stock et al.*, 2005) suggested that the gulf-wide model is a smoothed representation of observations, and cannot resolve the small-scale patchiness in reality. As such, the point-by-point comparisons may provide large misfit even for a perfect biological model. To avoid such aliasing, we spatially average all the observations within each survey to represent the overall bloom magnitude for that period. Based on the spatial-averaged bloom condition during each survey, reasonable agreement between modeled cell concentrations and in situ observations (in log₁₀ scale) was seen in the Taylor diagram (**Figure 5.7**). The temporal correlation coefficient for the seven surveys during April to August are greater than 0.7. Meanwhile, the root-mean square differences (RMSD, in log scale) are all smaller than 0.8 (therefore less than 7 cells/L in cell concentration). The standard deviation is essentially closely to 1, suggesting a good match of observed and modeled cell concentration variability. All these results suggest that a good model skill in capturing the temporal evolution and magnitude of the observed bloom.

5.3.3 Vertical Structure of Bloom

Many of the ship surveys had subsurface cell counts, and make it possible to evaluate vertical structures of the bloom along some cross-shelf transects, and the model's

performance in getting these bloom features. Taking data from *OC445* survey (late April and early May) along transects E₂, D₂, E₁ and D₁ for example (**Figure 5.8**), we see the model well reproduced the observed surface trapping feature of the bloom, and generally captured onshore/offshore distribution of the bloom. At this time, the model overestimated the bloom concentration along all 4 transects.

Better model-data agreements were seen in late May when *OC447* provided another set of cell observations in the WGOM. Both observation and model showed cells were largely trapped in the upper 15 meters (**Figure 5.9**). While no observations were available, the model suggested subsurface bloom of tens of cells L⁻¹ can extend to 50-60 m (D₃, E₂ and D₂ in **Figure 5.9**). A more detailed analysis of vertical structures will be provided in section **5.4.2**.

In summary, all the model-data comparisons presented above show that the coupled model is capable of reasonably well reproducing the temporal evolution and 3-dimensional spatial distribution of the 2008 bloom, allowing us to base on the model solutions to look into several aspects of bloom dynamics in details.

5.4. Discussions

5.4.1 Advection of cell flux

We sample the simulated bloom solutions along five cross-shelf transects: D₁, D₂, D₃ and N₁, N₂, and four offshore transects: D₁D₂, D₂D₃, D₃N₁ and N₁N₂ that are approximately parallel to the coastline (see their locations in **Figure 5.1**). The integrated cell

advection flux is defined as $\int_0^x \int_{-H}^0 uc \, dx dz$, where x is the transect distance from its initial station, u the ocean velocity normal to each transect, and c is the cell concentration, and z the water depth. Because the model validation only goes to upper 50m, we chose H as 50-m for this integration. The flux is integrated from onshore to offshore and from 50-m to surface. The cell flux is positive northeastward for the 5 cross-shelf transects, and positive onshore for the four offshore transect (e.g., D1D2). In a sense, the cell flux transports quantify the contribution of bloom coming from upstream and offshore to the EGOM-WGOM control volume that we have defined.

We computed cell flux along each of these transects every time step and averaged their values into monthly means. From April to July, the monthly-averaged cell flux is negative for all the cross-shelf transects (**Table 5.1**). This is associated with the dominant MCC system. Cell fluxes along five cross-shelf transects show there is larger temporal variability in the (downstream) WGOM region. For instance, the cell fluxes along transect D1 and D2 are at least twice larger in May than in other months. In contrast, cell fluxes in the upstream EGOM (for instance along M1 and M2) shows much less temporal variations between April and July.

Cell fluxes along four offshore transects are comparatively smaller, and flow in different directions at different time. For instance, flux along transect D1D2 is shoreward from April to June. Fluxes along D2D3 and D3N1 are offshore throughout the bloom season. Transect M1M2 intersects with the Jordan Basin gyre, here we see the cell flux is seaward (negative)

in April and May, but shoreward (positive) in June and July.

Except at N2, cell fluxes at all other four cross-shelf transects and four offshore transect have significantly larger standard deviation (STD, **Table 5.1**) than their respective means. We can trace the root of such variability to the changing coastal currents which are driven by both local forcing (wind, heat flux, tides, river runoff) and remote boundary forcing, and complex cell reproduction processes such as cyst germination, cell growth, and mortality which all vary in response to different ambient environment conditions (temperature, salinity, nutrient and light).

5.4.2 Germination potential and germination flux

Cyst germination flux is a critical element of *A. fundyense* population dynamics (Anderson et al., 2005c). The germination potential together with an endogenous clock, and cyst abundance determine the germination flux, such that

$$F_g = \int_0^{1cm} G(T, E(z), t) \times \text{cyst abundance} dz ,$$

where $G(T, E(z), t) = G(T, E(z)) * EC(t)$ is the germination rate, and z is the depth of the sediment layer (1-cm in this case, see Anderson et al., 2005c, McGillicuddy et al., 2005; Stock et al., 2005). $EC(t)$ is the germination endogenous clock, which is the ratio of the germination potential at any time (t) relative to the maximum potential (Stock et al., 2005). $G(T, E(z), t)$ is germination rate based on the bottom light condition $E(z)$ after light is

exponentially attenuated in the water column and the sediment layer, and the bottom temperature condition at a given time t . In our present modeling framework, the threshold for $E(z)$ is 2.4 w/m^2 for light condition and 0.024 w/m^2 (1% of light condition) for dark condition (Anderson *et al.*, 2005c). Light condition is ‘transitional’ between shallow and bright cyst bed nearshore and deeper, darker cyst bed offshore. Our result (not shown) indicates the monthly difference in bottom light condition during the period of our study (April–August) is negligible.

Figure 5.10 shows the seasonal evolutions of the area-averaged cell germination flux, its associated area-averaged bottom temperature, the area-averaged light condition, as well as the endogenous clock, respectively between April and August. The germination flux $G(T, E(z), t)$ is highest in middle June and lowest in March. The endogenous clock (EC) itself increases from April to May, but decreases sharply beginning in June. The irradiance increases from March to June, then largely levels off for the rest of season. It is clear that the highest germination flux in June 2008 was largely determined by the seasonal warming in bottom temperature, along with the modulation by irradiance and endogenous clock.

5.4.3 Principal modes for the cell concentrations

The major variability of the GOM bloom was characterized by the Empirical Model Function (EOF) analysis of the simulated cell concentration integrated over the upper 50m in GOM in log scale (**Figure 5.11**). We focused on the coastal variability, and neglect the

Georges Bank and other offshore regions from this analysis.

The 1st mode accounts for 97% of the total variance and therefore is the dominant mode (**Figure 5.11b**). The 1st mode eigenfunction (EOF1, **Figure 5.11a**) shows a gulf-wide in-phase variation, with stronger bloom taking place in the coastal western GOM. The temporal evolution function (PC1) indicates that the major variability is the seasonal cycle of bloom, which initiates in early March, gradually increases to its peak va

lue in late May, and monotonically decays afterward. Such an evolution initially mimics the increases of both net growth rate and germination flux. Then the net growth starts a dramatic decrease after June, which subsequently triggers the decrease of cell concentration. As earlier studies have shown, changes in net growth rate are related to the nutrient limited growth (*McGillicuddy et al.*, 2005) and large mortality which increases with warming of ambient water temperature (*He et al.*, 2008; *Li et al.*, 2009). The 2nd mode (**Figure 5.11c**) accounts for 1.5% of the total variance (**Figure 5.11d**). This mode shows a bimodal pattern sitting between the Mass Bay and its downstream area along with offshore area near Jordan Basin, and a broad region containing coastal EGOM and part of WGOM near Cape Ann, such that when there is bloom increase tendency in the coastal EGOM and a small portion of coastal WGOM, there is a corresponding bloom decrease tendency in downstream and offshore, and vice versa. The temporal evolution function (PC2) initiates from zero, encounters a sharp increase to become negative in the first four days, and then started to

increase monotonically. The value becomes persistently positive from middle April to late June, with its peak occurring in June. From July to August, time series becomes increasingly negative. The time series suggest that the spatial pattern shifts from a positive phase from development stage (April-late June), to a negative phase (July-August). This is coincident with the seasonal shift of the center of the bloom from western GOM to the coastal EGOM, as previously suggested by *McGillicuddy et al.*(2005). The dynamical factors accounting for the seasonal transition include nutrient-depletion later in the bloom season in the WGOM (*McGillicuddy et al.*, 2005) and the increased mortality rate in the WGOM later in the bloom season (*Li et al.*, 2009). In addition, the the cell advection flux may be responsible for sub-regional cell abundance as well.

In total the first two EOF modes accounts for 99% of bloom variance and can therefore explains most variability of upper layer (50-m) bloom field.

5.5. Summaries

The evolution of the 2008 *A. fundyense* bloom was studied using both *in-situ* observations and a coupled biophysical model simulations. Direct model-data comparisons indicated that the ROMS based circulation module reasonably well reproduced the general features of coastal circulation and hydrography (current velocity, temperature and salinity), and the *A. fundyense* population dynamics module generally captured the temporal evolution and spatial distribution of bloom throughout the bloom season.

Calculations of cell fluxes showed the bloom condition in the upstream and offshore waters have significant impact on the cell concentration in the downstream WGOM region. Except at N2, cell fluxes at all other 4 cross-shelf transects and 4 offshore transect examined in this study have significantly larger standard deviation (STD, **Table 5.1**) than their respective means. We can trace the root of such variability to the changing coastal currents which are driven by both local forcing (wind, heat flux, tides, river runoff) and remote boundary forcing, and complex cell reproduction processes such as cyst germination, cell growth, and mortality which all vary in response to different ambient environment conditions (temperature, salinity, nutrient and light). EOF analysis showed the 1st mode accounts for 97% of total variance, and the temporal evolution is closely linked with cell net growth rate and germination flux. The 2nd mode accounts for 1.4% of total variance. The temporal evolution function (PC2) well represents the seasonal shift of the center of bloom from WGOM to the upstream EGOM coastal region, as suggested by *McGillicuddy et al. (2005)*. The seasonal shift is subject to the environmental conditions such as nutrient availability (e.g., *McGillicuddy et al., 2005*) and increased mortality in the WGOM later in the bloom season (*Li et al., 2009*).

While the coupled modeling system captured the seasonal evolution of coastal hydrography and spatial distributions of bloom reasonably well, refinements in several modeling details may allow for some future improvement in model's prediction skill. For

instance, the cyst abundance was assumed unvaried during the bloom season, a dynamic cyst prediction considering bottom currents, tides and wave conditions may provide time-dependent cyst distribution and germination fluxes. The model used a new monthly nutrient climatology developed University of Maine based on objective analysis of all available nutrient data. As such, interannual variability in water mass and nutrient conditions (Townsend *et al.*, 2005; Garside *et al.*, 1996; Anderson *et al.*, 2008; McGillicuddy *et al.*, 2011) and its impact on *A. fundyense* bloom are not accounted for. Deterministic predictions of these aspects will clearly require advanced observational infrastructure together with sophisticated techniques for data assimilation.

Acknowledgements

We are very grateful for the outstanding efforts of the officers, crews, and shore support of *R/V Oceanus*, *R/V Endeavor*, and *R/V Tioga*, as well as the hard work of all those who participated in the seagoing science teams. S. Libby, M. Mickelson, and others associated with the Massachusetts Water Resources Authority monitoring program for Massachusetts Bay provided many valuable observations and helpful discussions. We thank Dr. David Townsend for providing the Gulf of Maine nutrient climatology used in the simulations. Thanks also to NOAA NCEP, USGS, and GoMOOS/NERACOOS for providing buoy observations online. Research support was provided by National Oceanic and Atmospheric

Administration grant NA06NOS4780245 for the Gulf of Maine Toxicity (GOMTOX) program. This is ECOHAB contribution number XXX.

References

- Anderson, D.M. (1997). Bloom dynamics of toxic Alexandrium species in the northeastern US. *Limnology and Oceanography*, 42, 1009-1022.
- Anderson D.M., Keafer, B.A., McGillicuddy, D.J., Mickelson, M.J., Keay, K.E., Libby, P.S., Manning, J.P., Mayo, C.A., Wittaker, D.K., Hickey, J. M., He, R., Lynch, D.R., Smith, K.W. (2005a). Initial observation of the 2005 Alexandrium fundyense bloom in the southern New England: general patterns and mechanisms. *Deep Sea Research II*, 52, 2856-2876.
- Anderson, D. M., Kulis, D. M, Keafer, B. A., Gribble, K.E., Marin, R., Scholin, C. A., (2005b). Identification and enumeration of Alexandrium spp. From the Gulf of Maine using molecular probes. *Deep Sea Research II*, 52 (19-21), 2467-2490.
- Anderson, D.M., C.A. Stock, B.A. Keafer, A. Bronzino Nelson, B. Thompson, D.J. McGillicuddy, M. Keller, P.A. Matrai, and J. Martin (2005c). *Alexandrium fundyense* cyst dynamics in the Gulf of Maine. *Deep Sea Research II* 52(19-21): 2522-2542.
- Anderson, D.M., J.M. Burkholder, W.P. Cochlan, P.M. Glibert, C.J. Gobler, C.A. Heil, R.M. Kudela, M.L. Parsons, J.E. Rensel, D.W. Townsend, V.L. Trainer, and G.A. Vargo (2008). Harmful algal blooms and eutrophication: Examining linkages from selected coastal regions of the United States, *Harmful Algae*, 8: 39-53.
- Bigelow, H.B. (1927). Physical Oceanography of the Gulf of Maine. *Fisheries Bulletin*, 40, 511- 1027.
- Flather, R. A. (1976). A tidal model of the northwest European continental shelf. *Mem. Soc. Roy. Sci. Liege*, Ser. 6, 10, 141-164.
- Franks, P.J.S., Anderson, D.M. (1992). Alongshore transport of a phytoplankton bloom in a buoyancy current: Alexandrium tamarensis in the Gulf of Maine. *Marine Biology*, 112, 153 - 164.
- Fennel, K., J. Wilkin, J. Levin, J. Moisan, J. O'Reilly, and D. Haidvogel (2006), Nitrogen cycling in the Middle Atlantic Bight: Results from a three-dimensional model and implications for the North Atlantic nitrogen budget, *Global Biogeochem. Cycles*, 20, GB3007, doi:10.1029/2005GB002456.
- Garside, C., J. C., Keller, M. D., Sieracki, M.E. (1996). The formation of high nutrient low salinity water in the Gulf of Maine: a nutrient trap? *Estuarine Coastal and Shelf Science*, 42 (5), 617-628.
- He, R., Weisberg, R.H. (2003). West Florida shelf circulation and temperature budget for the

1998 fall transition. *Continental Shelf Research*, 23, 777-800.

He, R., McGillicuddy, D.J., Lynch, D.R., Smith, K.W., Stock, C.A., Manning, J.P. (2005), Data assimilative hindcast of the Gulf of Maine coastal circulation. *Journal of Geophysical Research*, 110, C10011, doi:10.1029/2004JC002807.

He, R., D. J. McGillicuddy, D. R. Lynch, K.W. Smith, C.A. Stock, and J. P. Manning (2005). Data assimilative hindcast of the Gulf of Maine coastal circulation. *Journal of Geophysical Research*, 110, C10011, doi: 10.1029/2004JC002807.

He, R. and McGillicuddy D. J., 2008. The historic 2005 Toxic Bloom of Alexandrium fundyense in the west Gulf of Maine- Part 1: In Situ Observations of Coastal Hydrography and Circulation. *Journal of Geophysical Research*, 113, C07039, doi: 10.1029/2007JC004601.

He, R., McGillicuddy D. J., Keafer B.A., Anderson D. M., 2008. Gulf of Maine Harmful Algal Bloom in summer 2005- Part 2: Coupled Bio-physical Numerical Modeling, *Journal of Geophysical Research*, 113, C07040, doi: 10.1029/2007JC004602.

Kamykowski, D., reed, R.E., Kirkpatrick, G.J. (1992). Comparison of the sinking velocity, swimming velocity, rotation and path characteristics among six marine dinoflagellate species. *Marine Biology*, 113(2), 319-328.

Li, Y., He, R., D. McGillicuddy, and D. Anderson, B. Keafer (2009). Investigation of 2006 Alexandrium fundyense Bloom in the Gulf of Maine: In-situ Observations and numerical modeling, *Continental Shelf Research*, 29: 2069-2082.

Li, Y., R. He., and D.J. McGillicuddy (2012), Seasonal and Interannual Variability of the Gulf of Maine Coastal Circulation and Hydrography, *Deep Sea Research II*, in revision.

Lynch, D.R., Naimie C.E., and F.E. Werner (1996). Comprehensive coastal Circulation model with application to the Gulf of Maine, *Continental Shelf Research*, 16, 7, 875-906 (1996).

Lynch, D.R., Holboke M.J., Maimie, C.E. (1997). The Maine coastal current: spring climatological circulation. *Continental Shelf Research*, 17, 605-639.

Loder, J.W., G. Han, C.G. Hannah, D.A. Greeberg, and P.C. Smith (1997). Hydrography and baroclinic circulation in the Scotian Shelf Region: Winter vs. summer, *Can. J. Fish. Aquat. Sci.*, 54 (Suppl.1), 40-56, doi: 10.1139/cjfas-54-S1-40.

Love, R.C., Loder, T.C., Keafer, B.A., (2005). Nutrient conditions during Alexandrium fundyense blooms in the western Gulf of Maine, U.S.A. *Deep Sea Research II*, 52, 2450-2466.

- Keafer B.A., Churchill, J.H., McGillicuddy, D.J., Anderson, D.M (2005). Bloom development and transport of toxic Alexandrium fundyense population within a coastal plume in the Gulf of Maine. *Deep Sea Research II*, 52, 2674-2697.
- Lynch, D.R., Holboke M.J., Maimie, C.E. (1997). The Maine coastal current: spring climatological circulation. *Continental Shelf Research*, 17, 605-639.
- Luetlich, R. A., J, J, Westerink, and N. W. Scheffner (1992). ADCIRC: An advanced three-dimensional circulation model for shelves, coasts and estuaries. *U.S. Army Engineer Waterways Experiment Station*.
- Marchesiello, P., J.C. McWilliams, and A.F. Shchepetkin (2001). Open boundary conditions for long-term integration of regional oceanic models. *Ocean Modelling*, 3, 1-20
- Martin, J.L., F.H. Page, A. Hanke, P.M. Strain and M. M. LeGresley (2005). *Alexandrium fundyense* vertical distribution patterns during 1982, 2001 and 2002 in the Bay of Fundy, Eastern Canada. *Deep-Sea Research II* 52(19-21) 2569-2592.
- Mellor L.G. and T. Yamada (1982). Development of a turbulence closure model for geophysical fluid problems, *Reviews of Geophysics and space physics*, 20-4, 851-875.
- McGillicuddy D.J., Anderson, D.M., Lynch, D.R., Townsend D.W. (2005). Mechanisms regulating large-scale seasonal fluctuations in Alexandrium fundyense populations in the Gulf of Maine: Results from a physical-biological model. *Deep Sea Research II*, 52, 2698-2714.
- McGillicuddy, D.J., Townsend, D.W., He, R., Keafer, B.A., Kleindinst, J.L., Li, Y., Manning, J.P., Mountain, D.G., Thomas, M.A. and D.M. Anderson (2011). Suppression of the 2010 *Alexandrium fundyense* bloom by changes in physical, biological, and chemical properties of the Gulf of Maine. Submitted, *Limnology and Oceanography*.
- Mountain, D.G, and J.P. Manning (1994). Seasonal and interannual variability in the properties of the surface waters of the Gulf of Maine, *Continental Shelf Research*, 14, 1555-1581.
- Pettigrew, N. R., J. H. Churchill, C. D. Janzen, L. J. Mangum, R. P. Signell, A. C. Thomas, D. W. Townsend, J. P. Wallinga, and H. Xue (2005). The kinematic and hydrographic structure of the Gulf of Maine coastal current. *Deep Sea Research*, Part II, 52, 19-21, 2369-2391
- Rebuck, N.D. (2011): Nutrient distributions in the Gulf of Maine: An analysis of spatial and temporal patterns of dissolved inorganic nitrate and silicate. *PhD Dissertation, University of Maine, Orono*.
- Shchepetkin, A.F. and J.C McWilliams (2005). a split-explicit, free-surface, topographic following-coordinate oceanic model. *Ocean Modelling*, 9, 347-404.

Stock, C.A., McGillicuddy D.J., Solow, A.R., Anderson D.A (2005). Evaluating hypothesis for the initiation and development of Alexandrium fundyense blooms in the western Gulf of Maine using a coupled physical-biological model. *Deep Sea Research II*, 52, 2715-2744.

Townsend, D.W., N. R. Pettigrew, and A.C. Thomas (2005). On the nature of Alexandrium fundyense blooms in the Gulf of Maine, *Deep Sea Research II*, 52, 2715-2744.

Xue H., F., Chai, and N.R. Pettigrew (2000). A model study of the seasonal circulation in the Gulf of Maine, *Journal of Physical Oceanography*, 30, 1111-1135.

Chapter 6. Concluding Remarks

In this study, we investigated the seasonal and interannual variability in the GOM. Both observations and coupled bio-physical model were utilized. Observations provide the fundamental basis for understanding the coastal circulation, hydrography, and *A. fundyense* bloom variability, a key to all the following-up modeling works. Our research showed that cyst abundance is the first-order predictor of the overall bloom magnitude. However, anomalous hydrography and nutrient conditions resulting from both local and remote forcing may break up the relationship (e.g., 2010). An early monitoring of the nutrient and circulation conditions can be critical for the next generation *A. fundyense* forecast model.

The mean and interannual variability of the coastal connectivity were quantified based on realistic circulation hindcasts. Results showed that the source and destination strengths are of great value in understanding the relative importance of different oceanic domains in shaping the distribution of *A. fundyense* bloom. For example, the strong toxicity of *A. fundyense* bloom in the coastal EGOM was likely associated with strong destination strengths from the Bay of Fundy release.

The data assimilation improved the model performance in producing the realistic hydrographic conditions, and therefore held great promise for future modeling. One of our next steps is to investigate how the data assimilation is going to change the model skill of *A.*

fundyense. In addition, the mortality function used in the *A. fundyense* model was based on the model misfit of 2005 observations. While it is effective to capture the seasonal demise of the bloom, more research efforts are needed to improve this parameterizations based on more observations collected during 2004-2010.

In my previous M.S. study, the circulation and hydrographic conditions in 2006 was investigated, focusing on the evolution of the gulf-wide bloom. Results show that nutrient-limited growth constrains the overall growth term throughout the bloom period. In this dissertation study, the 2008 *A. fundyense* bloom is elucidated using the coupled biophysical model. Results show how the cyst germination is affected by bottom temperature and endogenous clock. The cell flux from eastern to western GOM is the highest in May, a finding that is important for the coastal management in the western GOM.

To sum up, we gained a more systematic understanding of coastal circulation and *A. fundyense* bloom dynamics through integrated analysis of observations and numerical modeling. Admittedly, we benefited from previous researches that set up the basis before any further investigation conducted here is achieved. The research also provides a benchmark for research, design and the operational nowcast-forecast system for the GOM, thereby the ongoing project for the prevention, control and mitigation (PCM) of *A. fundyense* bloom.

Table 2.1. Geostrophic transports in 2005, 2006, 2007 and 2010. Each value is obtained by integrating the alongshelf geostrophic velocity over the upper 5-20m along a transect off the Casco Bay (see blue line in Figure1).

Cruise period	May 2005	Jun 2006	May 2007	Jun 2007	May1-10 2010	May27-Jun3 2010	Jun30-Jul8 2010	Jul28-Aug7 2010
Alongshore transport(10^{-2} Sv)	3.55	4.56	2.92	1.01	1.39	1.30	2.73	2.94

Table 5.1. Monthly-mean and standard deviation (STD) of the integrated cell advection flux along various transects. The integrated cell advection flux was defined as $\int_0^x \int_{-H}^0 uc dx dz$, where x is the distance from initial station, and z the water depth. The flux is integrated from onshore to offshore and from 50m to surface. For cross-shelf transect, the cell flux is positive northeastward; While for the alongshore transect (e.g., D1D2), the cell flux is positive shoreward, and vice versa. Transect and station locations are shown in Figure 1. Units for the cell flux: $\text{cells}\cdot\text{s}^{-1}$.

Transect / Stages	April	May	June	July	Mean (STD)
D1	-0.39	-17.75	-2.20	-0.15	-4.14 (10.56)
D2	-3.72	-8.31	-3.67	-1.09	-3.41 (4.43)
D3	-2.53	-3.32	-3.97	-1.31	-2.33 (2.32)
N1	-0.79	-1.79	-2.21	-2.45	-1.64 (1.10)
N2	-0.45	-0.84	-1.34	-1.46	-0.95 (0.59)
D1D2	0.36	0.70	0.12	-0.04	0.23 (2.32)
D2D3	-0.87	-2.25	-1.14	-0.11	-0.88 (1.94)
D3N1	-0.06	-0.87	-0.50	-0.10	-0.32 (1.17)
D1N2	-0.11	-0.37	0.18	0.03	-0.06 (0.34)

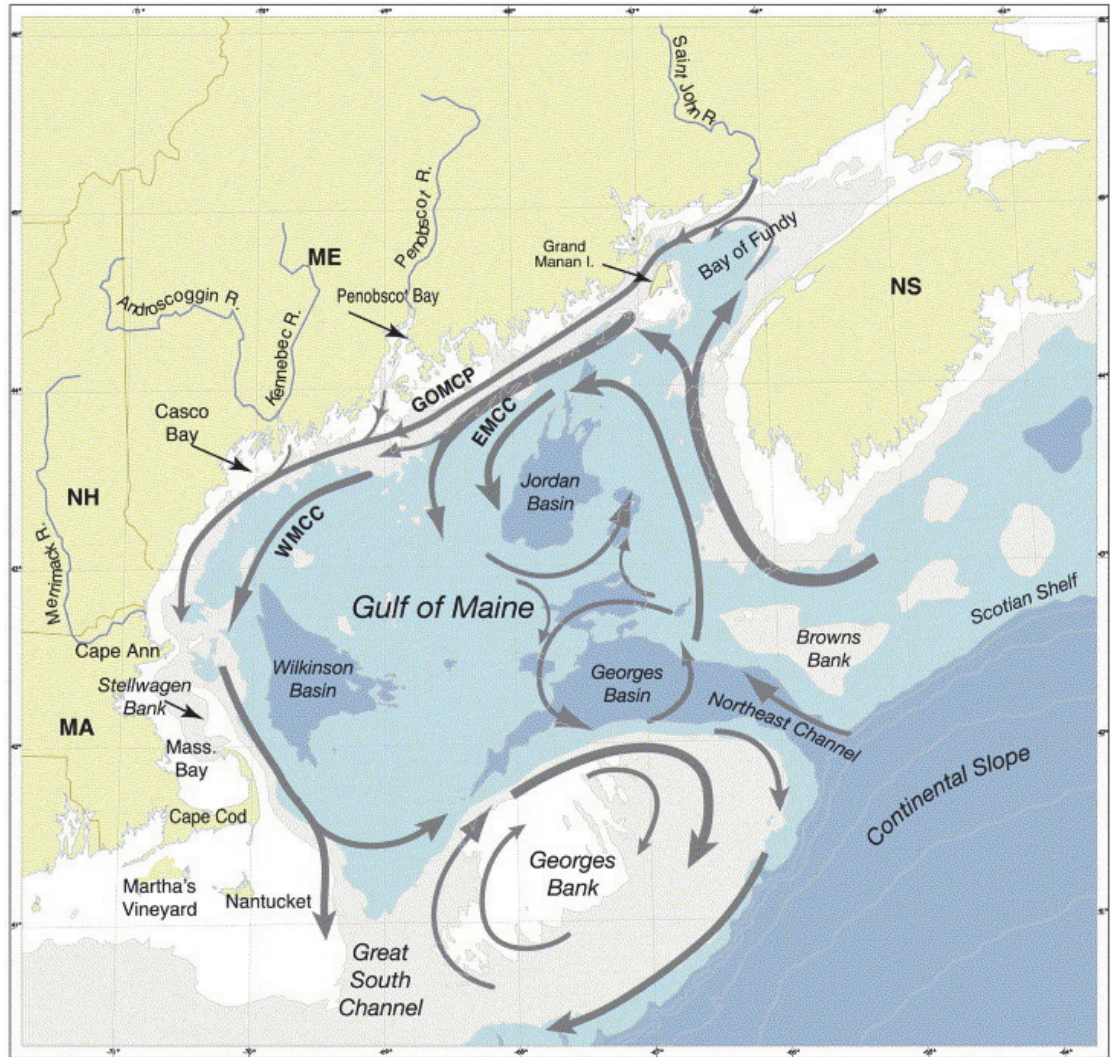


Figure 1.1. Schematic showing the summer near-surface circulation in the GOM. Several branches are present, namely the WMCC, EMCC, as well as the nearshore Gulf of Maine Coastal Plume (GOMCP). Figure from Pettigrew et al., 2005.

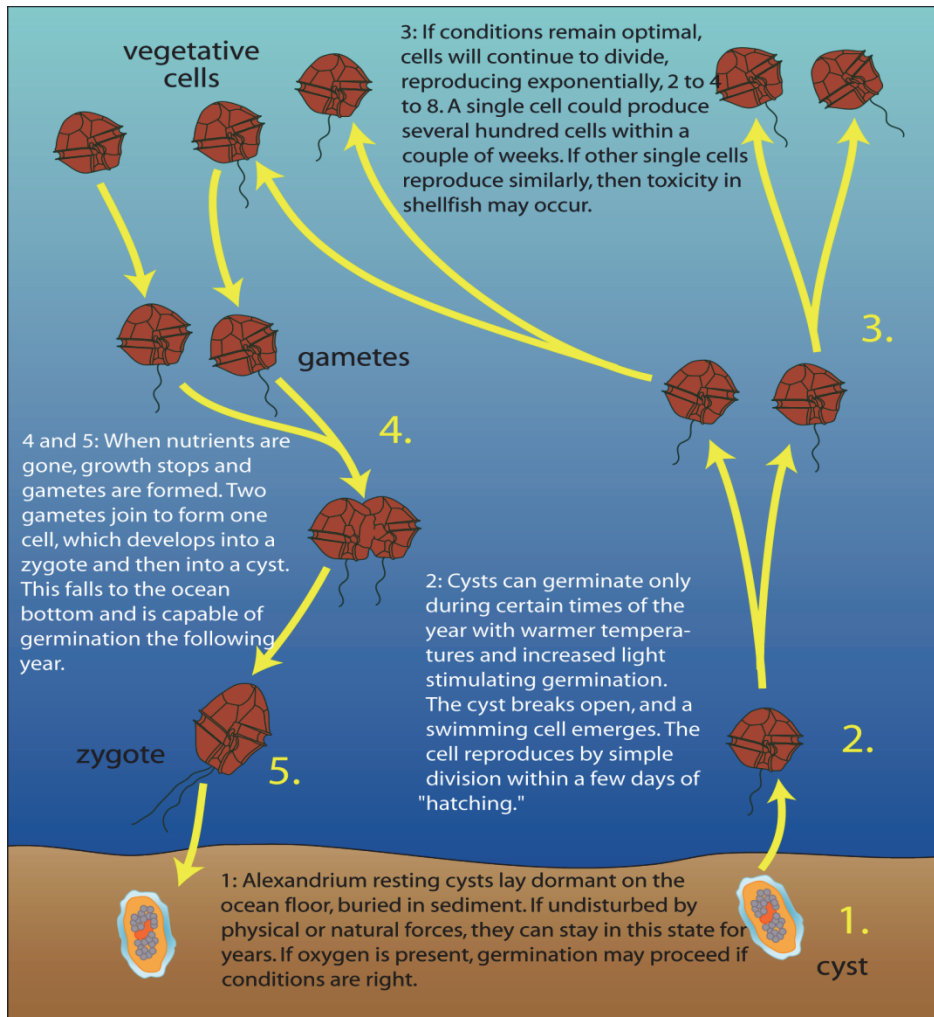


Figure 1.2. A cartoon showing the life cycle of *A. fundyense* bloom. Courtesy of Donald Anderson, Woods Hole Oceanographic Institution.

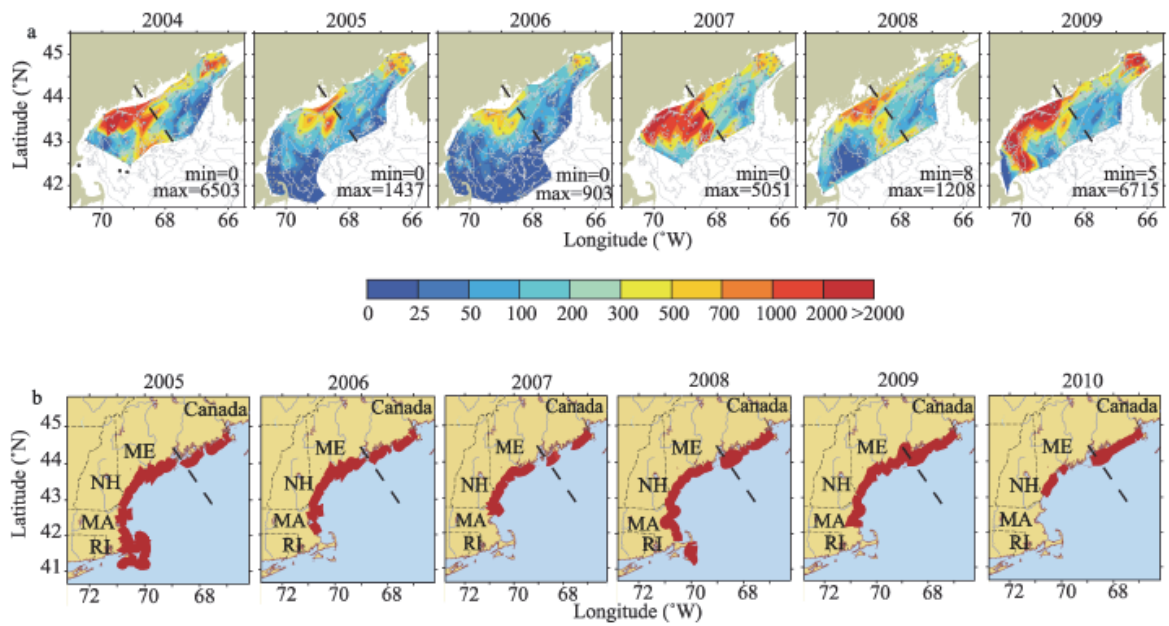


Figure 1.3. (a) Cyst abundance 2004–2009. Minimum and maximum values are indicated in each panel. Open circles denote the locations of sediment samples used to construct the maps. (b) Spatial extent of PSP closures 2005–2010. Figure from *McGillicuddy et al.*, 2011.

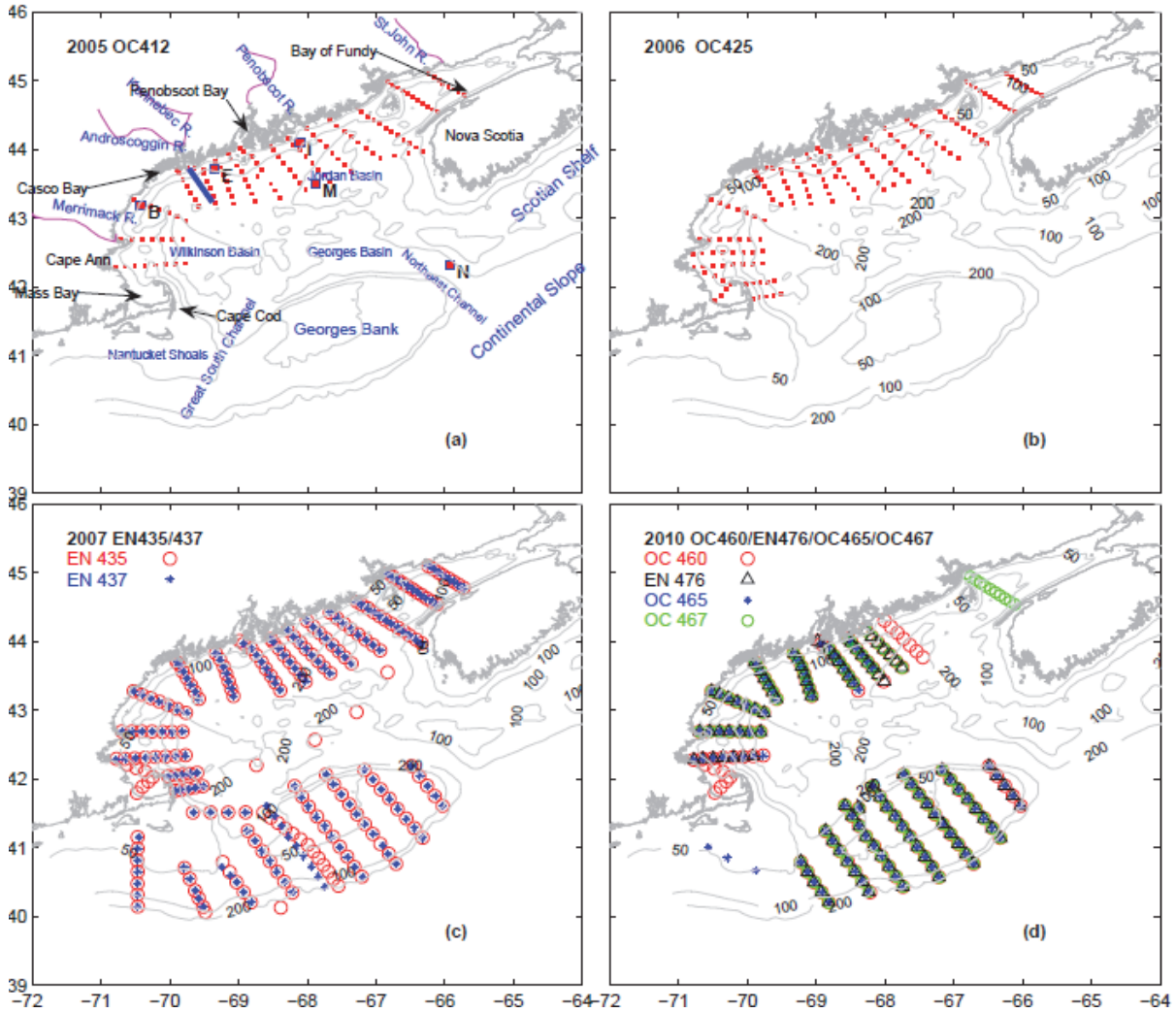


Figure 2.1. Locations of the NERACOOS buoys (pink squares) and CTD stations (red dots) of gulf-wide ship surveys (a) *Oceanus* 412 in 2005, (b) *Oceanus* 425 in 2006, (c) *Endeavor* 435/437 in 2007 and *Oceanus* (d) 460/465/467 and *Endeavor* 476 in 2010, respectively. Also shown are 50-m, 100-m and 200-m isobaths. The blue solid line indicates the transect off Casco Bay that is used for computing geostrophic current transport shown in Table 1.

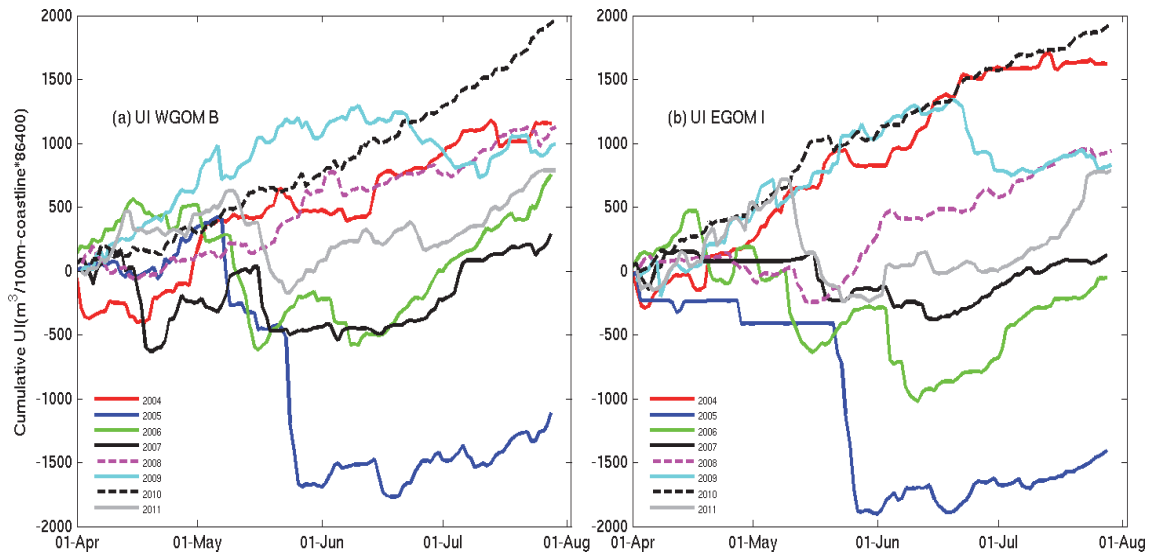


Figure 2.2. Cumulative upwelling indices (CUI) for 2004-2011 at (a) WGOM buoy B and (b) EGOM buoy I. The unit for the indices is $\text{m}^3 \times (100\text{m})^{-1} \times 86400$.

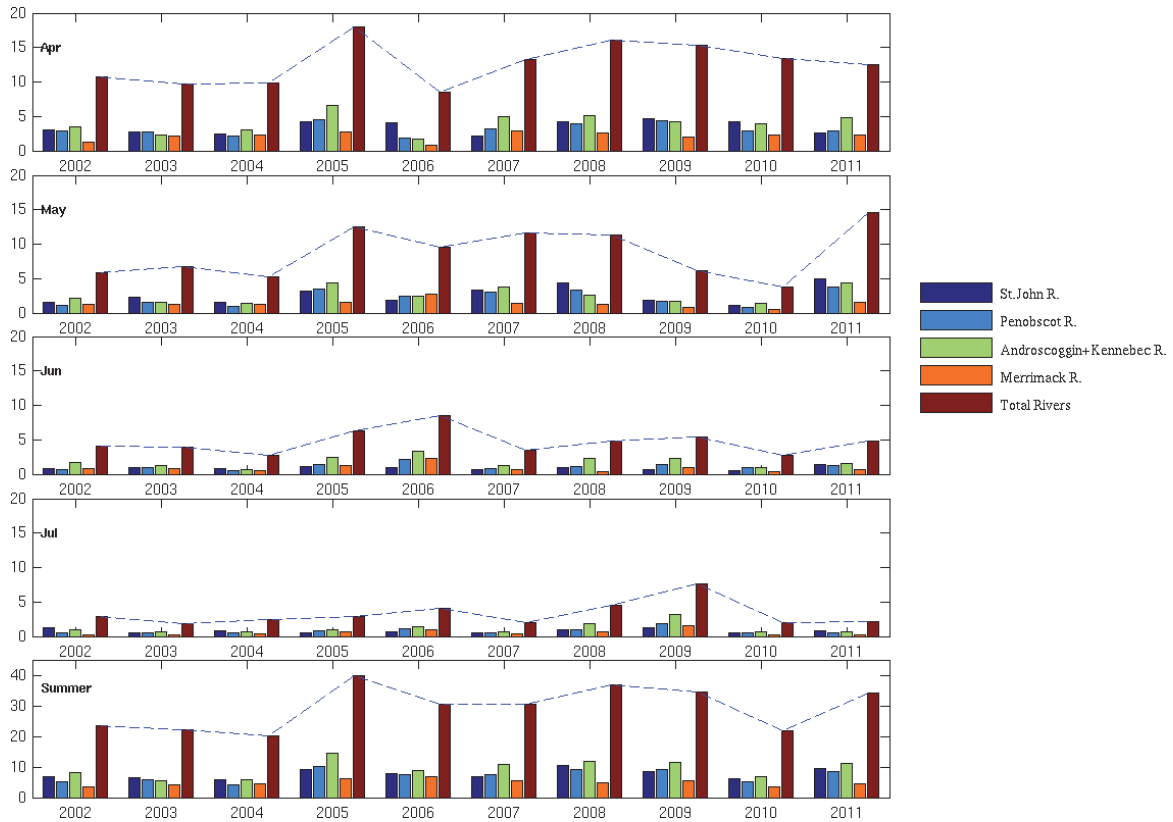


Figure 2.3. Monthly (April-July) and seasonal total river runoff of 4 major rivers (Canadian portion of the St. John, Penobscot, Androscoggin and Kennebec, and Merrimack) in the GOM. Units: $10^4 \text{ m}^3 \text{ s}^{-1}$.

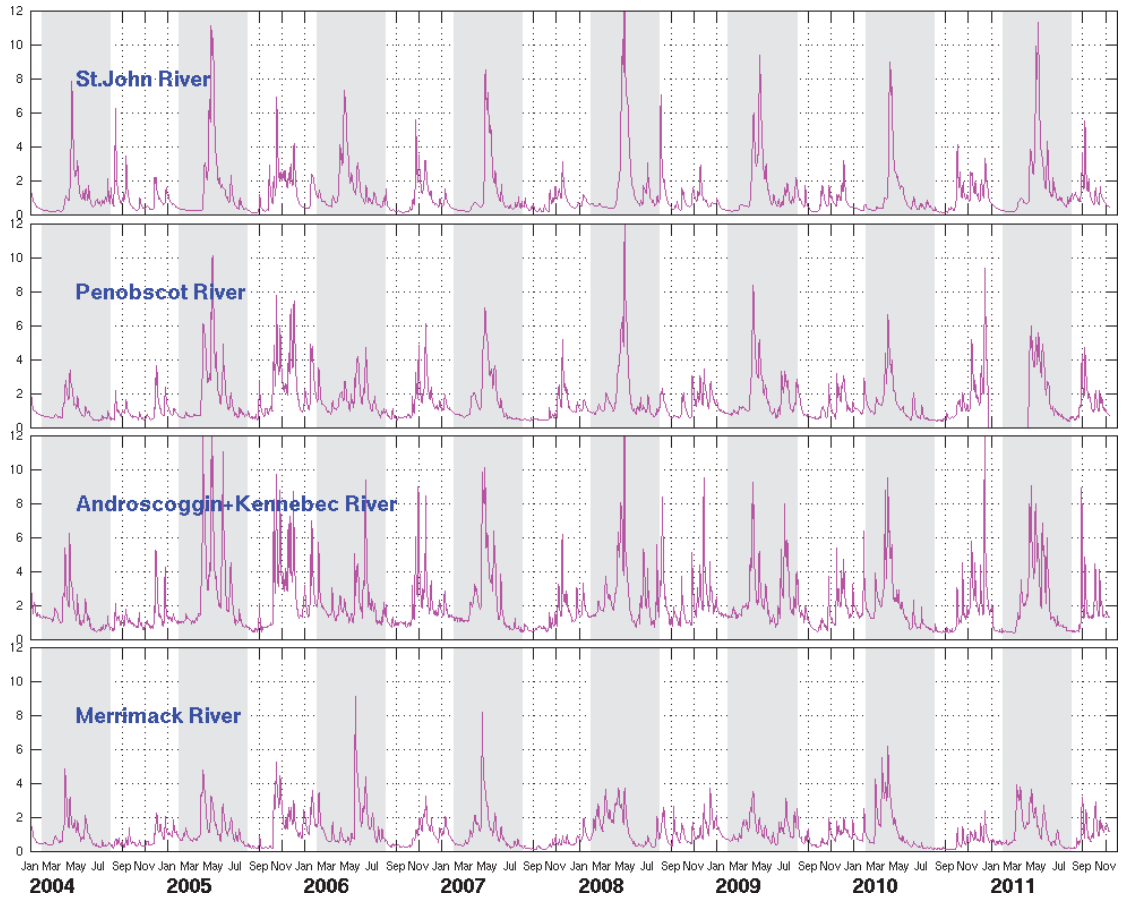


Figure 2.4. Daily river discharge time series for the St. John (U.S. portion), Penobscot, Androscoggin and Kennebec, and Merrimack rivers. Grey shaded areas indicate the summer months (February to August) of each year. Units: $10^4 \text{ m}^3 \text{ s}^{-1}$.

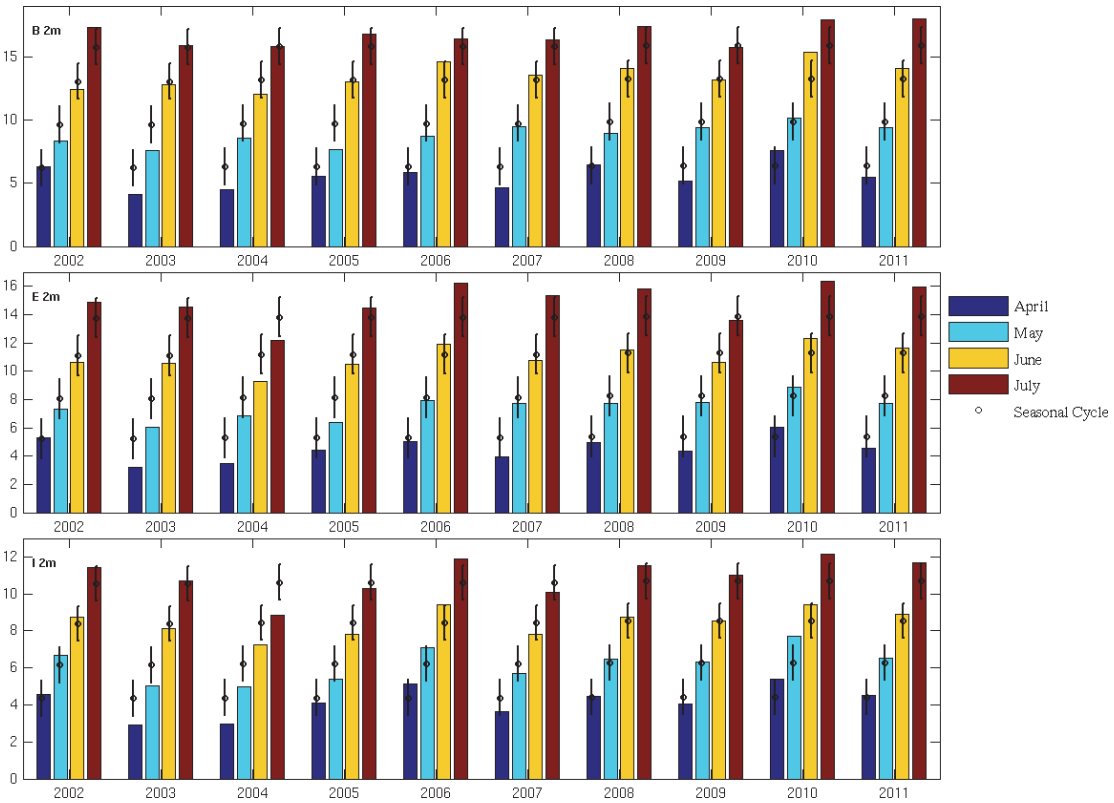


Figure 2.5. Monthly mean near-surface (2-m) water temperature in April-July 2002-2011 observed at NERACOOS buoys B, E, I. Also shown by black open circles and corresponding error bars are the mean seasonal cycle and the associated standard deviations. Unit: °C.

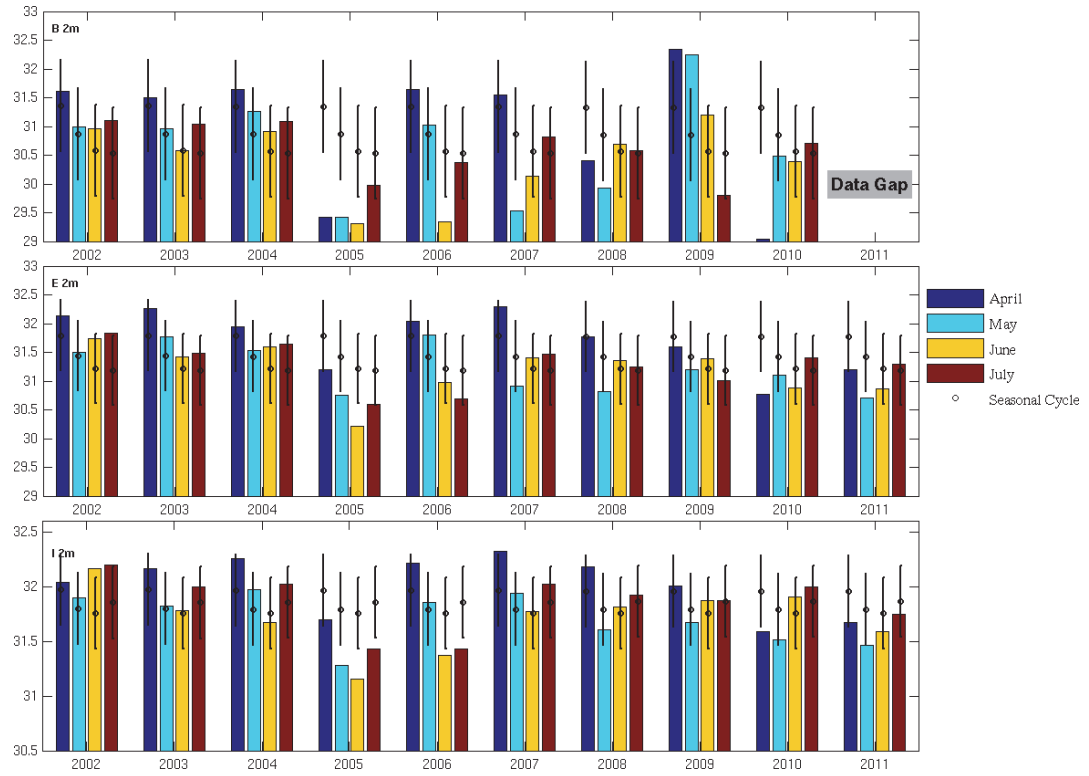


Figure 2.6. Same as Figure 5, but for near-surface salinity.

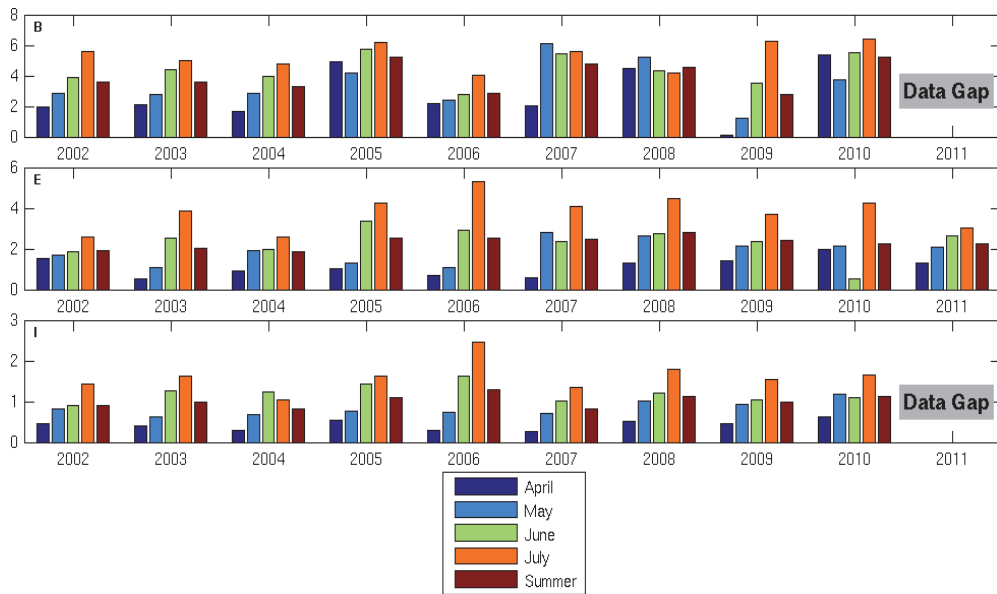


Figure 2.7. Same as Figure 5 and Figure 6, but for the Vaisala frequency (N^2) based on density at 2-m and 50-m. Unit: $S^{-2} \cdot 10^{-4}$.

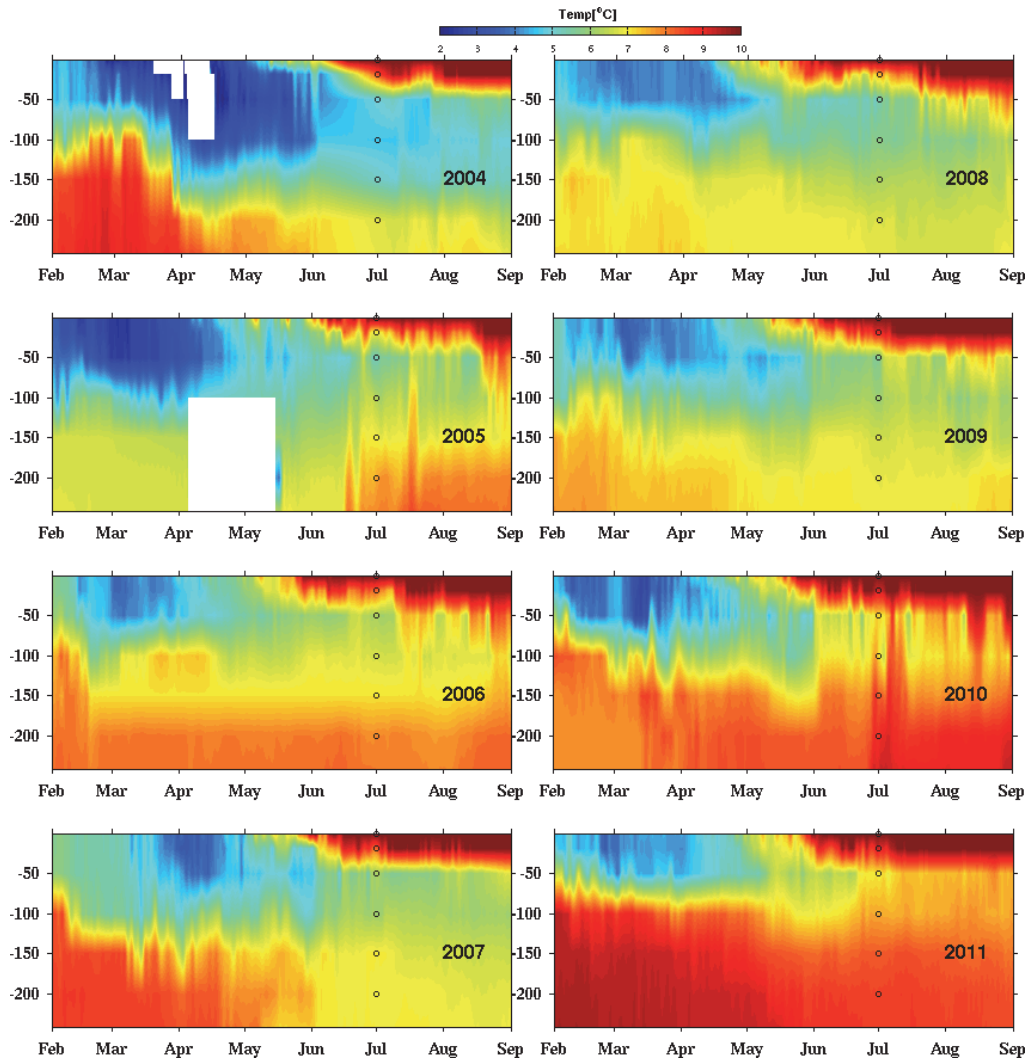


Figure 2.8. Time series of observed temperature at NERACOOS buoy M in Jordan Basin, February-September, 2004-2011. Black circles indicate the depths where observations are available. A 60-hour low-pass filter was applied to the time series to remove high-frequency noise.

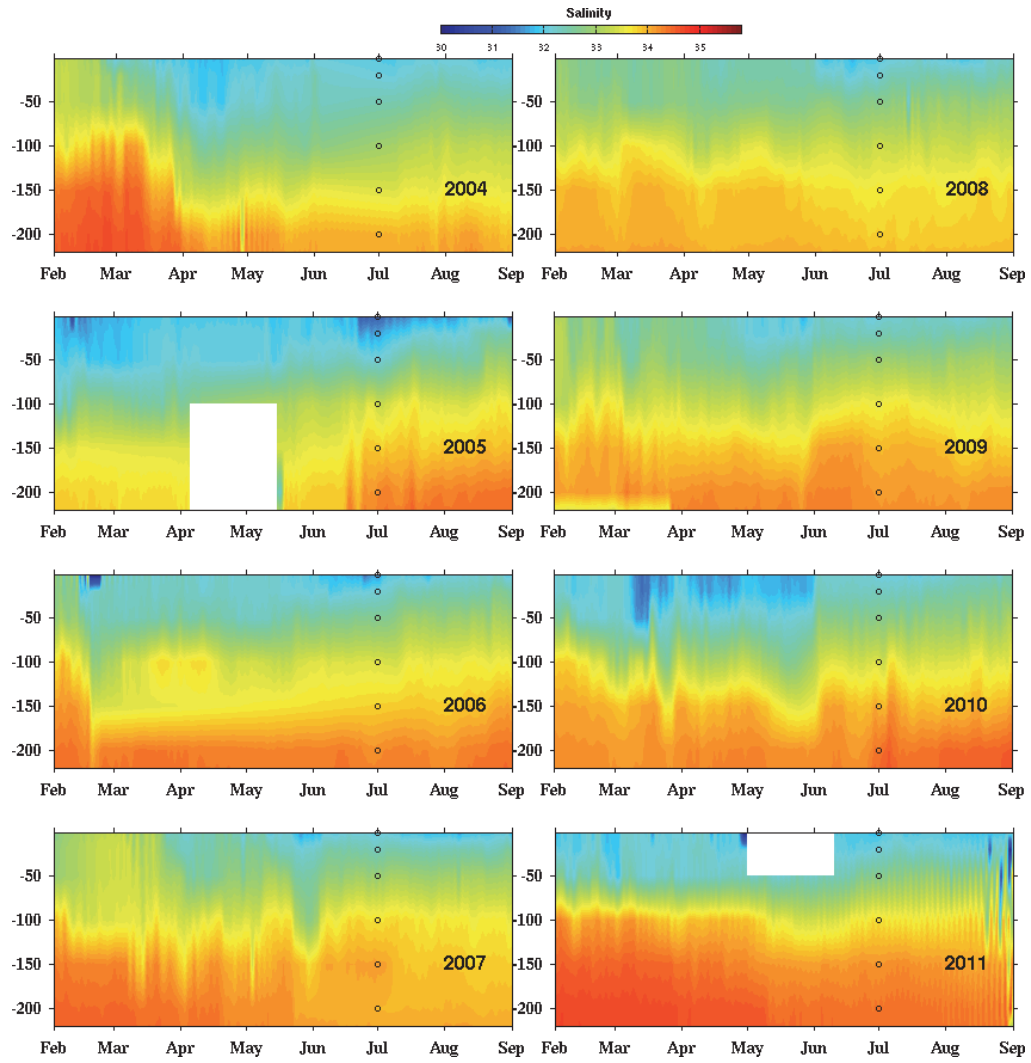


Figure 2.9. Same as Figure 2.8, but for the salinity time series at buoy M.

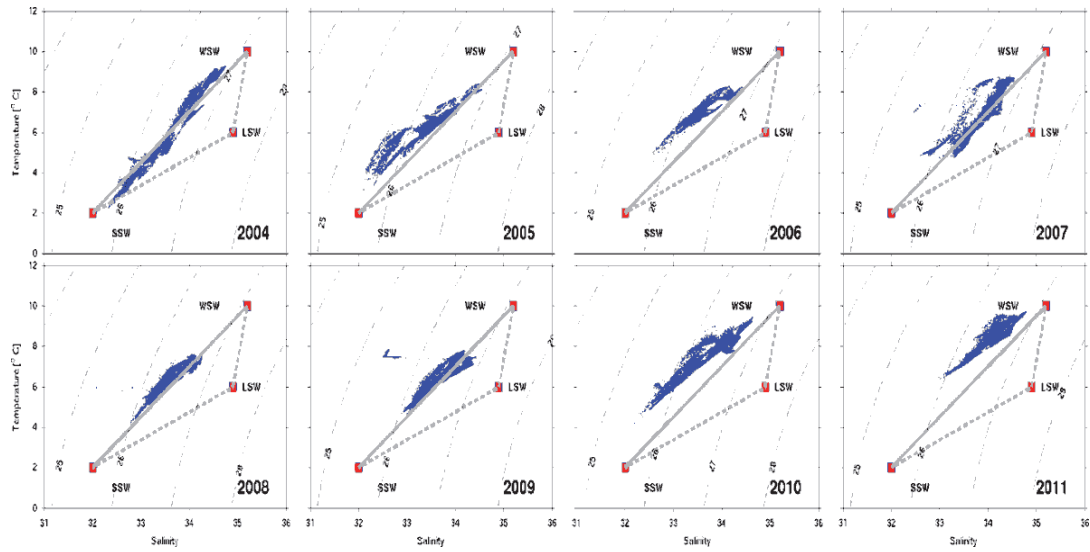


Figure 2.10. T-S diagrams for deep waters (depth>100m) in Jordan Basin. Temperature and salinity data are from buoy M in February-September, 2004-2011. Vertices of the mixing triangle are canonical end-member water-mass properties of Warm Slope Water (WSW), Scotian Shelf Water (SSW), and Labrador Slope Water (LSW) as described by *Smith et al.* (2001). Dotted contour lines represent density anomalies.

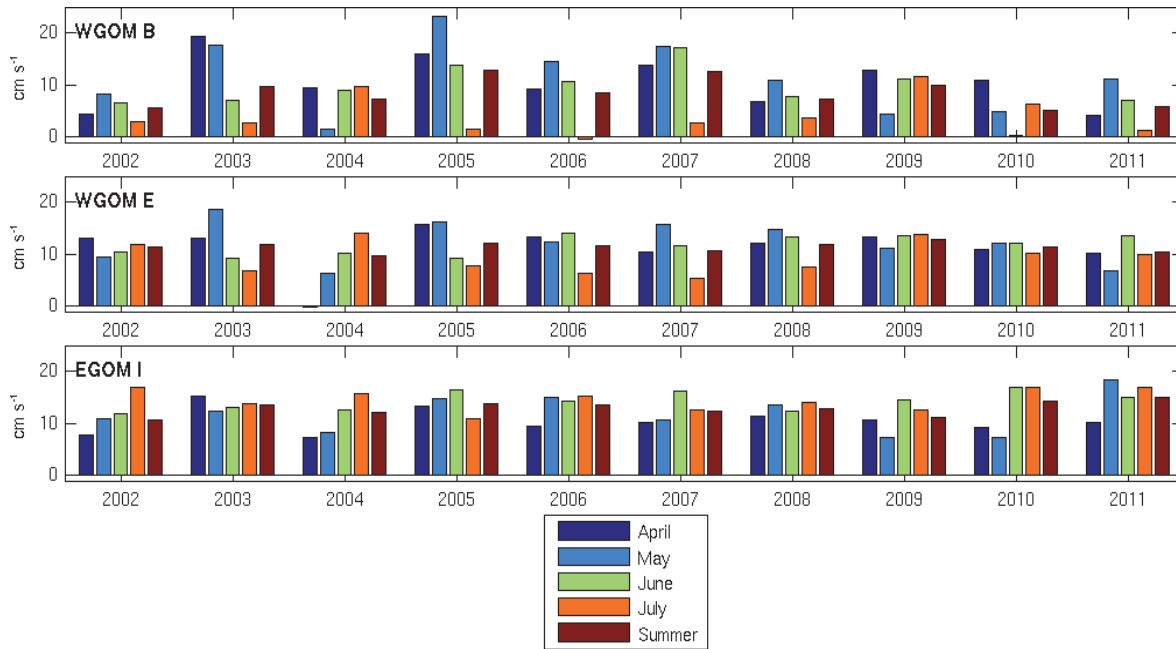


Figure 2.11. Monthly mean alongshore velocity in April-July, 2002-2010 observed at NERACOOS buoys B, E, I. The alongshore current is positive southwestward. Unit: cm s⁻¹.

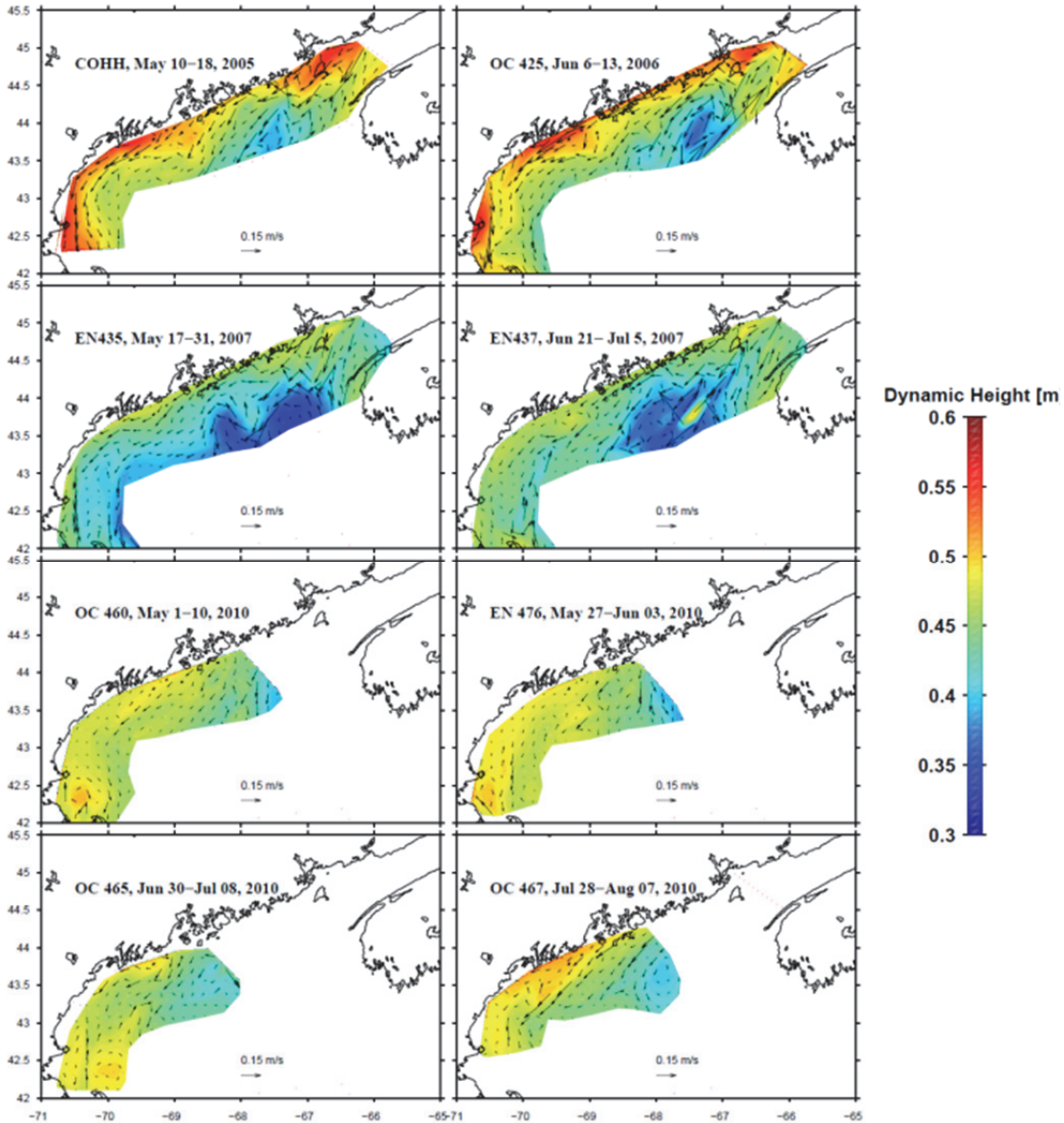


Figure 2.12. Dynamic height (in meters) and associated surface geostrophic velocity based on hydrographic data collected in May 2005, June 2006, June 2007, May 1–10, 2010, May 27–June 3, 2010, June 30–July 8, 2010, and July 28–August 7, 2010, respectively. The dynamic height was computed assuming the level of no motion at bottom, integrated from the bottom to the surface.

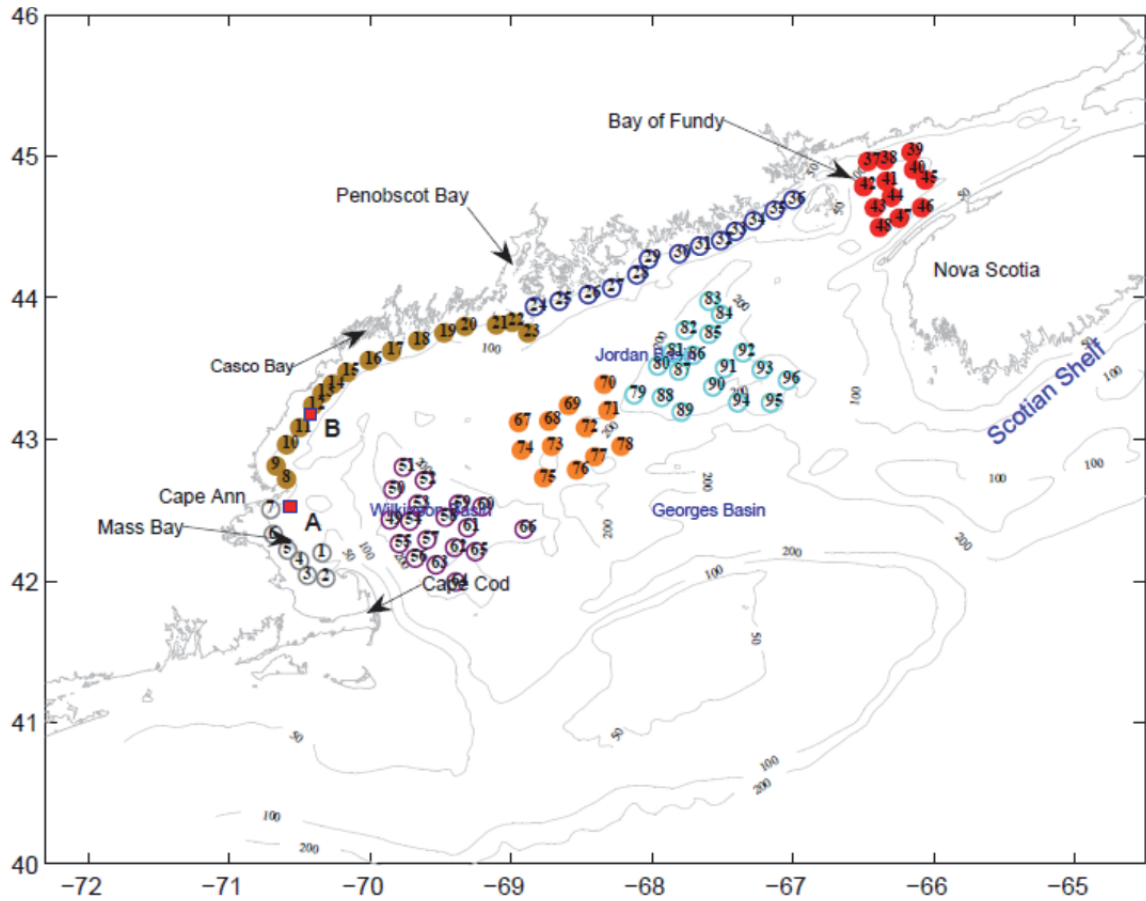


Figure 3.1. Locations of 7 particle release regions in the Gulf of Maine, which include the Massachusetts Bay (Mass, in grey), the western Gulf of Maine (WGOM, in brown) coastal area, the eastern Gulf of Maine release (EGOM, in blue) coastal area, the Bay of Fundy (BOF, in red), the Wilkinson Basin (WK, in purple), the Jordan basin (JB, in orange), and the area Off the Penobscot Bay (OFFPB, in cyan). For each site, the initial release points are chosen based on a 6-km radius circular area. Red rectangular represents the location of NERACOOS buoy A and B. Also shown are the coastal bathymetry contours (50m, 150m, and 200m), and other important geographic sites and locations of five major rivers in the GOM.

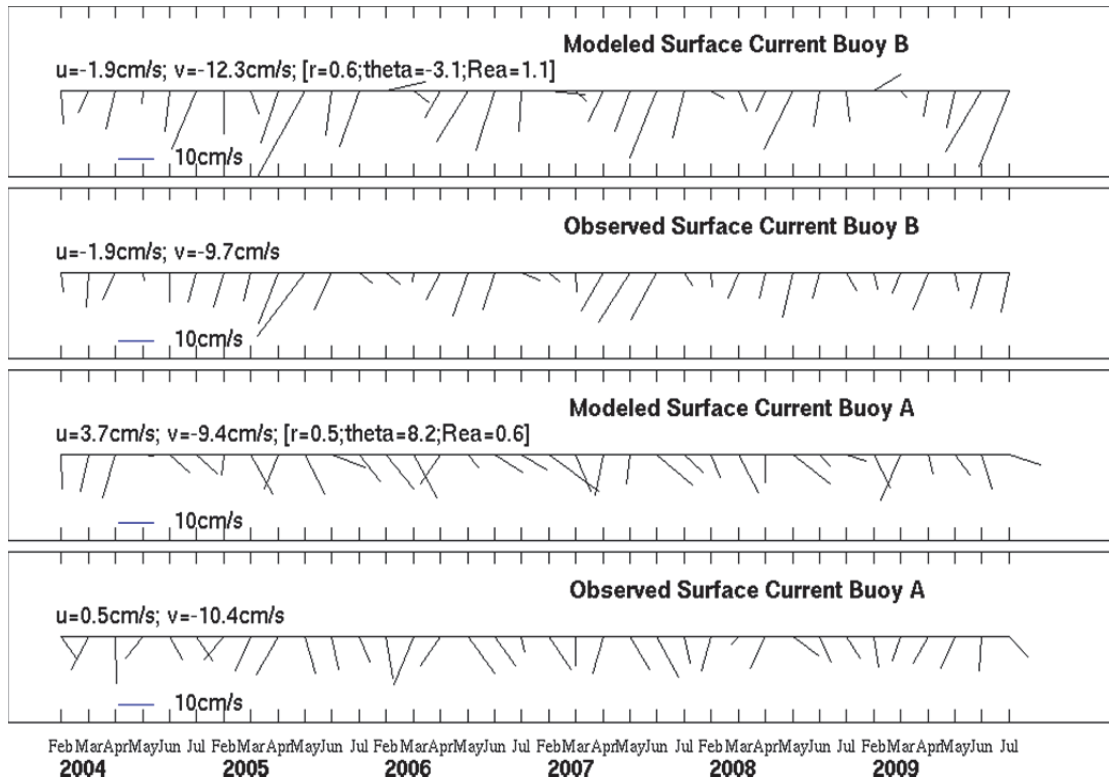


Figure 3.2. Comparisons between model simulated and observed monthly surface currents at buoy B (upper 2 panels) and at buoy A (lower 2 panels). Each vector current time series is accompanied by its mean east and north velocity components (left-hand couplet), and each model/data comparison is quantified by its complex correlation coefficient r , phase angle difference θ (angular deviation of the model vectors from the data vector measured counterclockwise), and amplitude regression slope Rea (right-hand triplet within the bracket).

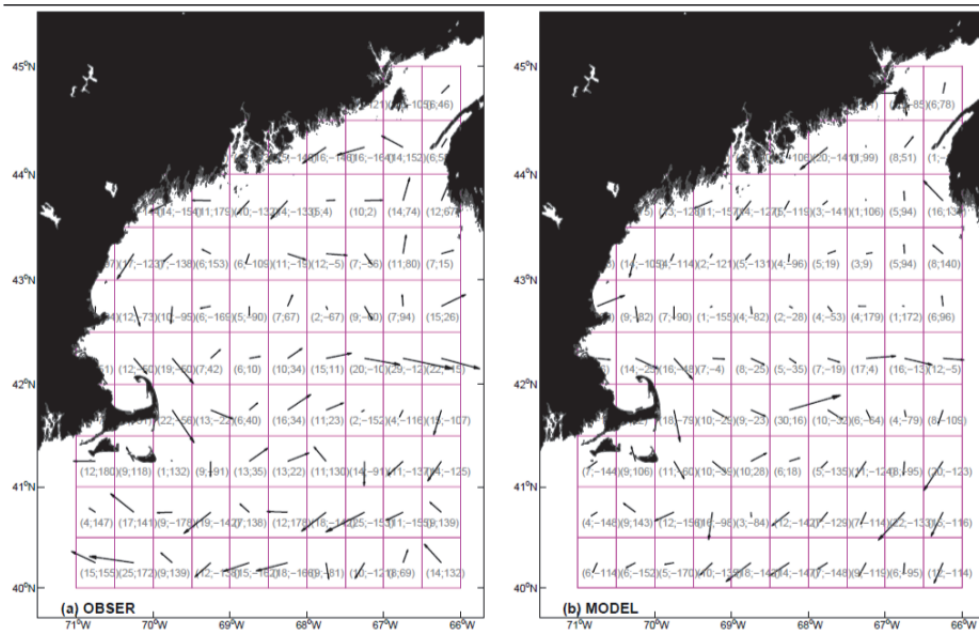


Figure 3.3. Comparisons between observed and simulated mean surface currents in $\text{cm}\cdot\text{s}^{-1}$. The observed surface currents are derived on a $1/2^\circ$ grid from long-term drifter data by *Manning et al. (2009)*, whereas the modeled mean surface currents are derived by temporally averaging of regional model hindcast solutions from 2004 to 2009. Couplet inside each grid box indicates the mean current amplitude and direction.

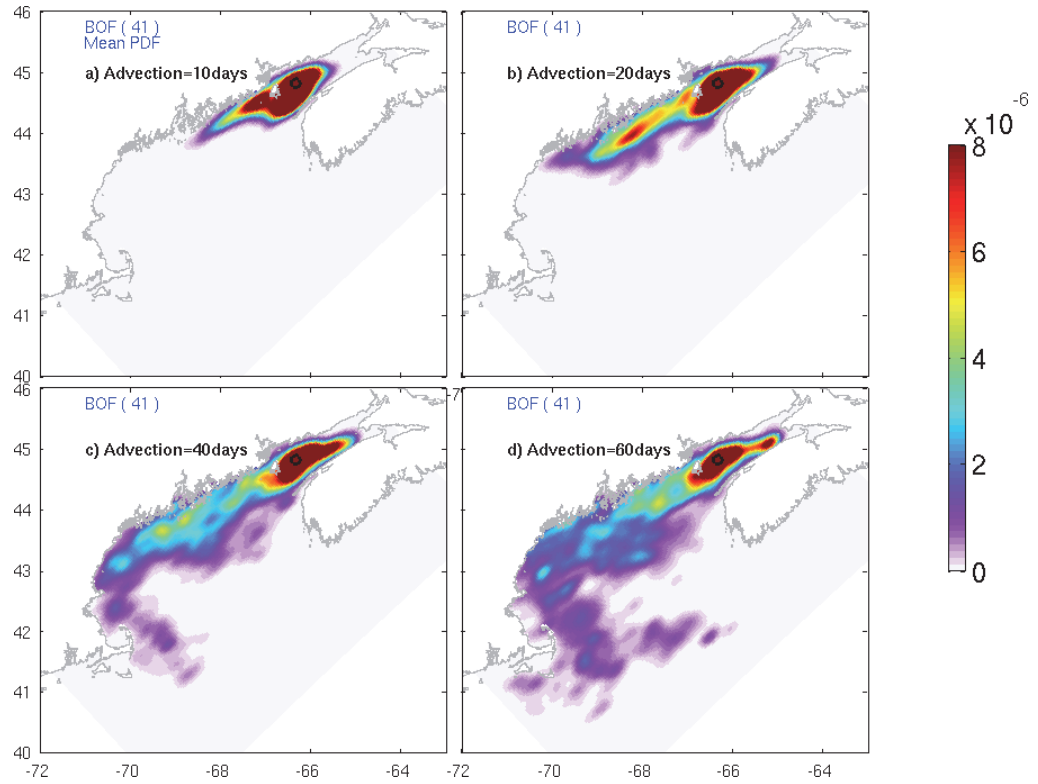


Figure 3.4. Mean Lagrangian probability density functions (LPDFs) (unit: km^{-2}) for a single release site (site 41, as shown in Figure 1) in the BOF based on the tracking with (a) 10-days, (b) 20-days, (c) 40-days, and (d) 60-days as the advection time.

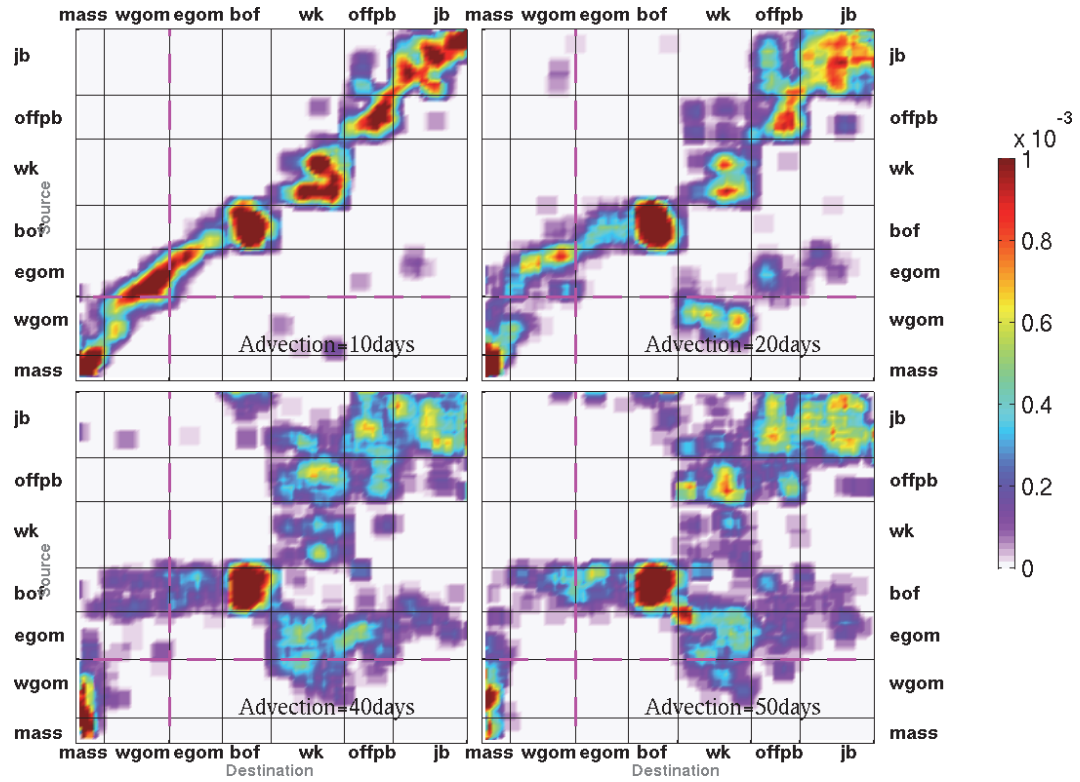


Figure 3.5. Mean Gulf of Maine coastal connectivity matrix based on the particle tracking using a) 10-days, b) 20-days, c) 40-days, and d) 50-days as the advection time scale. Y axis outlines each source locations under study, whereas and X axis outlines each destination locations under study. Both axis runs from site 1 to site 96 as noted in Figure1. The connectivity matrices are normalized so that the summation of mean connectivity over all possible combinations is one. Pink dashed line indicates the borderline between eastern and western GOM sites.

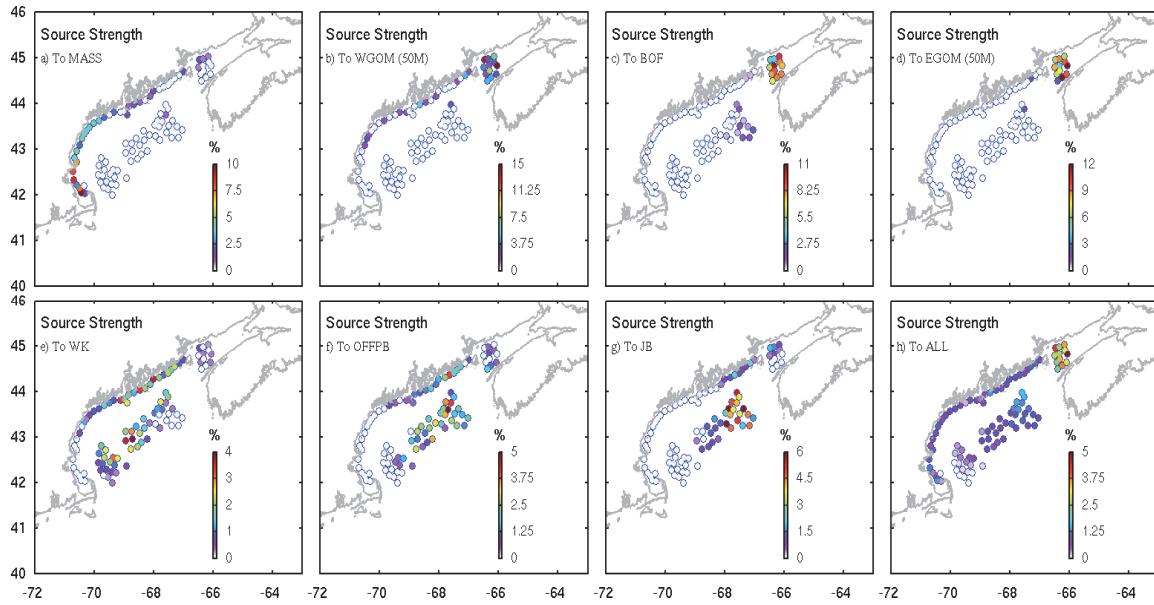


Figure 3.6. The source locations and source strength functions of surface particles that are transported to the (a) MASS, (b) WGOM coastal area, (c)BOF, (d) EGOM coastal area, (e) WK, (f) OFFPB, (g) JB, and (h) all sites in the GOM.

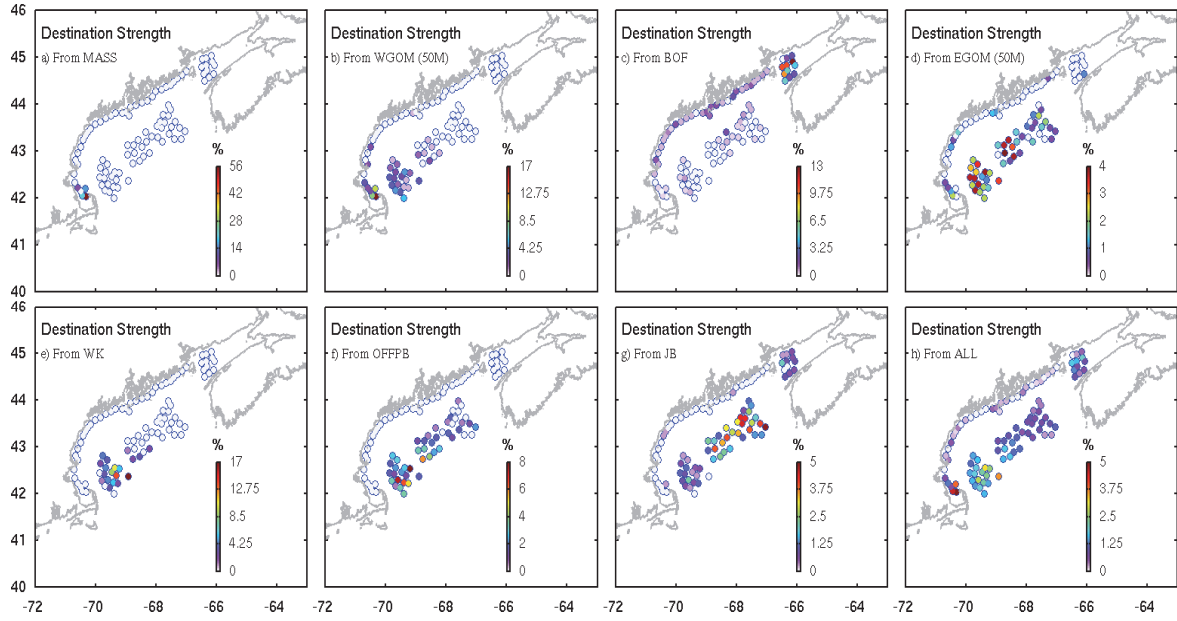


Figure 3.7. The destination locations and destination strength functions of surface particles that are transported from the (a) MASS, (b) WGOM coastal area, (c) BOF, (d) EGOM coastal area, (e) WK, (f) OFFPB, (g) JB, and (h) all sites in the GOM.

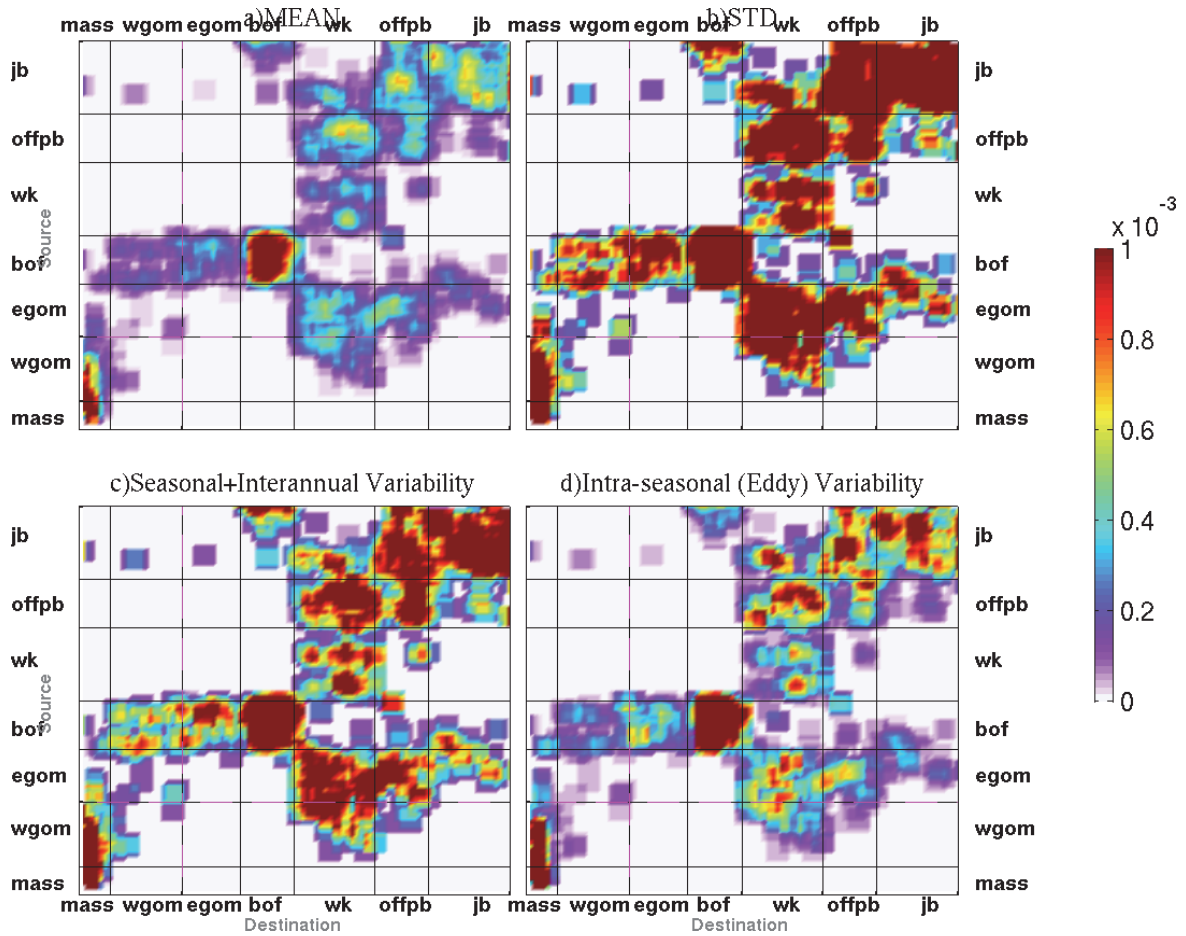


Figure 3.8. (a) Mean, (b) Standard Deviation (STD), (c) low-frequency (seasonal and interannual) variability, and (d) intra-seasonal variability of the GOM connectivity matrix. Notations are same as in Figure 5.

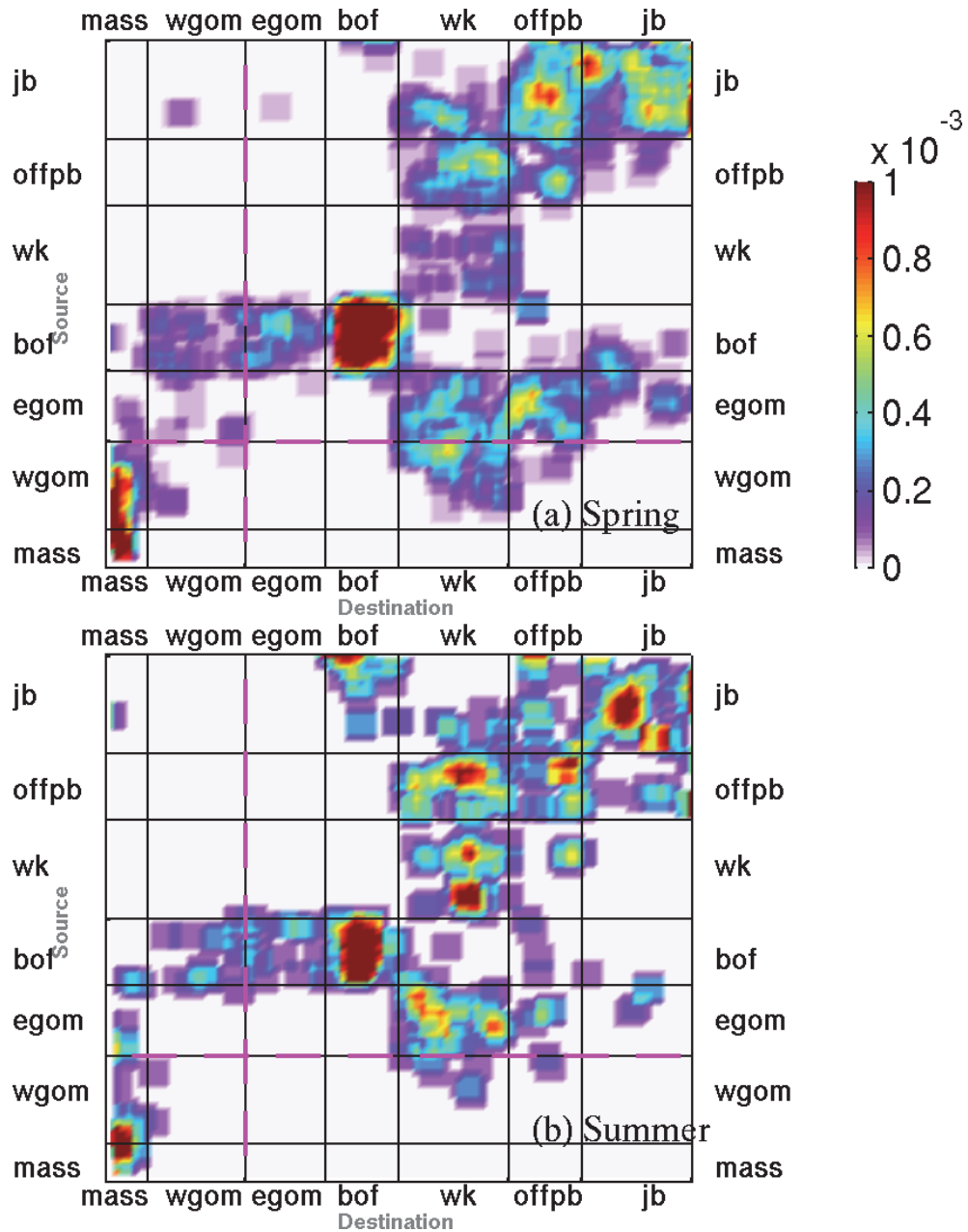


Figure 3.9. (a) Spring (FMA) and (b) Summer (MJJ) mean conditions for the connectivity matrix showing the seasonal variability of the GOM connectivity matrix. Notations are same as in Figure 3.5 and Figure 3.8.

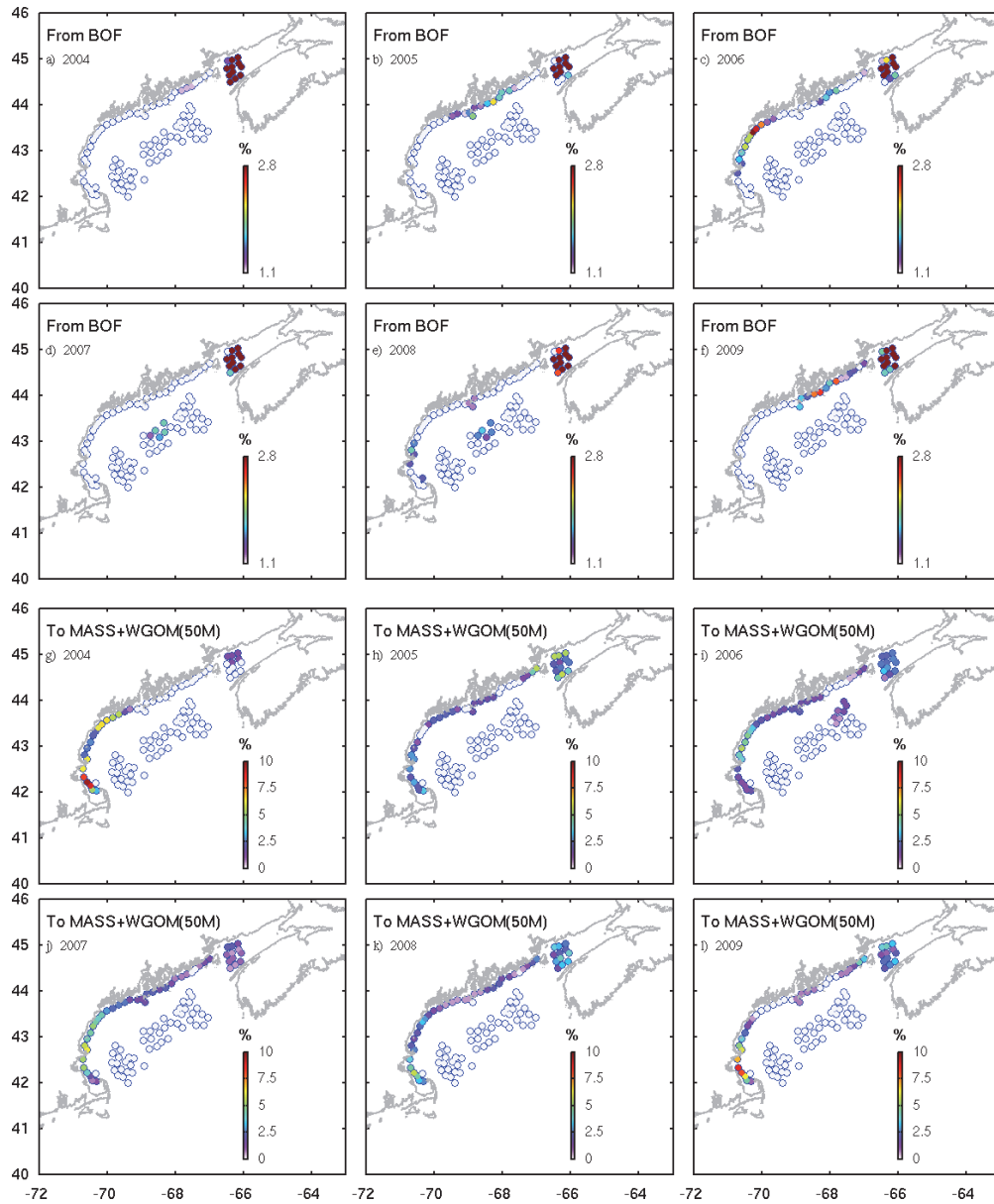


Figure 3.10. The destination locations and strength functions of surface particles that are transported from the BOF in 2004-2009 (a)-(f); and the source location and strength of the surface particles that are transported to the MASS and coastal WGOM in 2004-2009 (g)-(i).

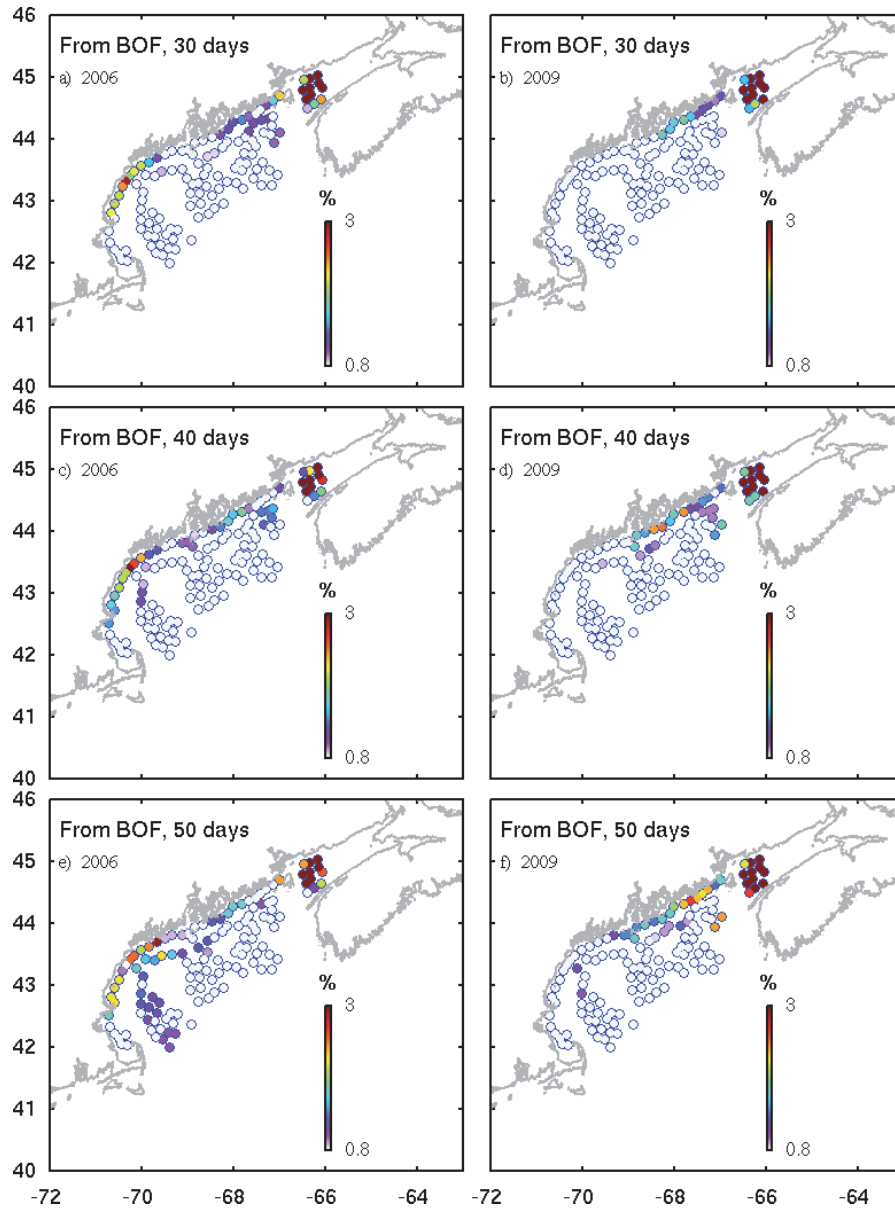


Figure 3.11. Interannual variability of the destination strength functions for particles released in the BOF in 2006 and 2009, respectively. Sensitivities to different advection time scales are examined here. From top to bottom are the results using 30-day (a, b), 40-day (c, d), and 50-day (e, f) as the advection time scale, respectively.

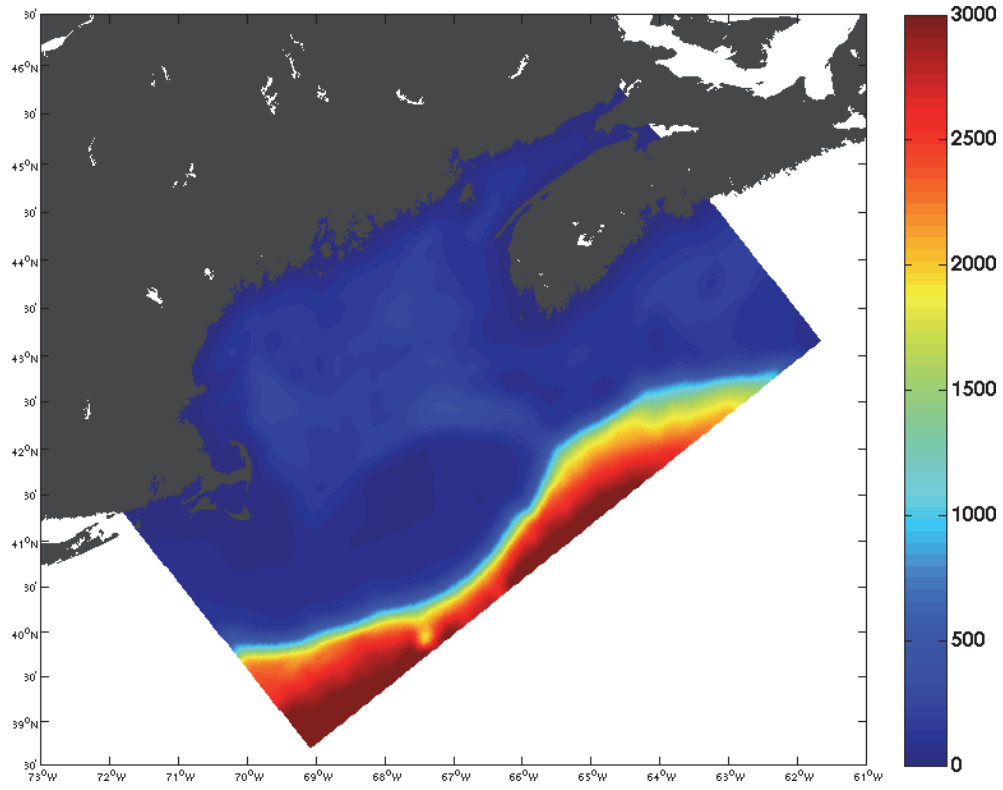


Figure 4.1. Model domain and bathymetry for the Gulf of Maine (GOM) 5-km model.

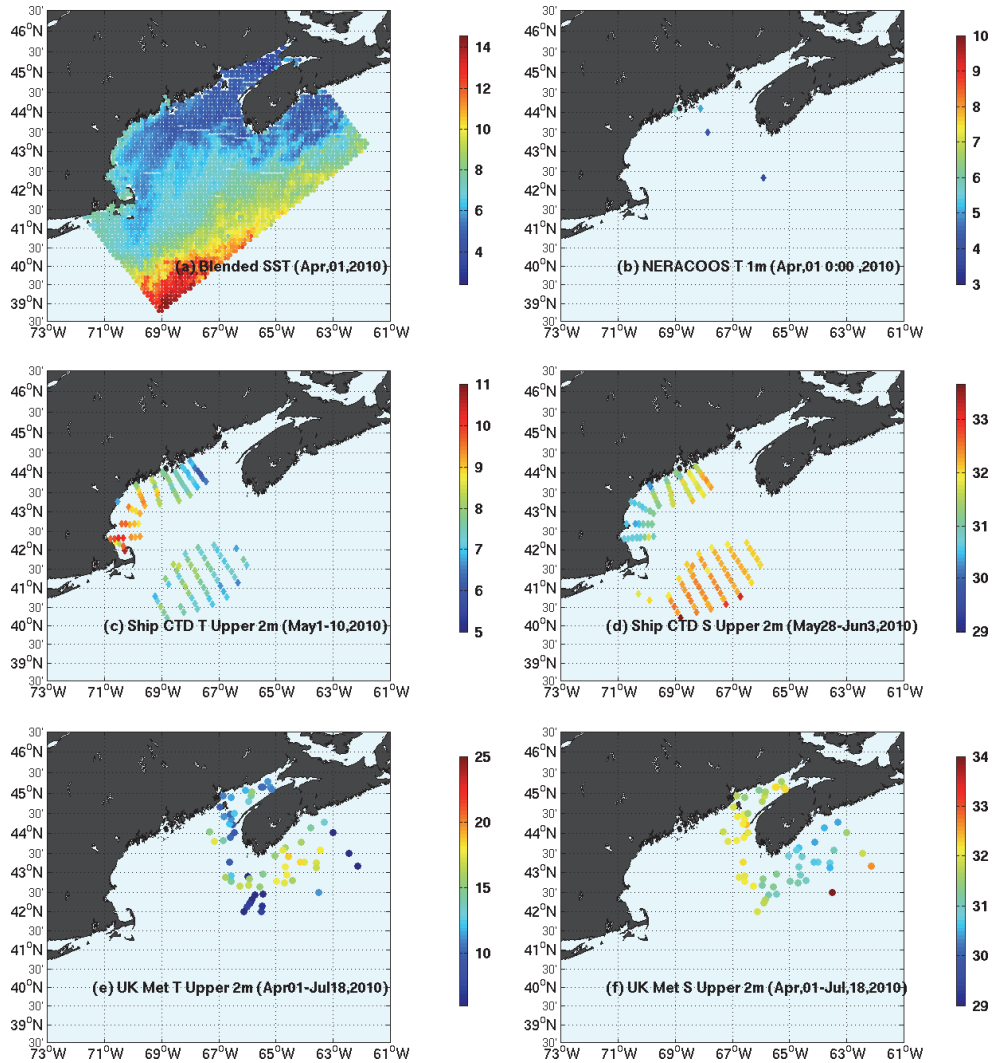


Figure 4.2. Observations assimilated into the GOM 4DVAR system: (a) Blended SST for April, 01, 2010; (b) NERACOOS temperature observations at 1-m at 0:00Z April, 01, 2010; Shipboard CTD observed (c) surface temperature for May, 1-10, 2010, and (d) surface salinity for May, 28-June, 03, 2010; (e) and (f) show the locations for the surface temperature and salinity observations collected by UK Met Office during the April, 01-July, 18, 2010.

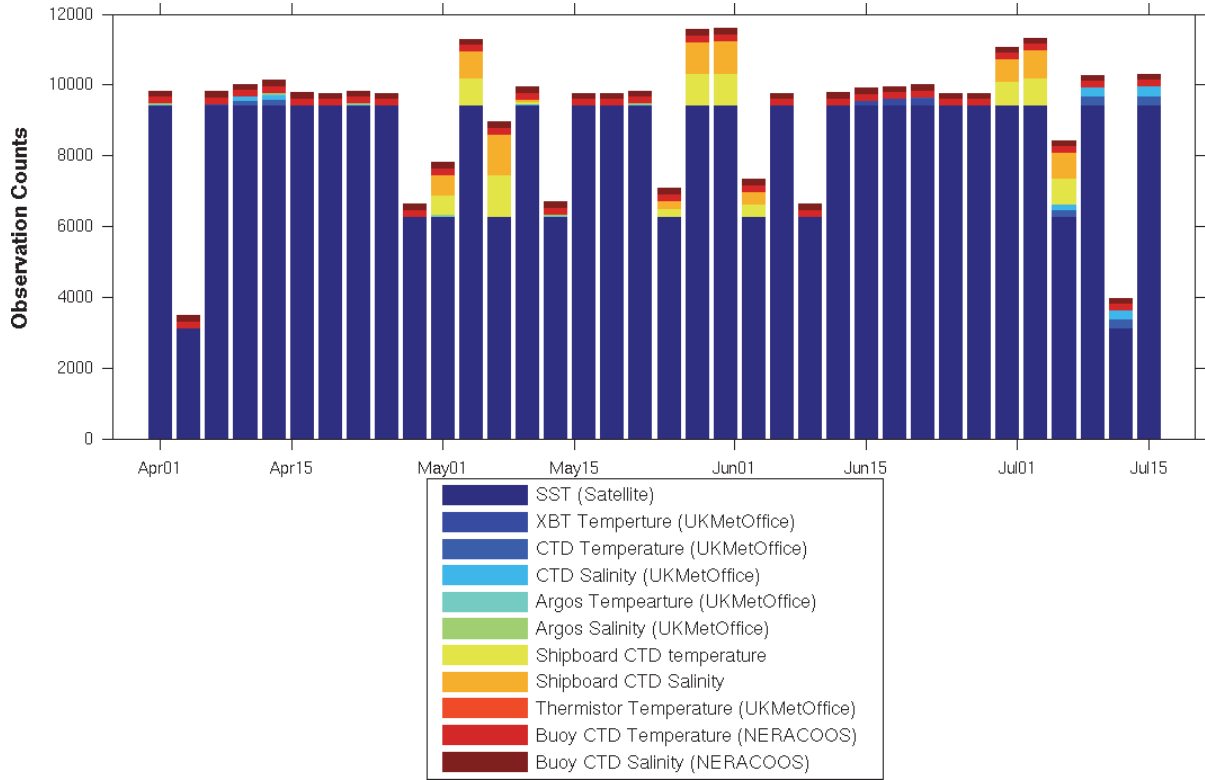


Figure 4.3. Temporal evolution of observation counts within each 3-day data assimilation window during April-July 18, 2010. Various data sources are shown in different colors—Satellite Sea Surface Temperature (SST), U.K. Met Office collected XBT temperature, CTD temperature, CTD Salinity, Argos temperature, Argo Salinity, Surface thermistor observed temperature. Additional datasets are temperature and salinity observations from gulf-wide ship surveys (positions are shown in **Figure 4.2c** and **d**), along with NERACOOS temperature and salinity observations.

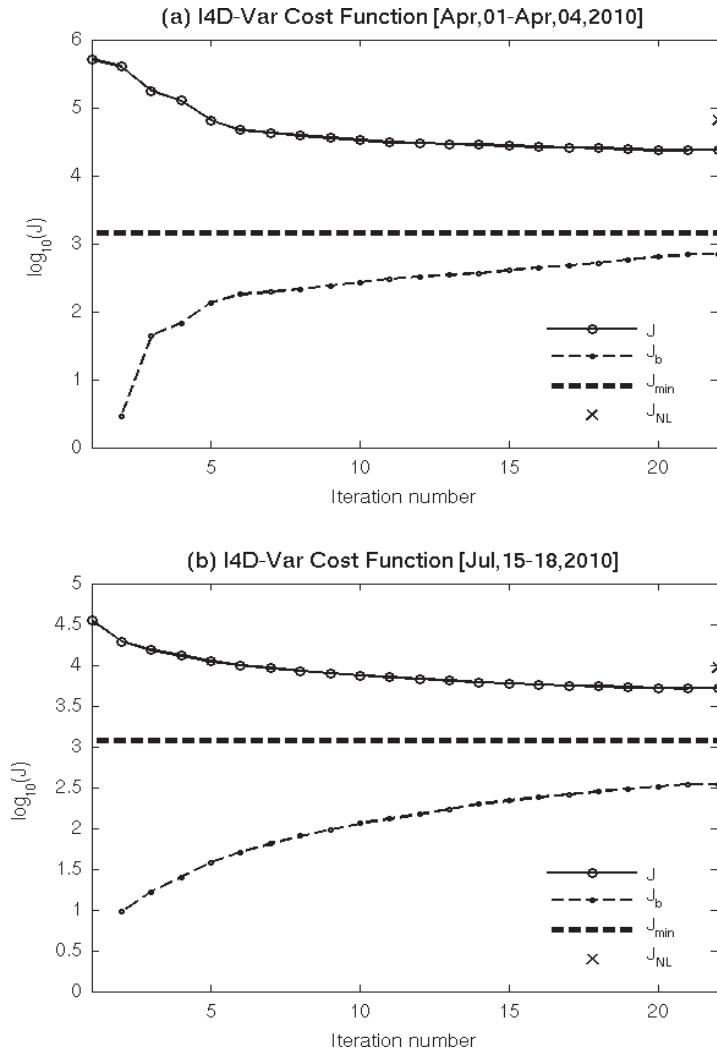


Figure 4.4. 4DVAR cost function (J) as a function of number of iterations of inner loops for (a) the first assimilation window (Apr, 01- April, 04, 2010), and (b) last assimilation window (July 15-July 18, 2010). Solid line is the total coast function (J), and dash dotted line is the background cost function (J_b). Theoretical minimum cost function ($J_{min}=1/N_{obs}$) is shown in dotted line, and the cross represents nonlinear model cost function (J_{NL}) after data assimilation.

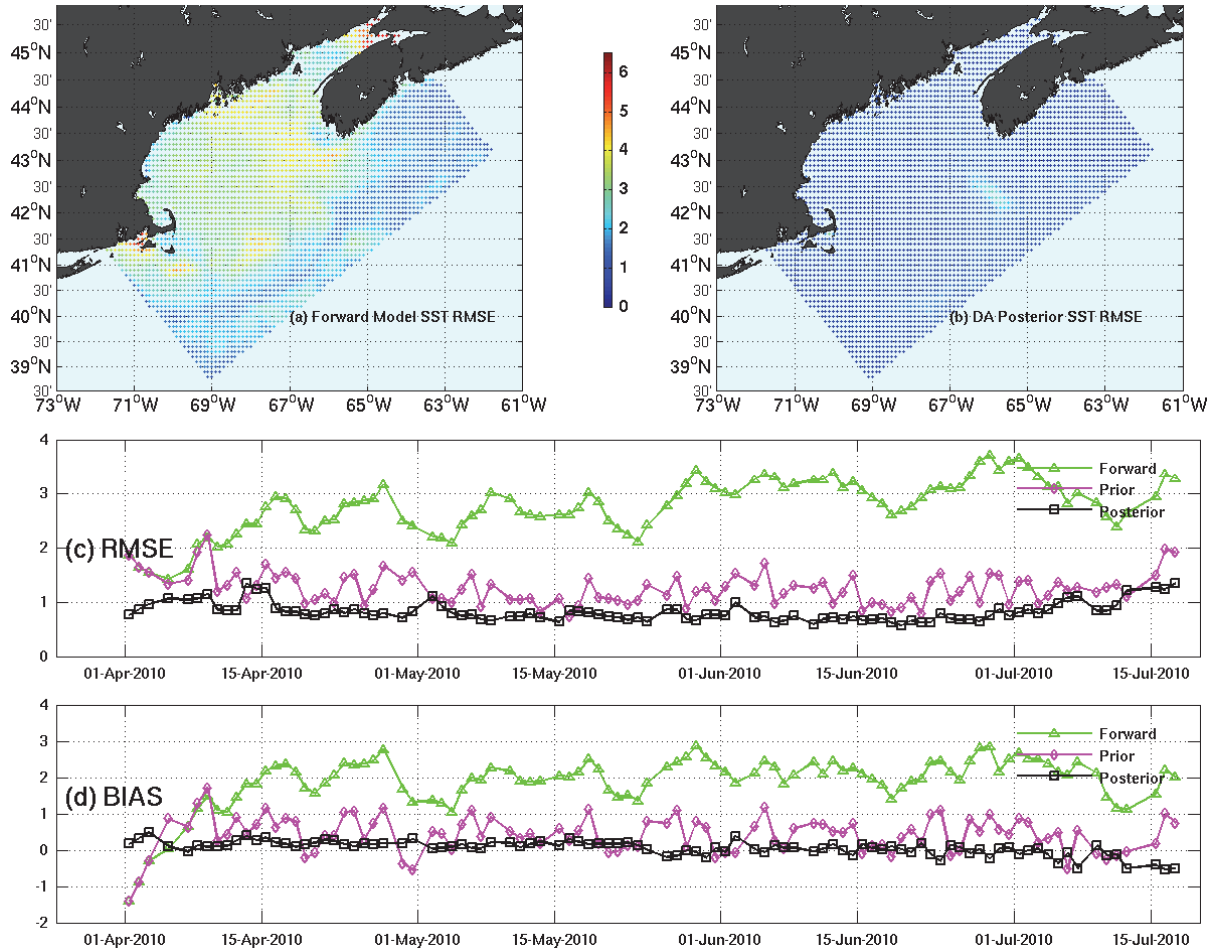


Figure 4.5. Spatial distribution of the temporal SST Root mean square error (RMSE) between observations and (a) forward model solutions and (b) DA posteriors solutions. Temporal evolution of spatial SST RMSE and BIAS between observations and (c) forward model solutions and (d) DA posteriors solutions.

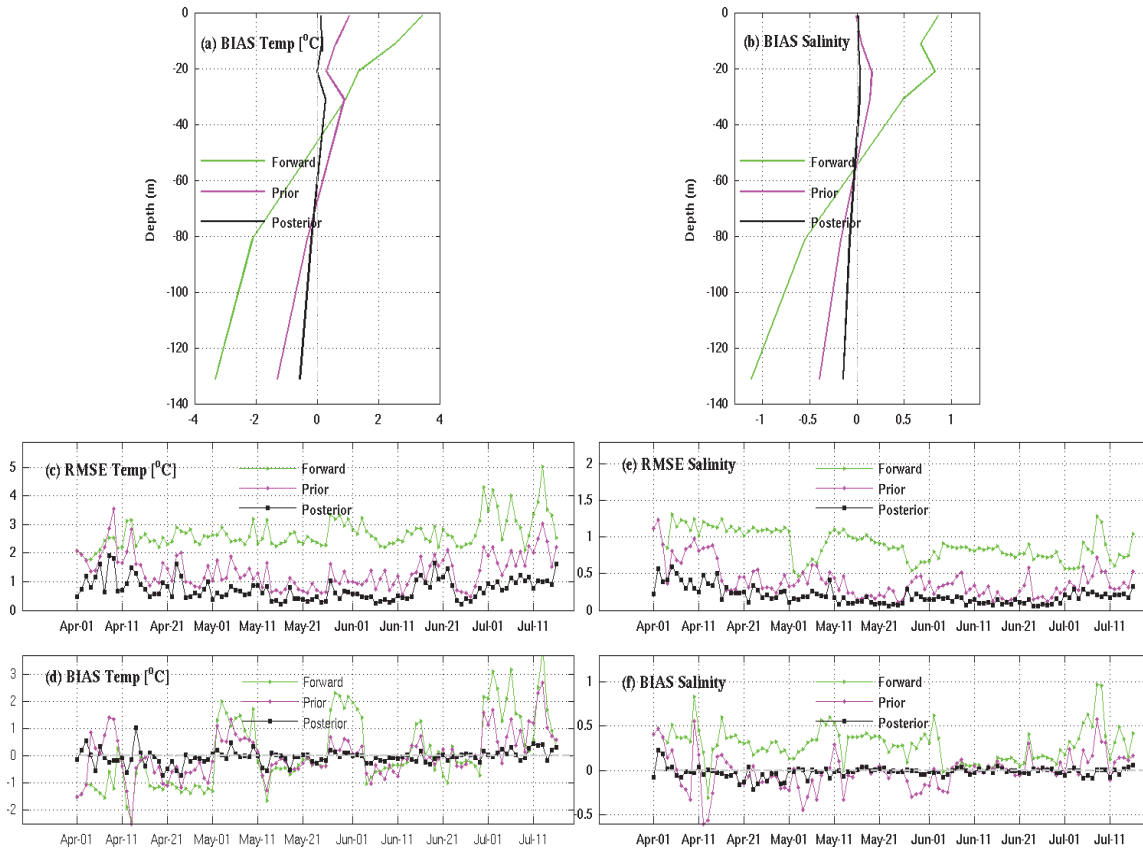


Figure 4.6. Vertical profiles of subsurface (a) temperature and (b) salinity BIAS between observations and forward and DA posterior model solutions. Temporal evolutions of subsurface (c) temperature and (d) salinity BIAS between observations and forward and DA posterior model solutions.

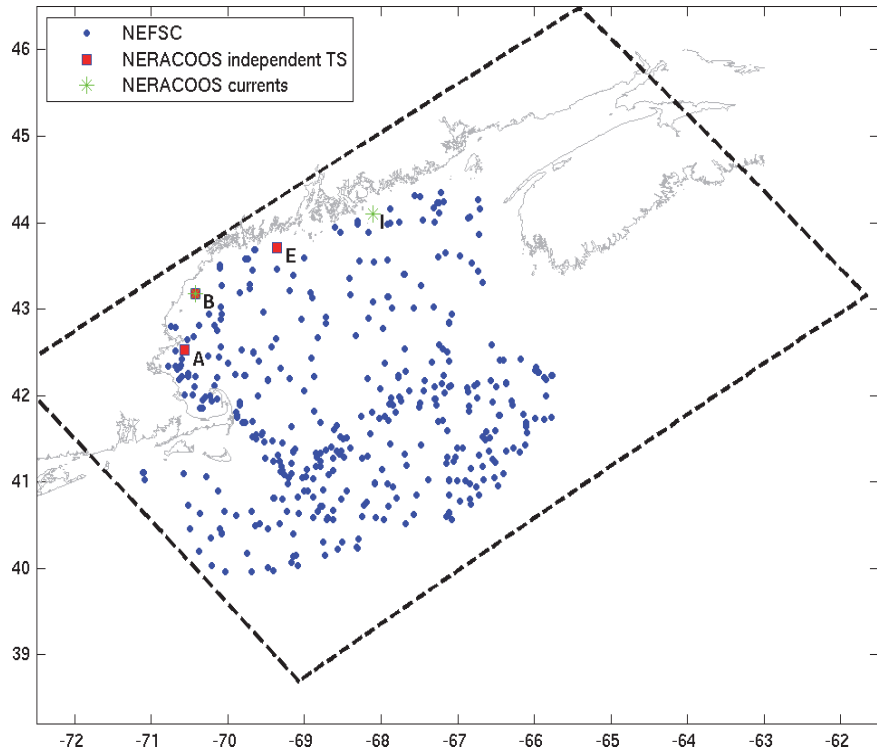


Figure 4.7. Station locations of CTD stations for the Northeast Fisheries Science Center (NEFSC) ship survey data (blue dots) inside the model polygon (model boundaries are plotted in dashed black lines) during April, 01-July, 18, 2010. Also shown are the NERACCOS stations, the data of which were used for independent comparisons. Specifically, buoys A, B and E (pink squares) are used for T/S comparisons, and buoys B and I are used for current comparisons.

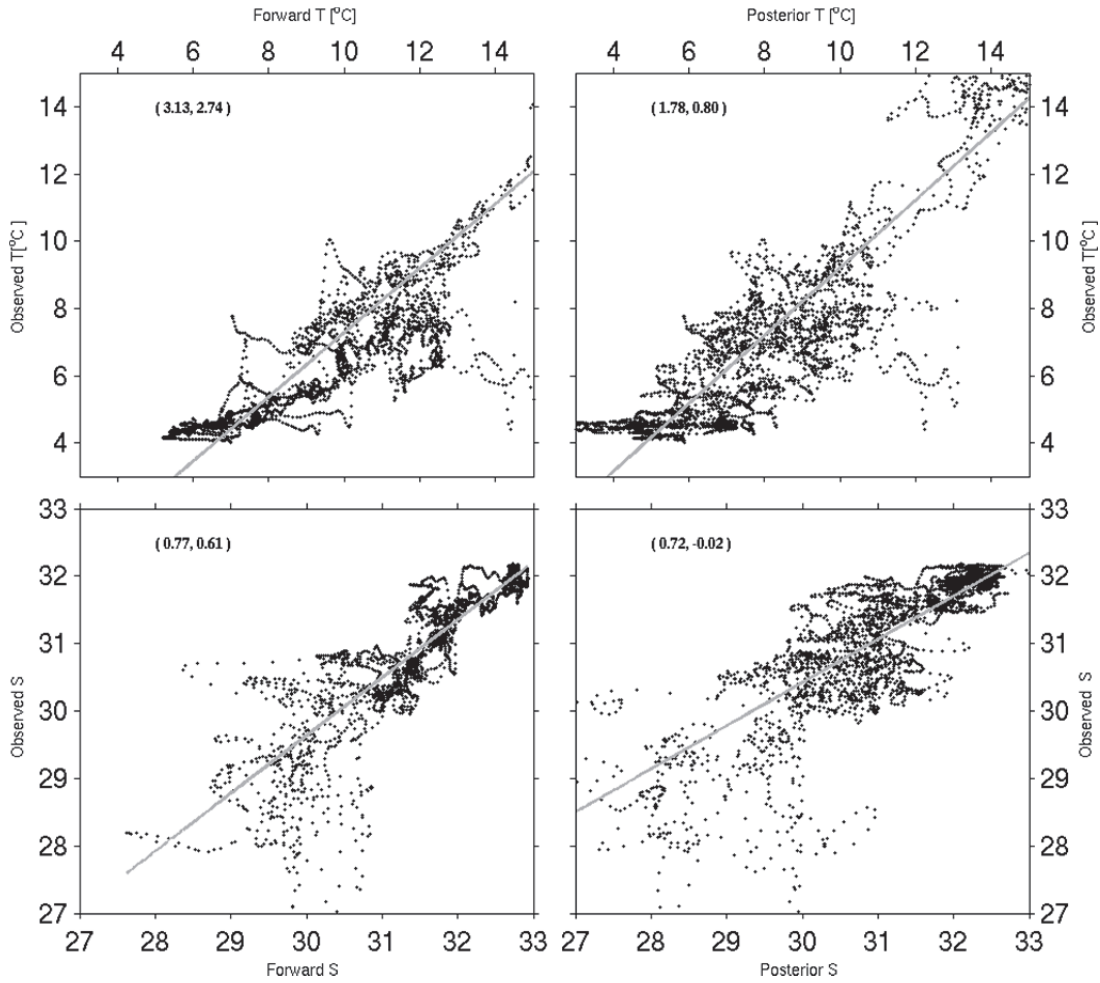


Figure 4.8. Scatter plots of observed temperature and salinity at buoy A, B and E against model forward and posterior solutions. Gray line represents the linear fitting based on model solutions. Doublets in the brackets are model-data RMSE and bias, respectively. The profiles are not assimilated into the model and are used as independent data.

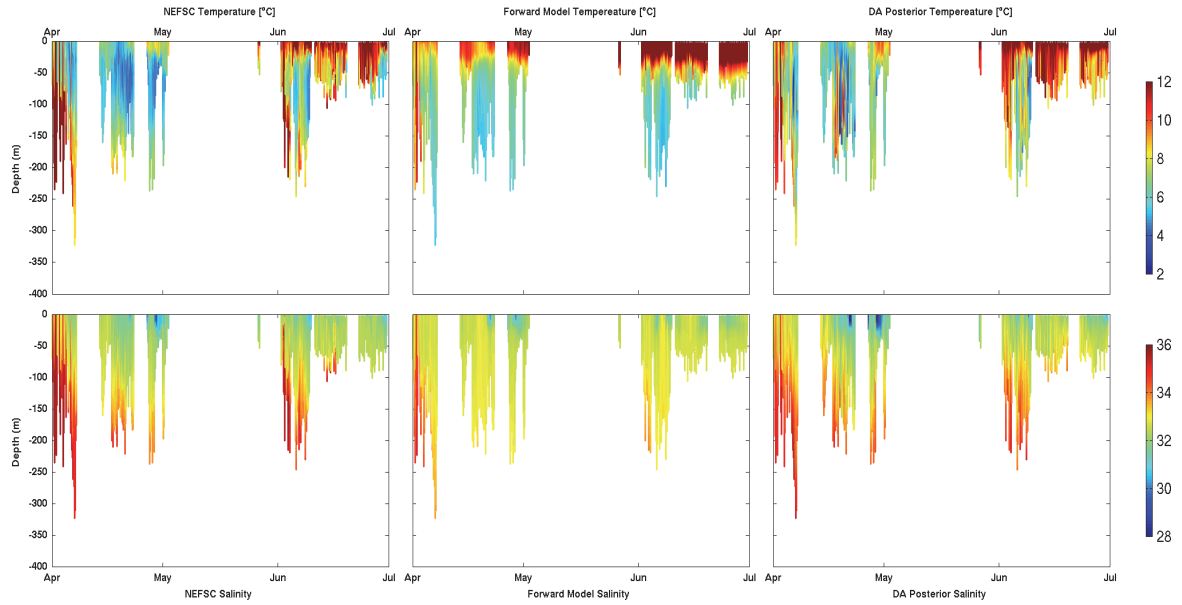


Figure 4.9. Comparisons between NEFSC temperature and salinity data (left column) and forward model (central column) and DA posterior counterparts. X-axis is observation time, and y-axis denotes the depth of the data in meters.

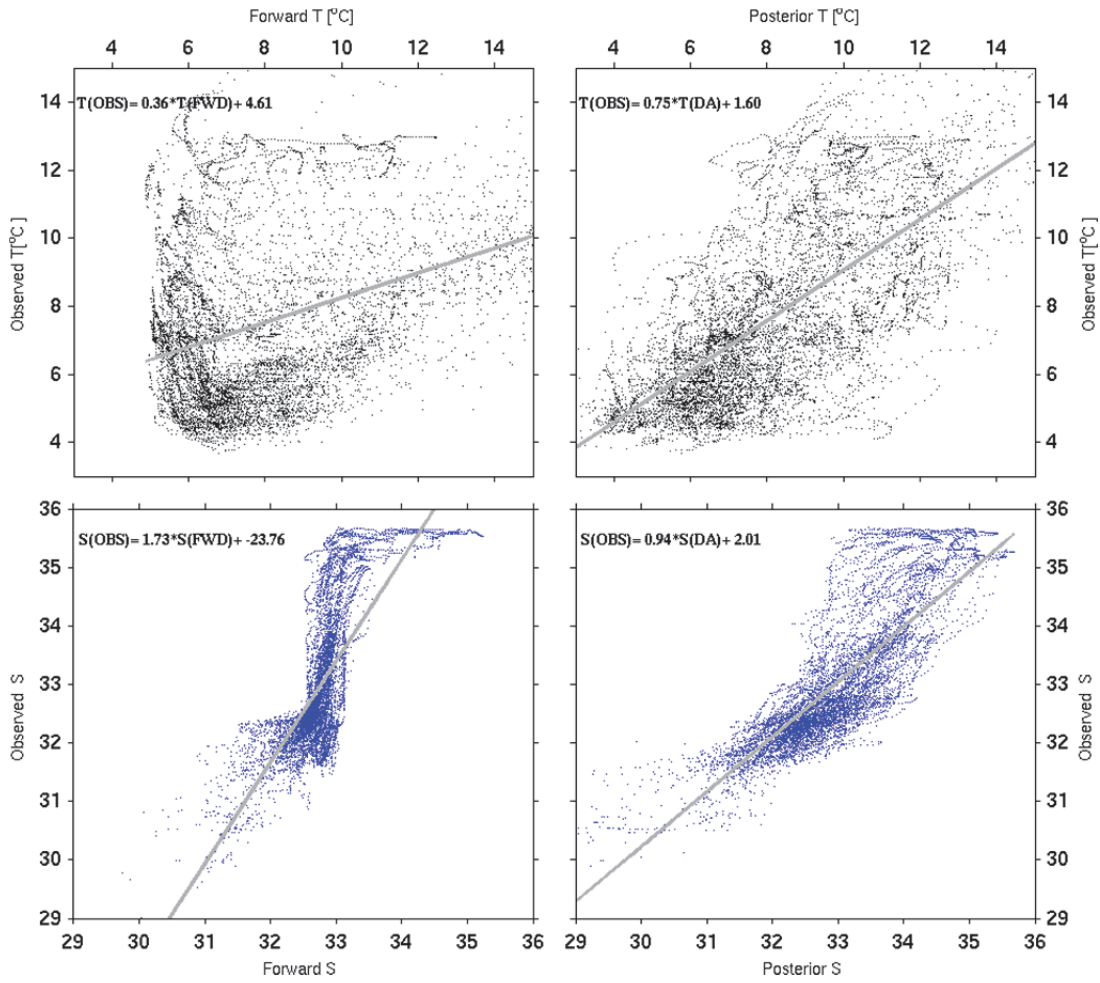


Figure 4.10. Scatter plots of observed NEFSC temperature and salinity data against model forward and posterior solutions. Gray lines represent the linear fitting based on model solutions. Formulations show the fitting slope and intercepts between model and observations.

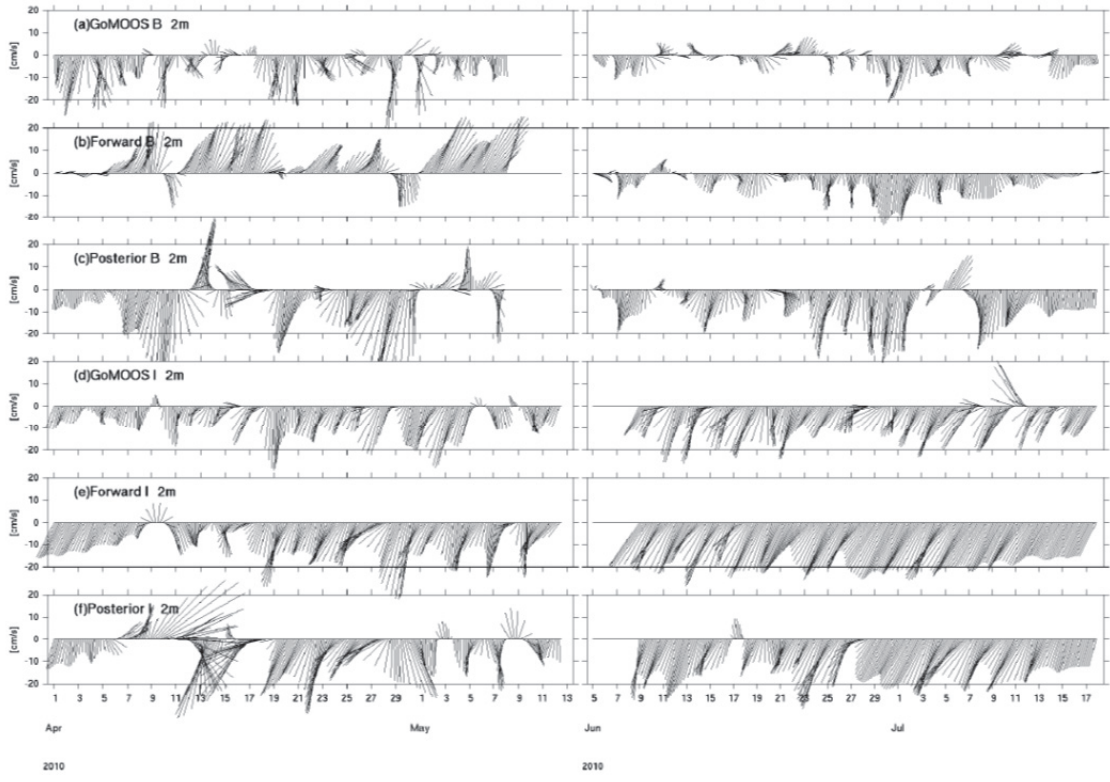


Figure 4.11. Comparisons of 2-m surface currents between observations and model forward and posterior solutions for buoy B in the western GOM and buoy I in the eastern GOM, respectively. Model solutions are not shown during middle May to early June when there is no observed current available.

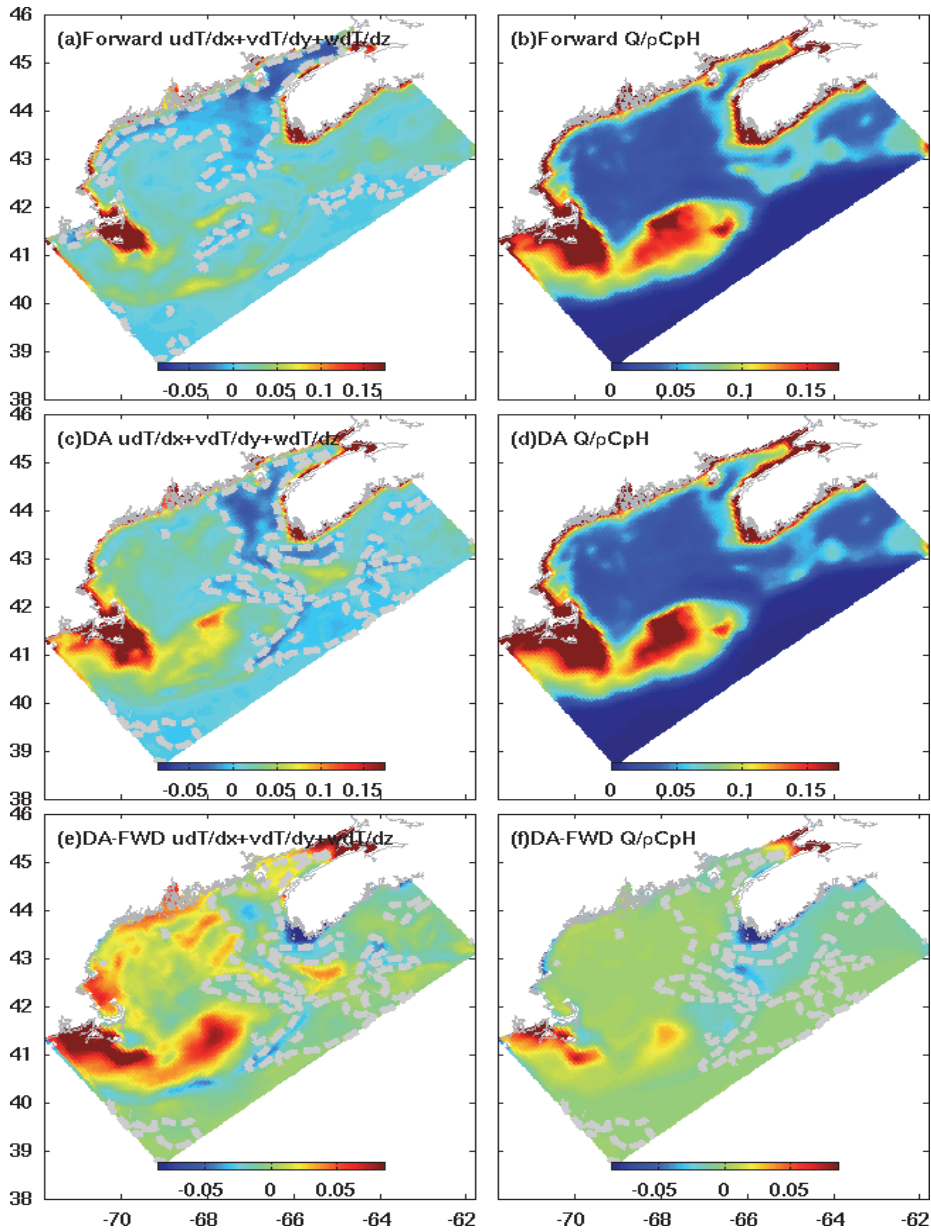


Figure 4.12. Term-by-term diagnostics of depth-averaged temperature budget. (a) and (b) are advection and heat flux terms for forward model, and (c) and (d) are the DA posterior counterparts. (e) and (f) stand for the DA posterior and forward model differences in the two terms. Dotted grey line represents the contour of zero line in each panel. Unit for the plot is in $^{\circ}\text{C day}^{-1}$.

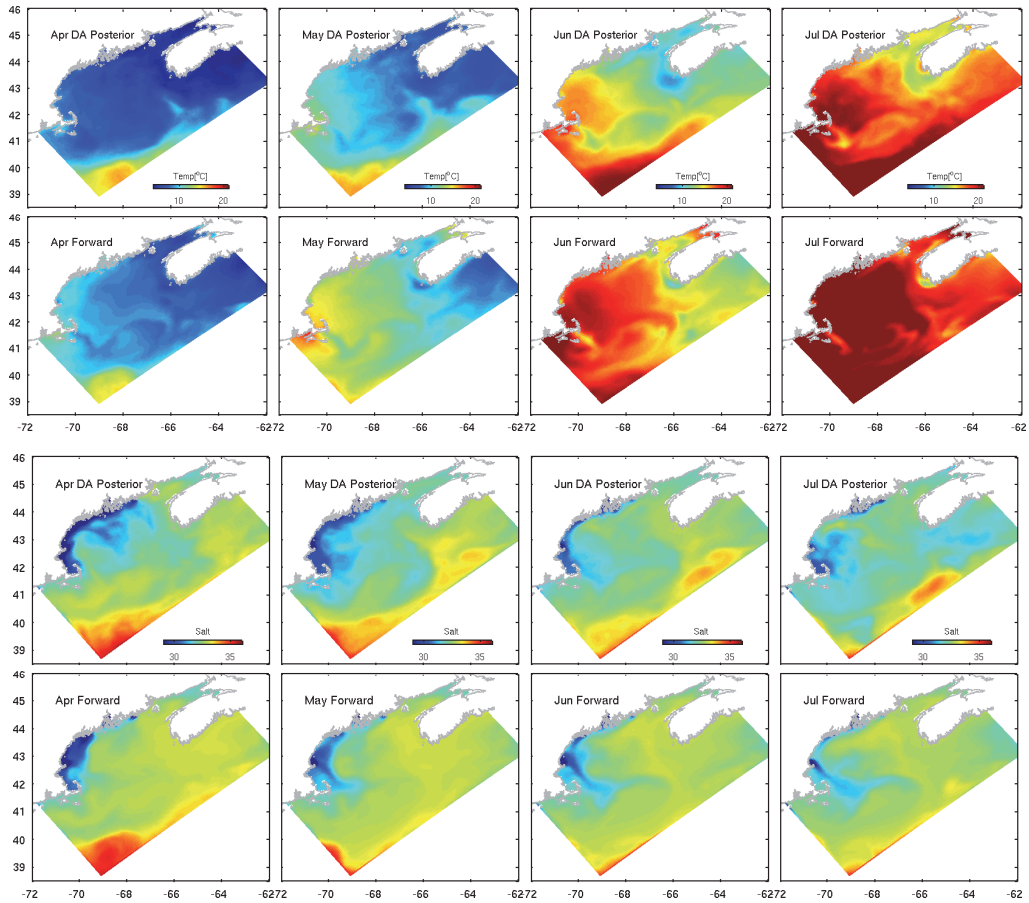


Figure 4.13. Monthly-mean model trajectories for the surface temperature and salinity for model forward and posterior solutions, separately.

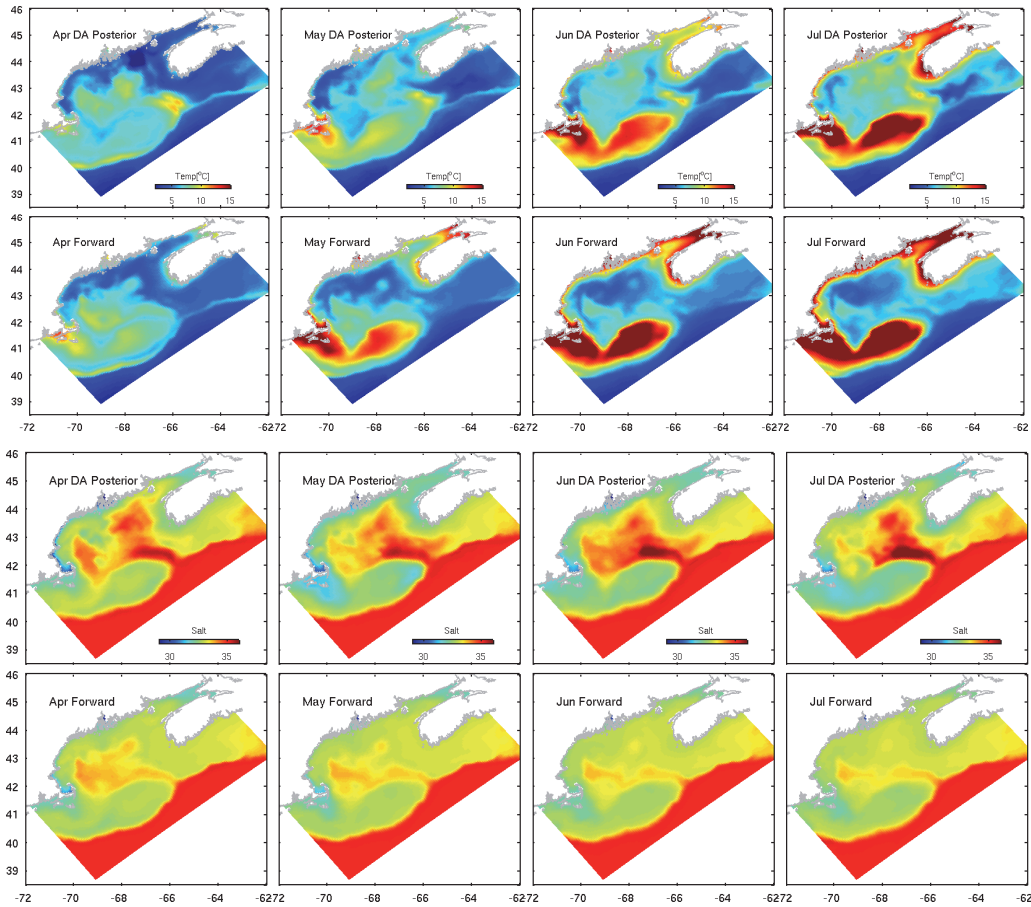


Figure 4.14. Monthly-mean model trajectories for the bottom temperature and salinity for forward and posterior model solutions, separately.

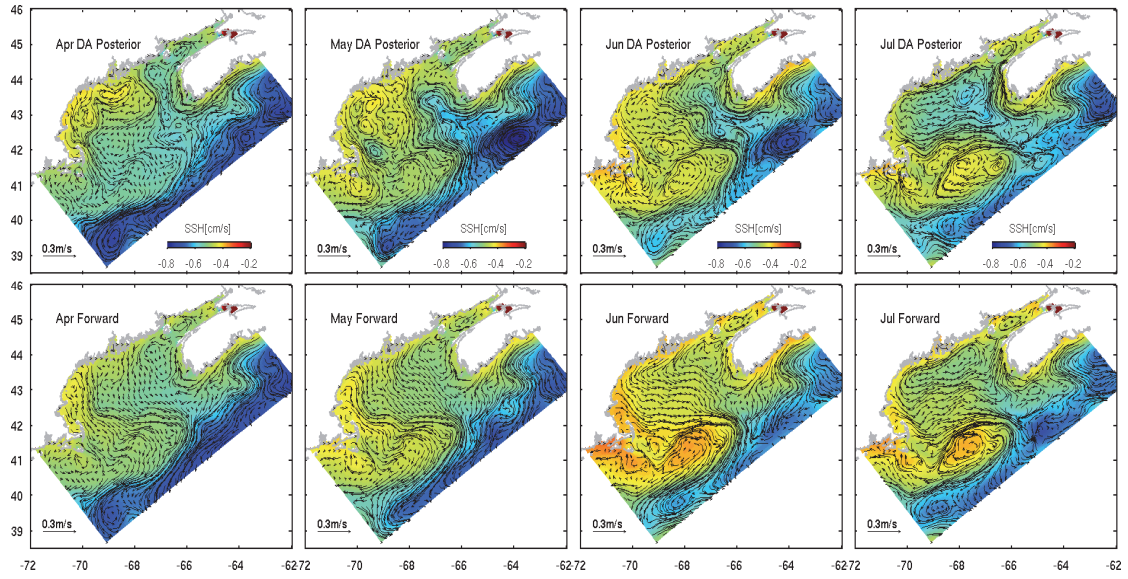


Figure 4.15. Monthly-mean model trajectories for the surface currents for model forward and posterior model solutions.

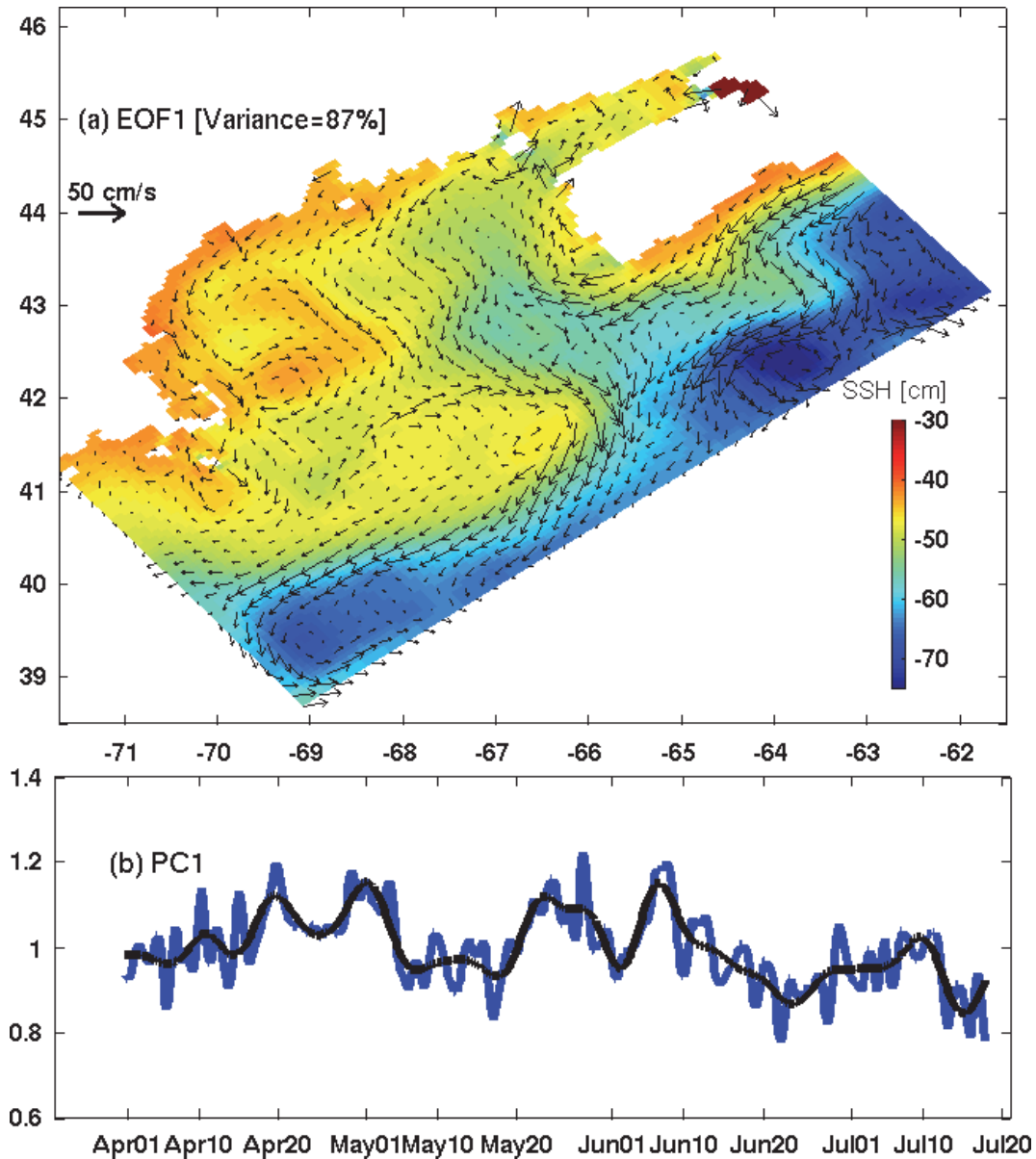


Figure 4.16. (a) First EOF of coastal current and sea surface height (SSH). Horizontal arrow stands for the current scale of 50 cm/s. Number inside the brackets represents the variances of mode 1; (b) first principal component (PC1, time series) of the EOF analysis. Blue line is the original 4-hourly data, and black line is the 7-day low-pass filtered counterpart.

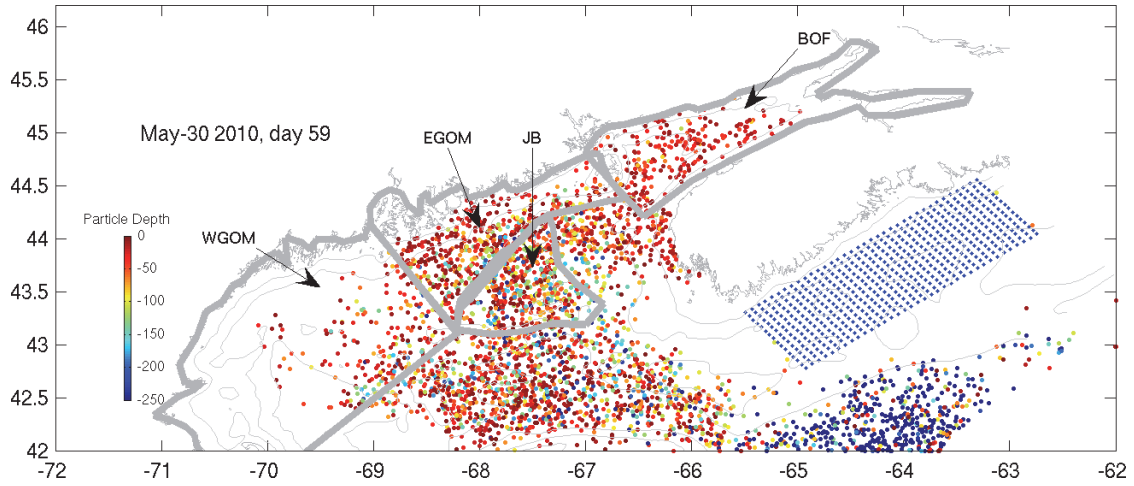


Figure 4.17. Snapshot at day 59 for the particles released from Scotian Shelf to the four destination areas of interest-- The Bay of Fundy (BOF), the eastern GOM (EGOM), the Jordan Basin (JB), and the western GOM (WGOM). Color represents the final depth of the particles in meters. Initial locations for the particle released near the Scotian Shelf in April 01, 2010 are shown in blue dots.

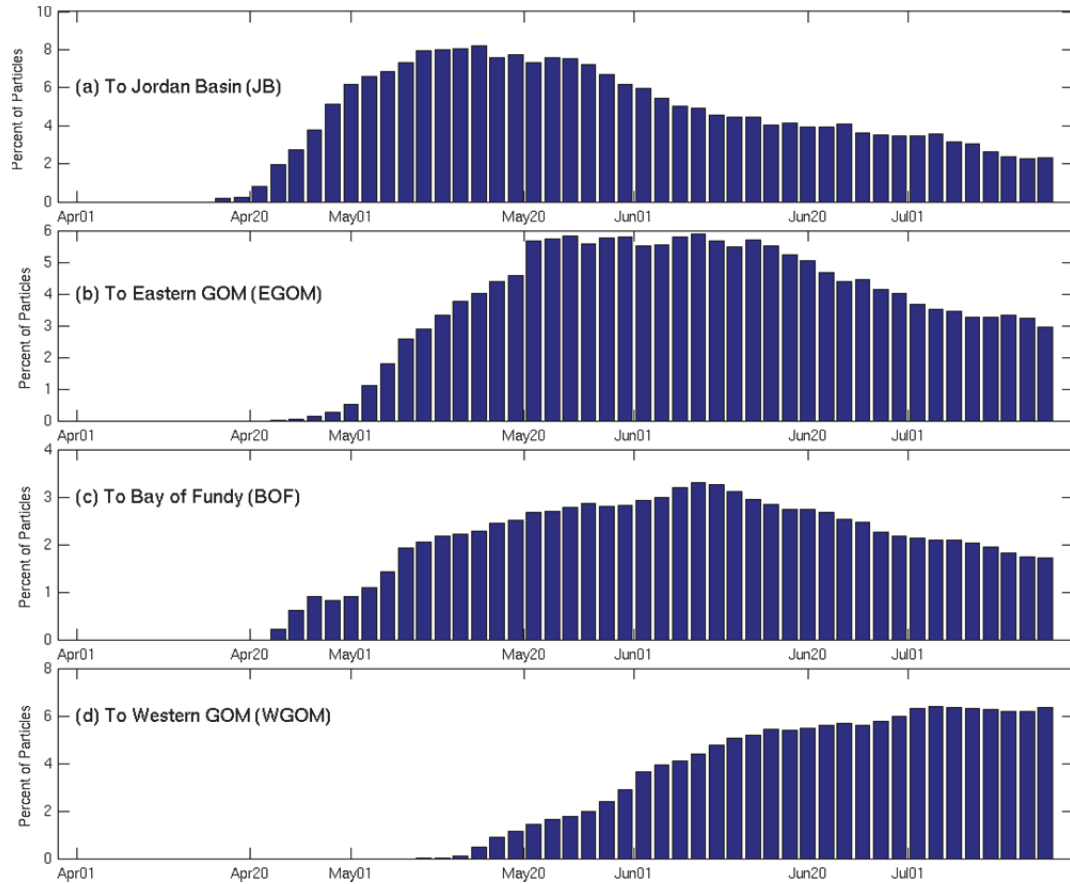


Figure 4.18. Temporal evolutions of percent of particles released from Scotian Shelf on April 1st that are transported to (a) Jordan Basin (JB), (b) eastern GOM (EGOM), (c) Bay of Fundy (BOF) and (d) western GOM (WGOM). Initial locations and destination polygons are defined in Figure 16.

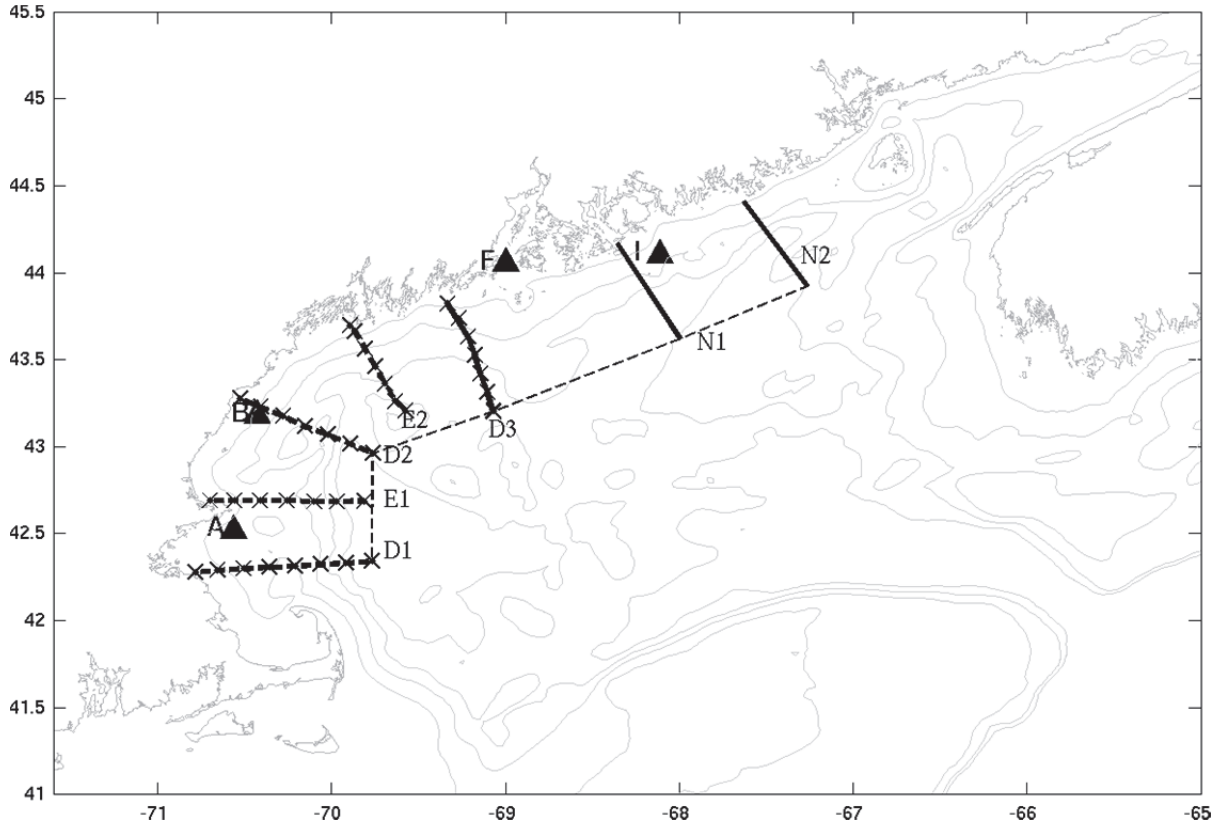


Figure 5.1. A map showing the spatial distribution of station locations for NERACOOS buoys A, B, F and I (grey triangle). Also shown are the station locations (crosses) in research cruise Oceanus 447 (OC 447) conducted on May 29-June 04, 2008. D1, E1, D2, E2 and D3 stand for five observational transects, whereas the two black solid lines in the eastern Gulf of Maine represent transects N1 and N2 where cell fluxes are sampled from the biophysical model.

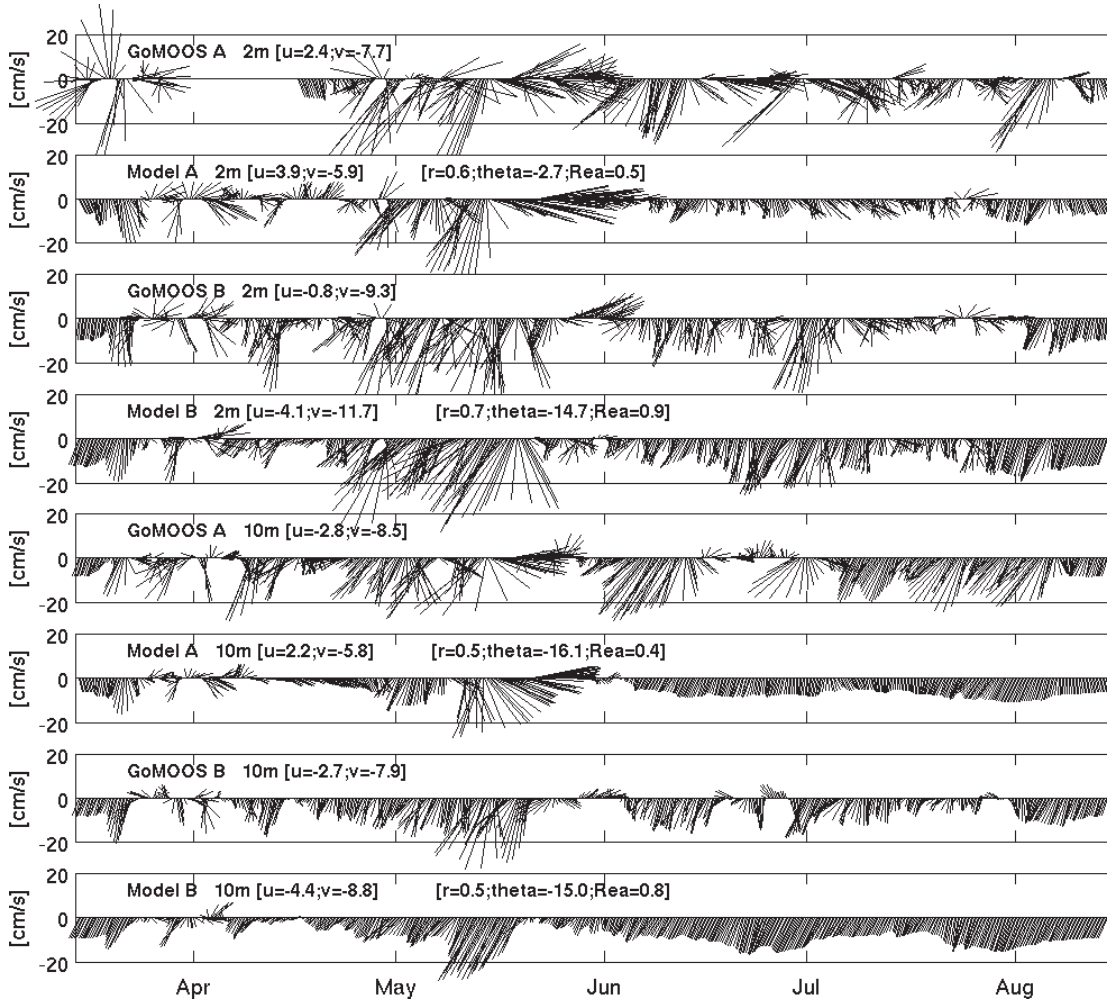


Figure 5.2. Comparisons of simulated and observed surface (2m) and sub-surface (10m) currents at NERACOOS mooring A and B. Current time series are sampled daily for better visualization. Each vector current time series is accompanied by its seasonal mean east and north velocity components (left-hand couplet), and each model-data comparison is quantified by its complex correlation coefficient, phase angle (or angular deviation of the model vectors from the data vector measured counterclockwise), and regression coefficient (right-hand triplet).

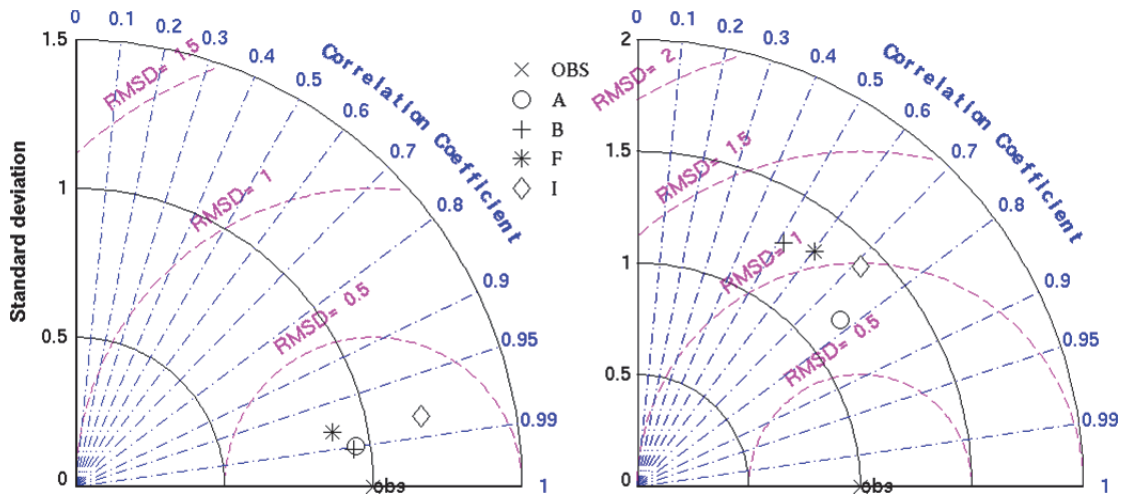


Figure 5.3. Taylor diagrams comparing simulated and observed surface temperature (left panel) and salinity (right panel) at GoMOOS coastal buoy A, B, F in the western GOM and buoy I in the eastern GOM. The radial distances from the origin are proportional to the ratio standard deviations; the azimuthal positions indicate the correlation coefficient; and the distance between the “test” (modeled) points and the “reference” (observed) point indicates the centered RMS difference (RMSD).

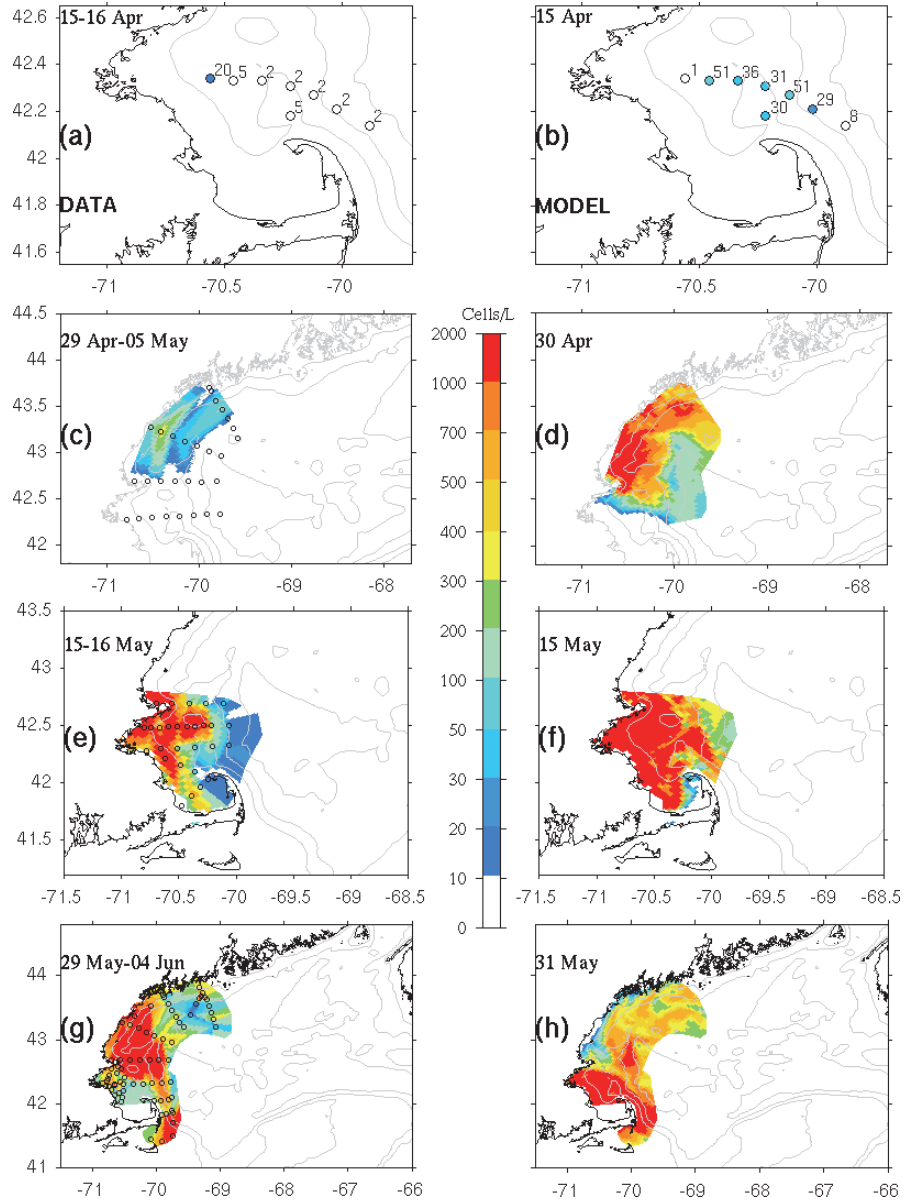


Figure 5.4. Comparisons between observed (left column) and modeled (right column) surface *A. fundyense* cell concentrations from April to early June, 2008. Open circles represent the locations where observations were collected during each survey.

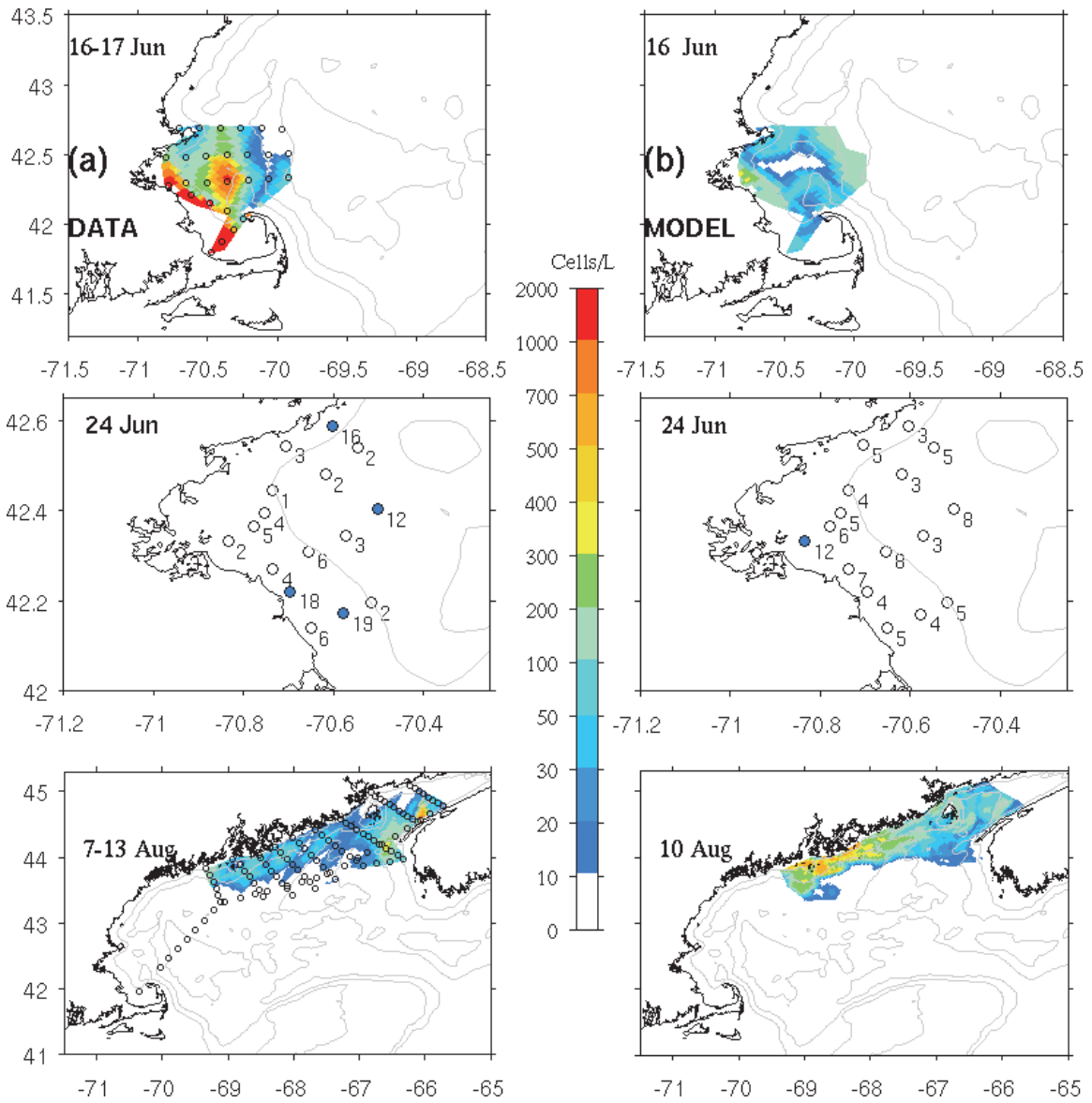


Figure 5.5. Same as Figure 5.4, but for the periods from middle June to middle August.

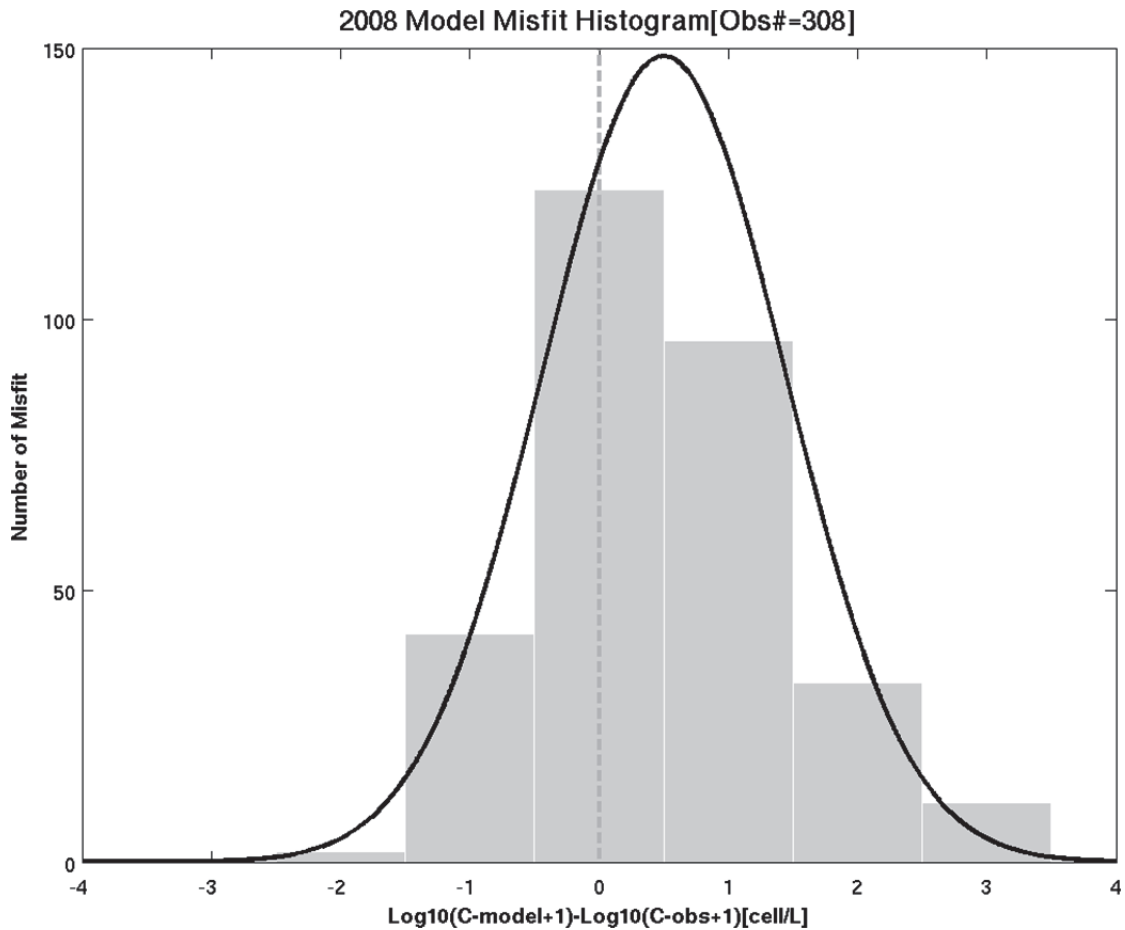


Figure 5.6. Histogram showing point-by-point model-data misfit between observed and simulated surface cell concentrations at a total of 308 stations in the 2008 bloom season. X-axis stands for the model-data misfit and y-axis is the number of misfits. Grey vertical line represents the theoretical misfit for normal distribution, while black curve denotes the fitted normal distribution between observations and model. A log10 scale is used for better visualization purpose.

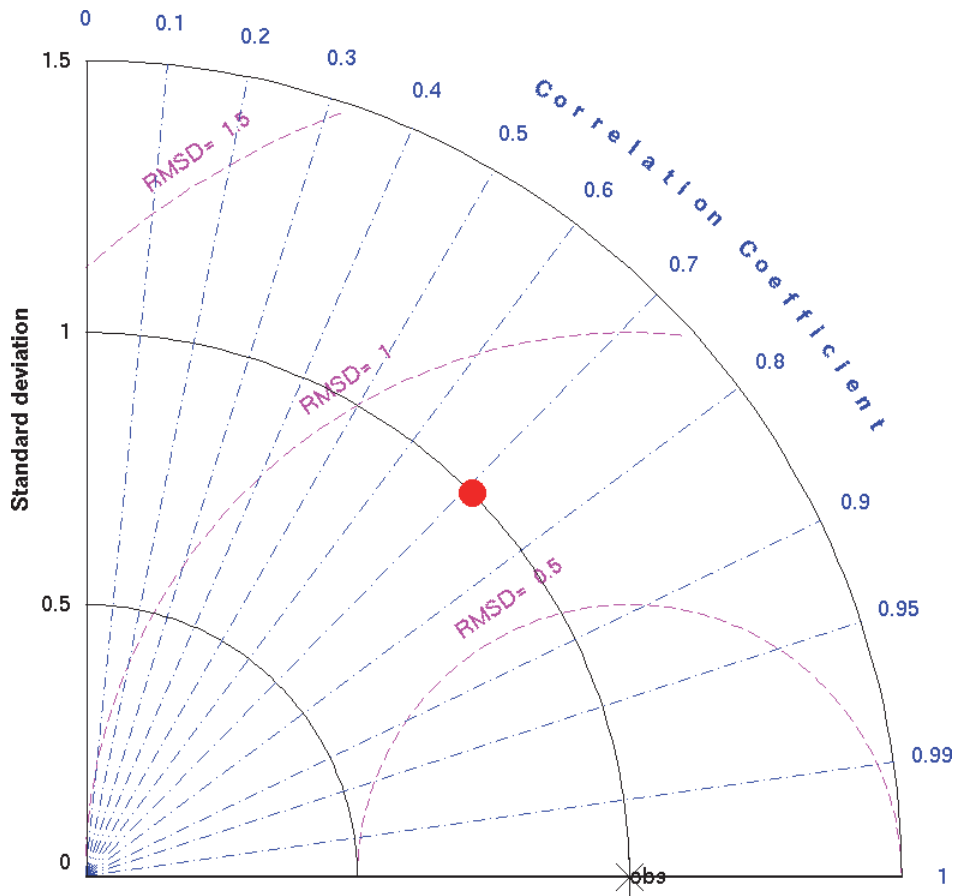


Figure 5.7. Same as Figure 5.3, but the Taylor diagrams comparing simulated and observed surface cell concentrations (in log10 scale) during the seven cruise surveys as shown in Figure 4 and Figure 5. To avoid point-by-point concentration, we averaged the cell concentrations during each survey to compute the spatial-mean cell concentration. As such, the statistics shown in the Taylor diagram are indeed the temporal correlation coefficient, temporal root-mean-square different, and standard deviation.

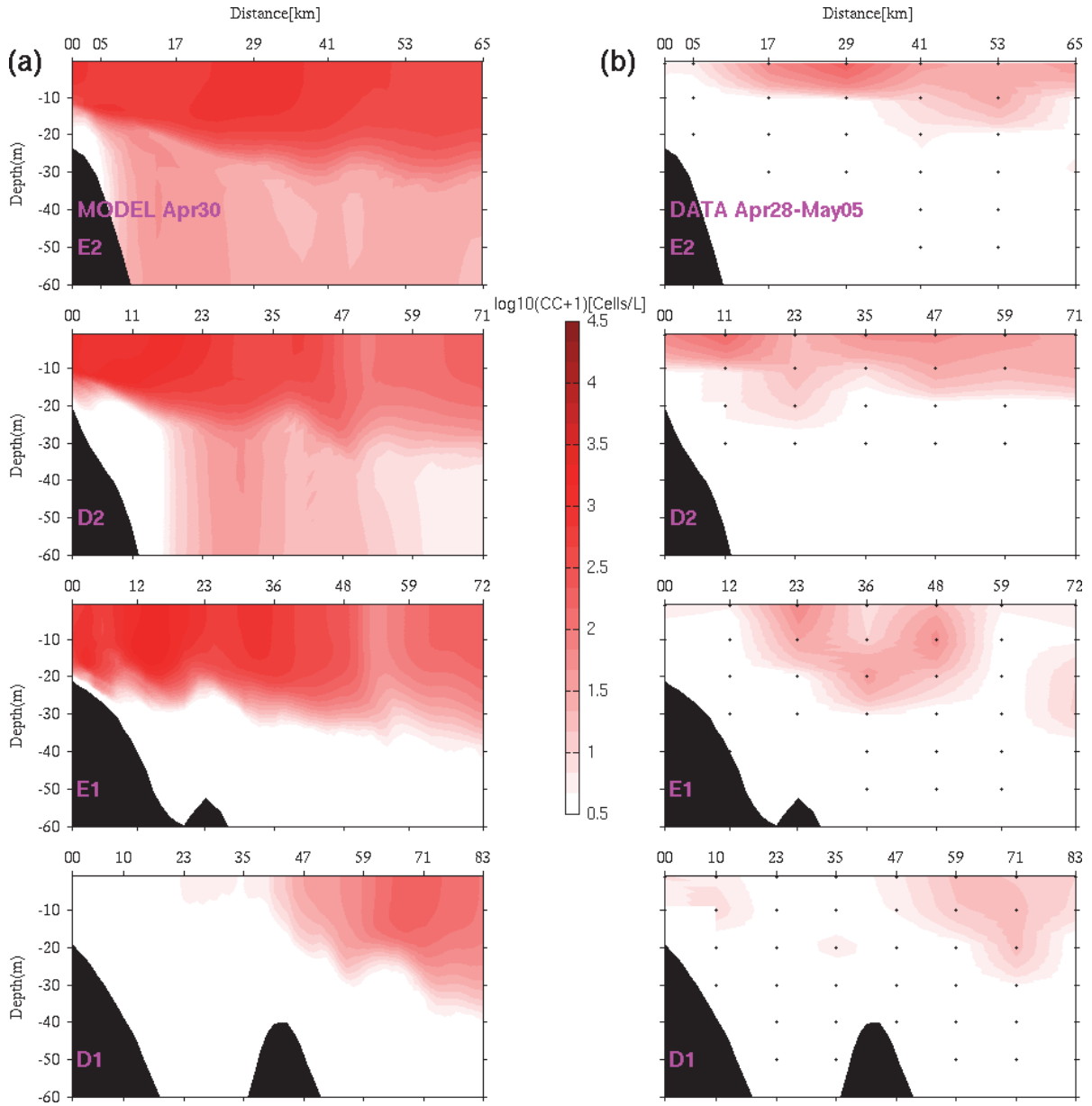


Figure 5.8. Comparisons between simulated (left column) and observed (right column) *A. fundyense* cell concentration along several cross-shelf transects of for survey *OC445*. Open circle represents the depths where observations were available. X-axis is the distance from the onshore-most locations. A log10 scale was used for better visualizations.

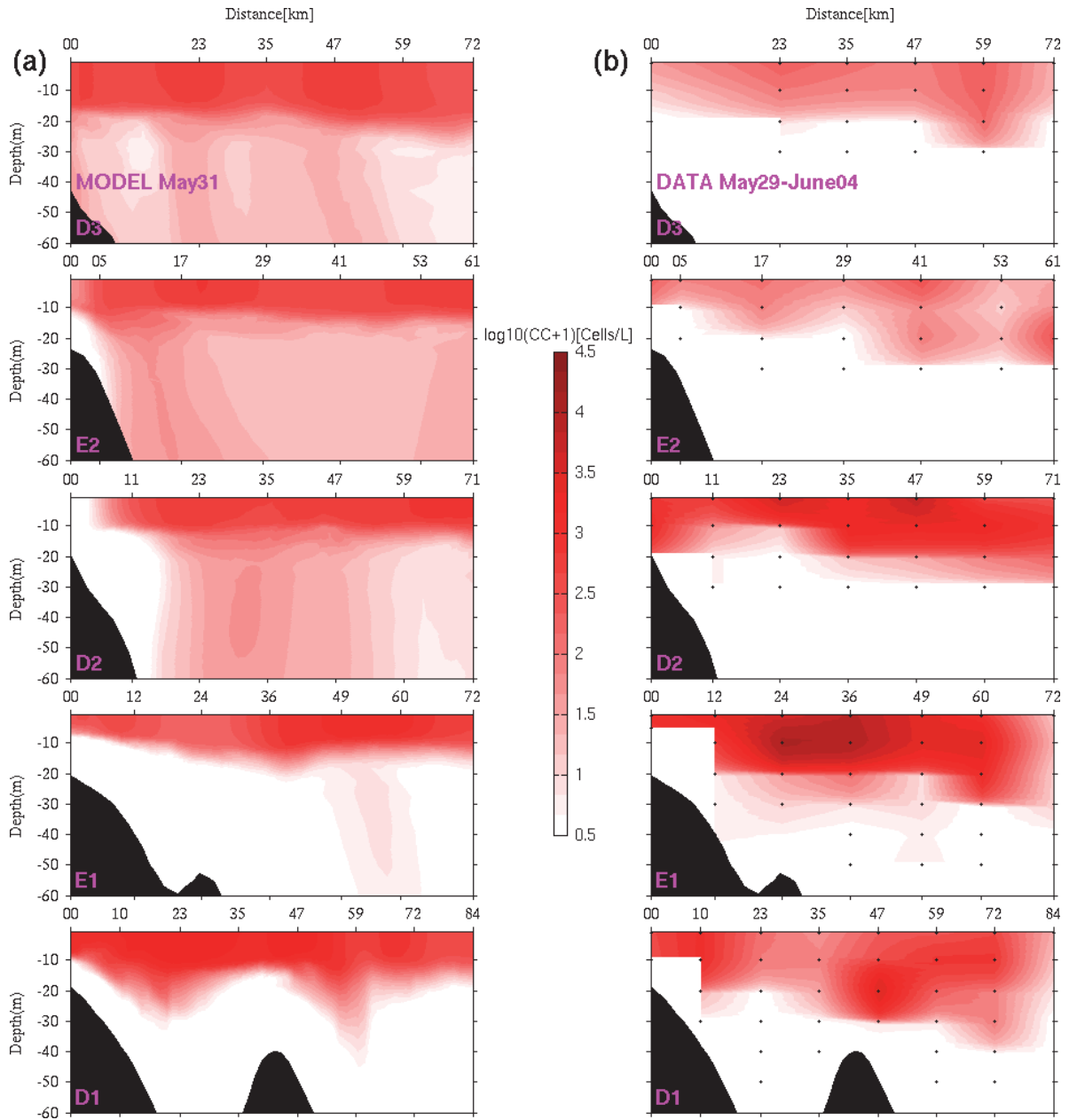


Figure 5.9. Same as Figure 5.8, but for survey *OC447* conducted in late May.

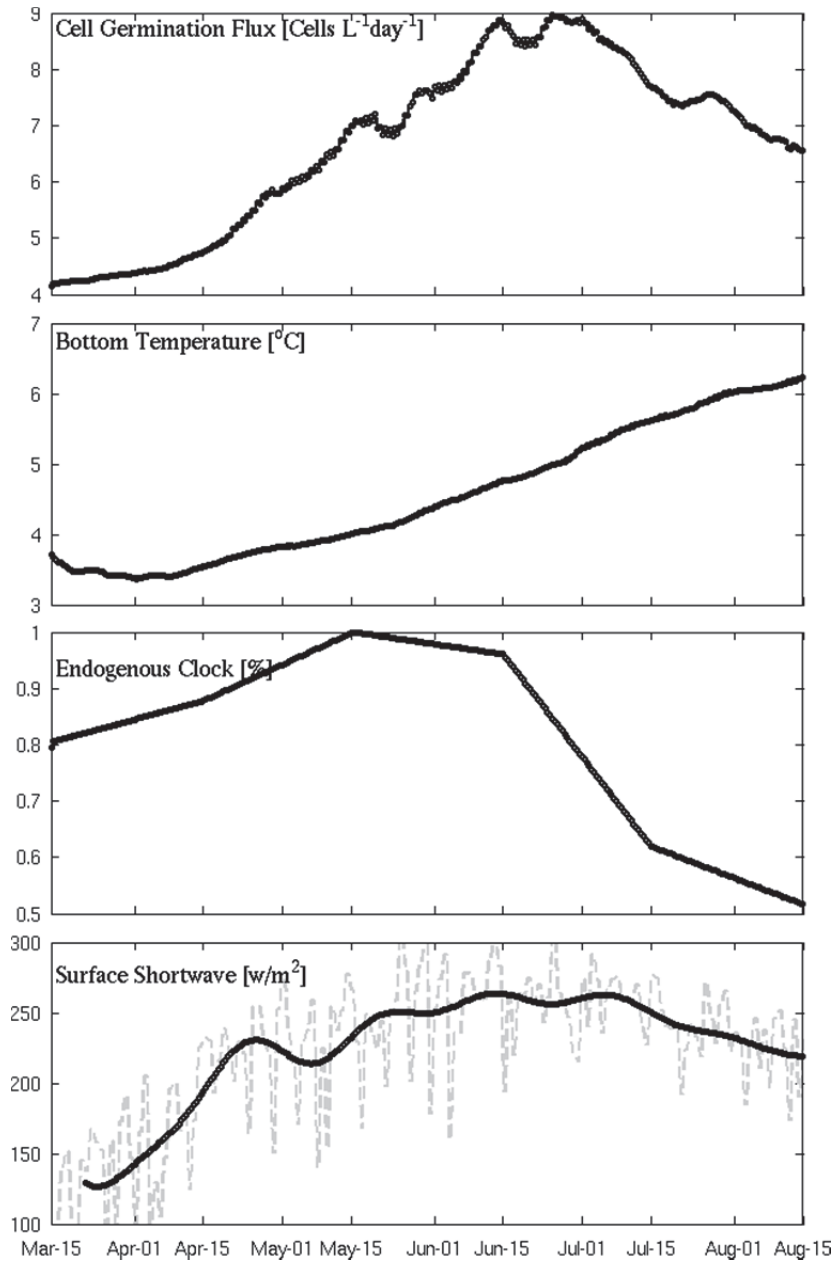


Figure 5.10. Time series of daily cell germination flux from cyst bed, bottom temperature, endogenous clock (percent of germination) and surface shortwave radiation. For the shortwave radiation in the bottom panel, the grey line denotes the 12-hourly data and black curve is its 30-day low-pass filtered rendition.

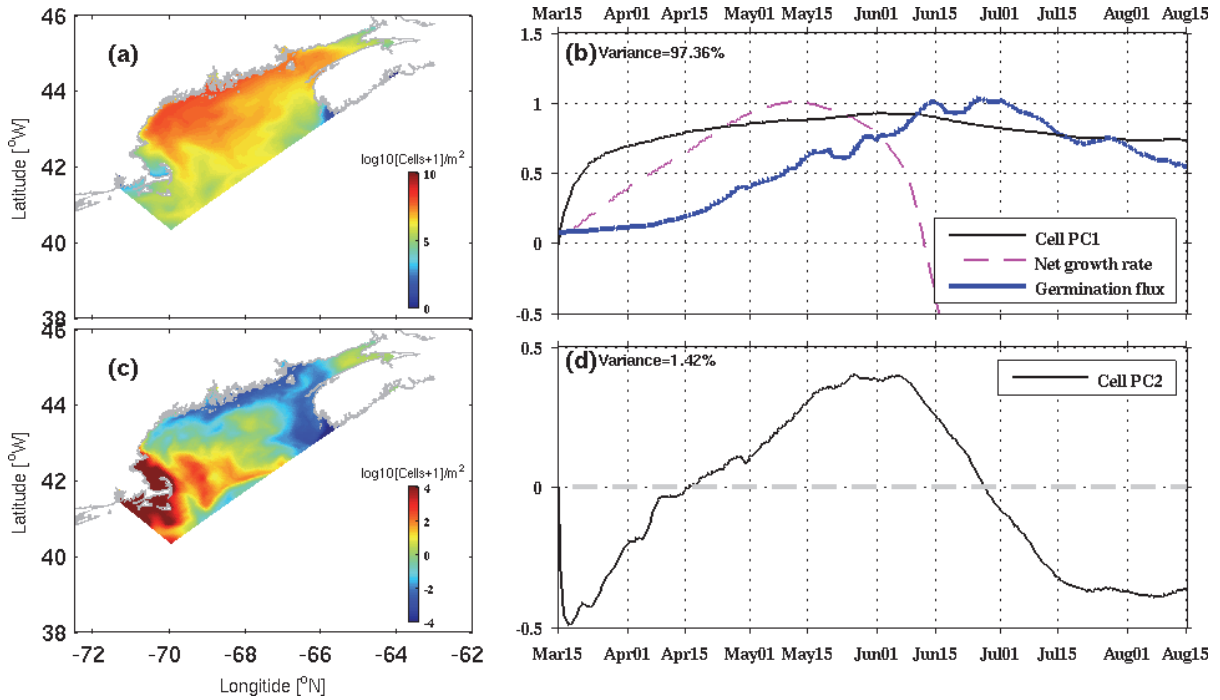


Figure 5.11. (a) First EOF mode of the cell concentration and (b) its principal component (PC1, black line), also shown in this panel are the normalized gulf-wide spatial-averaged net growth rate (pink dashed line) and normalized germination flux (blue solid line), (c) second EOF mode of the surface cell concentration, and (d) its principal component (PC2, black line). Note that the cell concentrations are integrated over the upper 50m water column, and are then transformed into a log scale form. For each PC, the modal contributions to the total variances are also shown. We focus on the coastal GOM and the offshore areas including the George Bank are not considered in the calculation.

APPENDIX

Appendix: A. fundyense model parameterizations

The evolution of *A. fundyense* can be expressed as a single advection – diffusion - reaction equation (Stock et al., 2005; McGillicuddy et al., 2005; He et al., 2008):

$$\frac{\partial C}{\partial t} + (\vec{u} + w_a) \cdot \nabla C = \nabla \cdot K \nabla C + (\mu - m)C + F_g \quad (1),$$

where C is the cell concentration of *A. fundyense*, \vec{u} and w_a are the fluid velocity and *A. fundyense* upward swimming velocity (10 m day⁻¹ as determined from laboratory experiments; Kamykowski et al., 1992); K is the diffusivity coefficient, μ and m are the cell growth and mortality terms respectively, and F_g is the germination flux from cysts in the sediment layer to vegetative cells in the water column. Details of each term are described below.

(1) Cyst germination flux F_g is a critical element of *A. fundyense* population dynamics (Anderson et al., 2005c) and is found to be the first-order predictor for the overall magnitude of the *A. fundyense* bloom in the Western GOM (e.g., McGillicuddy et al., 2005; He et al., 2008; Li et al., 2009). The germination potential together with an endogenous clock, and cyst abundance determine the germination flux, such that

$$F_g = \int_0^{1cm} G(T, E(z), t) \times cyst\ abundance\ dz \dots \dots \dots (2),$$

where $G(T, E(z), t) = G(T, E(z)) \times EC(t) \dots \dots \dots (3),$

$G(T, E(z), t)$ is rate of germination (% of initial cysts day⁻¹) based on the bottom light condition $E(z)$ after light is exponentially attenuated in the water column and the

sediment layer, and the bottom temperature condition at a given time t . z is the depth of the sediment layer (top 1-cm in this case, see *Anderson et al.*, 2005c, *McGillicuddy et al.*, 2005; *Stock et al.*, 2005).

First, $G(T, E(z))$ is the value of germination rate (**Figure A-1a**) as expressed in the following formulations:

$$G(T, E(z)) = G(T, E_{lgt}) \quad \text{when in a light-germination condition, i.e., } E(z) \geq E_{lgt},$$

$$G(T, E(z)) = G(T, E_{drk}) \quad \text{when in a dark-germination condition, i.e., } E(z) \leq E_{drk},$$

$$G(T, E(z)) = G(T, E_{drk}) + (G(T, E_{lgt}) - G(T, E_{drk})) \times \frac{E - E_{drk}}{E_{lgt} - E_{drk}}$$

$$\text{when in an transitional-germination condition, i.e., } E_{lgt} \geq E(z) \geq E_{drk}.$$

In the above equations, $G(T, E_{lgt})$ and $G(T, E_{drk})$ are expressed as:

$$G(T, E_{lgt}) = G_{\min}(E_{lgt}) + \frac{(G_{\max}(E_{lgt}) - G_{\min}(E_{lgt}))}{2} \times \{ \tanh(\alpha(E_{lgt})T - \beta(E_{lgt})) + 1 \},$$

$$G(T, E_{drk}) = G_{\min}(E_{drk}) + \frac{(G_{\max}(E_{drk}) - G_{\min}(E_{drk}))}{2} \times \{ \tanh(\alpha(E_{drk})T - \beta(E_{drk})) + 1 \},$$

in which E_{drk} and E_{lgt} refer to the irradiance under the ‘‘light’’ and ‘‘dark’’ experimental conditions. In our present modeling framework, the threshold for $E(z)$ is $E_{lgt} = 2.4 \text{ w m}^{-2}$ for light germination condition and $E_{drk} = 0.024 \text{ w m}^{-2}$ (1% of E_{lgt}) for dark germination condition (*Anderson et al.*, 2005c). Transitional germination condition is ‘transitional’ between shallow and bright cyst bed nearshore and deeper, darker cyst bed offshore.

G_{\max} and G_{\min} occur over broad ranges (Anderson, 1998), and is chosen as 8.72 (4.26) and 1.5012 (1.04) day^{-1} for light (dark) condition in our model. Slopes over

moderate temperature- α and β are chosen to be 0.790 (0.394) and 6.27 (3.33) for light (dark) condition, respectively.

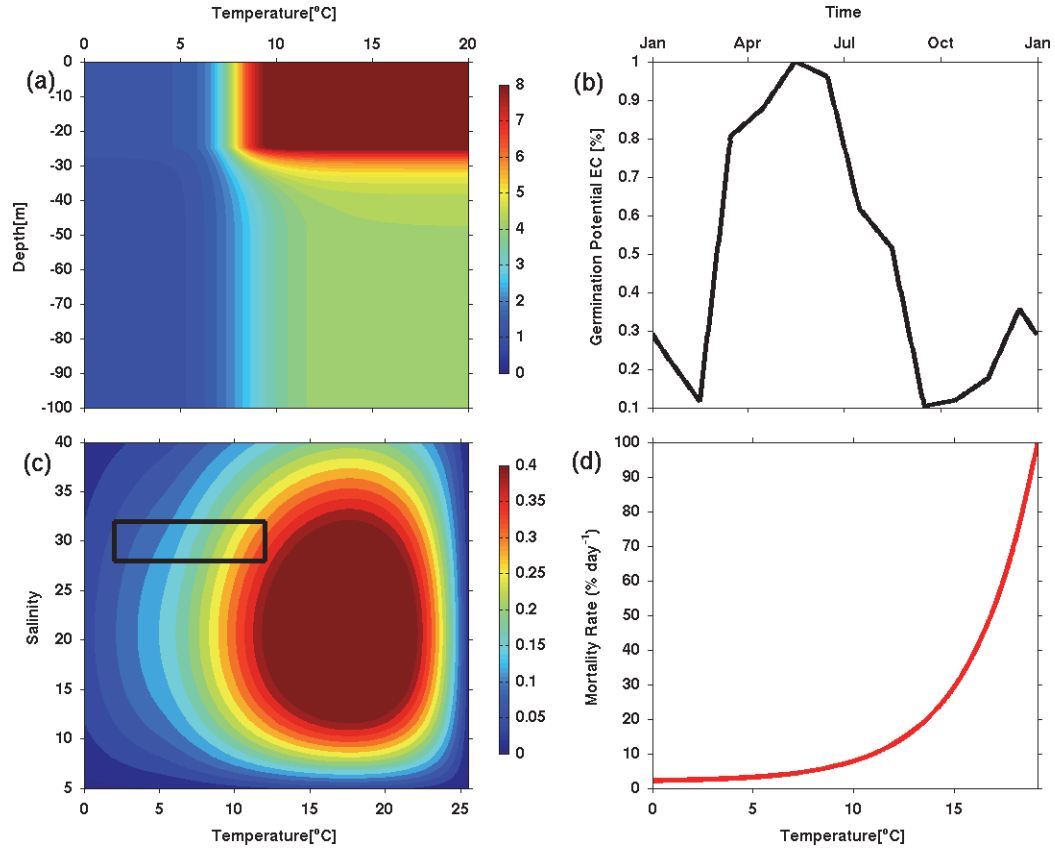


Figure A-1: Biological model summary adapted from *Stock et al. (2005)* and *He et al. (2008)*. (a) Germination rate $G(T, E(z))$ (% day⁻¹) at sediment surface as a function of temperature and light attenuation. Light was converted to depth using an attenuation coefficient of 0.2 m⁻¹ and a characteristic surface irradiance of 345.5 w m⁻². (b) Endogenous clock function (EC) showing the germination potential in percentage with respect to the maximum germination rate $G(T, E(z), t)$. (c) The light-saturated growth rate ($\mu_{max}(T, S)$ in equation 6 in day⁻¹) as a function of temperature and salinity. We used the optimal growth rate $\mu_{max}(T, S)=0.58$ day⁻¹. Box area represents the majority of range of temperature and salinity conditions in the model simulation. (d) Mortality rate (% of cells

Second, $EC(t)$ is the germination endogenous clock (**Figure A-1b**), which is the ratio of the germination at any time t relative to the maximum potential $G(T, E(z), t)$ (Stock *et al.*, 2005).

Third, cyst abundance is based on the sediment core from gulf-wide ship survey conducted in the preceding fall. Continuous monitoring of the cyst abundance enables the modeling of the *A.fundyense* possible (**Figure A-2**).

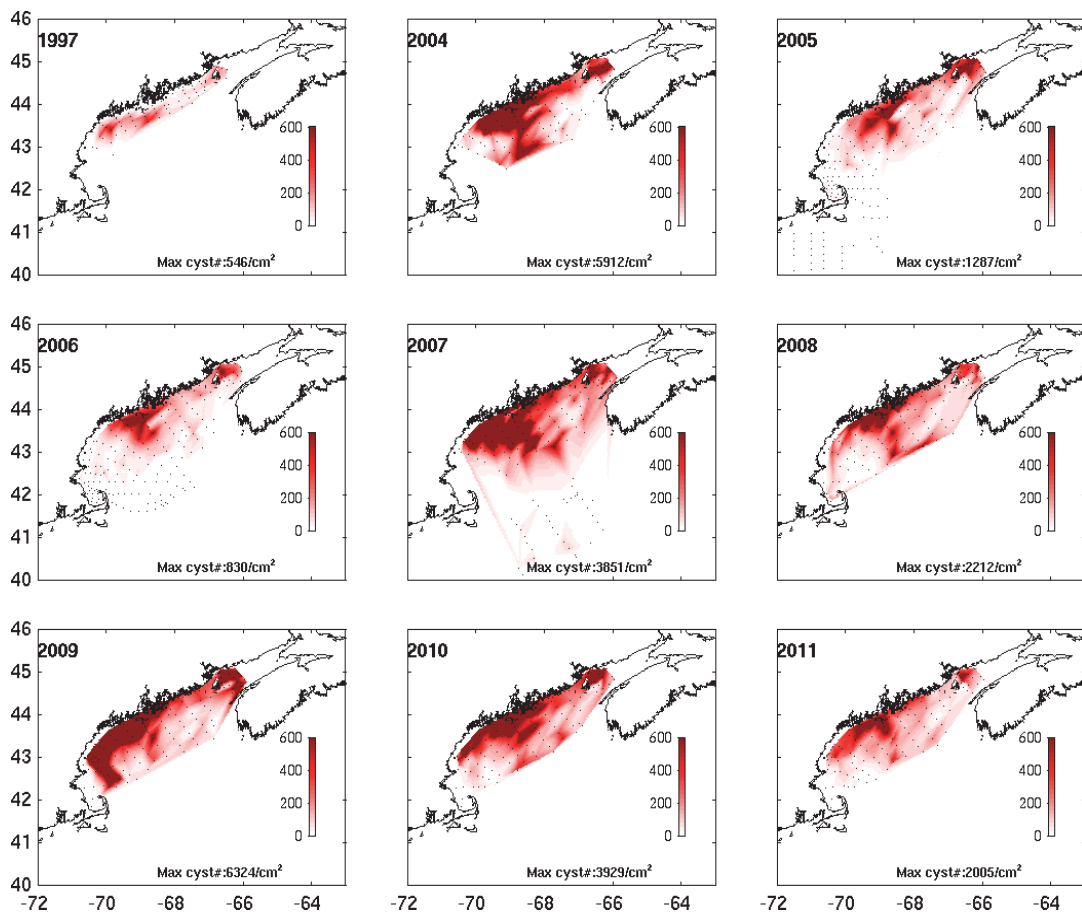


Figure A-2. Maps of the cyst abundance in the upper 1-cm sediment layer collected during fall season of 2004-2011 (in cm^{-2}). Scattered dots are the observation locations and colored plots represent the cyst abundance.

(2) The growth term μ is dependent on temperature (T), salinity (S), solar non-spectral irradiance (E) and nutrient concentration (NO_3 in our model).

The temperature and salinity dependence $f(T)$ and $f(S)$ were formed from laboratory experiments (Stock *et al.*, 2005):

Temperature dependence:

$$\begin{aligned} f(T) &= -0.000513 T^3 + 0.0160 T^2 - 0.0867 T + 0.382 T \text{ when } (T \geq 5 \text{ }^\circ\text{C}) \\ f(T) &= f(T=5) - 0.0345 (5 - T) \text{ when } (T < 5 \text{ }^\circ\text{C}) \end{aligned} \quad (4)$$

Salinity dependence:

$$f(S) = 0.0000882 S^3 - 0.00808 S^2 + 0.220 S - 0.872 \quad (5)$$

Then the light limited growth term ($\mu(E, T, S)$) and the nutrient limited growth rates $\mu(NO_3, T, S)$ are defined as follows:

$$\begin{aligned} \mu(E, T, S) &= (\mu_{\max}(T, S) + \mu_0^r) \tanh\left(\frac{\alpha_g E}{\mu_{\max}(T, S) + \mu_0^r}\right) - \mu_0^r \\ \mu(NO_3, T, S) &= \mu_{\max}(T, S) \times \frac{[NO_3]}{K_N + [NO_3]} \end{aligned} \quad (6)$$

Where $\mu_{\max}(T, S) = \mu_{\max}(T_{opt}, S_{opt}) \times f(T) \times g(S)$ as shown in **Figure A-1c**.

$\mu_{\max}(T_{opt}, S_{opt}) = 0.575$ is the growth rate at optimal temperature and salinity. $\mu_0^r = 0.25$ is the maintenance respiration rate, while $\alpha_g = 0.036$ denotes the growth efficiency. $[NO_3]$ is the nutrient concentration that takes effect. $K_N = 3.0$ is the half-saturation constant for the nutrient limiting growth term. E in $w m^{-2}$ is net short wave radiation obtained from NCEP reanalysis (<http://www.cdc.noaa.gov/>). The overall growth rate is then determined according

to Liebig's Law (*Liebig*, 1845) of the minimum of

$$\mu(E, NO_3, T, S) = \min(\mu(E, T, S), \mu(NO_3, T, S)) \quad (7)$$

(2) The mortality (**Figure A-1d**) is parameterized as a function of water temperature based on Q_{10} formulation (*He et al.*, 2008):

$$m = a \cdot Q_{10}^{[(T-10.35)/10]} + 0.019 \quad (8)$$

where $a=0.066$, and Q_{10} is 21.75. The assumption is that the predator feeding on *A. fundyense* cells will increase as temperature increases, just as growth rate of *A. fundyense* grows with temperature. This parameterization is proven to be more effective in capturing the late-season demise of the bloom, even though ongoing research is trying to further improve the representation (*He et al.*, 2008).